UNIVERSITY OF MILANO - BICOCCA
Department of Materials Science

PhD School in Nanostructures and Nanotechnologies
XXVII cycle

First principles simulations of phase change materials for data storage

A. A. 2013 – 2014

PhD dissertation of:
Silvia Gabardi

Tutor:
Prof. Marco Bernasconi

Contents

Introduction

Phase change compounds are a class of materials employed for data storage applications such as rewritable optical disks (CD-RW, DVD-RW, Blue-Ray disks) and electronic memories of new concept, named Phase Change Memories (PCM) [1, 2]. These applications rely on a fast (50 ns) and reversible change between the crystalline and the amorphous phases upon heating. The two phases correspond to the two states of the memory, i.e. the 0 and 1 bits, that can be discriminated thanks to a large difference in their optical and electronic properties. The phase transition is induced by heating due to either a laser pulse in the optical memories or to electric pulses in PCMs.

A PCM device consists of a resistor made of a thin film of a phase change material between a metallic top contact and a resistive electrode that heats up the active layer. The readout of the memory consists of the measurement of the resistivity of the cell at low bias (mV) which changes by about three orders of magnitude across the phase transition. In fact, the amorphous phase is semiconducting, while the crystal is metallic. The programming operations are performed at a higher bias (few Volts) in order to have a current flow high enough to induce by Joule heating either the melting of the crystal and subsequent amorphization or the recrystallization of the amorphous phase. The materials employed in PCMs are typically Te-based chalcogenide alloys such as $(GeTe)_x(Sb_2Te_3)_y$ pseudo-binary alloys and in particular the $Ge_2Sb_2Te_5$ (GST) compound [2, 3]. These devices are already commercial products; PCM at the 45 nm technological node have been delivered to the market by the company Micron in early 2013 mostly for applications in mobile phones. These devices provide a better cyclability, scalability and a much higher programming speed with respect to Flash memories [4].

In order to widen the fields of applicability of these devices, alternative materials with a crystallization temperature higher than that of GST are under scrutiny in order to increase the thermal stability of the amorphous phase and to ensure a data retention for 10 years at 125 °C as required for instance by the automotive market. In this respect, InSbTe [5, 6] and GaSbTe [7, 8] alloys have been investigated for PCM applications because of their crystallization temperature about 100 °C higher than that of $Ge_2Sb_2Te_5$ and a still high crystallization speed. Different compositions have been proposed and PCM operation has been demonstrated for the compositions $In_3Sb_1Te_2$, $In_3Sb_{2.7}Te_{0.8}$, $In_3Sb_{2.5}Te_{1.1}$ [6, 9] and $Ga_4Sb_6Te_3$ [8]. Materials with high crystallization/melting temperatures are also of interest for the realization of core-shell nanowires [10] (e.g. InSbTe/GST) that might be used to implement multi-bits memory cells [11]. PCM based on nanowires are of interest also because nanostructuring seems to

mitigate the phenomenon of resistance drift [12]. This effect, consisting of an increase of the electrical resistance of the amorphous phase with time, is detrimental for PCM operation and it should be kept as low as possible [13].
In this thesis, we have addressed two issues in this context which, in spite of their great technological relevance, are still unsolved, namely *i*) the atomistic structure of the amorphous phase of InSbTe and GaSbTe alloys and *ii*) the microscopic origin of the resistance drift. The knowledge of the atomistic structure of the amorphous phase is actually mandatory to achieve a microscopic understanding of its functional properties including the nature of the structural relaxations which lead to the resistance drift.
In this work, we have addressed these problems by molecular dynamics simulations based on Density Functional Theory (DFT). Models, 300-atom large, of the amorphous phase of $In_3Sb_1Te_2$, $In_{13}Sb_{11}Te_3$ and $Ga_4Sb_6Te_3$ compounds have been generated by quenching from the melt within DFT molecular dynamics simulations. To assess the reliability of our computational framework, we first studied the properties of amorphous InSb for which experimental structural data are available. These preliminary simulations allowed us to choose the more suitable approximation to the exchange and correlation functional. A comprehensive analysis of the structural, electronic and vibrational properties of the amorphous models have then been carried out for the ternary systems. The simulations have actually provided some clues on the origin of the higher stability of the amorphous phase of these compounds.
The DFT models are, however, still too small to address the study of the resistance drift. This effect is in fact believed to originate from an aging of the amorphous phase which leads to a change in the localized electronic states close to the band edges (Urbach tails) and deep inside the mobility gap. These states are actually controlling the conductivity of the amorphous phase. A sufficiently good statistics in the distribution of defect states is therefore needed to address the study of the drift. To this end, we have then chosen to study the drift in the phase change compound GeTe for which a reliable interatomic potential is available. The potential is based on the fitting of a huge database of DFT energies with a Neural Network scheme [14]. The potential allows simulating several thousands atoms by keeping an accuracy close to that of the underlying DFT method.
Large models of about two thousand atoms of amorphous GeTe have then been generated by quenching from the melt within classical molecular dynamics simulations by using a Neural-Network potential. The electronic structure has then been analysed after geometry optimization at the DFT level. The aging of the amorphous phase has been mimicked by either annealing the models at 500 K and by means of metadynamics simulations to accelerate the drift process at room temperature. The evolution in time of the defect states allowed us to propose a microscopic model for the resistance drift and to establish a link between the extent of structural relaxations in the amorphous phase and the speed of the crystallization process.
This study have been carried out within the goals of the European FP7 project SYNAPSE on the "Synthesis and functionality of chalcogenide nanostructures for phase change memories"

which aims in particular at realizing core-shell nanowires for multi-bit memories.
The thesis is organized as follows. In Chapter 1 we introduce the general features of phase change memories and the physical properties of the most studied GST and GeTe compounds. Available experimental information on InSbTe and GaSbTe alloys are also briefly reviewed. Generalities on the crystallization process and on the drift phenomenon in phase change materials are presented in details in Chapter 1. Chapter 2 is devoted to a brief introduction to the theoretical methods that we have used, namely DFT molecular dynamics simulation techniques and the metadynamics method. A novel simulation technique to efficiently generate amorphous models developed by our coworkers is also presented, as it has been used in the preliminary simulations on InSb. The results on the structural, electronic and vibrational properties of amorphous InSb, InSbTe and GaSbTe alloys are reported in Chapter 3. Finally, Chapter 4 reports our results on the simulation of the drift phenomenon in amorphous GeTe.

1. Phase Change Materials

1.1. General features

Phase change materials are of great technological interest for their application in rewritable optical memories as CD-RW, DVD-RW, Blue Rays and DVD-RAM. In the last few years, these compounds have also been proposed as active materials in a new type of electronic non-volatile memories: the Phase Change Memory (PCM) [1, 2].
The operating principle of PCMs consists of a very fast ($\sim$50 ns) and reversible transformation between the amorphous and crystalline phases of a small portion of the active material. The transition is induced by heating using a laser pulse in optical memories or via Joule-effect using electrical pulses in PCMs [3].
The two phases are the 0 and 1 states of the memory cell that can be discriminated because these materials show a large contrast in optical properties and electrical conductivity between the two phases. The readout of the device consists of a measurement of reflectivity in optical memories and of resistivity in PCMs.
The first materials showing phase change properties were discovered in the late Sixties by J. F. Dewald [15] and S. R. Ovshinsky [16], but the crystallization speed of these alloys was too low for a practical application. In the '90, the need of faster rewritable optical discs led to the discover of several phase change compounds based on chalcogenides alloys. PCMs realized with this kind of materials show a readout speed comparable to that of Flash memories and a considerably higher writing speed (50 ns against 1-1000 μs of Flash technology) together with better cycling and scaling properties with respect to other devices on the market. The 45 nm technological node PCM device [17, 18] became available on the market in 2012 and smaller scale devices are under development. The increase of the spatial density of information in the memory device it is also possible by implementing multi-bit memory cells through the PCM technology as discussed in Section 1.1.1. The future goal is to use phase change memories to realize so called storage class memories which are not volatile but with access speed not far from that of DRAM [19].
A PCM cell (Figure 1.1) is composed by a transistor and a resistor. The transistor works as a selector that modulates the current pulse during the read and write operations, while the resistor is made by a thin film of active material between a metallic contact and a resistive electrode, usually TiN or TiSiN, that can heat up the chalcogenide material causing the phase transition. The device can be read by measuring the resistance using voltages of 100 mV and

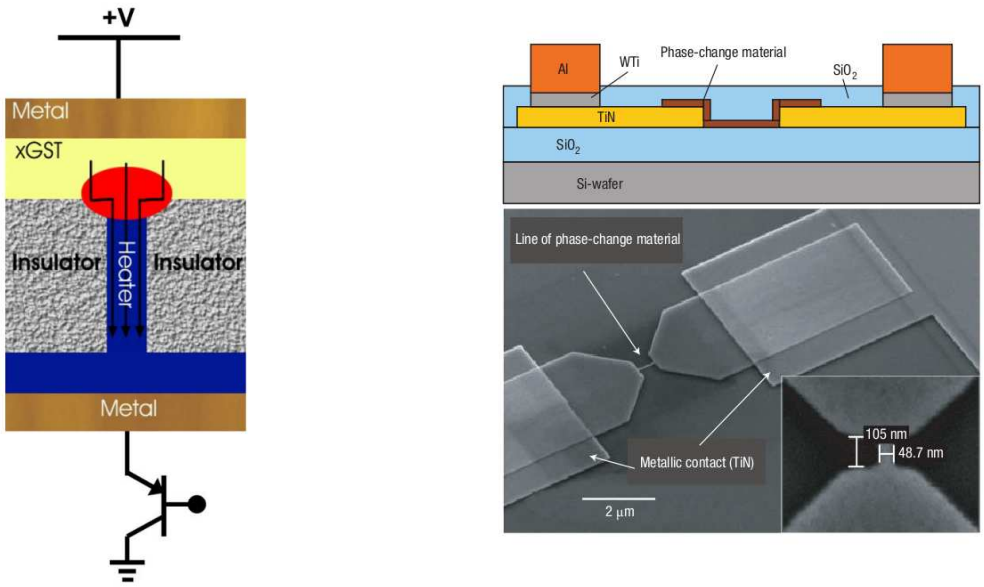

(a) **(b)**

Figure 1.1.: Different geometries of a PCM device. The scheme of the so called "mushroom" PCM cell is shown in (a). The thin layer at the chalcogenide/heater interface is the active region. [1]. (b) Section and SEM (Scanning Electron Micrograph) image of a memory cell in the bridge configuration [20].

current pulses 50 ps long. In fact, the amorphous is an insulator, while the crystal is metallic and the two phases present a difference in conductivity of at least three orders of magnitude. Programming the cell (Figure 1.2), is realized by two different processes: SET and RESET. During the RESET operation, the temperature of the active layer in the memory cell is raised over the melting temperature T_m by using a short and intense current pulse. Since only a small portion of the material is heated up, the temperature gradient generated inside the cell is very high leading to high cooling rates (10^{10} K/s) that prevent the crystallization of the melt obtaining an amorphous structure with an electrical resistance of the order of MΩ. To revert the transformation from the amorphous to the crystalline phase, the material is heated up to a temperature higher than the glass transition temperature T_g at which the atomic mobility is high enough to allow the recrystallization on the time scale of tens of ns. This process is called SET operation and is the slower step of the programming procedure as longer current pulses are applied. The resistance of the cell in the SET state is of the order of kΩ.
Although the amorphous phase shows high electrical resistivity at low voltages (mV), by increasing the applied bias above a threshold voltage (V_{th}) of the order of few Volts, the material undergoes an electronic transition to a high conducting state. This phenomenon called threshold switching allows for Joule heating of the amorphous phase that induces the recrys-

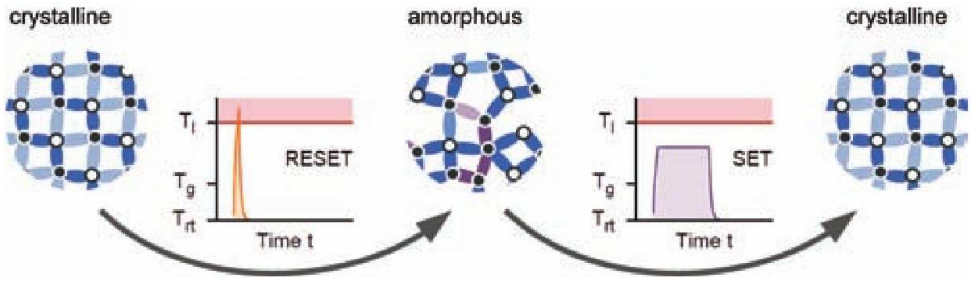

Figure 1.2.: Scheme of the SET and RESET operations in a phase change device [21]. The two processes are based on the amorphous-crystalline reversible transition. Amorphization (RESET) occurs by quenching from the liquid phase obtained by heating the cell above the melting temperature with a short electric pulse. Crystallization (SET) proceeds from the amorphous by using a longer and less intense pulse.

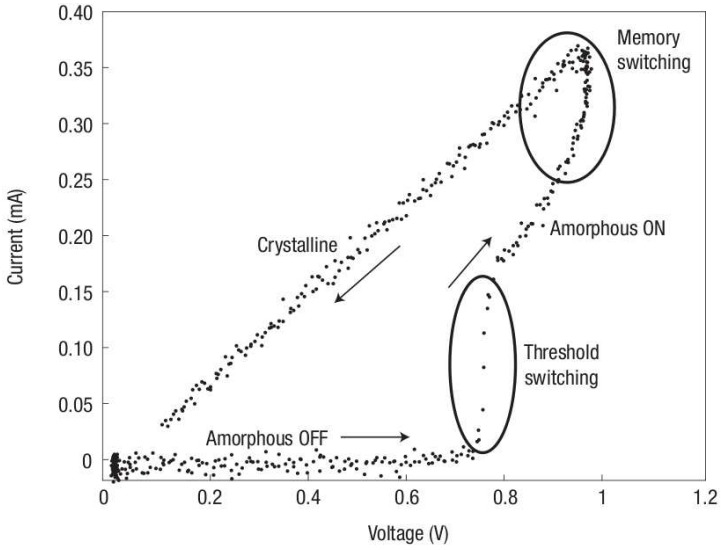

Figure 1.3.: Typical current-voltage characteristic of a phase change device. When the applied voltage is low, a very low current flows through the amorphous material, while, by applying a bias above a threshold voltage of about 0.7 V, the resistance drops down and the current intensity increases (threshold switching) inducing recrystallization (memory switching). The crystalline phase is metallic with a low ohmic resistance [3].

tallization at a moderate voltage. During the readout of the memory, the applied voltage is lower than the V_{th}. The plot in Figure 1.3 shows the current-voltage characteristic for the two phases.

1.1.1. Multi-bit phase change memories

A way to increase the information density in a memory device is the storing of more than one bit in a single cell [11]. In the case of PCMs, the realization of multi-bit memories was firstly proposed by Ovshinsky and co-workers in 1995 [22] exploiting the possibility to reach intermediate-resistance states by controlling the dimensions of the amorphized region within the memory element. Since phase change materials have a resistivity contrast greater than three orders of magnitude [23], as reported in Figure 1.4, it is in principle possible to have well separated intermediate resistance values to realize a multi-bit cell.

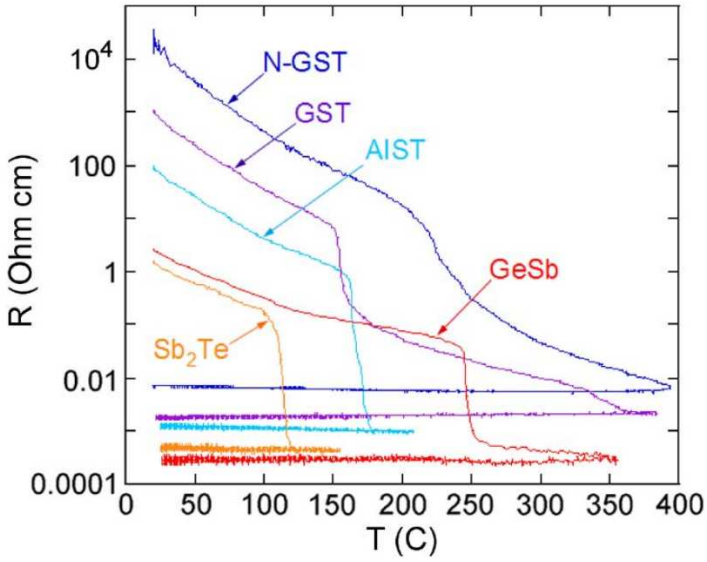

Figure 1.4.: Resistivity as a function of temperature for phase change alloys. Resistance drops sharply when the crystallization temperature is reached. The resistivity of the crystalline phase can be even six orders of magnitude lower than that of the amorphous. GST → $Ge_2Sb_2Te_5$, N-GST → 7 at. % N-doped GST, GeSb → $Ge_{15}Sb_{85}$, AIST → Sb_2Te doped with 7 at. % Ag and 11 at. % In [23].

A multi-bit PCM that stores a number N of bits in a single cell, needs to have 2^N different and non overlapping resistance values, which are called "levels". For instance, a 2-bits PCM device has got 4 different levels. It was shown that up to 16 intermediate levels could be programmed in a cell [24]. Figure 1.5 shows schematically a 2-bits or 4-levels PCM cell.
In order to realize multi-bit memories, one possibility is to use cell architectures composed by a stacking of different chalcogenide layers [25–27]. An example of a 2-bits stacked PCM cell is reported in Figure 1.6a [27]. Tungsten acts as a metallic electrode and SiO_2 is a thermal

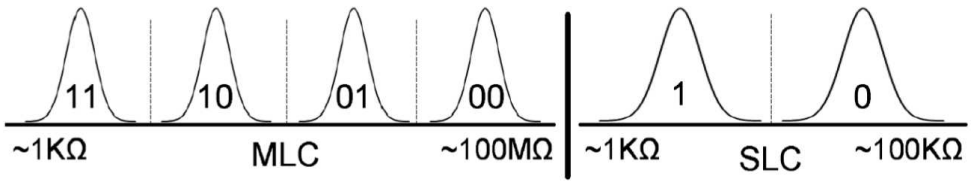

Figure 1.5.: Schematic representation of the separate resistance values for a 2-bits PCM (MLC) and a single-bit PCM (SLC). The single-bit cell shows two different resistance levels (0 and 1 bits), while the 2-bits cell has four different resistance levels each of them indicating a couple of bit: 11, 10, 01 and 00. The distributions of resistance values for each level are broad but do not overlap.

and electrical barrier. The active area of the cell is made of a stack of three layers of phase change material with three heaters. The different size of the heaters is the key to make the phase change material transforming layer by layer. This configuration allows achieving four different resistance values (Figure 1.6b). Multi-bit phase change memories can be realized also with the classic "mushroom" configuration. In this case, it is often necessary to engineer the active material, for instance through doping as for nitrogen-doped GST. Whit respect to GST, the doped alloy shows a smoother change of the resistance as a function of temperature allowing to reach intermediate resistance values upon heating [24, 28]. Different programming protocols are also needed in order to amorphize or crystallize different volume sizes of the chalcogenide material, resulting in conduction paths with different resistance values [24, 29] (Figure 1.7).

To obtain well separated resistance values in the multi-level PCM device, it is also essential to operate an iterative procedure during the programming process. In fact, it is possible that the same pulse voltage leads to different temperatures in different cells because of nanoscale variations in the cell structure. To avoid overlap of the resistance distributions for different levels, a read-verify-write algorithm [24] can be applied. This method iteratively applies a writing pulse on a cell and reads the resistance value. If this value does not lay within the target bandwidth, a new slope for the programming pulse is calculated on the basis of the read resistance and the cell is programmed again. It has been demonstrated that an average of three of these programming cycles is sufficient to achieve well separated resistance values for 16 intermediate levels. This technique enables a write speed of about 3.5 MB/s and a readout time of about 120 ns for a 2-bits cell [30].

Another realization of multi-bit PCMs is based on core-shell nanowires (CS-NW). In this configuration the active region of the memory cell consists of a CS-NW made of two different chalcogenide materials that feature different electrical and thermal properties. Single-level PCM devices with GeTe or In_2Se_3 NW have already been realized [31] showing a lower power consumption compared to conventional PCMs. NWs allow also to further scale down the size

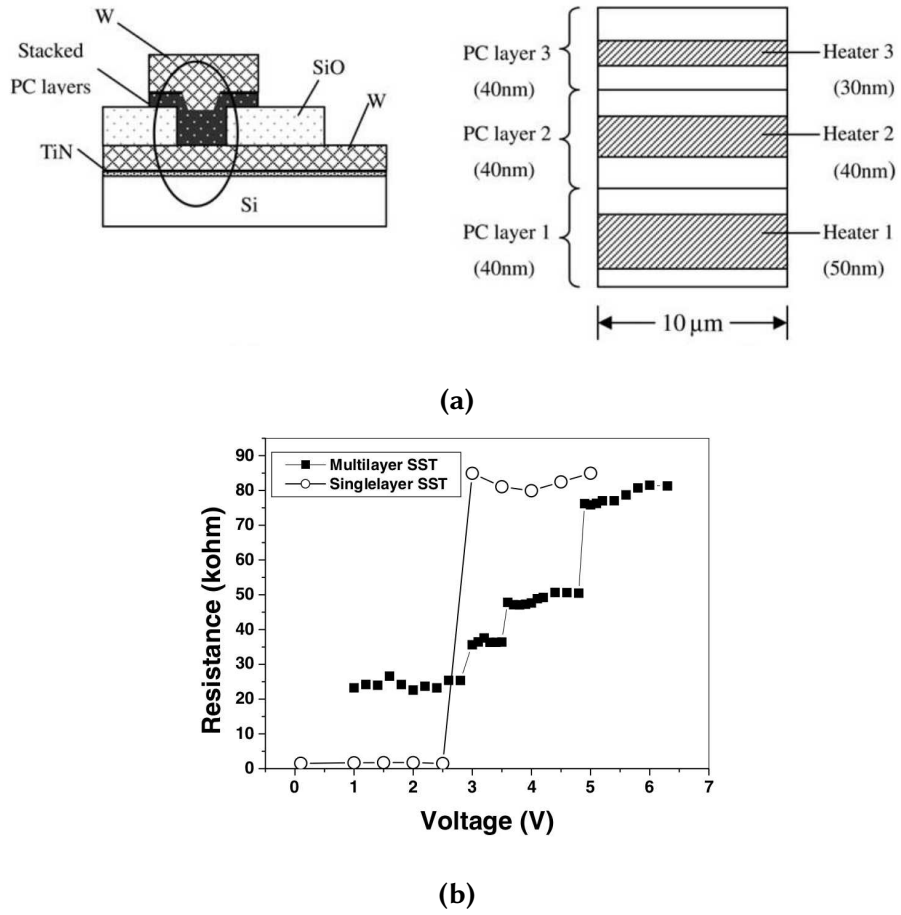

Figure 1.6.: Scheme of a stacked 2-bits phase change memory cell (a). The TiN layer improves the bonding capability between tungsten electrode and Si substrate. SiO_2 acts as a heat insulator. The active region is formed by three layers of the chalcogenide material spaced out by three heaters of different size. This configuration provides a four level resistance-voltage characteristic (b) [27].

of the device and to obtain defect-free crystalline structures. Multi-level devices can be realized by using CS-NW where the two phase change alloys of the core and shell have a different melting temperature. Programming can be carried out by applying current pulses of different intensity in order to induce a sequential melting of the components of the wire reaching intermediate values of resistance.

Multi-level memories with CS-NW made of $Ge_2Sb_2Te_5$ (core) and GeTe (shell) have been realized [10] obtaining devices showing three separated levels (Figure 1.8). The cell has the lowest resistance when both the GST and GeTe are in the crystalline phase. By applying a current pulse of 1.2 mA, the GST core melts and amorphize, while GeTe remains crystalline obtaining an intermediate value for the resistance. The higher resistive state is reached when both GST

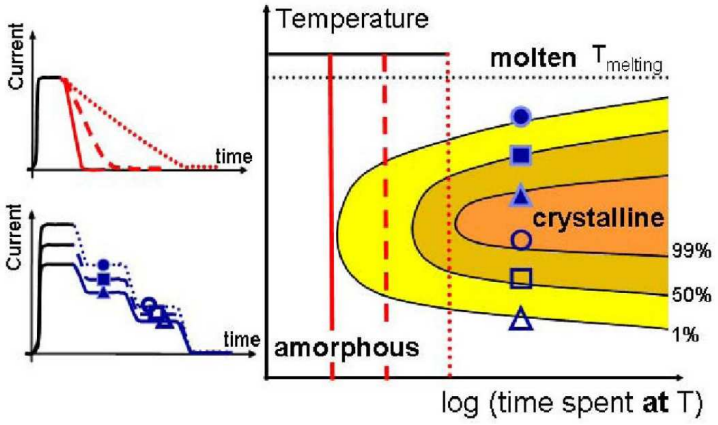

Figure 1.7.: Sketch of the time-temperature-transformation-chart in a multi-level PCM. Starting from a large molten region, the same brief time spent under a linear pulse (vertical line each temperature) or a stair-case pulse (symbols marking significant time at a few temperatures) provides control over resistance through the time- and temperature-dependent recrystallization of the amorphous plug [24].

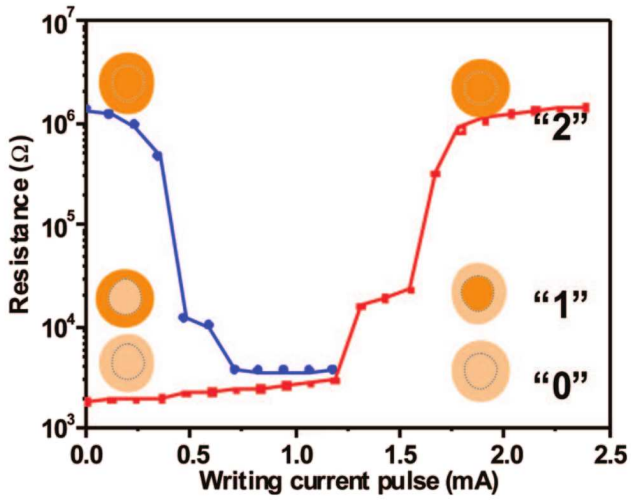

Figure 1.8.: Variation of resistance of a core/shell GST/GeTe nanowire device as a function of current pulses with varying amplitudes. Pulse durations are 100 ns for amorphization and 300 ns for crystallization. The three different resistive states (low, intermediate, and high) achieved with application of current pulses are clearly distinct. The schematic represents the cross section of the core/shell nanowire at each stage of transition, where color change corresponds to the phase transition: light orange represents crystalline phase, and dark orange is amorphous. Blue line refers to an initially amorphous nanowire, while red line to a nanowire initially in the crystalline phase [10].

and GeTe are in the amorphous phase.
One of the more important issues in the fabrication of multi-bit phase change memory is the drift of the amorphous resistance that can lead to an overlap of the intermediate levels that will be discussed in Section 1.4.

1.1.2. Typical phase change alloys

The materials most commonly used in optical discs are tellurium-based chalcogenides alloys [2] (Figure 1.9), in particular along the pseudo-binary tie-line such as $(GeTe)_x(Sb_2Te_3)_y$. The first compound found to display a fast recrystallization and a high optical contrast was actually germanium telluride, GeTe [32]. Later Ge, Sb and Te-based alloys have been deeply investigated, in particular the composition $Ge_2Sb_2Te_5$ which was employed in DVD-RAM and it is now utilized in commercial PCM devices. Another class of alloys with phase change properties includes SbTe-based chalcogenides doped with Ag, In, Ge or Ga. A composition close to $Ag_5In_5Sb_{60}Te_{30}$ forms the active layer of DVD-RW and DVD+RW. The composition $Ge_8Sb_2Te_{11}$ is used instead in blue-ray discs.
Regarding PCMs, $Ge_2Sb_2Te_5$ or GST is actually the material chosen for industrial applications because it represents a good compromise between speed of crystallization and stability of the amorphous phase. In fact, the amorphous phase is a metastable state and it spontaneously tends to crystallize causing the loss of the data. In the last years, the need of devices stable at high temperature for automotive applications has driven the search for materials stable at higher temperature in the amorphous phase to ensure a data retention for ten years

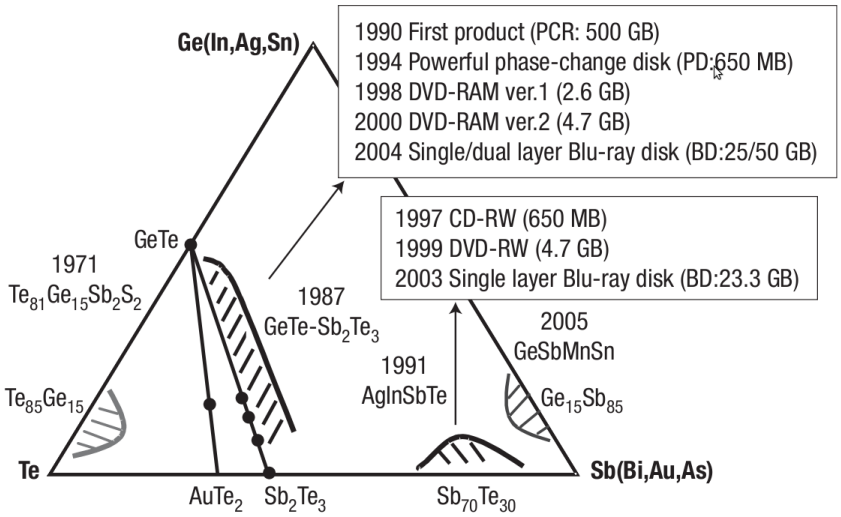

Figure 1.9.: Ternary phase diagram with different phase change materials, their discovery year and their employment in different optical memories [3].

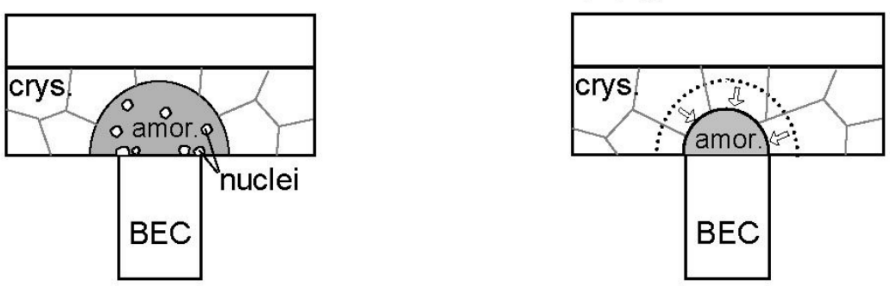

(a) homogeneous nucleation

(b) growth from crystal-amorphous interface

Figure 1.10.: Crystallization mechanisms in a PCM cell [35]. (a) Homogeneous crystallization is the process that characterizes compounds like $Ge_2Sb_2Te_5$ and GeTe, while (b) in GeSb and antimony rich GeSbTe alloys the crystallization proceeds from the amorphous/crystal interface.

at 125 °C. Some of the materials proposed for this purpose are nitrogen- and oxygen-doped $Ge_2Sb_2Te_5$ [33, 34], indium- and gallium-based alloys such as $InGeTe_2$ [35], $In_3Sb_1Te_2$ [36] and $Ga_4Sb_6Te_3$ [37], antimony-rich GeSbTe alloys [38] and doped germanium telluride [39, 40]. All these compounds have a crystallization temperature higher than that of GST which implies a greater stability of the amorphous phase and a better retention at high temperature. Concerning the crystallization mechanism, it is possible to classify phase change materials in two different groups: compounds displaying a homogeneous nucleation (nucleation driven) and compounds displaying a crystal growth from the crystalline/amorphous interface (growth driven). $Ge_2Sb_2Te_5$ presents a homogeneous crystallization mechanism [3] with the rapid formation of several subcritical nuclei in the supercooled liquid (Figure 1.10a). Growth driven phase change compounds are, among others, GeSb, antimony-rich GeSbTe alloys [38] and $Ga_{16}Sb_{84}$ [41]. In these case the crystallization proceeds from the crystalline-amorphous interface (Figure 1.10b). Materials that crystallize homogeneously present fewer scaling problems since the kinetic of crystallization is lesser dependent on the volume of the active material.
The origin of the fast crystallization has been addressed in several works and it will be discussed in details in Section 1.2.2.

1.2. Physical properties of phase change compounds

1.2.1. GeTe and $Ge_2Sb_2Te_5$

Germanium telluride was the first phase change chalcogenide material proposed for data storage applications. Although GST was firstly preferred for PCM devices, GeTe is now being reconsidered for applications at high temperatures due to its higher crystallization temperature [42]. Burns *et al.* [43] have also demonstrated that the SET pulse duration can be reduced down to 1 ns for a GeTe ultrascaled device.
GeTe presents two crystalline phases at normal pressure [44]. The stable phase at low temperature is the trigonal α-phase with space group $R3m$, lattice parameter $a = 4.2398$ Å and angle $\alpha = 57.9°$ [45], that originates from a distortion of an NaCl-type lattice along the $< 111 >$ direction (Figure 1.11). In this configuration, Ge atoms are six-fold coordinated forming three

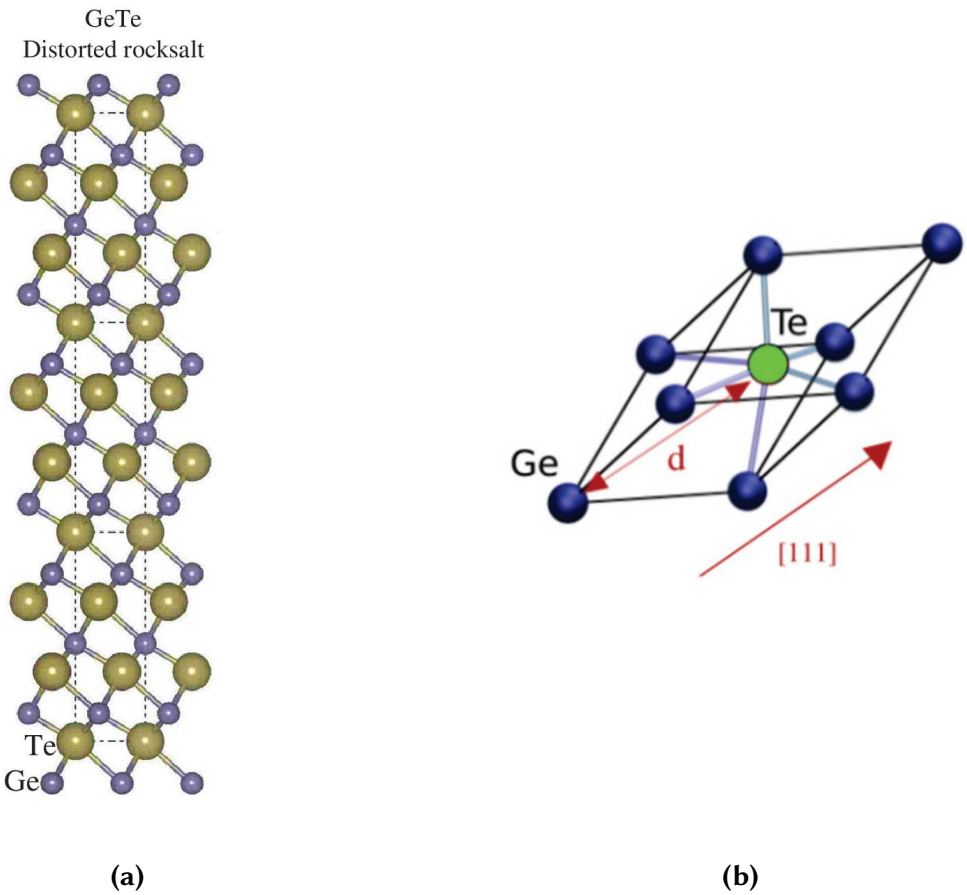

Figure 1.11.: (a) Crystalline structure of α-GeTe, the stable trigonal phase, [49] and (b) the trigonal cell that can be seen as a NaCl-type lattice with a distortion along the $< 111 >$ direction [14].

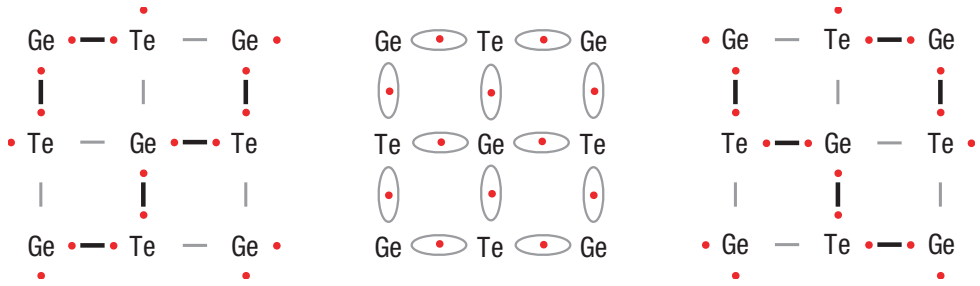

Figure 1.12.: Schematic representation of the ideal resonant bonding in crystalline GeTe. In the two limiting structures on the left and on the right, each Ge atom two three $p-p$ bonds along two perpendicular directions. The situation, shown in the middle of the figure, is a superposition of the two limiting cases with delocalized p electrons [50]. In the real system, a symmetry breaking (Peierls distortion) leads to a partial resonance with the formation of long and short bonds.

shorter and three longer GeTe bonds of 2.84 and 3.17 Å, respectively, resulting in a "$3+3$" coordination (Peierls distortion) [45].
β-GeTe is the stable phase above 430 °C with a cubic rocksalt structure (space group $Fm\bar{3}m$) and a lattice parameter $a = 5.996$ Å. The $3+3$ coordination with shorter and longer bonds locally survives also in the cubic phase. In fact, the Peierls distortion occurs in a disordered manner along all equivalent $<111>$ directions, as revealed by EXAFS measurements [46]. In this configuration, each p orbital forms a long and a short bond in two opposite directions. This situation was called "resonant bonding" by Pauling and is schematically explained in Figure 1.12 where two limiting cases are shown on the left and on the right with Ge atoms forming two bonds with the p orbitals along two perpendicular directions. The real configuration is a superposition of the two limiting structures with the p electrons delocalized along all the six directions leading to a high electronic polarizability. However in crystalline GeTe, a symmetry breaking (Peierls distrortion) leads to two non-equivalent limiting structures and a weakening of the resonance.
Above 725 °C GeTe melts [47] in a semiconducting liquid that still shows locally a "$3+3$" coordination originated by the Peierls distortion [48]. Although the stable phase at room temperature is the trigonal one, the crystalline structure of interest in PCM cells is the rocksalt phase. In fact, the amorphous phase can crystallize in the metastable cubic phase which can be recovered at normal conditions.

$Ge_2Sb_2Te_5$ or GST is the material of choice for commercial PCM devices and DVD-RAM thanks to the stability of the amorphous phase and the very fast phase transition. GST presents two crystalline phases as well at normal pressure: the stable structure has a hexagonal symmetry with space group $P\bar{3}m1$ (Figure 1.13a) [51]. The unit cell has a high aspect ratio and

contains nine atoms in an octahedral coordination arranged in nine layers stacked along the *c* axes. Each layer is shifted by 1/3 with respect to the previous along the $[\bar{1}10]$ direction in a cubic close packing. Weak Te-Te bonds are present across a van der Waals (vdW) gap. The arrangement of Ge and Sb atoms in the stacks is still debated and three sequences have been experimentally proposed:

A Te–Sb–Te–Ge–Te–Te–Ge–Te–Sb–Te
from XRD measurements [51];

B Te–Ge–Te–Sb–Te–Te–Sb–Te–Ge–Te
from high resolution transmission electron microscope (HR-TEM) [52];

C Te–(Sb/Ge)–Te–(Sb/Ge)–Te–Te–(Sb/Ge)–Te–(Sb/Ge)–Te
from XRD measurements with a random distribution of Ge and Sb [53].

Calculations based on density functional theory (DFT) revealed that stacking **A** is the most stable, but the computed energy difference between **A** and **C** is very small [54]. More recent

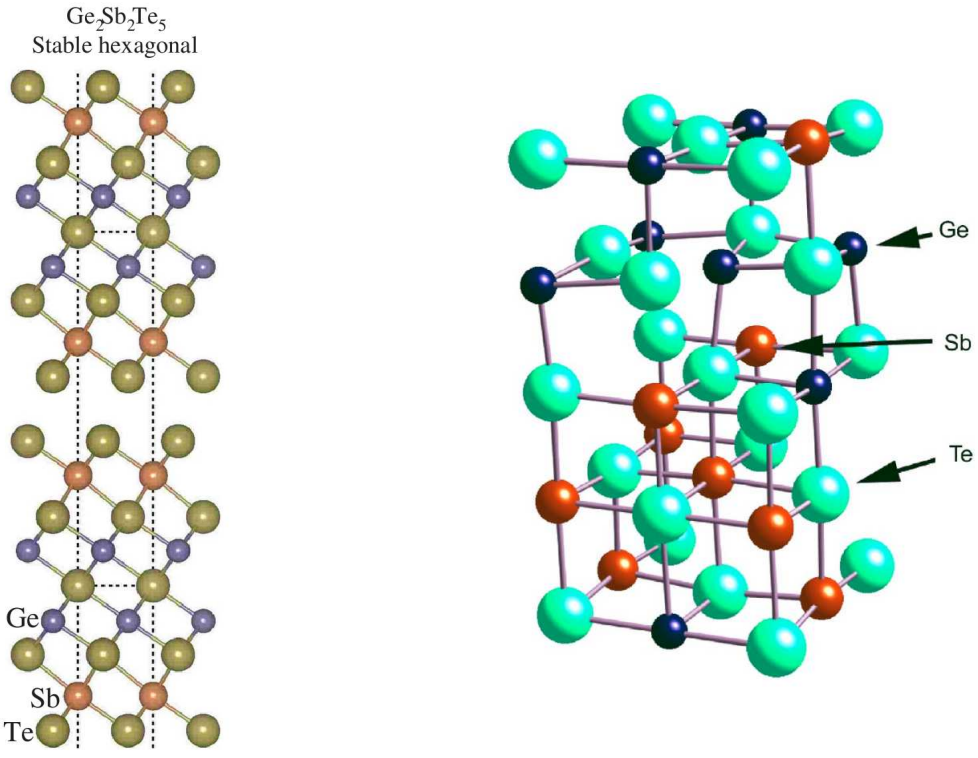

Figure 1.13.: Representation of the structure of the two crystalline phases of GST: (a) hexagonal [49] and (b) cubic rocksalt-like [60].

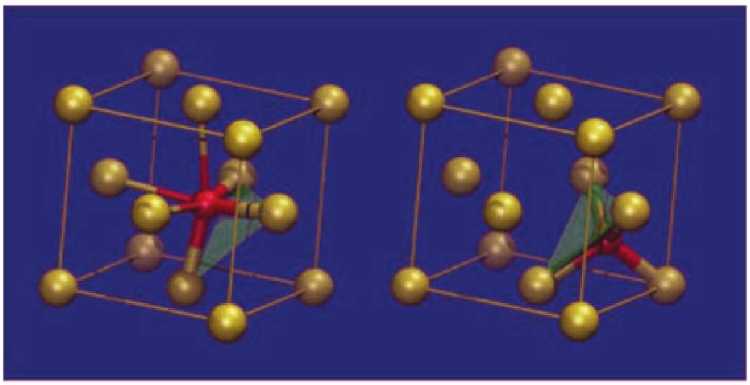

Figure 1.14.: Local structure of GST in the neighbourhood of a Ge atom in the crystalline phase (left) and in the amorphous phase (right) in the model proposed by Kolobov *et al.* [65]. The structural transformation due to the "umbrella flipping" is sketched.

theoretical analysis based on Raman spectra calculations seem to indicate model **C** as the best description of atomic species sequence in hexagonal GST [55]. Transmission electron microscopic analysis of $Ge_2Sb_2Te_5$ nanowires also suggest the disordered structure **C** [56].
Upon heating above the melting temperature (620 °C) and rapidly cooling down, thin films of GST crystallize in a metastable cubic phase with a rocksalt-like structure (Figure 1.13b), space group $Fm\bar{3}m$ and lattice parameter $a = 6.0293$ Å [53]. This is the crystalline phase the amorphous transforms into upon heating in PCM devices. As shown by differential scanning calorimetry (DSC) measurements [57], the cubic phase transforms into the hexagonal phase at a temperature of about 550 °C.
XRD measurements [53, 58, 59] on cubic GST showed that the anionic sublattice is entirely occupied by Te atoms, while the cationic sublattice is formed by Ge and Sb in a random arrangement with 20 % of vacancies. In this configuration, there are, on average, three p electrons per lattice site leading to a closed shell system. Also cubic GST shows a $3+3$ coordination with three shorter and three longer resonant bonds. Both GeTe and GST at the ideal composition are semiconductors with a band gap of the order of $0.5-0.7$ eV. These crystals turn into degenerate p-type semiconductors due to self-doping in the form of Ge/Sb deficiencies (see also Section 1.4).

By cooling down the liquid phase of a phase change material as GeTe or GST sufficiently fast to avoid crystallization or by deposition by different means (e.g. sputtering, MOCVD), it is possible to obtain the amorphous phase (a-GeTe and a-GST). As occurs for other phase change alloys, the amorphization of GeTe and GST is associated with a change in the local structure that is responsible for a change in properties between the crystal and the amorphous. The structure of the amorphous phase thus plays a crucial role in determining the

characteristics of phase change alloys and it has been matter of debate for years.
Extended X-Ray absorption fine structure (EXAFS) analysis [61–63] of amorphous GeTe and GST revealed a four-fold coordination of Ge atoms, as opposed to six-fold $(3+3)$ coordination in the crystal, which immediately suggested a tetrahedral bonding geometry. On the basis of EXAFS data, Kolobov *et al.* [64, 65] proposed a crystallization mechanism based of the conversion of Ge atoms from a tetrahedral to an octahedral geometry, the so called "umbrella flipping" model (Figure 1.14). Other studies based on reverse Monte Carlo (RMC) simulations and synchrotron-radiation x-ray diffraction data [66] showed, instead, no evidence of tetrahedral structures. Later, first principles molecular dynamics (MD) simulations on GeTe and GST provided a deeper insight into the structure of the amorphous phase revealing the coexistence of tetrahedral and defective octahedral-like structures [67–72] (Figure 1.15). MD simulations provided also the total and partial pair correlation functions of GeTe and GST (Figure 1.16a) revealing the presence of homopolar Ge-Ge bonds and Ge-Sb bonds. Both these types of bonds are absent in the crystalline phases and are referred to as "wrong bonds". The partial coordination numbers for GST emerged from the simulations are reported in Table 1.1.
As shown by the coordination number distributions of Figure 1.16b, Ge and Sb atoms are

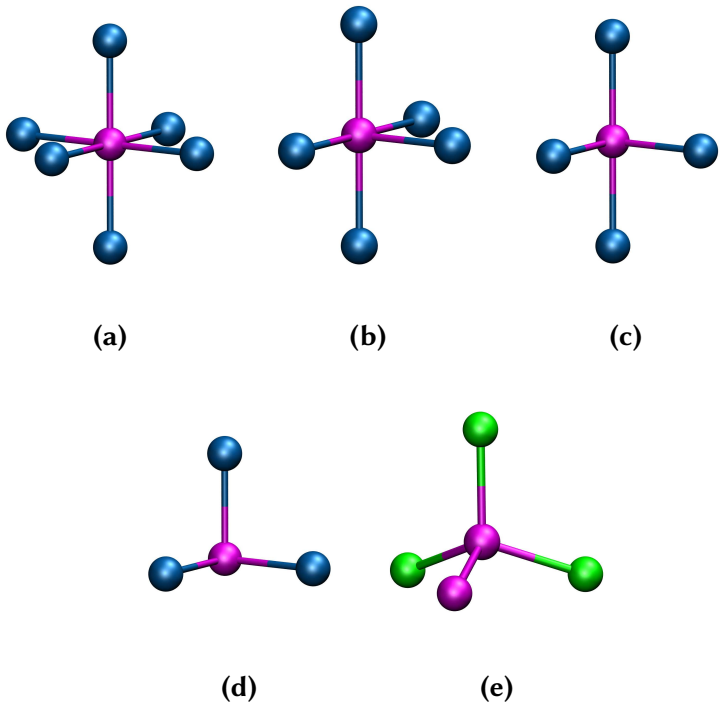

Figure 1.15.: Schematic representation of the octahedral-like and tetrahedral environments present in phase change alloys: (a) octahedral, (b), (c), (d) defective octahedral-like with five-, four- and three-fold coordinated atoms and (e) tetrahedral coordination.

Average coordination numbers				
	with Ge	**with Sb**	**with Te**	**total**
Ge	0.29	0.36	3.31	3.96
Sb	0.36	0.43	3.36	4.15
Te	1.33	1.34	0.30	2.97

Table 1.1.: Partial average coordination numbers of a-$Ge_2Sb_2Te_5$ from DFT simulations [72].

mainly four-fold coordinated, while Te is three-fold coordinated. However, only about one third of the Ge atoms was found to be in a tetrahedral environment for both GeTe and GST. In fact, the most abundant bonding geometry for both Ge and Sb is the four-fold octahedral-like one of Figure 1.15c, while Te atoms have a pyramidal bonding geometry as in Figure 1.15d. Regarding the medium-range order, four-membered rings dominate in the amorphous models of GeTe and GST (Figure 1.17) and the majority of the four-membered rings is of type ABAB, where A is Ge in GeTe and Ge or Sb in GST and B is Te. These rings are the building blocks

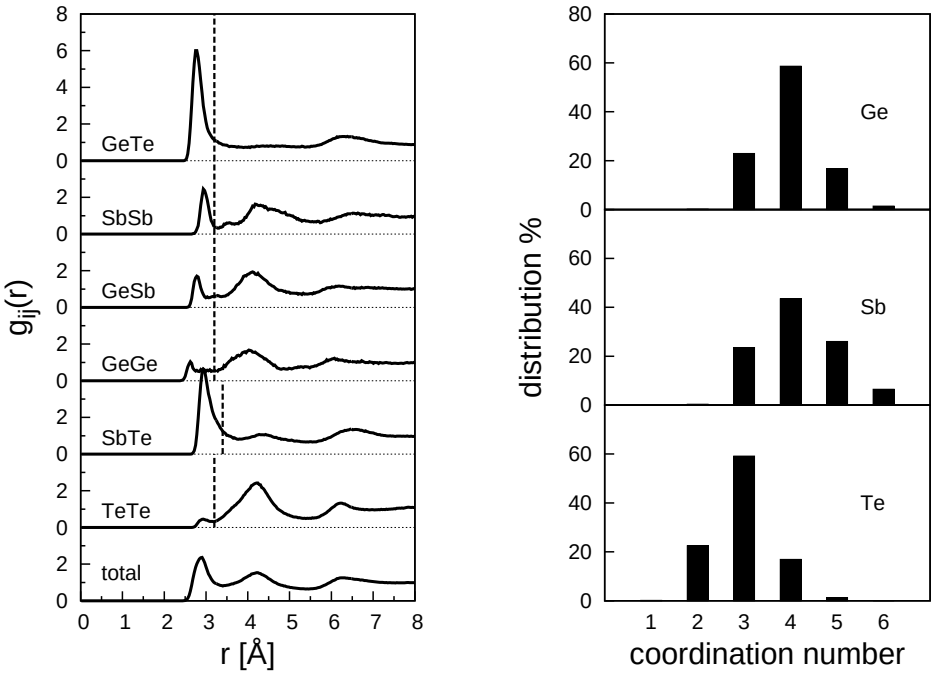

Figure 1.16.: (a) Partial and total pair coorelation functions and (b) coordination number distributions of a-$Ge_2Sb_2Te_5$ from DFT simulations [72].

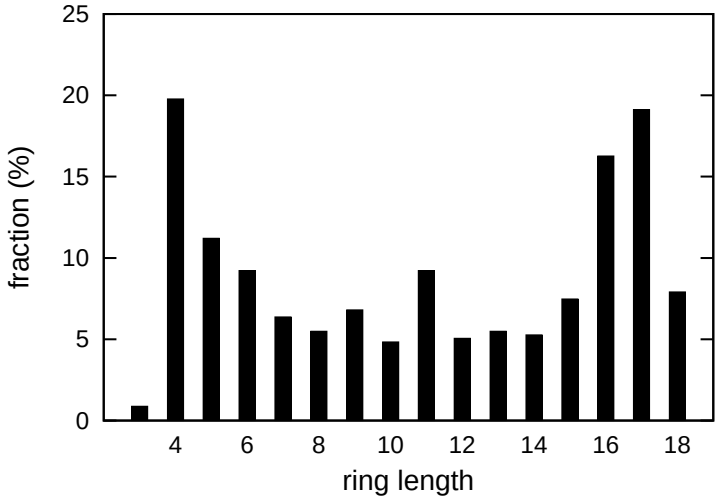

Figure 1.17.: Distribution of the ring lengths in a-$Ge_2Sb_2Te_5$ from DFT simulations [72].

of the cubic rocksalt crystalline phase as well.
The models emerged from the simulations were also able to reproduce the experimental Raman spectra of GeTe and GST [73–75]. Other *ab-initio* MD simulations [76] showed that the fraction of tetrahedral Ge atoms depends on the preparation conditions of the amorphous samples. In fact, in as-deposited GST, the amount of tetrahedral structures is greater than in GST models obtained by quenching from the melt. Although the amorphous partially keeps the coordination typical of the rocksalt structure with shorter and longer bonds in the octahedral-like structures, the absence of medium-range order hinders the formation of resonant bonds, resulting in a lower static polarizability and hence in a lower reflectivity with respect to the crystal [50].
As reported by Raman spectroscopy [61, 64, 75], EXAFS [61, 62], RMC [66] and, as already discussed, by first principles MD studies [67–69, 71, 72], GeTe and GST present a not negligible fraction of homopolar Ge-Ge bonds which seem to favour the tetrahedral coordination of Ge atoms [71]. In fact, the sp^3 configuration is favoured with respect to $p-p$ bonds for Ge-Ge bonds while the reverse is true for Ge-Te bonds [77]. Tetrahedral structures are absent in the crystalline phase and they can represent an obstacle to the crystallization process at low temperatures that causes the loss of the data in the PCM cell. Thus, a high concentration of wrong bonds in the amorphous is supposed to hinder the phase change below the glass transition, enhancing the stability of the amorphous phase and the retention of data at low temperatures.

1.2.2. Crystallization in phase change materials

As already mentioned, the DFT simulations revealed that the local bonding geometry in the amorphous is actually much more similar to that of the crystal than previously assumed as only about 1/3 of the Ge atoms is in a tetrahedral environment. The network topology also consists of mostly four-membered ABAB rings which are the same building blocks of the crystalline phase. The high speed of crystallization in phase change materials actually allows addressing the mechanism of the phase change by atomistic simulations. Indeed in the last few years, several works have been reported on the early stage of crystal nucleation and growth by DFT molecular dynamics simulations which aimed at validating the "umbrella flipping" model proposed by Kolobov *et al.* [64, 65].

An alternative mechanism of crystallization was actually proposed by Hegedüs and Elliott [67] suggesting that the phase transition occurs thanks to a fast realignment of four-membered ABAB rings present in both the amorphous and crystalline phases. [66, 68, 78] (Figure 1.18a). The alignment of square rings was also suggested to be aided by the presence

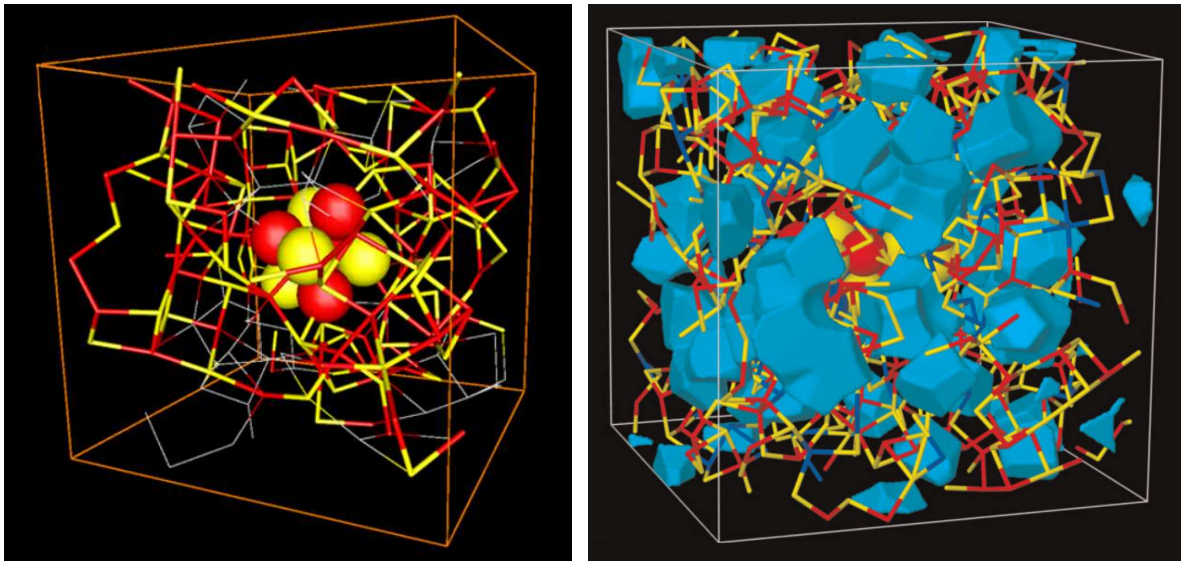

(a) **(b)**

Figure 1.18.: (a) Image of the simulation cell of a-GeTe in Ref. [70] where ABAB four-membered rings are highlighted. Six ABAB rings forming a cube are depicted with balls. Red represents Ge and yellow represents Te. (b) Representation of the cavities in melt-quenched $Ge_8Sb_2Te_{11}$ [81].

of nanovoids (Figure 1.18b) in the amorphous phase [68].
However, one should consider that in PCM devices the crystallization occurs at a temperature well above the glass transition temperature T_g where the system is supposed to be in a super-

cooled liquid state [18]. Thus, the crystallization mechanism during the SET operations and the high speed of crystallization peculiar of phase change materials should actually depend on the properties of the supercooled liquid. Recent ultra-fast differential scanning calorimetry (DSC) measurements on GST [79] and MD simulations [80] actually ascribed the fast crystallization of these materials to the fragility of the liquid phase as we will describe below.

Fragility

Supercooled liquids can be classified as fragile or strong depending on the temperature dependence of the viscosity η. Strong liquids show an Arrhenius behaviour of η as a function of temperature T in the range between the melting temperature T_m and the glass transition temperature T_g with a single activation energy. Fragile liquids, instead, are characterized by

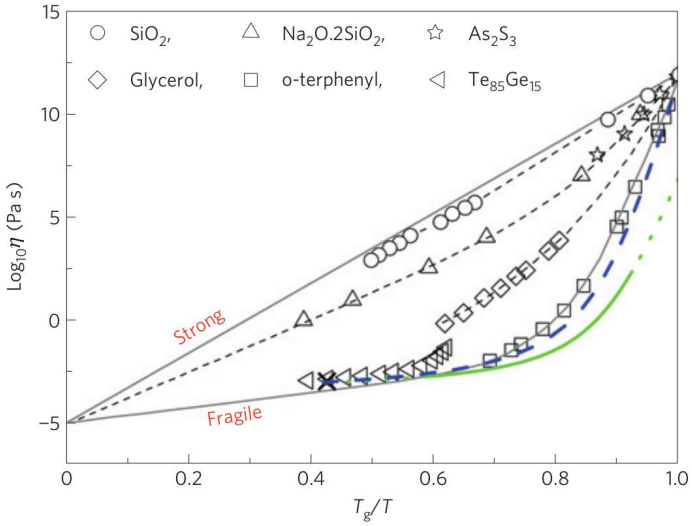

Figure 1.19.: Behaviour of the viscosity as a function of the reduced temperature for different supercooled liquids. In strong liquids the viscosity follows an Arrhenius behaviour, while a super-Arrhenius behaviour is observed for fragile liquids. The blue (green) curve represent the η values estimated in Ref. [79] for $Ge_2Sb_2Te_5$ from ultra-fast DSC. By assuming (neglecting) a breakdown of the Stokes-Einstein relation between the viscosity and the self-diffusion coefficient (see text).

a super-Arrhenius shape of η (Figure 1.19) often described, close to T_g, by a Vogel-Tammann-Fulcher (VTF) equation [82]

$$\eta = \eta_0 e^{\frac{E}{k_B(T-T_0)}} \tag{1.1}$$

where η_0, $T_0 < T_g$ and E are fitting parameters and k_B is the Boltzmann constant. The degree of fragility is quantified by the fragility index m as

$$m = \left.\frac{d(\log_{10}\eta)}{d(T_g/T)}\right|_{T=T_g} \tag{1.2}$$

which is of the order of few tens for typical strong liquids ($m = 15$ for SiO_2) and of few hundreds for highly fragile liquids ($m = 192$ for PVC). For fragile liquids, η can be very low down to temperatures close to T_g resulting in a high atomic diffusivity which can boost the crystallization speed. In fact, as predicted by the classical nucleation theory, the diffusion coefficient D appears as a kinetic prefactor for the nucleation rate I and the speed of crystal growth u:

$$I \propto De^{-\frac{\Delta G_C}{k_B T}} \tag{1.3}$$

$$u \propto D\left(1 - e^{-\frac{\Delta\mu}{k_B T}}\right) \tag{1.4}$$

$$\tag{1.5}$$

where ΔG_c is the formation free energy of the critical nucleus and is in turn defined by

$$\Delta G_c = \frac{16\pi\gamma^3}{3(n_s\Delta\mu)^2} \tag{1.6}$$

where γ is the liquid-solid interfacial tension, n_s the number density of particles and $\Delta\mu$ the chemical potential difference between the liquid and the solid which represents the driving force for the crystallization process. The self diffusion coefficient D and $\Delta\mu$ have an opposite behaviour in temperature (Figure 1.20) that makes the nucleation rate and the crystal growth velocity to have a maximum at different temperatures.

In a fragile liquid, the presence of a low viscosity at temperatures well below T_m where the driving force for crystallization $\Delta\mu$ is high, may result in a high crystallization speed, as found for phase change materials. The first evidence of a high fragility in GST was recently provided by Orava *et al.* [79] on the basis of ultra-fast DSC measurements. The crystal-growth velocity (Figure 1.21) was obtained from the analysis of the heat transfer rate and information on the viscosity was also inferred by the temperature dependence of the speed of crystal growth (Figure 1.19). These results on the crystal-growth velocity revealed the presence of two regimes of crystallization with two different activation energies. The first occurs at high temperature, well above T_g, and is characterized by an activation energy of about 0.5 eV as also obtained from electrical measurements directly on PCM devices [83]. The second regime appears at low temperatures near T_g with a higher activation energy of about 2.4 eV [83–86]. The high temperature regime is relevant for programming operations in the PCM cell when crystallization

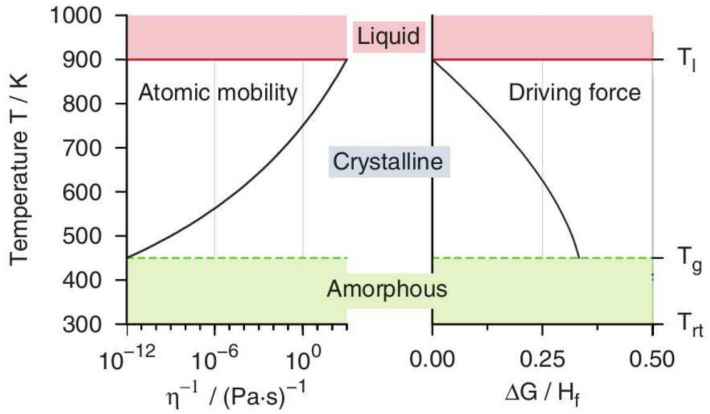

Figure 1.20.: Schematic plot of the behaviour for increasing temperatures of the atomic mobility $1/\eta$ (left) and of the free energy difference between the liquid and the crystalline phase (right), which represent the driving force for the crystallization process [21].

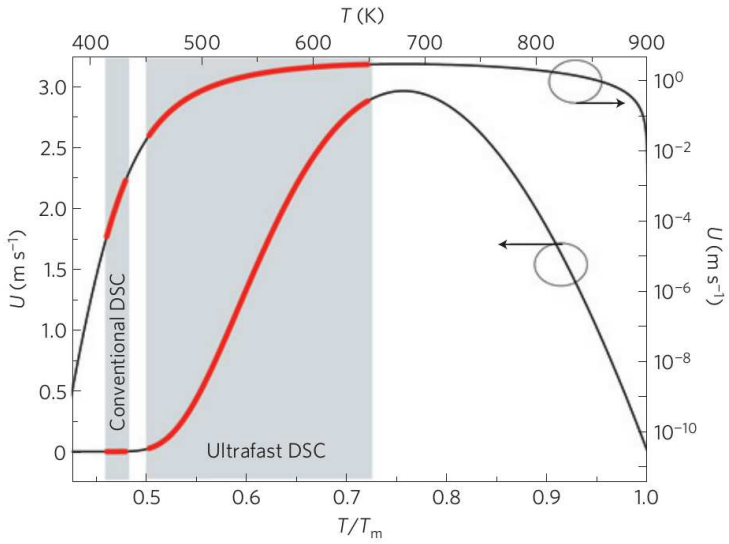

Figure 1.21.: Crystal-growth velocity for GST as a function of temperature obtained from ultra-fast differential scanning calorimetry [79].

proceeds from the supercooled liquid (SET operations). The low activation energy makes the phase transformation easier at high temperature. The low temperature regime, instead, controls the data retention at normal temperature. The high activation energy for crystallization close and below T_g guarantees the stability of the amorphous phase and thus data retention at normal conditions.

Breakdown of Stokes-Einstein relation

Another factor that boosts the crystallization speed in phase change materials is the breakdown of the Stokes-Einstein relation (SER) which is often observed in fragile liquids. The Stokes-Einstein relation links the self diffusion coefficient D to the viscosity:

$$D = \frac{k_B T}{6\pi\eta r_{sph}} \tag{1.7}$$

where r_{sph} is the average dimension of the particles. The breakdown of the SER in GST was firstly proposed in Ref. [79]. However, to deduce the temperature behaviour of the self diffusion coefficient and of the viscosity, many crucial assumptions have been made on the crystallization process and on the value of T_g itself. In fact, a direct measure of D and η at the operating conditions of a PCM device has not been performed yet.
In this respect, MD simulations provide a useful tool to estimate independently the diffusivity, the viscosity and the crystal-growth velocity. MD simulations based on a Neural Network potential (see Section 2.7) by using large (4096 atoms) GeTe models [80] allowed indeed the independent calculation of D and η which confirmed the breakdown of SER below 700 K (Figure 1.22). This means that, despite the high viscosity found for temperatures close to T_g, the system still features a high atomic diffusivity that allows for a fast structural reorganization and crystallization. Both the fragility and the breakdown of SER make the self diffusion coef-

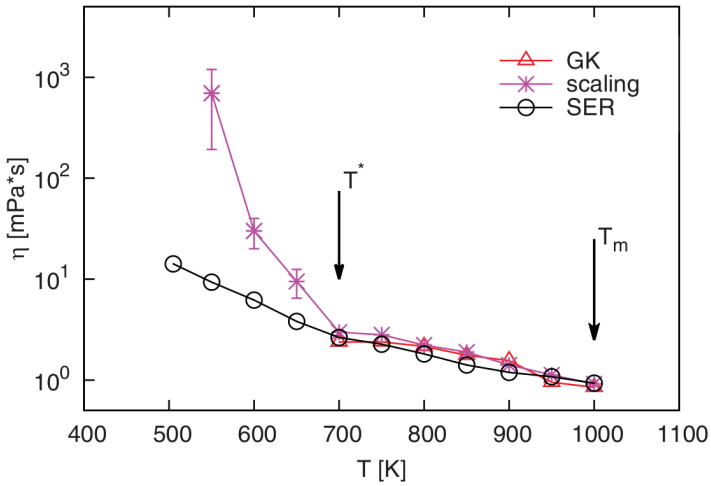

Figure 1.22.: Viscosity calculated as a function of temperature from the Green-Kubo formula (red triangles), from the scaling of the diffusion coefficient with the simulation cell size (stars) and from the self-diffusion coefficient of a 4096-atom cell and the application of the Stokes-Einstein relation (open circles) [80]. For temperatures below 700 K the Stokes-Einstein relation is no longer applicable.

ficient of the supercooled liquid to be very high even at temperatures well below the melting point where the driving force for the crystallization $\Delta\mu$ is very high. These features lead to high nucleation rate I and high speed of crystal growth u. Molecular dynamics simulations allowed also to compute the crystallization speed and the activation energy of the crystallization process in GeTe [87] in the high temperature regime. It was shown that indeed the crystallization speed can be well described by the classical nucleation theory (CNT) expression $u \propto D(1-e^{-\Delta\mu/k_BT})$ with values of u of about m/s in the temperature range $500-700$ K, consistent with experimental data on GST (Figure 1.21). The simulations confirmed that the high crystallization velocity is actually due to the large value of D resulting from the fragility of the liquid and the breakdown of the SER.

Dynamical heterogeneity

The Stokes-Einstein relation between D and η is valid when the liquid can be treated as a continuum where all the particles have a homogeneous dynamics. A breakdown of the SER actually occurs in the presence of dynamical heterogeneities in the supercooled liquid that make the continuum approximation no longer applicable. Dynamical heterogeneities (DH) consist of spatially localized regions where atoms move with a higher speed and regions where atoms move slower and have been experimentally observed in many liquid systems, in particular in colloidal glasses [88].
Classical MD simulations on 4096-atom models [89] showed indeed the presence of DH in supercooled liquid GeTe. In fact, for temperatures above T_m where the SER holds, faster and slower atoms are spatially randomly distributed in the system, while at lower temperatures where the breakdown of SER occurs, faster and slower atoms cluster into separated domains (Figure 1.23). No particular structural features were found in clusters of slower atoms, while clusters of faster atoms contain a fraction of homopolar Ge-Ge bonds higher than the average. Clusters of mobile atoms turned out to form around chains of homopolar Ge-Ge bonds. Despite the fraction of Ge-Ge bonds, the number and the length of Ge-Ge chains in the whole system decrease upon cooling, the fraction of homopolar bonds in clusters of faster atoms increases, as well as the number and the length of the Ge-Ge chains. Thus the DH in supercooled liquid GeTe originates from a structural heterogeneity due to the presence of chains of homopolar Ge-Ge bonds. Chains of Ge atoms with homopolar bonds are thus responsible for the DH in liquid GeTe leading to the high mobility at high supercooling which is the ultimate source of the high crystallization speed exploited in PCMs.
As we will see, these outcomes are of relevance for the analysis of the drift phenomenon in amorphous GeTe (see Section 1.4) addressed in this thesis. A correlation between the presence of homopolar bonds and the fragility of the supercooled liquid was found also for the GeAsSe compounds [90].

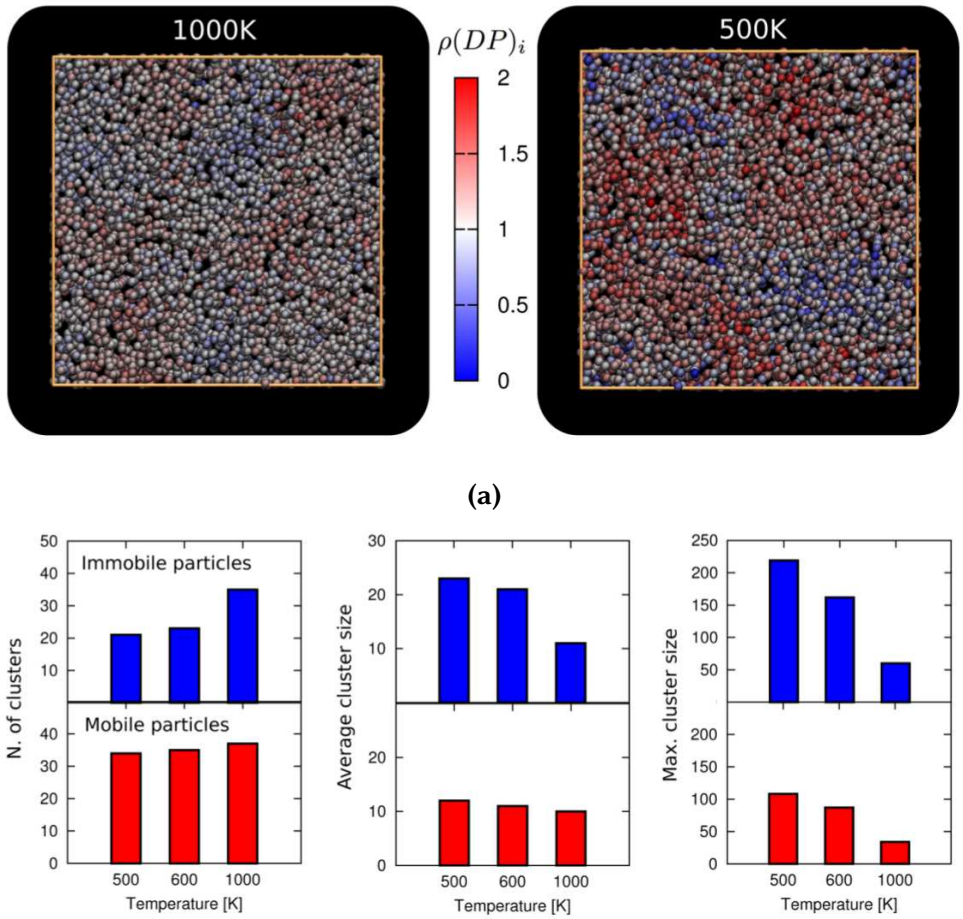

Figure 1.23.: (a) Colour map of the distribution of dynamical propensity $\rho(DP)_i$, indicating the tendency of each atom *i* to move, at 1000 and 500 K. (b) Number of clusters, average cluster size and maximum cluster size (number of particles) of most immobile (MI) and most mobile (MM) atoms at different temperatures [89]. These maps were obtained from averages of the mean square displacements in the isoconfigurational ensemble (see Ref. [89] for details).

1.3. InSbTe and GaSbTe alloys

In addition to GeTe, other promising candidates to replace GST in phase change memories are the ternary SbTe-based chalcogenide alloys with gallium or indium. In fact, both these alloys present a high thermal stability due to their high crystallization temperature. This feature can also be exploited to realize core-shell nanowires with GST for multi-level PCM applications [10]. However, very few experimental and theoretical information are nowadays available on the structure and the properties of the crystalline and the amorphous phases of these alloys.

1.3.1. InSbTe alloys

Indium-based alloys have initially attracted interest for application in optical memories. The phase change compounds actually employed in the realization of DVD and rewritable CD were, in fact, SbTe alloys doped with In and Ag [91]. More recently, indium phase change compounds like $InGeTe_2$ [35] have been proposed for phase change memory application due to their high thermal stability over 125 °C.

In this respect the InSbTe (IST) ternary system is even more promising because of the presence of compositions with high melting [92] and crystallization temperatures [5]. Crystallization is also very fast (ns) at high temperatures [93]. Furthermore, it has been shown that many of these alloys undergo a sequence of transformations from the amorphous to the crystal through intermediate phases [6, 9, 94, 95] that make them suitable for multi-bit memories applications [6, 94].

InSbTe thin films for PCM can be grown by chemical vapour deposition (MOCVD) obtaining layers of different composition by controlling the working pressure [96]. In the perspective of the development of ultra-scaled PCM devices, InSbTe nanowires (Figure 1.24) with an approximative composition of $In_{3.0}Sb_{1.0}Te_{3.2}$ were also obtained by MOCVD [97]. The $In_3Sb_1Te_2$

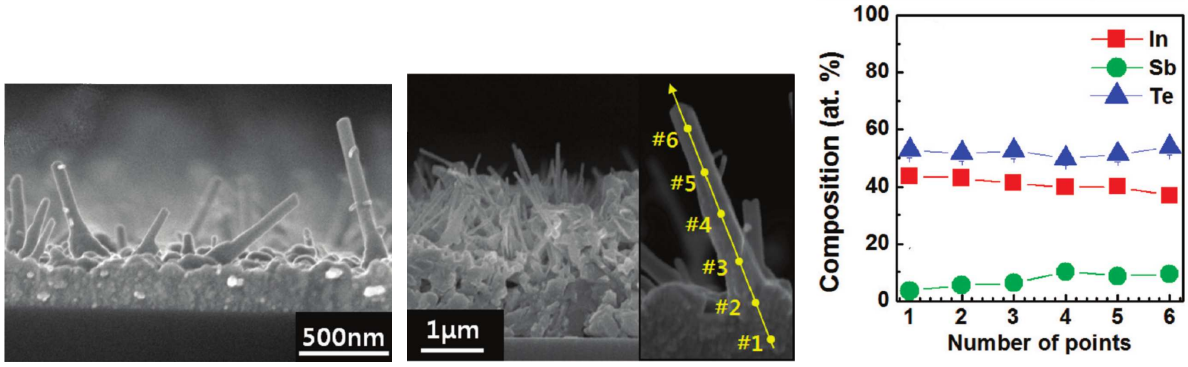

Figure 1.24.: SEM cross-sectional images of InSbTe nanowires grown at $9.1 \cdot 10^2$ Pa (a) and at $13 \cdot 10^2$ Pa (b) with a zoomed nanowire on the right. The numbers on the nanowire indicate the points in which the nanowire composition plotted in (c) was measured [97].

composition along the pseudobinary InSb-InTe tie line (Figure 1.25) is particularly interesting because of the existence of a single-phase ternary crystal [98]. Moreover, the amorphous phase shows a very high stability with a crystallization temperature T_x of about 292 °C [6] and high activation energy for crystallization of the order of 3 eV close to T_x [99]. Although crystalline $In_3Sb_1Te_2$ is stable only in the temperature range 555 °C—435 °C, it can be recovered as a metastable phase upon quenching at normal conditions, bypassing the decomposition into InTe and InSb expected below 435 °C [100]. In the past, this composition was proposed for

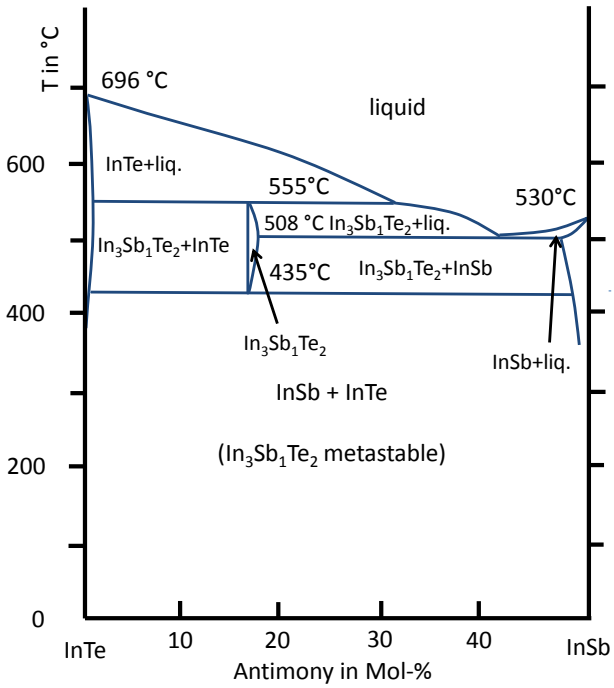

Figure 1.25.: Phase diagram of InSbTe alloys [100]. The stoichiometric composition $In_3Sb_1Te_2$ is metastable at room temperature and can be obtained through a rapid quench avoiding phase separation.

application in DVDs as well [5, 99]. More recently, crystallization times of about 100 ns were observed for this compound in PCM devices with about two orders of magnitude increase in electrical conductivity upon crystallization and good cyclability [94] (Figure 1.26).
The crystal structure of cubic $In_3Sb_1Te_2$ was assigned to the $Fm\bar{3}m$ space group with a lattice constant of 6.126(1) Å and a rocksalt geometry [98] with In occupying the cation sublattice and Sb and Te atoms occupying the anion sublattice in a random manner (Figure 1.27a) as shown by recent x-ray and neutron diffraction experiments [101]. In this arrangement, there are, on average, 2.3 p electrons per lattice site leading to an open shell system with metallic properties i.e. high electrical (3.2×10^4 S·cm^{-1} at 25 °C) and thermal conductivity (23 Wm^{-1}K^{-1}) [101]. It is interesting to note that GST also crystallizes in a metastable rocksalt phase in which, however, the cation sublattice is occupied randomly by Sb, Ge, and 20% of vacancies, the anionic sublattice being occupied by Te only [53]. Antimony is thus cationic in $In_3Sb_1Te_2$ and anionic in GST. The octahedral-like bonding geometry of the cubic ternary $In_3Sb_1Te_2$ has to be contrasted with the tetrahedral bonding geometry of the binary compounds InTe (Figure 1.27b) and InSb (Figure 1.27c). In fact, InSb crystallizes in a zincblende structure, while crystalline InTe is made of chains of edge-sharing $InTe_4$ tetrahedra intercalated by weakly bound, interstitial-like In ions [102].

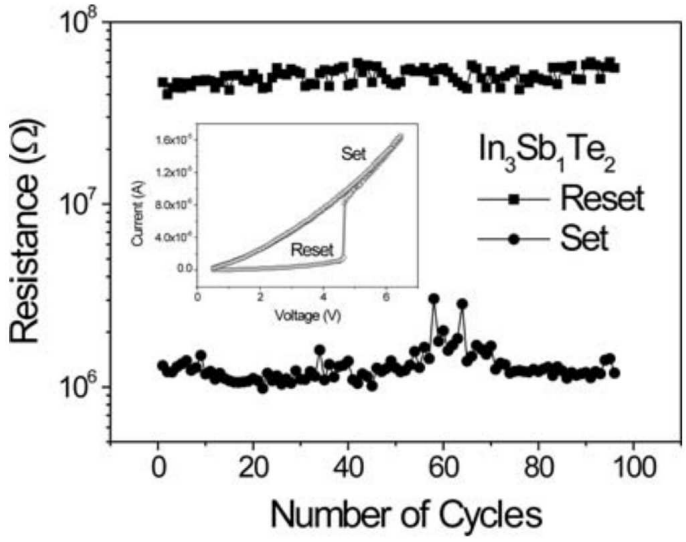

Figure 1.26.: Electrical resistance as a function of the number of cycles of a PCM cell with $In_3Sb_1Te_2$. The phase transition is reversible and the device can be cycled without loss of resistivity contrast [6].

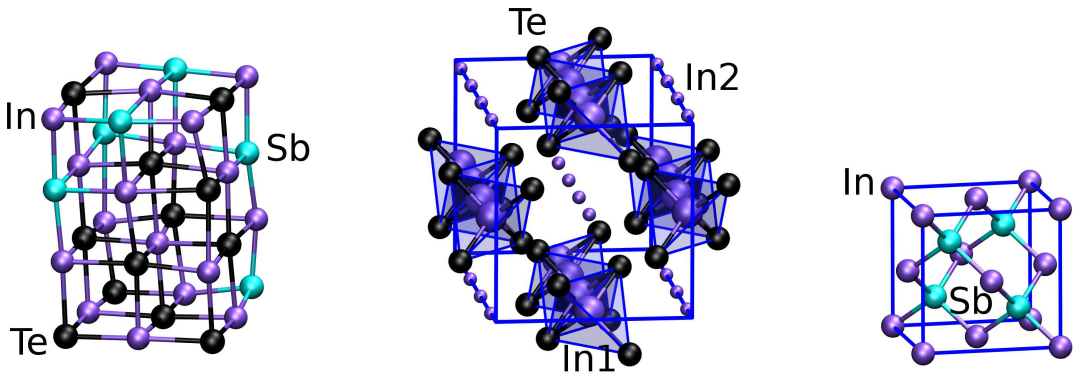

(a) **(b)** **(c)**

Figure 1.27.: Representation of the crystalline structure of (a) $In_3Sb_1Te_2$ in the rocksalt phase with In atoms occupying the cationic sublattice and Sb and Te atoms occupying randomly the anionic sublattice, (b) InTe with interstitial In atoms (In2) and tetrahedral In atoms (In1) forming chains of edge-sharing tetrahedra, (c) InSb in the zincblende structure. Indium atoms are depicted by violet spheres, Sb atoms by cyan spheres and Te atoms by black spheres.

The $In_3Sb_1Te_2$ alloy is interesting also for multi-bit phase change memory devices because the amorphous to crystalline transformation proceeds via successive structural transformations of the ternary compound [6]. Each step is characterized by a different resistance as reported in Figure 1.28. In the first step at about 5.1 V (about 300 °C) the crystalline phase of InSb is formed from amorphous $In_3Sb_1Te_2$. At about 6.5 V, corresponding to a temperature of 400 °C, a second step appears due to the formation of crystalline InTe, while above 450 °C (7 V) InSb and InTe react forming crystalline $In_3Sb_1Te_2$.

Concerning the amorphous phase of $In_3Sb_1Te_2$, very little is known on its structure. The main

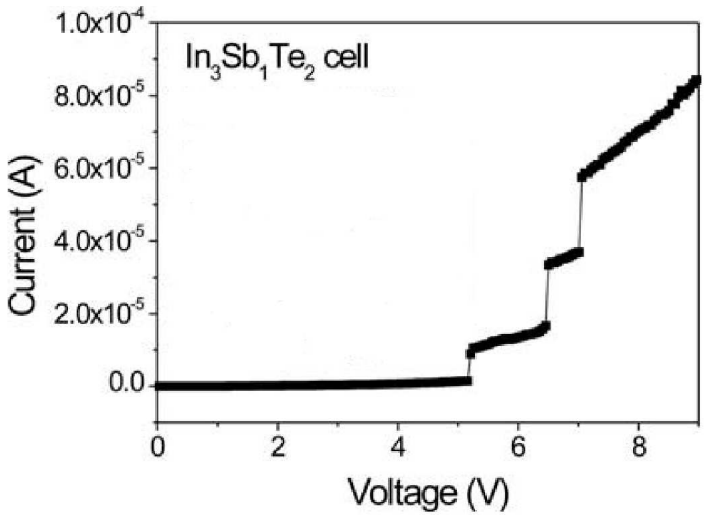

Figure 1.28.: Measured $I-V$ characteristic of a $In_3Sb_1Te_2$ PCM device showing steps at different resistance values when transforming from amorphous to crystalline. Each step correspond to a different crystalline phase obtained through phase separation [6].

question that arises is whether the bonding geometry in the amorphous phase is octahedral-like as in the ternary crystal or tetrahedral-like as in the crystalline phase of the two binary compounds the ternary system is made of.

InSbTe films with different compositions were also grown by MOCVD in the perspective to realize a conformal deposition for PCM applications [9]. The compositions $In_3Sb_{2.7}Te_{0.8}$ and $In_3Sb_{2.5}Te_{1.1}$ were obtained with a noticeable dependence on the Te content of the electrical performance of PCM devices. A better endurance and a wider programming window has been found for $In_3Sb_{2.5}Te_{1.1}$ with respect to the composition with a lower Te content (Figure 1.29). When heated up at 260 °C, both these alloys transform into a *fcc* polycrystalline phase with composition $InSb_{0.8}Te_{0.2}$ with the segregation of elemental amorphous Te.

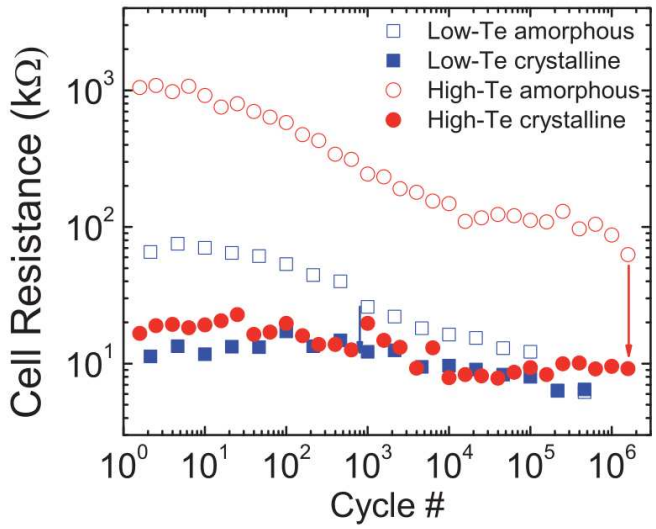

Figure 1.29.: Cyclability of PCM cells made of InSbTe alloys with composition $In_3Sb_{2.7}Te_{0.8}$ (low Te content) and $In_3Sb_{2.5}Te_{1.1}$ (high Te content). The former compound shows a better cyclability. Measurements were performed on 93×93 nm^2 cells in the SET (crystalline) and RESET (amorphous) state [9].

1.3.2. GaSbTe alloys

Gallium-based phase change alloys were proposed [7, 8, 41, 103] as well to substitute GST in PCMs operating at high temperatures. In particular, the binary GaSb system has been proposed as a possible contender for PCM applications [7, 104] because it is free of the toxicity of Te. The alloy with composition $Ga_{16}Sb_{84}$ in the form of ultra-thin film (< 10 nm) actually shows a fast single-phase crystallization and high crystallization temperature (about 250 °C) [41]. Unlike the majority of the phase change materials, the Ga_1Sb_1 composition has a reverse optical contrast being the amorphous more reflective than the crystal [7]. Recent *ab-initio* molecular dynamics simulations on Ga_1Sb_1 [105] have investigated the origin of this peculiar behaviour showing that, upon crystallization, amorphous Ga_1Sb_1 moves from a less tetrahedral structure with few $p-p$ resonant bonds to the completely tetrahedral coordination of the zincblende structure. This situation is opposite with respect to other phase change alloys like GeTe, GST or $Ga_{16}Sb_{84}$ which form crystals with an octahedral-like coordination and resonant bonds. In fact, as demonstrated for GST and GeTe the presence of resonant bonds in the crystal and their disappearance in the amorphous is the key to understand the high optical contrast between the two phases [50].
Among ternary compounds, the GaSbTe alloys with a high Sb content and composition $Ga_{25}Te_8Sb_{67}$ and $Ga_{18}Te_{12}Sb_{70}$ present a high crystallization temperature above 245 °C that ensures a 10 years data retention at 210 °C in PCM [103]. Upon annealing at 300 °C, both

these alloys crystallize in a hexagonal-close-packed (*hpc*) structure with space group $R3m$, the same as pure crystalline Sb, with Ga and Te atoms randomly substituting Sb in the crystalline lattice [103]. Compositions along the Sb_7Te_3-GaSb and Sb_2Te_3-GaSb tie line (Figure 1.30) were also studied for application in rewritable DVDs [106]. Compounds on the GaSb-

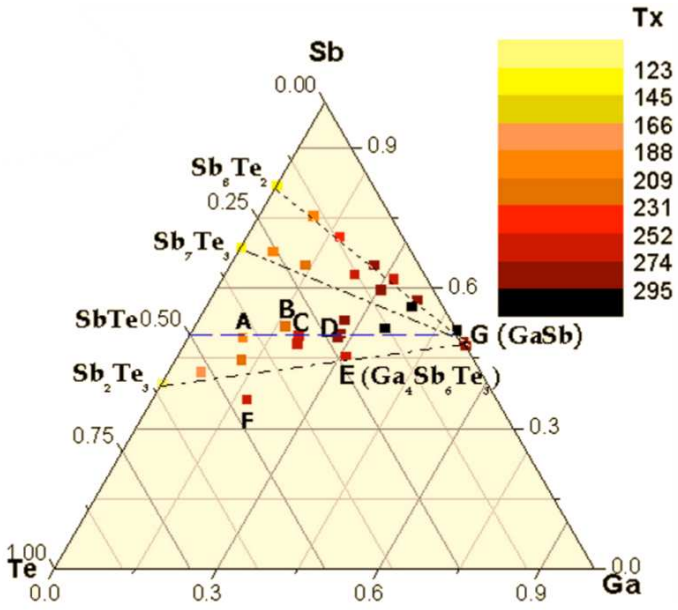

Figure 1.30.: Ternary phase diagram of Ga-Sb-Te. The pseudobinary lines are indicated with dashed lines. The scale on the right side indicates the crystallization temperature of different GaSbTe alloys [8]. A: $T_x = 193$ °C, B: $T_x = 215$ °C, C: $T_x = 227$ °C, E: $T_x = 271$ °C, F: $T_x = 254$ °Cand G: $T_x = 295$ °C.

Sb_8Te_2 pseudobinary line like $Ga_3Sb_8Te_1$ have a high crystallization temperature (277 °C) in spite of a low melting temperature (about 570 °C) [107], while the $Ga_2Sb_7Te_1$ composition has a very high activation energy for crystallization (5.76 eV [108]). PCM devices with a good stability at very high temperatures ($\sim$ 250 °C) were realized (Figure 1.31) with these alloys [108]. Quaternary systems like Si-$Ga_2Sb_7Te_1$ with different Si/$Ga_2Sb_7Te_1$ ratios are also under investigation [109] because they show good data retention and high cyclability (Figure 1.32). At the peritectic composition, the $Ga_4Sb_6Te_3$ alloy on the GaSb-Sb_2Te_3 tie line shows interesting properties for applications in PCMs. In particular, $Ga_4Sb_6Te_3$ displays a fast crystallization speed, a very high crystallization temperature (271 °C) of interest for high temperature applications, and high electrical contrast [8]. Amorphous thin films of $Ga_4Sb_6Te_3$ crystallize in a rhombohedral phase with the same composition and lattice parameters $a = 4.28$ Å and $c = 17.04$ Å [8], similar to elemental Sb. The presence of an intermetallic crystalline phase for the ternary alloy and the lesser Sb content with respect to non-stoichiometric alloys make Sb segregation during phase transformation less likely in $Ga_4Sb_6Te_3$ which is thus a promising candidate for PCM applications with high cyclability.

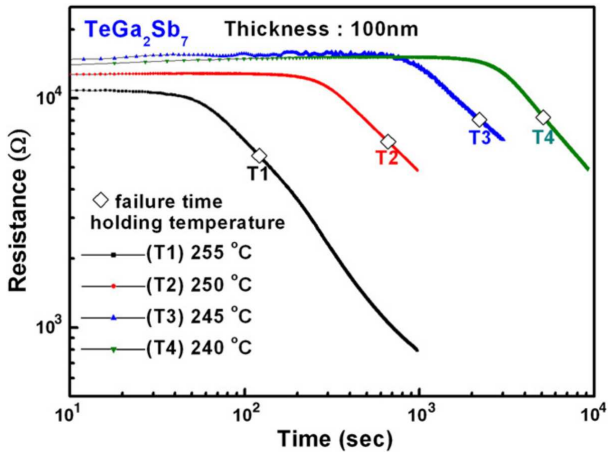

Figure 1.31.: Electrical resistance versus holding time at four different holding temperatures of $Ga_2Sb_7Te_1$ thin films [108]. The failure-time is defined as the time when the resistance decline to a half of its original value at a specific temperature.

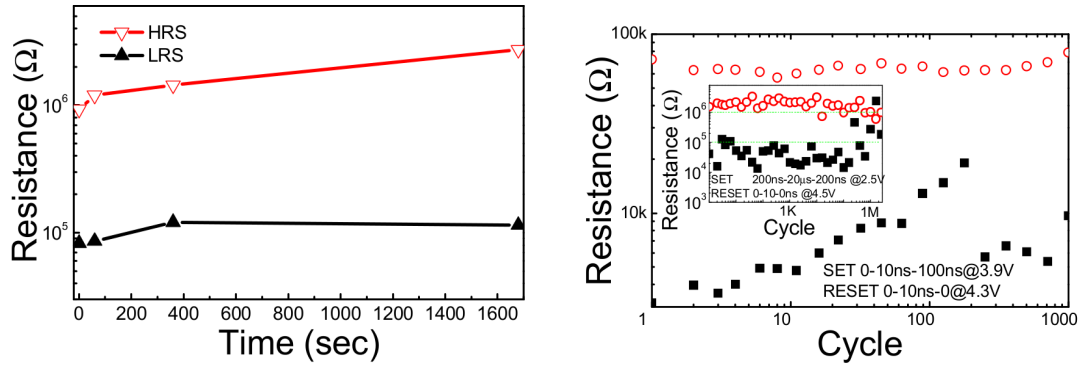

(a) **(b)**

Figure 1.32.: (a) Data retention of $Si_{29.4}(Ga_2Sb_7Te_1)_{70.6}$ devices at 250 °C beyond 1500 s. (b) Cycle endurance test for $Si_{29.4}(Ga_2Sb_7Te_1)_{70.6}$ using a fast switching mode and a slower switching mode (inset) [109].

Regarding the amorphous phase of $Ga_4Sb_6Te_3$, neither experimental nor theoretical data on its structure are available.

1.4. Resistance drift in the amorphous phase

One of the unsolved problems for the optimum operation of PCM devices is the drift phenomenon which consists of an increase of the electrical resistance of the amorphous phase with time on the scale of months at room temperature. The change of resistance in time is a common feature of amorphous semiconductors which is due to aging effects of the metastable amorphous state. In amorphous silicon, for instance, a decrease with time of the number of dangling bonds accompanied by an enhancement of the resistance has been observed [110]. Similarly, SiC shows a resistance drift explained by the relaxation of dangling bonds, distorted bonds and undercoordinated atoms [111]. Annealing-induced resistance drift has been observed in amorphous carbon [112].
Concerning chalcogenide materials, the drift of resistance is present in all Ge-, Ga- and In-SbTe alloys, but the process can be faster or slower in the different materials [113] and it can be accelerated by annealing at high temperature [114, 115]. This phenomenon has been intensively studied because it is detrimental for PCM operations. It is particularly critical for multi-level programming where the different values of the resistance in different states must not overlap with time to ensure data retention. In spite of its great technological relevance, the microscopic origin of resistance drift has not been fully understood yet.
In order to introduce the phenomenological models that have been proposed over the years to describe the drift phenomenon we first discuss in the next sections the electronic structure and the electrical conduction mechanisms in the amorphous state of phase change materials.

1.4.1. Electronic structure of the amorphous phase

The typical electronic density of states of an amorphous semiconductor is shown in Figure 1.33. States in the valence (conduction) band are delocalized below (above) a threshold energy known as mobility edge. The two mobility edges define a mobility gap as shown in Figure 1.33. Transport of holes in valence band or electrons in conduction band outside the mobility gap can be usually described by a Boltzmann like approach which applies when $kL \gg 1$ where L is the mean free path and k is the wavevector. Localized states are instead present inside the mobility gap typically forming exponential tails referred to as Urbach tails (Figure 1.33). The density of states in the Urbach region is roughly proportional to $e^{-(E-E_{me})/U}$, where E_{me} is the energy of the mobility edge and U is a measure of the width of the tail, known as the Urbach energy. Localized states inside the mobility gap also contribute to the conduction via thermally-activated hopping process.
Deep states close to midgap can also be found. This is the case for a-Si where dangling bond localized states pin the Fermi level at midgap.
Concerning phase change materials, few information are actually available on the electronic density of states of the amorphous phase. The optical gap is generally about 0.5-1.0 eV wide

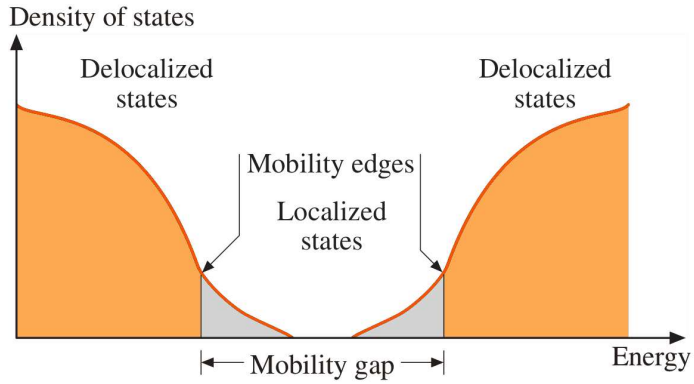

Figure 1.33.: Schematic representation of the electronic density of states of a typical amorphous semiconductor. The delocalized states of the valence and conduction band are highlighted in orange, while the localized states of the Urbach tails are represented in gray [116].

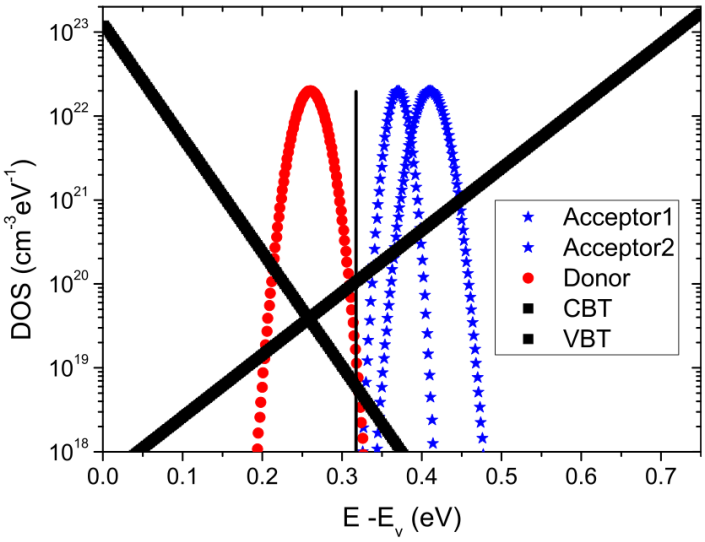

Figure 1.34.: Electronic density of states of amorphous GeTe that reproduces the experimental results from steady-state photo conductivity, modulated photocurrent and photothermal deflection spectroscopy measurements [118]. The large conduction and valence band tails (CBT and VBT) are a signature of the disorder usually encountered in amorphous materials.

(0.85 eV for a-GeTe [117]). The presence of deep [117, 118] (Figure 1.34) and shallow [117] localized defect states in the mobility gap was experimentally detected for a-GeTe, a-$Ge_{15}Te_{85}$ and a-GST. Modulated photo-current measurements on a-GeTe [118] have revealed Urbach tails in the valence and conduction bands with a Urbach energy of about 30 meV for the valence band and of 63 mV for the conduction band [118]. Regarding the position of the Fermi level, different groups report a pinning of E_F at about midgap [119], but the origin of the

pinning is controversial: on the basis of photo-thermal deflection spectroscopy, Luckas *et al.* [117] stated that the pinning is due to the presence of negative U defects, while Huang and Robertson [120] proposed a pinning of the Fermi energy caused by an overlap of the valence and conduction band Urbach tails.
The pinning of the Fermi level at midgap in the amorphous phase is actually the key to understand the contrast in resistivity with respect to the crystal. In fact, GeTe and GST in the crystalline phase are degenerate p-type semiconductors with a Fermi level close or even inside the valence band due to the presence of defects in stoichiometry in the form of Sb/Ge vacancies. The crystalline phases are thus self-doped by Sb/Ge deficiencies. On the contrary, the amorphous phase at the same composition can accommodate the Sb/Ge deficiencies by still keeping a closed shell configuration with E_F at midgap [72, 120].

1.4.2. Conduction in the amorphous phase

The description of electrical conduction in amorphous materials is a challenging task as band theory and Boltzmann transport equation can not often be applied to disordered systems. Regarding chalcogenide alloys, many different models were proposed over the years for the electrical conduction in the amorphous phase. The model proposed by Ielmini *et al.* [115, 121–124] seems so far the more viable as it is able to reproduce both the non-ohmic current-voltage characteristic below threshold and also several features of the threshold switching itself. The model assumes that conduction is controlled by disorder-induced localized states in the mobility gap via two mechanisms:

- thermally activated hopping among localized states in the mobility gap;
- a field assisted carrier injection from localized states (either electrons or holes) to delocalized states outside the mobility gap.

In the latter case the injected carriers can experience conventional band (Boltzmann) conduction with $kL \gg 1$ (see Section 1.4.1).
Both mechanisms are assisted by the electric field which reduces either the activation energy for hopping among localized states (Poole effect) or the barrier for ionization of the defect (trap) state according to the Poole-Frenkel effect. The barrier lowering due to the electric field are depicted in Figure 1.35, while a sketch of the band diagram of the amorphous used in the model is shown in Figure 1.36. For a high concentration of defects, electrons hop from trap to trap by overcoming an activation barrier. The applied voltage V_A induces a barrier lowering ΔU_P as given by the Poole relation [122]

$$\Delta U_P = \frac{qV_A\Delta z}{2u_a} \tag{1.8}$$

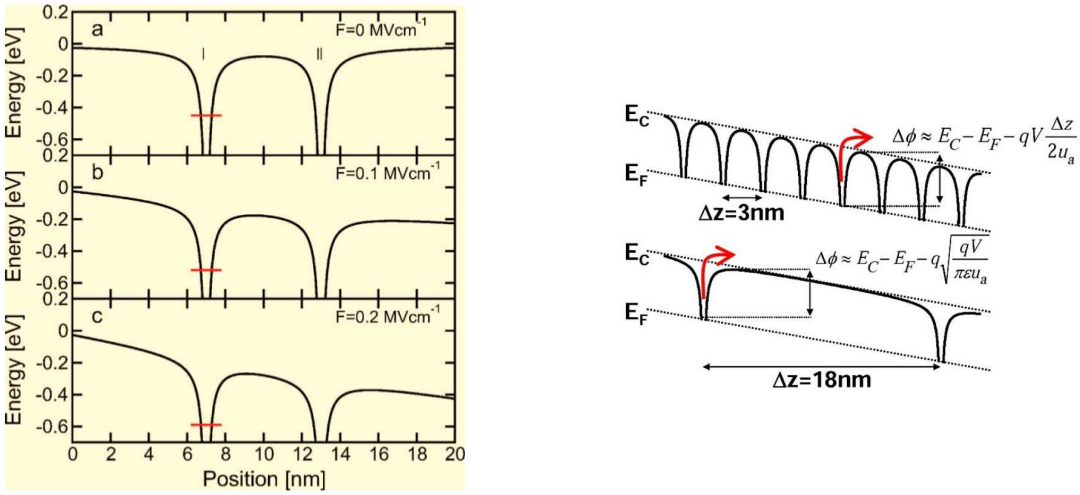

(a) (b)

Figure 1.35.: Potential profile of trap centers in an amorphous structure for an increasing applied electric field (a) [122] and for different inter-trap distances (b) [124]. The barrier between trap I and II becomes lower along the direction of the field. By varying the inter-trap distance, the dependence of the barrier lowering from the applied field changes.

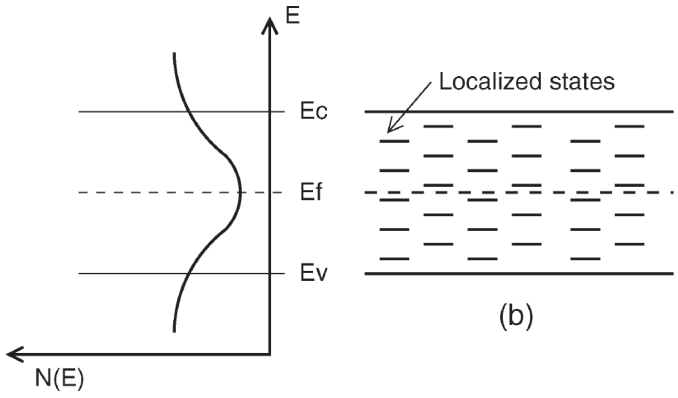

Figure 1.36.: Sketch of the band diagram of the amorphous phase of a chalcogenide material. The electronic density of states is reported on the left, while a schematic band gap view is shown on the right. E_v and E_c indicate the valence and the conduction mobility edges and E_F is the Fermi level [124].

where q the elementary charge, u_a the amorphous thickness and Δz the inter-trap distance. ΔU_P is linearly dependent from V_A which leads to a current which depends exponentially on the applied voltage (see below). If the traps are far away from each other, carriers do not hop among the traps but they are promoted outside the mobility gap by ionization of the traps. The external field induces a lowering of the barrier which depends linearly on the square root

of the applied bias (Poole-Frenkel effect):

$$\Delta U_{PF} = \sqrt{\frac{q^3 V_A}{\pi \varepsilon_\infty u_a}} \tag{1.9}$$

where ε_∞ is the amorphous dielectric constant for clamped ions. The height of the total barrier, corresponding to the activation energy of the conduction process, can thus be written as

$$E_a = E_c - E_F - \Delta U \tag{1.10}$$

where E_c is the conduction band edge, E_F the Fermi level and ΔU is assigned by the Poole (1.8) or by the Poole-Frenkel (1.9) model.
In the subthreshold regime, the electric current along the same direction of the field (forward current) is given by

$$I_\rightarrow = qAN\frac{\Delta z}{\tau_\rightarrow} \tag{1.11}$$

where A and N are the area of the contact and the trap concentration, respectively and τ is the time that an electron needs to escape from a trap center. Since the escaping process is thermally activated, τ can be written as

$$\tau_\rightarrow = \tau_0 e^{\frac{Ea}{k_B T}} \tag{1.12}$$

where τ_0 is the characteristic attempt-to-escape time for a trapped electron, k_B the Boltzmann constant, T the temperature of the system and E_a the barrier height given by equation (1.10). The current I has thus an Arrhenius like behaviour:

$$I_\rightarrow = qAN\frac{\Delta z}{\tau_0} e^{-\frac{Ea}{k_B T}}. \tag{1.13}$$

For small applied fields, the probability that a trapped electron jumps back to a trap in a direction opposite to that of the electrostatic force can not be neglected and a reverse current has to be taken into account:

$$I_\leftarrow = qAN\frac{\Delta z}{\tau_0} e^{-\frac{E_C - E_F + \Delta U}{k_B T}}. \tag{1.14}$$

In the reverse direction the potential barrier to overcome is higher with respect to the zero field case.
The net current is the difference between the forward and the reverse contributions:

$$I = I_\rightarrow - I_\leftarrow = 2qAN\frac{\Delta z}{\tau_0} e^{-\frac{E_C - E_F}{k_B T}} \sinh\left(\frac{\Delta U}{k_B T}\right). \tag{1.15}$$

For small voltages, the sinh function can be approximated by a linear dependence for both the Poole and the Poole-Frenkel case:

$$\begin{aligned} I_P &\sim \frac{q^2 A N \Delta z^2}{k_B T \tau_0 u_a} e^{-\frac{E_C - E_F}{k_B T}} V_A \\ I_{PF} &\sim \frac{2q^{5/2} A N}{\sqrt{\pi \varepsilon u_a}} \frac{\Delta z}{\tau_0} e^{-\frac{E_C - E_F}{k_B T}} \sqrt{V_A}. \end{aligned} \tag{1.16}$$

In the high field regime, the barrier to overcome in the direction opposite to the field is too high and the probability of a jump back too low. The reverse current is thus negligible and the net current equals the forward current $I_{\rightarrow}$.
On the basis of numerical simulations, it has been demonstrated by Ielmini *et al.* [123] that the Poole model better describes the system in case of low bias, while the Poole-Frenkel model better applies for higher voltages. Moreover, a crossover between the Poole and Poole-Frenkel regime is observed upon annealing as shown in Figure 1.37 due to the reduction of defect states.

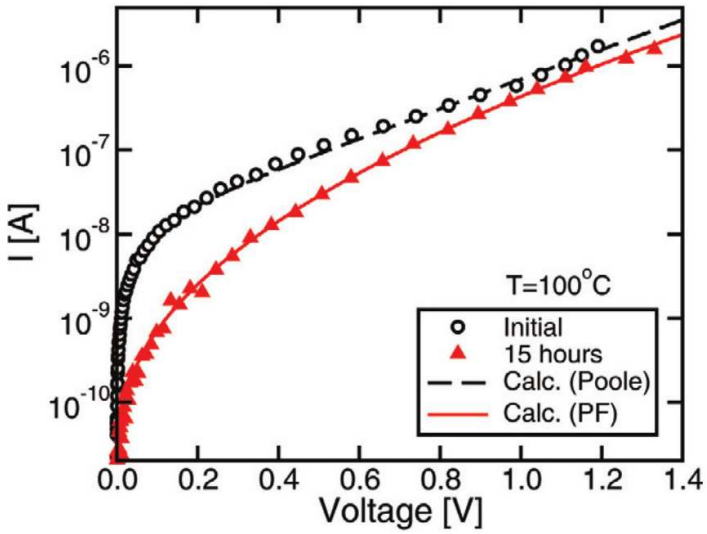

Figure 1.37.: Experimental curves taken before and after a bake of 15 hours at 100 °C. The curve before bake follows a Poole dependence. The curve after bake follows a Poole-Frenkel dependence

1.4.3. Drift of resistance

As demonstrated by time-resolved analysis of the electrical resistance R in PCMs [125], the evolution of R in time (Figure 1.38) shows a rapid increase for short times (few nanoseconds) after the RESET and then a slower monotonic increment. This second process is the so called

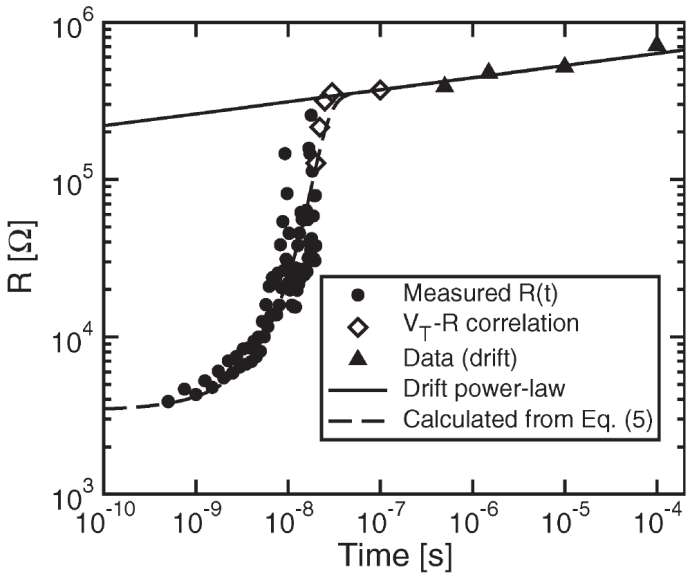

Figure 1.38.: Plot of the resistance of the amorphous phase as a function of time. For short times, R shows a transient in which it raises exponentially, then resistance increases following a power law (1.18) [125].

resistance drift and saturates in 10^4 s at 75 °C [126]. The saturation time at room temperature has not been calculated yet since it exceeds normal experimental times, but the predicted value is 10^7 s [126].
Immediately after the application of the programming pulse, the resistance of the amorphous phase rises up from values close to the resistance of the crystalline phase (tens of kΩ) to values typical of the amorphous (MΩ). This transient lasts few tens of nanoseconds and results from the presence of residual free and trapped carriers that recombine. In this stage the evolution of R is described by the equation

$$R(t) = R(0)e^{t/\tau} \tag{1.17}$$

where $R(0)$ is the resistance at time zero in the transient and τ is the effective recombination time for excess carriers [125]. In order to have a resistance window wide enough to distinguish between the crystalline and the amorphous bit, the readout of the cell should thus not be performed below a time of 15 ns from the RESET process.

After this transient the resistance increases with a power low [13, 125] (Figure 1.39)

$$R(t) = R_0 \left(\frac{t}{t_0} \right)^{\nu} \tag{1.18}$$

where R_0 is about 1 MΩ, t_0 is the reference time and ν is the power-law time exponent. The drift parameter ν is of about 0.1 for GST at room temperature [127, 128].

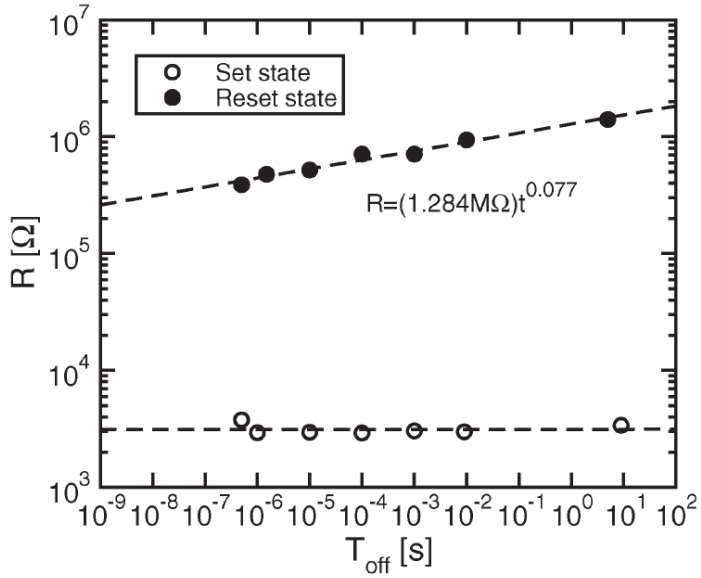

Figure 1.39.: Bilogarithmic plot of measured resistance as a function of time in a GST-PCM device for the RESET (amorphous) and the SET (crystalline) state. The amorphous shows a power-law dependence of the resistance while no resistance drift is detected for the crystal [125].

1.4.4. Possible mechanisms of the resistance drift

The microscopic process responsible for the resistance drift is still unclear. Two main interpretations of the drift mechanism have been proposed. The first ascribes the drift to the relaxation of compressive stress in the amorphous. In fact, the crystalline and the amorphous phase of a phase change material show a difference in density of about 6 %, being for instance 0.033 atoms/Å^3 for cubic GST and 0.031 atoms/Å^3 for amorphous GST [129]. In PCMs, the phase change occurs within a small droplet of the amorphous phase embedded in crystalline matrix which is in turn covered by hard materials such as TiN or W. The amorphous phase can not thus adjust its density and it is subject to a compressive stress. Since the band gap decreases upon the application of a compressive stress in these materials [130], the relaxation

of stress in the amorphous could give rise to an increase of the mobility gap and hence of the activation energy for the conduction process, since E_F is pinned at midgap. This argument is supported by experimental studies on GST nanowires of different size [12] (Figure 1.40) which show that nanowires with free surfaces have a smaller drift coefficient with respect

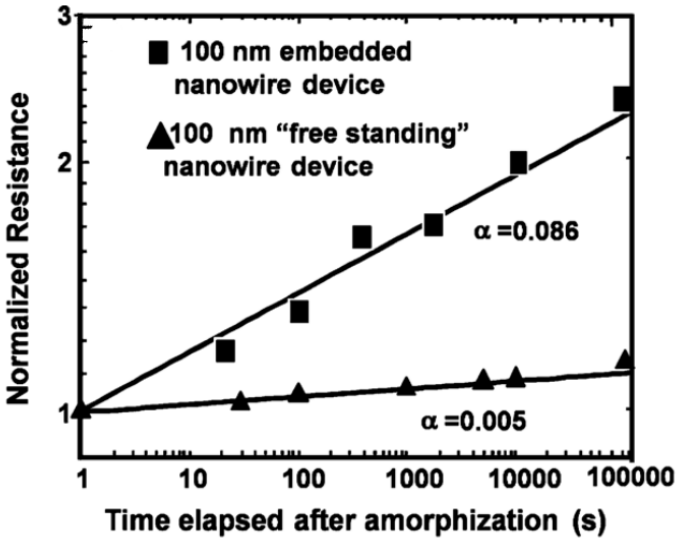

Figure 1.40.: Resistance drift measured in amorphous GST-nanowires unembedded and embedded in a dielectric matrix. In the "free standing" nanowires, the drift process is faster than in the embedded nanowires supporting the thesis of resistance drift driven by a stress relaxation process [12].

to thin films and to nanowires embedded in a dielectric matrix of SiO_2, Si_3N_4. Unembedded nanowires could better release the compressive stress resulting in a weaker drift. Measurements in PCM arrays have also shown that the drift coefficient ν depends on the size of the amorphous volume and the increase of the resistance could thus be due to stress relaxation [131]. Furthermore, *ab-initio* calculations on amorphous GST models 72-atoms wide [132] reported that models generated under pressure show a higher number of defect states and a smaller band gap.
However, resistance measurements on stress-free GST films yielded the same drift exponent obtained from PCM devices [128] which suggest that the stress relaxation can not be considered the main origin of the drift process.

A second more viable source of the resistance drift was thus identified with the structural relaxations, a phenomenon occurring in semiconductors and metallic glasses [133–135] as well as in phase change chalcogenide materials [136]. Since the amorphous is a metastable phase, the structure tends to evolve in time leading to a more stable configuration with a different defect density. This process could result in a modification of the electronic structure in proximity of the mobility edges and inside the mobility gap with a decrease of the number of in-gap states and, as a consequence, an increase of the activation energy for the conduction process. The structural relaxation was also indicated to be responsible of the drift in amorphous Si [110], SiC [111] and C [112].
A model of the time dependence of the resistance as due to structural relaxation activated by temperature has been in fact able to reproduce the experimental data on resistance of GST samples with different degree of annealing [127].
Recent ellipsometric measurements on a-GST thin films joint with electrical measurements [137, 138] reported that the resistance drift is accompanied by a widening of the optical (Tauc) band gap E_g of about 0.04 eV after 173 hours for an amorphous GST film [137] (Figure 1.41a).

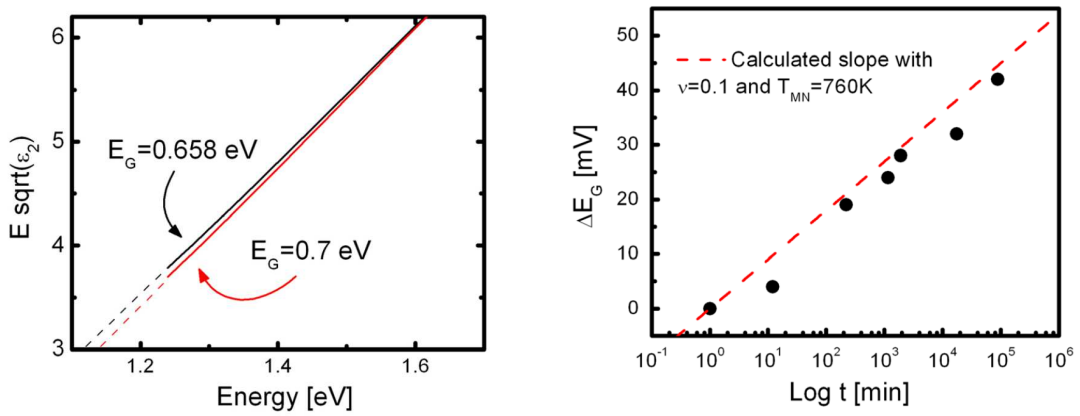

(a) **(b)**

Figure 1.41.: (a) Tauc plot for optical absorption before and after the drift $E\sqrt{\varepsilon_2}$ is plotted versus E, where E is the photon energy and ε_2 the imaginary part of the dielectric function. (b) Band gap widening during time. The dashed line represents the analytical increase of the activation energy for conduction calculated with the equation 1.20. The results were obtained from ellipsometric measurements on amorphous GST thin films [137].

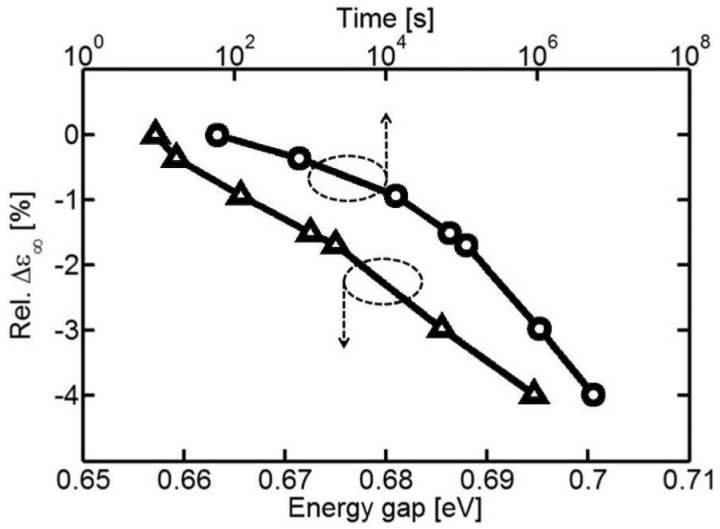

Figure 1.42.: Correlation between the ε_∞ decrease and the increase of the band gap (triangles) and decrease of ε_∞ as a function of time (circles) [138] in amorphous GST thin films.

By considering the Meyer-Neldel rule for the conduction process (see Ref. [127])

$$R = R_{00} e^{\frac{E_a}{k_B T_C}} e^{\frac{E_a}{k_B T}} \tag{1.19}$$

and the drift power law (1.18), the enhancement of the activation energy in time ΔE_a can be linked with the drift exponent obtained from electrical measurements by

$$\Delta E_a(t) = \frac{\nu k_B T}{1 - \frac{T}{T_C}} \ln\left(\frac{t}{t_0}\right). \tag{1.20}$$

This relation provides a good agreement with the time dependence of the optical gap ΔE_g measured by ellipsometry (Figure 1.41b). The widening of the optical Tauc gap is also accompanied by a reduction of the Urbach tails [137]. A Kramers-Kronig analysis of the amorphous spectra also provided the dependence on time of the static dielectric constant ε_∞ and its correlation with the band gap [138]. Once plugged in equation (1.9), the change in ε_∞ measured optically was also able to reproduce the change in time of the Poole-Frenkel contribution to the subthreshold current [138].

Modulated photo-current and photo-thermal deflection measurements also show a widening of the band gap with time in a-GeTe [117]. The evolution of the in-gap states upon drift is instead controversial as both an increase [139] or a decrease [117] of deep defect states have been reported. We remark that in addition to a gap widening, also the reduction of the Urbach band tails would result in an increase in resistivity.

The reduction of defect states close to the band edges would in fact lead to a decrease of both

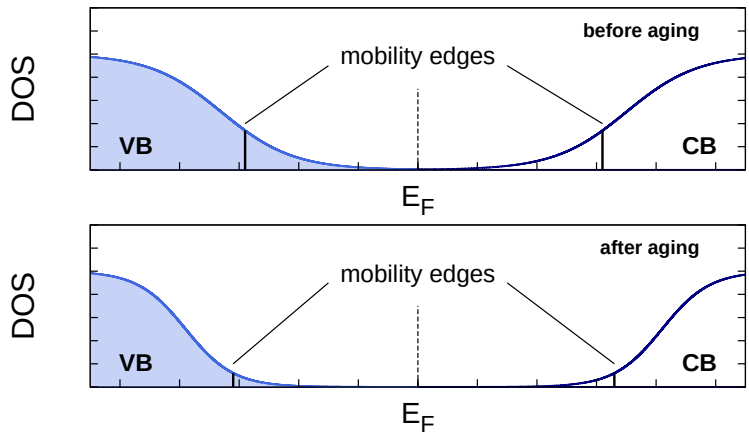

Figure 1.43.: Schematic representation of the electronic density of states (DOS) of the amorphous before and after aging. Before aging, electrons at the top of the valence band can be promoted by the electric field via the Poole-Frenkel effect into empty localized states in the proximity of the valence band edge leaving holes in the valence band. The aging process reduces the width of Urbach tails and a smaller number of empty defect states is available for Poole-Frenkel injection of holes in the valence band.

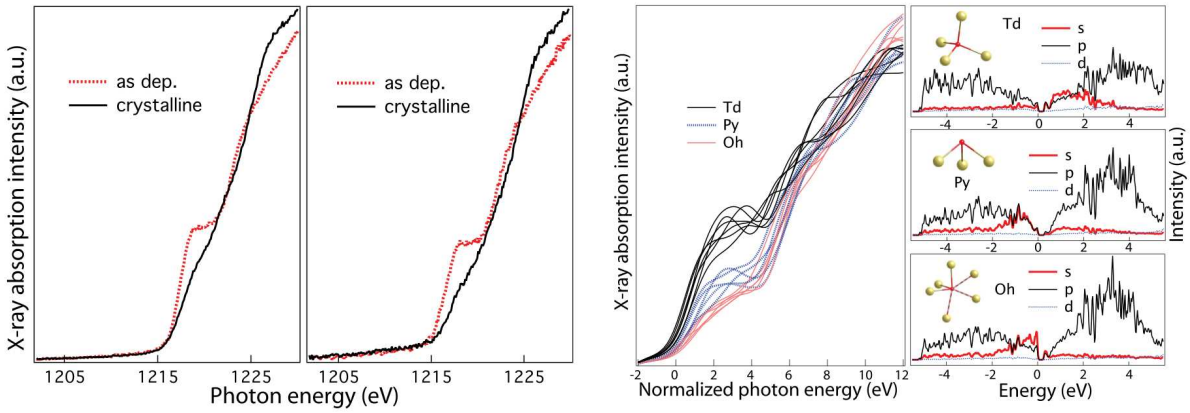

(a) **(b)**

Figure 1.44.: (a) Experimental Ge L_3-edge XANES spectra measured for as-deposited amorphous (red dotted line) and crystalline (black solid line) GeTe (left panel) and GST (right panel). (b) Ge L_3-edge XANES spectra simulated for each of the 20 Ge atoms in a model for amorphous GST (left panel) which demonstrate contribution of octahedral (red), pyramidal (blue), and tetrahedral (black) structural units to the overall XANES spectrum. Averaged local projected density of states for tetrahedrally, octahedrally, and pyramidally coordinated Ge atoms are given in the right panel [141].

carrier hopping among defect states and carrier injection in valence/conduction bands via the Poole-Frenkel mechanism (see Section 1.4.2 and Figure 1.43).
Information on the structural relaxations responsible for the drift have been recently obtained from Ge K-edge x-ray absorption near-edge structure (XANES) measurements on amorphous GST samples annealed at different temperatures. A correlation was found between the resistance drift and the reduction of tetrahedral Ge atoms [140]. Indeed, it was shown that the drift is correlated with the reduction of a step-like feature in the pre-edge XANES spectra [140]. The same feature was actually previously ascribed to the presence of tetrahedrally coordinated Ge from the comparison between experimental spectra and ab-initio XANES spectra computed for small atomistic models [141] (Figure 1.44). The results seem thus to suggest that the drift is correlated with a reduction of Ge in tetrahedral sites.

2. Computational methods

In this chapter we describe the computational methods employed in the analysis of phase change materials. The amorphous phase of the InSbTe and GaSbTe alloys of interest for their high crystallization temperature was studied by generating melt quenched models through *ab-initio* Molecular Dynamics (MD) simulations based on density functional theory (DFT). The calculations were performed with three different approaches to molecular dynamics: Car-Parrinello MD, Car-Parrinello MD in the scheme proposed by Kühne *et al.* [142] and inverse simulated annealing (ISA). These methods allow simulating models few hundreds-atom large, enough to have a description of the structural properties of the amorphous phases. In particular, the scheme proposed by Kühne *et al.* [142] allow speeding up substantially the DFT-MD simulations. The ISA method is devoted to generating amorphous models by imposing constraint on structural data available from experiments.
In order to study the structural relaxations leading to the change in the electronic structure responsible for the drift process, larger amorphous models of thousands of atoms are needed to have a sufficiently good statistics on the electronic defect states. In this case, classical MD simulations were performed to generate amorphous models of GeTe by using a Neural-Network interatomic potential for GeTe. To accelerate the occurrence of the structural relaxations, we also used a metadynamics technique that allows overcoming large activation barriers on the short time scale accessible by the simulations. In this chapter we briefly introduce some generalities on MD simulations and DFT theory, we then discuss in more details the scheme proposed by Kühne *et al.* [142], the ISA method and finally the metadynamics technique.

2.1. Molecular Dynamics

Molecular Dynamics (MD) is a technique that allows calculating equilibrium and dynamical properties of a many-body classical system once the initial conditions of positions, velocities and the interaction potential between particles at time t_0 are known. Position and velocity of all the particles at any instant value of time after t_0 are calculated by numerically integrating the Newton's equations of motion. The reliability of the calculation depends on the accuracy of the interaction potential.
In classical molecular dynamics, the interatomic potential is generally described by an analytical expression that contains empirical parameters obtained from the fitting of experimental

or *ab-initio* data. In this respect, the reliability of the results is closely linked to the transferability of the potential which generally well describes the system only in conditions similar to those at which the parameters of the potential were obtained. This approach allows for long simulations (several ns) of very large systems, up to 10^7 atoms.
In *ab-initio* molecular dynamics, ions are still considered as classical particles but the forces acting on the ions are obtained by solving the electronic problem within the Born-Oppenheimer approximation. The Schrödinger equation for electrons is thus solved for every ionic configuration. This method ensures a much better accuracy with respect to classical MD, but it is more computationally demanding and allow simulating small systems of at most several hundred atoms for few hundreds of ps.
Once the forces acting on the ions are known, the time evolution is ruled by the equation of classical mechanics:

$$M_I \ddot{\mathbf{R}}_\mathbf{I} = \mathbf{F}_I \tag{2.1}$$

where $\mathbf{F}_I$ is the force on the I-th nucleus and M_I and $\ddot{\mathbf{R}}_\mathbf{I}$ are the nuclear mass and acceleration, respectively. The numerical integration of the equation of motion (2.1) is performed by a finite difference method by discretizing the time in steps Δt [143–146]. One of the most simple and stable algorithm is the Velocity Verlet algorithm [145, 146]. In this method, positions $\mathbf{R}_i$ and velocities $\mathbf{v}_i$ at time $t+\Delta t$ can be obtained from the values at time t from

$$\begin{aligned} \mathbf{R}_I(t+\Delta t) &= \mathbf{R}_I(t) + \mathbf{v}_I(t)\Delta t + \frac{\mathbf{F}(\{\mathbf{R}_I(t)\})}{2M_I}(\Delta t)^2 \\ \mathbf{v}_I(t+\Delta t) &= \mathbf{v}_I(t) + \frac{\mathbf{F}_I(\{\mathbf{R}_I(t)\}) + \mathbf{F}_I(\{\mathbf{R}_I(t+\Delta t)\})}{2M_I}\Delta t. \end{aligned} \tag{2.2}$$

The atomic trajectories allow computing microscopic observables A which can be expressed as a function of ions positions and velocities. Under the assumption of the ergodic hypothesis, A is obtained as a time average over the trajectories

$$\langle A \rangle_{ens} = \langle A \rangle_{exp} = \lim_{\tau\to\infty} \frac{1}{\tau} \int_0^\tau A(\{\mathbf{R}_I(t)\}, \{\mathbf{v}_I(t)\}) dt. \tag{2.3}$$

The solution of the equations of motion (2.1) allows one to obtain a trajectory that, under the ergodic assumption, correctly samples the microcanonical ensemble (NVE). However, constant temperature averages can also be obtained in molecular dynamics simulations. By introducing an external thermostat coupled to the ions, it is possible to suitably modify the trajectory of the ions in such a way that the time average (2.3) corresponds to the average over the canonical ensemble (NVT). A possible scheme is the Langevin dynamics [147] in which the equation of motion is modified as

$$M_I \ddot{\mathbf{R}}_I = -\frac{\partial V}{\partial \mathbf{R}_I} - \gamma_L \dot{\mathbf{R}}_I + \Xi(t) \tag{2.4}$$

where γ_L is a friction coefficient and Ξ represent the stochastic forces. In order to sample the canonical ensemble, γ_L and Ξ must be chosen in order to fulfill the fluctuation-dissipation theorem [148] which states that

$$\langle \Xi_I(t)\Xi_I(t^{'})\rangle = 6\gamma_L M_I k_B T \delta(t-t^{'}). \tag{2.5}$$

2.2. Density functional theory

First principles MD simulations on amorphous models were performed within the density functional theory (DFT), a very efficient scheme to calculate the ground state electronic structure based on the celebrated theorems by Hohenberg and Kohn [149] and Kohn and Sham [150].

Density functional theory can be applied to any system of interacting particles in an external potential $V_{ext}(\mathbf{r})$. According to the Hohenberg and Kohn theorem, the ground state energy E of the electronic Hamiltonian can be written as a unique functional of the electron density $n(\mathbf{r})$:

$$E[n(\mathbf{r})] = \int d\mathbf{r} V_{ext}(\mathbf{r}) n(\mathbf{r}) + \frac{1}{2}\int d\mathbf{r} d\mathbf{r}' \frac{n(\mathbf{r})n(\mathbf{r}')}{|\mathbf{r}-\mathbf{r}'|} + F[n(\mathbf{r})]. \tag{2.6}$$

The second term in equation (2.6) represents the Coulomb interaction between electrons in the mean field (Hartree) approximation, while the third term $F[n(\mathbf{r})]$ is a universal functional of the ground state electron density which describes the kinetic energy and the exchange and correlation energy of the system. The calculation of the ground state energy does not require the knowledge of the ground state wavefunction which depends on the position of all the electrons in the system, but it can be obtained by minimizing the functional which is variational with respect to the density. The density $n(\mathbf{r})$ that minimizes the functional is the ground state electron density $n_0(\mathbf{r})$. However, the calculation of the ground state energy requires the knowledge of the universal functional $F[n(\mathbf{r})]$ whose exact expression is unknown.

A method to find reliable approximations for $F[n(\mathbf{r})]$ was proposed by Kohn and Sham. It is based on the introduction of an auxiliary system made of non-interacting particles with a ground state electronic density $n_0(\mathbf{r})$ equal to the density of the original problem of interacting particles (Kohn-Sham *Ansatz*). The single particle wave functions of this non-interacting system ψ_i satisfy the condition

$$n(\mathbf{r}) = \sum_i |\psi_i|^2 \tag{2.7}$$

and the energy of the system can be written as

$$E = \sum_i \left\langle \psi_i \left| -\frac{\nabla^2}{2} \right| \psi_i \right\rangle + \int d\mathbf{r} V_{ext}(\mathbf{r}) n(\mathbf{r}) + E_H + E_{xc} \tag{2.8}$$

where the first term is the kinetic energy of non-interacting electrons, E_H is the Hartree energy and E_{xc} is the exchange and correlation energy which contains all the terms in $F[n(\mathbf{r})]$ not included in the kinetic term. The Kohn-Sham eigenstates ψ_i are obtained by minimizing the functional of equation (2.8) which yields a self-consistent single particle equation

$$H_{KS}\psi_i(\mathbf{r}) = \left[-\frac{1}{2}\nabla^2_{\mathbf{r}} + V_{ext}(\mathbf{r}) + V_H(\mathbf{r}) + V_{xc}(\mathbf{r})\right]\psi_i(\mathbf{r}) = \varepsilon_i\psi_i(\mathbf{r}) \tag{2.9}$$

where ε_i are the Kohn-Sham eigenvalues.
The Hartree electronic potential $V_H(\mathbf{r})$ is defined by

$$V_H(\mathbf{r}) = \int d\mathbf{r}' \frac{n(\mathbf{r}')}{|\mathbf{r}-\mathbf{r}'|} \tag{2.10}$$

while the exchange and correlation potential $V_{xc}(\mathbf{r})$ is the functional derivative of the xc energy with respect to the electron density:

$$V_{xc}(\mathbf{r}) = \frac{\delta E_{xc}[n(\mathbf{r})]}{\delta n(\mathbf{r})}. \tag{2.11}$$

This is the unknown term of equation (2.9). The total energy of the system can thus be expressed as

$$E = \sum_{i_{occ}} \varepsilon_i - \frac{1}{2}\int d\mathbf{r}d\mathbf{r}' \frac{n(\mathbf{r})n(\mathbf{r}')}{|\mathbf{r}-\mathbf{r}'|} + E_{xc}[n(\mathbf{r})] - \int d\mathbf{r} n(\mathbf{r}) V_{xc}(\mathbf{r}). \tag{2.12}$$

The Kohn-Sham equation (2.9) is solved self-consistently with iterative methods, once the xc functional has been defined. Although the energy $E_{xc}[n(\mathbf{r})]$ represents only a small fraction of the total energy of the system, it gives an essential contribution to the formation of chemical bonds, therefore the correct estimate of the exchange and correlation energy is crucial to determine the energy of a system.
A first approximation for the exchange and correlation functional was proposed by Kohn and Sham. The energy density of the system was locally set equal to that of a homogeneous gas $\varepsilon_{xc}(n(\mathbf{r}))$ of free electrons (*jellium*) with the same local density of the non-homogeneous system. Thus the xc energy can be written as a local functional of the density as

$$E^{LDA}_{xc}[n(\mathbf{r})] = \int d\mathbf{r} \varepsilon^{gas}_{xc}(n(\mathbf{r}))n(\mathbf{r}). \tag{2.13}$$

This approximation for the xc functional, known as the Local Density Approximation (LDA), gives accurate results even for solids with highly inhomogeneous electron densities as semiconductors and insulators. It is possible to take into account the spin degrees of freedom by separating the electron density into the contributions $n_\uparrow$ and $n_\downarrow$ for spin up and spin down

electrons (Local Spin Density Approximation, LSDA).
The agreement with experimental data can be improved by using xc functionals based on the Generalized Gradient Approximation (GGA) [151, 152] where the exchange and correlation energy depends on the local electron density and on its gradient:

$$E_{xc}^{GGA}[n(\mathbf{r})] = \int d\mathbf{r}\varepsilon_{xc}[n_{\uparrow}(\mathbf{r}), n_{\downarrow}(\mathbf{r}), \nabla n_{\uparrow}(\mathbf{r}), \nabla n_{\downarrow}(\mathbf{r})]n(\mathbf{r}) \tag{2.14}$$

where $n_{\uparrow}$ and $n_{\downarrow}$ are the spin resolved electron densities.
Although the KS eigenvalues do not formally represent, within DFT, the single particles eigenstates, they provide a good description of the band structure of solids. However, xc functionals in the local and semi-local approximation typically underestimate the band gap of semiconductors and insulators which actually hinders the possibility to perform a quantitative analysis of electronic in-gap states in the amorphous materials we are interested in. In order to overcome this limitations of LDA and GGA functionals we resort to hybrid functionals discussed in the next section which better describe the band gap.

2.3. Hybrid functionals

Hybrid exchange and correlation functionals were firstly introduced by Becke [153]. These functionals combine a fraction of the exact Hartree-Fock exchange energy E_x^{HF} with a fraction of exchange and correlation energy in the LDA or GGA approximation. Hybrid functionals better reproduce the experimental gap of insulators and semiconductors. The xc functional proposed by Becke was initially given by

$$E_{xc} = \frac{1}{2}(E_x^{HF} + E_x^{DFA}) + E_c^{DFA} \tag{2.15}$$

where E_x^{DFA} and E_c^{DFA} are the LDA o GGA exchange and correlation energy.
More recently, new density functional approximations to the hybrid functionals have been proposed mixing exact exchange and the DFT energy in different ratios. For large systems the calculation of exchange integrals can be computationally very demanding due to the slow decay of the Hartree-Fock exchange interaction with the interatomic distance. To overcome this problem, screened hybrid functionals, which take into account only a short range term of the HF exchange, have been introduced.
To calculate the electronic structure of the amorphous models of InSbTe and GaSbTe alloys, the screened Heyd-Scuseria-Ernzerhof HSE06 functional [154] was used. This functional combines a fraction of HF exchange with a fraction of GGA exchange and correlation proposed

by Perdew, Burke and Ernzerhof (PBE) [151] as

$$E_{xc}^{HSE03} = \frac{1}{4}E_x^{HF,sr} + \frac{3}{4}E_x^{PBE,sr} + E_x^{PBE,lr} + E_c^{PBE} \tag{2.16}$$

where superscripts sr and lr indicate the short- and long-range components, respectively. The separation of the short- and long-range terms is obtained by decomposing the $1/r$ term, defined as $r = |\mathbf{r} - \mathbf{r}'|$, as

$$\frac{1}{r} = S_\mu(r) + L_\mu(r) = \frac{erfc(\mu r)}{r} + \frac{erf(\mu r)}{r} \tag{2.17}$$

where $S_\mu(r)$ and $L_\mu(r)$ represent the short- and long-range terms, while $erf(\mu r)$ and $erfc(\mu r)$ are, respectively, the error function and the complementary error function and μ is an empirical parameter indicating the characteristic distance at which the short-range interactions of the HF term become negligible.
It has been shown that calculations with the screened HSE06 functional give results very similar to those of calculations with the corresponding non-screened hybrid functional PBE0 [155].

2.4. Quickstep algorithm

To generate models of amorphous InSbTe and GaSbTe alloys we used the CP2K code with the particular implementation of the DFT method that we describe here. By expanding the Kohn-Sham (KS) states on a finite basis set, the single particle differential equation (2.9) turns into the problem of diagonalization of a matrix. For condensed systems, a plane wave basis set is usually used which allows to efficiently calculate the Hartree energy E_H and the exchange and correlation energy E_{xc}. In quantum chemistry codes the eigenfunctions ψ_i are instead expanded on a set of Gaussian functions localized on the atoms. The main advantage of this approach is that the number of Gaussian functions required for a good description of the ψ_i wavefunctions is significantly lower with respect to the number of plane waves. However, the solution of the Poisson equation becomes in this case more difficult. A good compromise between the two approaches, is offered by the hybrid Gaussian and Plane Waves (GPW) method [156], implemented in the Quickstep algorithm [157]. This scheme employs a mixed basis set by expanding the ψ_i on a set of Gaussian functions and the electron density $n(\mathbf{r})$ on a plane wave set:

$$n(\mathbf{r}) = \frac{1}{\Omega}\sum_{\mathbf{G}} \tilde{n}(\mathbf{G}) e^{i\mathbf{G}\cdot\mathbf{r}} = \sum_{\mu\nu} P^{\mu\nu}\varphi_\mu(\mathbf{r})\varphi_\nu(\mathbf{r}) \tag{2.18}$$

where $\psi_i = C_i^\mu \varphi_\mu$, $P^{\mu\nu} = \sum_i C_i^\mu C_i^\nu$ are the elements of the density matrix, $\varphi_\mu(\mathbf{r}) = \sum_i d_{i\mu} g_i(\mathbf{r})$ with $g_i(\mathbf{r})$ Gaussian functions with contraction coefficients $d_{i\mu}$, Ω is the unit cell volume and

G a reciprocal lattice vector limited by the cut-off imposed on the plane waves expansion.
Once the representation of the electronic density in real space is known, it is possible to obtain its representation in reciprocal space with a Fast Fourier Transform (FFT) technique which allows solving the Poisson equation efficiently. By using this dual representation of the density and KS orbitals, the expression of the energy has the form

$$\begin{aligned} E[n] &= E_T + E_{ext} + E_H + E_{xc}[n] + E_{II} \\ &= \sum_{\mu\nu} P^{\mu\nu} \langle \varphi_\mu(\mathbf{r}) | -\frac{1}{2}\nabla^2 | \varphi_\nu(\mathbf{r}) \rangle + \sum_{\mu\nu} P^{\mu\nu} \langle \varphi_\mu(\mathbf{r}) | V_{PP}^{loc}(r) | \varphi_\nu(\mathbf{r}) \rangle \\ &+ \sum_{\mu\nu} P^{\mu\nu} \langle \varphi_\mu(\mathbf{r}) | V_{PP}^{nl}(\mathbf{r}, \mathbf{r}') | \varphi_\nu(\mathbf{r}') \rangle + 2\pi\Omega \sum_{\mathbf{G}} \frac{n^*(\mathbf{G}) n(\mathbf{G})}{\mathbf{G}^2} \\ &+ \frac{1}{2} \sum_{I \neq J} \frac{Z_I Z_J}{|\mathbf{R}_I - \mathbf{R}_J|} + E_{xc}[n(\mathbf{r})] \end{aligned} \tag{2.19}$$

where E_T is the electronic kinetic energy, $E_{ext}[n]$ the electronic interaction with ionic cores, $E_H[n]$ the Hartree electronic energy, $E_{xc}[n]$ the exchange and correlation energy and E_{II} the ion-ion interaction.
Core electrons are not explicitly considered and only valence electrons are taken into account. The interaction between the valence electrons and the ionic cores is actually described by pseudopotentials V_{PP} built on an all-electrons calculation on isolated atoms. In the Quickstep scheme the pseudopotentials are expressed as a linear combination of Gaussian functions as proposed by Gödecker, Teter and Hutter (GTH) [158, 159] which ensures an efficient evaluation of the E_{ext} term in equation (2.19). The pseudopotential is written as the sum of a local $V_{pp}^{loc}(\mathbf{r})$ and non-local $V_{pp}^{nl}(\mathbf{r}, \mathbf{r}')$ terms.
Once solved the electronic problem, the forces acting on the ions are obtained from the Hellmann-Feynman [160] theorem:

$$\mathbf{F}_I = -\frac{\partial \langle \hat{H} \rangle}{\partial \mathbf{R}_I} = -\left\langle \frac{\partial \hat{H}}{\partial \mathbf{R}_I} \right\rangle \tag{2.20}$$

where $\hat{H}$ represents the hamiltonian operator that describes the electrons and the ion-electron interactions.
In Born-Oppenheimer molecular dynamics the electronic problem is solved at each step of the ions dynamics.

2.5. Car Parrinello ab-initio molecular dynamics

An alternative approach to Born-Oppenheimer *ab-initio* MD was proposed in 1985 by Car and Parrinello [161]. This technique, employed in this thesis to generate small models (100

atoms) of amorphous $Ga_4Sb_6Te_3$, is based on the transformation of the Kohn-Sham states in classical fields to which a fictitious kinetic energy is associated in the Lagrangian given by

$$L = \sum_i \frac{1}{2}\mu \int_\Omega |\dot{\psi}_i(\mathbf{r})|^2 d\mathbf{r} + \sum_I \frac{1}{2} M_I \dot{\mathbf{R}}_I^2 - E_{DFT}[\{\psi_i(\mathbf{r})\}, \{\mathbf{R_I}\}]. \tag{2.21}$$

The Euler-Lagrange equations obtained from Lagrangian (2.21) with the holonomic constraint of ortho-normality of the ψ_i, generate a dynamics in which the fields ψ_i adiabatically follow the nuclear motion by oscillating on the Born-Oppenheimer (BO) surfaces assigned by the E_{DFT} functional. The adiabatic separation requires, however, fictitious masses μ small enough to ensure that the characteristic oscillation frequencies of the fields ψ_i are considerably larger than the characteristic vibrational frequencies of the ions. This scheme avoids the self-consistent solution of the Kohn-Sham problem at each step of the ionic dynamics at the cost of using a time step of the order of $1/10 - 1/100$ of that used in BO-MD, because of the need of describing the fast dynamics of the electronic fields.

Recently, Kühne *et al.* [142] proposed a new method that combines the advantages of the Car-Parrinello and of the BO schemes. In this approach, the electronic states are propagated without solving the self-consistent problem but by still using the typical time steps of the BO-MD. This scheme allowed us to generate large models (200-300 atoms) of amorphous InSbTe and GaSbTe alloys by slowly quenching from the melt (up to 300 ps).

In this method the wave functions are calculated in a self-consistent way only in the first steps of the dynamics and then the density matrix $\mathbf{P} = \mathbf{C}\mathbf{C}^T$ is propagated with the Always Stable Predictor Corrector (ASPC) algorithm of Ref. [162]. The expansion coefficients of the Kohn-Sham states $\mathbf{C}$ on the local basis set are calculated through the Predictor algorithm

$$\mathbf{C}^p(t_n) \cong \sum_{m=1}^{K} (-1)^{m+1} m \frac{\binom{2K}{K-m}}{\binom{2K-2}{K-1}} \underbrace{\mathbf{C}(t_{n-m})\mathbf{C}^T(t_{n-m})}_{=\mathbf{P}(t_{n-m})} \mathbf{S}(t_{n-m})\mathbf{C}(t_{n-1}) \tag{2.22}$$

where $\mathbf{S}$ is the overlap matrix of the basis functions. In equation (2.22) the **PS** matrices of the previous K steps are linearly combined. **PS** is invariant with respect to a unitary transformation of the coefficients $\mathbf{C}$ and hence, as opposed to the $\mathbf{C}$ coefficients, it varies slowly as the ionic positions change and it can be easily extrapolated.

Once the coefficients are obtained, the Corrector algorithm is applied to the $\mathbf{C}^p(t_n)$ in order to minimize the error in the propagation:

$$\mathbf{C}(t_n) = \omega MIN[\mathbf{C}^p(t_n)] + (1-\omega)\mathbf{C}^p(t_n) \tag{2.23}$$

where

$$\omega = \frac{K}{2K-1} \tag{2.24}$$

and $MIN[\mathbf{C}^p(t_n)]$ represents a single minimization step. This procedure obviously introduces an error in the calculation of the ground state density. $\mathbf{C}(t_n)$ is an approximated eigenfunction of $H[n^p]$ in the subspace sampled by the finite basis set used and this implies that the error on the forces is negligible only if $\mathbf{C}(t_n)$ is close to the ground state. However, it can be demonstrated that the forces calculated with this method are very close to those obtained with a self-consistent procedure and the error on the forces can be approximated by a white noise.
The deviation from the BO surface leads to a dissipative dynamics which can be, however, compensated by a thermostat as described below. It has been shown that the forces F_{PC}, obtained from the Predictor-Corrector step, differ from that obtained in a conservative BO dynamics by a dissipative term as

$$\mathbf{F}_{PC} = \mathbf{F}_{BO} - \gamma_D \dot{\mathbf{R}}_I \tag{2.25}$$

where γ_D is a friction coefficient. In order to correctly sample the canonical ensemble the dissipative term can be compensated by stochastic forces $\Xi_I^D(t)$ according to a Langevin dynamics (see Section 2.1) as

$$M_I \ddot{\mathbf{R}}_I = \mathbf{F}_{PC} + \Xi_I^D(t). \tag{2.26}$$

Moreover, it is also necessary to introduce a second Langevin thermostat at the target temperature with friction coefficient γ_L and stochastic force $\Xi_I^L(t)$ to provide a fast equilibration. Thus, the overall equations of motion are

$$\begin{aligned} M_I \ddot{\mathbf{R}}_I &= \mathbf{F}_{PC} - \gamma_L \dot{\mathbf{R}}_I + \Xi_I^L(t) \\ &= \mathbf{F}_{BO} - (\gamma_D + \gamma_L)\dot{\mathbf{R}}_I + \Xi_I(t) \end{aligned} \tag{2.27}$$

where $\Xi_I(t) = \Xi_I^D(t) + \Xi_I^L(t)$. While the choice of γ_L is arbitrary, the value of γ_D must be determined so that the associated white noise compensates the dissipation due to the error in the calculation of the forces, keeping the energy constant during the dynamics.

2.6. Inverse simulated annealing

The Born-Oppenheimer or the Car-Parrinello like methods described in the previous section can be used to generate models of the amorphous phase by quenching from the melt. However, preparation methods different from melt-quenching such as deposition by sputtering or MOCVD might lead to different amorphous structures. These polyamorphisms might make the comparison between theory and experiments problematic when the theoretical models are generated only by quenching from the melt.
An alternative method to generate amorphous models has been proposed recently by Los and Kühne [163]. This method, called Inverse Simulated Annealing (ISA), is a combination of a simulated annealing and Reverse Monte-Carlo (RMS) scheme and exploits the advantages of

both the techniques. In this scheme, the potential energy calculated at the DFT level is minimized under soft constraints imposed by experimental data. The use of DFT in this method rules out the possibility of generating unphysical structures which are sometimes found by traditional RMC fitting of the experimental data. Moreover, the method allows generating amorphous models at a desired target pressure which is particularly needed if the experimental density of the amorphous is not known or when it is anyway expected to differ from the theoretical equilibrium density.

The ISA simulations allow generating amorphous models suitable to reproduce available experimental data and at the same time to lie in a low local minimum of the potential energy surface. In this work, the ISA method was applied to InSb alloys in order to generate amorphous models at the theoretical equilibrium density by fitting the available experimental structural data on amorphous samples grown by sputtering.

In the ISA technique, the ionic positions $\mathbf{R}_I$ are assigned by minimizing a function of the form

$$\tilde{U}(\mathbf{R}) = U(\mathbf{R}) + \sum_p w_p \left(\chi_p(\mathbf{R}) - \chi_p^{exp}\right)^2 \tag{2.28}$$

where $\mathbf{R} = \{\mathbf{R}_i\}$, U is the DFT potential energy and χ_p are properties of the system for which experimental data χ_p^{exp} are available. These ones may include structural properties from scattering data, but also properties related to the electronic structure, such as the band gap. Alternatively, χ_p^{exp} in equation 2.28 could be replaced by a target property, e.g. a desired property for a certain application.

The minimizer of the function $\tilde{U}(\mathbf{R})$ is a Monte-Carlo (MC) method with all atom trial moves that involve the forces and follows an NVE approach with the corresponding acceptance probability. The all atom trial moves are generated by a single, energy conserving, Velocity-Verlet [145, 146] MD step (see equation 2.2) but with a randomly chosen time step $dt \in (0, dt_{max})$, where dt_{max} is fixed and, typically, up to an order of magnitude larger than the time step in a normal MD simulation. From MC simulation within the NVE ensemble, the acceptance probability of the trial move is given by

$$P = \min\left(1, \left(\frac{E - \tilde{U}'}{E - \tilde{U}}\right)^{\nu\left(\frac{3N}{2}-1\right)}\right) \tag{2.29}$$

where E is the total energy, N is the number of atoms in the system, $\tilde{U}'$ the energy of equation 2.28 calculated for the new trial move and ν is a number larger than zero adjusted on the fly to achieve the desired acceptance rate (generally 50 %). Indeed, for $\nu \to 0$, $P \to 1$ and all move are accepted, while for very large ν only moves for which $\tilde{U}' < \tilde{U}$ are accepted, excluding the possibility to cross energy barriers of any height. In a NVE simulation, the total energy E is fixed while the average temperature is assigned by $E - U = K = \frac{3}{2}Nk_BT$, where K is the kinetic energy.

In an annealing simulation T is linearly lowered from T_{high} to $T_{low} = 0^+$ as a function of the MC step, still preserving the NVE features. In this scheme, E is updated in steps as soon as the measured temperature T_{meas} is outside a given window ΔT_{window} around the applied temperature T. The measured or actual "temperature", T_{meas}, is associated to the kinetic energy K of the system by $K = E - \tilde{U} = \frac{3}{2} N k_B T_{meas}$. After each accepted move, whenever $|T_{meas} - T| > \Delta T_{window}$, E is adjusted such that the kinetic energy, and correspondingly the velocities, are in agreement with the applied temperature, i.e. such that $E - \tilde{U} = \frac{3}{2} N k_B T$.
A flowchart of the minimization algorithm used in the ISA method is reported in Figure 2.1.

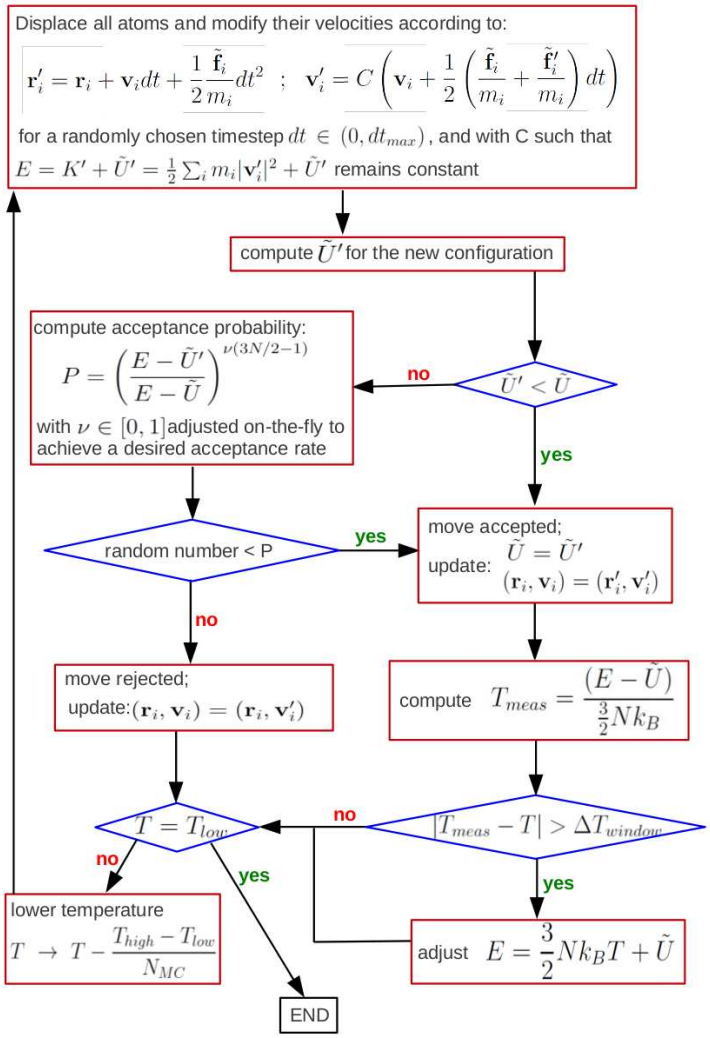

Figure 2.1.: Flowchart of the minimization algorithm used in conjunction with ISA. In the upper panel, $\mathbf{v}_i$ is the velocity of atom i and $\tilde{\mathbf{f}}_i$ is the best approximation of the total force $\partial U / \partial \mathbf{r}_i$ on atom i.

2.6.1. Volume fluctuations

A minimization with ISA at constant volume will in general lead a structure with non-zero stress, depending on the chosen density. In fact, the experimental density is often not known and, anyway, it would be preferable to generate an amorphous model at the theoretical equilibrium density which might differ from the experimental one because of the inaccuracies of the interatomic potential (exchange and correlation functional) used. An amorphous model at zero pressure can be generated by including volume fluctuations in the ISA scheme, similarly to standard MC simulations at constant pressure. In order to keep the pressure fluctuating around a given target pressure P_{ext} , we may simply add the volume dependent contributions to the Gibbs free energy to the function to be minimized, which then turns into (calling it $\tilde{G}$):

$$\tilde{G}(\mathbf{R},V) = U(\mathbf{R}) + P_{ext}V - Nk_BT\ln(V) + \sum_p w_p \left(\chi_p(\mathbf{R},V) - \chi_p^{exp}\right)^2. \tag{2.30}$$

One then applies the standard MC acceptance probability for volume changes

$$P = \min\left(1, \left(e^{-\beta\Delta\tilde{G}}\right)\right) \tag{2.31}$$

with $\beta = 1/(k_BT)$ and where $\Delta\tilde{G}$ is the change in $\tilde{G}$ due to the volume change. Without the contributions from the constraint terms, this probability would be equal to the standard probability for volume fluctuation in NPT MC simulations [164]. Indeed, minimization of $\tilde{G}(\mathbf{R},V)$ with respect to V leads to

$$\begin{aligned}
\frac{d\tilde{G}}{dV} &= -P_{vir} + P_{ext} - P_{kin} + 2\sum_p w_p \left(\chi_p(\mathbf{R},V) - \chi_p^{exp}\right)\frac{d\chi_p}{dV} \\
&= P_{ext} - P_s + 2\sum_p w_p \left(\chi_p(\mathbf{R},V) - \chi_p^{exp}\right)\frac{d\chi_p}{dV} \\
&= 0
\end{aligned} \tag{2.32}$$

where $P_{vir} = -dU/dV$ is the virial contribution and $P_{kin} = Nk_BT/V$ the ideal vapor (kinetic) contribution to the total pressure $P_s = P_{kin} + P_{vir}$. Hence, without the constraint terms, the condition $d\tilde{G}/dV = 0$ implies $P_s = P_{ext}$. In that case the actual pressure P_s of the system in an NPT MC simulation fluctuating around P_{ext}, the size of the fluctuations depending on temperature. How to achieve this situation with the constraint terms is not obvious. Note that in general $d\chi_p/dV$ is non-zero, and neither is $\chi_p(\mathbf{R},V) - \chi_p^{exp}$ during the simulation. As a general rule to circumvent or reduce the problem of spurious pressure contributions coming from the constraint terms one should choose the weight factor w_p as small as possible, but at the same time large enough to achieve the desired agreement with the experimental property. For certain properties the above problem can be solved in a more rigorous way by defining

the constraint term in a form that is invariant under volume fluctuations. In particular, this holds for a very important property, for which experimental data are often available, namely the pair correlation function (PCF). For this property, the constraint term, $\tilde{U}_g$, can be defined in a scale invariant form as:

$$\tilde{U}_g(\mathbf{R}) = w_g \sum_{n=1}^{N_{rn}} \left(g_s(\mathbf{R}; s_r r_n) - g^{exp}(r_n)\right)^2 \tag{2.33}$$

where the sum runs over the N_{rn} grid points r_n on which the experimental PCF, $g^{exp}(r_n)$, is tabulated and where $s_r = (V/V_{exp})^{(1/3)} = (\rho_{exp}/\rho)(1/3)$ is a scale factor with $\rho = 1/V$ the actual density of the system and $\rho_{exp} = 1/V_{exp}$ the experimental density. Using the scale invariant form for $\tilde{U}_g$ in equation 2.33, the constraint is restricted to the shape of the PCF, so that differences between the experimental and theoretical density due to bond distance under-/overestimation by DFT are not penalized by $\tilde{U}_g$. For the reduced PCF (RPCF), defined as $G(r) = 4\pi r\rho(g(r) - 1)$, the scale invariant form of the constraint term reads:

$$\tilde{U}_G(\mathbf{R}) = w_G \sum_{n=1}^{N_{rn}} \left(s_r^2 G_s(\mathbf{R}; s_r r_n) - G^{exp}(r_n)\right)^2. \tag{2.34}$$

2.7. Neural Network interatomic potential

In order to study the microscopic origin of defect states in the amorphous phase whose aging is responsible for resistance drift, large models of thousands of atoms are needed. Unfortunately, such large-scale simulations are not accessible by *ab-initio* MD. We thus restricted ourselves to the study of the resistance drift in amorphous GeTe for which a reliable interatomic potential was available and suitable to be used in simulations with several thousands of atoms. The interatomic potential for GeTe was generated by fitting a database of DFT energies [14] with the Neural Network (NN) method proposed by Behler and Parrinello [165].
Neural Networks (NN) are a class of algorithms widely applied to classification problems as speech [166] and text recognition [167], to financial market analysis [168] or weather forecast [169] and as fitting algorithms [170]. In this respect, it has been demonstrated that NNs can fit any continuous real-valued function of any dimension with arbitrary accuracy [171]. Among simulation techniques applied to materials science, Neural Networks become particularly useful to fit the potential energy surface (PES) of a system. In fact, other fitting algorithms fail in case of high dimensional functions as for example the PES of large models. NN, instead, can be nested to create hierarchical algorithms that provide a very high degree of flexibility, being able to handle fitting procedures of high dimensional functional mapping in a massively parallel way.
The potential energy surface can be represented by a feed-forward neural network which is

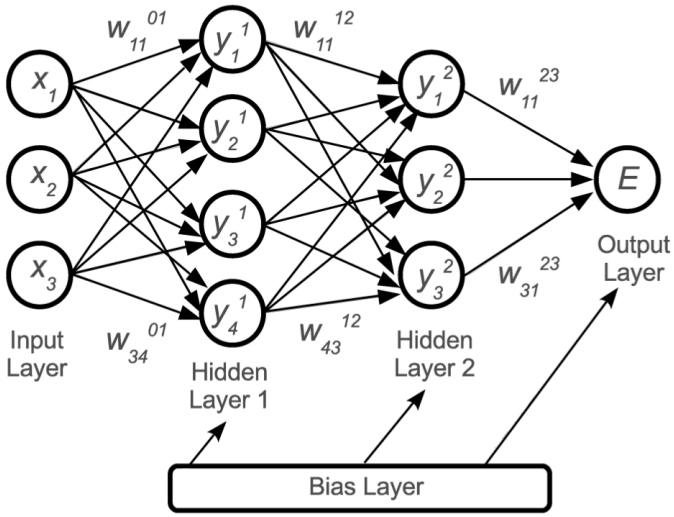

Figure 2.2.: Schematic representation of a simple feed-forward NN topology with two hidden layers.

a type of artificial NN formed by different layers where the information always moves in one direction, from the input layer to the output layer and never goes backwards. A schematic representation of a simple feed-forward NN is reported in Figure 2.2. The input and output layers are always present, while a variable number of hidden layers can be present between inputs and outputs. Each layer can be thought as a single neuron in a biological neural network and is composed by a certain number of nodes. The flexibility of the NN can be increased by increasing the number of hidden layers or the number of nodes in the hidden layers and hence the number of fitting parameter on which the function depends. These fitting parameters are sort of "weights" that connect the nodes in a layer with the nodes in the next one. In Figure 2.2 the parameter that weighs the i node in the k layer connecting it with the j node in the l layer is indicated by w_{ij}^{kl}. Moreover, the hidden layers can be linked with a bias layer with weights b_i^j.

In order to calculate the output of the neural network, each point x_i of the fitting dataset is assigned to a different node in the input layer and the output values y_j^1 of the first hidden layer are calculated through two steps. In the first step the input values are linearly combined with the weights w_{ij}^{01} and a bias value b_j^1 is added

$$\chi_j^1 = b_j^1 + \sum_i^4 w_{ij}^{01} \cdot x_i. \tag{2.35}$$

Then, a highly non-linear function f_j^1 is applied to the χ_j^1 values

$$y_j^1 = f_j^1(\chi_j^1). \tag{2.36}$$

The f_j^1 is an activation function that makes the NN able to fit any arbitrary function. In a similar way, the values of the nodes of the next layers and of the output can be obtained from the values calculated in the previous layers. The output of the NN may be an array of values or a single number calculated by summing up the results of the hidden layers as exemplified by the equation

$$E = f_1^3\left(b_1^3 + \sum_{i=1}^{3} w_{i1}^{23} + f_i^2\left(b_i^2 + \sum_{j=1}^{4} w_{ji}^{12} f_j^1 - \left(b_j^1 + \sum_{k=1}^{3} w_{kj}^{01} x_k\right)\right)\right) \tag{2.37}$$

that describe the procedure sketched in Figure 2.2.
Within the Neural Network, an activation function f is applied to the nodes in each hidden layer. The f function is generally a non-linear function that asymptotically converges to a finite value for very large and very small arguments, while in between it displays a non-linear behaviour. Different types of activation functions can be used, for example the sigmoid function (Figure 2.3)

$$f(x) = \frac{1}{1+e^{-x}}, \tag{2.38}$$

the hyperbolic tangent or Gaussian functions.
All these functions have a narrow range of possible values which may not match the range of values of interest in the functional mapping and need to be rescaled or shifted by a proper adjustment of the weights. The bias weights, instead, shift the position of the non-linear region of the activation function. Generally, from the last hidden layer to the output layer, the activation functions are linear in order to avoid any constraint in the range of output values.
In order to determine the values of the fitting parameters, an error function Γ, that describes how far is the i-th output value of the NN $\mathrm{E}_{i,NN}$ from a reference value $\mathrm{E}_{i,ref}$ of the dataset, must be defined:

$$\Gamma = \frac{1}{2N}\sum_{i=1}^{N}\left(E_{i,NN} - E_{i,ref}\right)^2 \tag{2.39}$$

where N is the number of points in the dataset. If the activation functions in the neural network are differentiable, also the output of the NN will be differentiable with respect to both input variables and weights and hence the error function Γ is a differentiable function of the weights. The error functions can thus be minimized by finding the roots of the partial derivatives of the error function with respect to the weights through a minimization procedure. The algorithm for evaluating the derivatives of the error function is known as “back propagation”, since it corresponds to a propagation of errors backwards through the NN. The process by

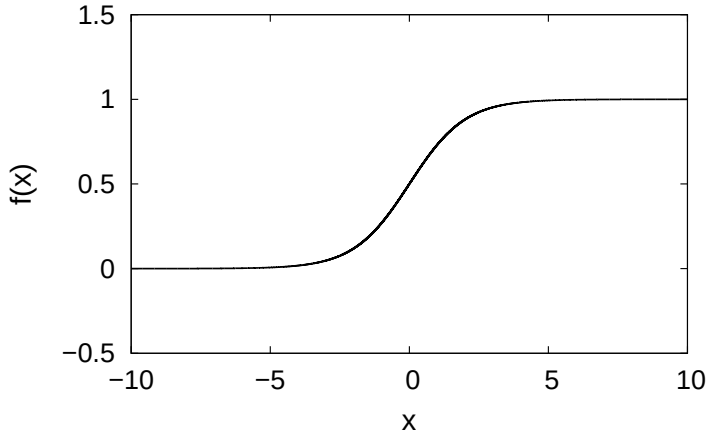

Figure 2.3.: Illustration of the sigmoid function of equation (2.38).

which the weights are iteratively improved until they provide a reasonable approximation of the underlying function is called ”training” or ”learning”, and each iteration of this process is known as ”epoch” in the NN context.

2.7.1. Neural Network potential energy surfaces for atomistic simulations

Neural networks have been used in atomistic simulations to build the potential energy surface of many different systems such as small molecules [172] and isolated gas molecules interacting with a surface [173]. In these cases a single NN is used to calculate the energy of the molecule and the NN potential is easy to implement due to the small number of degrees of freedom. However, once the fitting parameters of the NN are determined, the resulting potential have a very little transferability since it cannot be applied to systems with a different number of atoms. In fact, the number of input nodes, and hence the values of the weights, is fixed and assigned by the number of degrees of freedom of the system.
When the NN tool is applied to large systems of thousands of atoms, the fitting procedure gets longer and it would be not feasible to generate a different NN potential for each system size.
A first NN scheme to reproduce potential energy surfaces with a large number of degrees of freedom independently on the system size was proposed by Hobday *et al.* [174] for carbon-based systems. In this work, the chemical environment of each bond in the model was decomposed into a variable number of input vectors characterizing three-atom chains, which all have the same dimensionality. Starting from this idea, in a new approach to NNs the total energy of the system has been written as sum of the atomic energies, each obtained from a single atomic NN [175]. Each of these individual NNs has an input vector with a fixed number

of elements that describe the local environment of the atom and returns as output an atomic energy. This scheme was later used to generate a NN potential for silicon giving good results [176].
A further development of this method was proposed in 2007 by Behler and Parrinello [165] starting from the definition of the total energy as sum of the atomic energies

$$E_{tot} = \sum_{i=1}^{N} E_i(\{\mathbf{r}\}). \tag{2.40}$$

In this approach (Figure 2.4), the architecture of the NN is fixed for a given chemical element allowing to use a standard NN for each atom. An input vector for each atom describe the local environments considered up to a cut-off distance. In order to have a number of input nodes independent on the number of neighbours of each atom, the environment is described not in terms of Cartesian functions, but through special types of many-body "symmetry functions". The symmetry functions give information on the radial and angular arrangement of neighbours for each atom in the system. The symmetry functions must be chosen in order to ensure the invariance of the energy with respect to symmetry operations such as translations and rotations of the whole system and the exchange of two atoms of the same species. The input values of an individual atomic NN are a vector of symmetry function values $\{G_i\}$, each of them depending on the coordinates of all the atoms of the environment within the cut-off. For a given atomic species, the architecture and the fitting parameters of the NN are fixed, ensuring the invariance of the total energy with respect to the exchange of two atoms of the same type. The weights of the neural network are determined by fitting the total energies of different configurations obtained from DFT calculations.

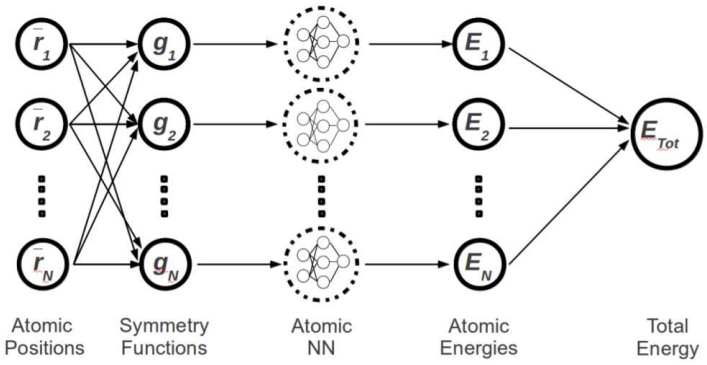

Figure 2.4.: Sketch of a neural network according to the scheme proposed by Behler and Parrinello [165].

Symmetry functions

In the generation of the NN potential for GeTe [14], two types of symmetry functions have been used: radial symmetry functions built by summing up two-body terms, and angular symmetry functions which contain three-body terms. The radial environment of atom i is described by two different radial functions with the form

$$\begin{aligned} G_i^1 &= \sum_j f_c(R_{ij}) \\ G_i^2 &= \sum_j e^{-\eta(R_{ij}-R_s)^2} \cdot f_c(R_{ij}). \end{aligned} \tag{2.41}$$

The cut-off function f_c is defined by

$$f_c(r_{ij}) = \begin{cases} 0.5\left[cos\left(\frac{\pi r_{ij}}{r_c}\right)+1\right] & \text{for } r_{ij} < r_c, \\ 0 & \text{for } r_{ij} > r_c. \end{cases} \tag{2.42}$$

Function G_i^1 is the sum on all the neighbouring j atoms within the cut-off, while G_i^2 is a sum of Gaussian functions centered at a certain radial distance R_s and multiplied by the cut-off function. These "shifted" G_i^2 functions are suitable to describe a spherical coordination shell around the reference atom. The radial distribution of neighbours can be described by using a set of radial functions with different spatial extensions, for example G_i^1 functions with different cut-off radii, or G_i^2 functions with different cut-offs and/or η and R_S parameters. The radial functions are sums over all the neighbours and hence they describe the pair correlation function of the system within the cut-off distance. Typical forms of the radial symmetry func-

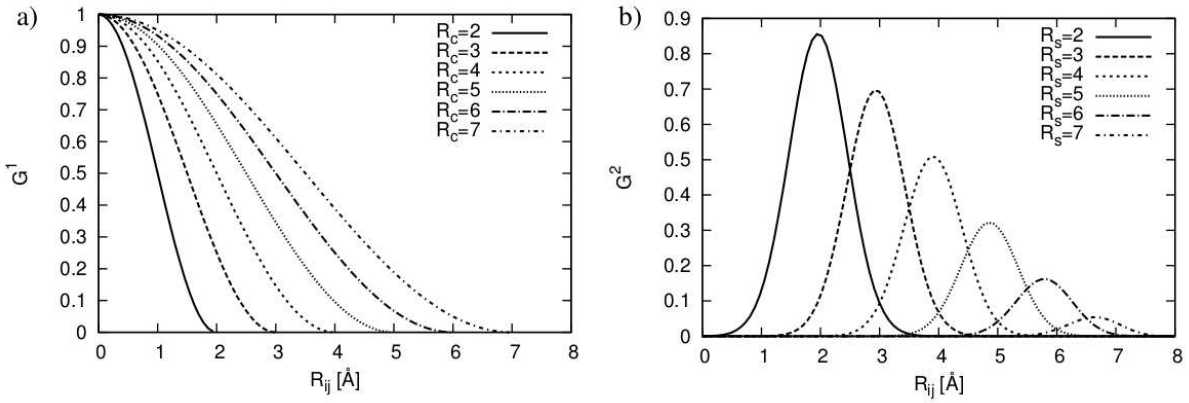

Figure 2.5.: Radial symmetry functions. a) G_i^1-type symmetry functions for different cut-off radii. b) G_i^2-type symmetry functions for different radial distances R_s with η=2 and R_c=8 Å respectively.

tions are plotted in Figure 2.5 for several parameter values. Angular symmetry functions are defined as functions of the bond angle θ_{jik} that the i-th atom forms with its two neighbours j and k and have the form

$$G_i^3 = 2^{1-\xi} \sum_{j,k\neq i}^{all} (1+\lambda cos\theta_{ijk})^{\xi} \cdot e^{-\eta(R_{ij}^2+R_{ik}^2+R_{jk}^2)^2} \cdot f_c(R_{ij}) \cdot f_c(R_{ik}) \cdot f_c(R_{jk}). \tag{2.43}$$

The parameter λ assumes values ± 1 shifting the maxima from 0° and 180° to 90°. The angular resolution is controlled by the parameter ξ, high ξ values yield a narrower range of non-zero symmetry function values (Figure 2.6). A set of angular functions with different ξ-values can thus be used to obtain a measure of the bond angle distribution function of each reference atom. The angular distribution is sampled at various distances from the central atom by a suitable choice of η and R_c, which control the radial part. The parameters that define the symmetry functions are fixed in the training process of the NN. The total number of values of symmetry functions describing a given structure is much larger than the number of degrees of freedom of the system. This ensures that the full dimensionality of the system is captured and the resulting redundancy of the information is not usually a problem for a NN algorithm.

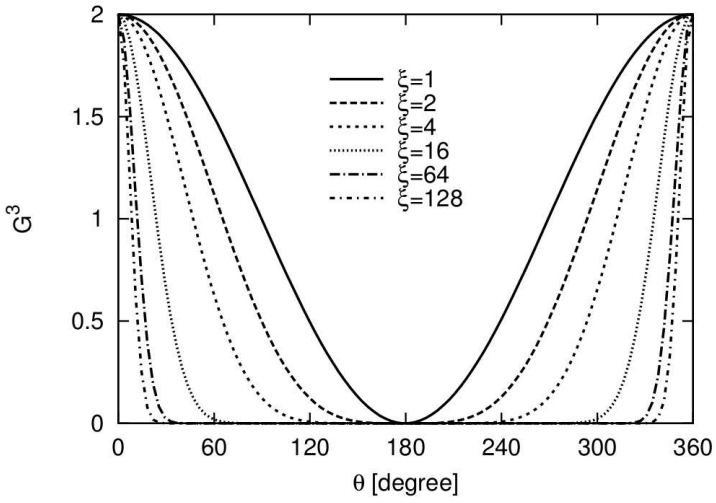

Figure 2.6.: Angular symmetry functions G_i^3 for several values of ξ with $\lambda = 1$.

Forces and stress evaluation

Since the NN energy is an analytical function of the symmetry functions, which in turn depend on the atomic coordinates, the energy is an analytical function of the ionic coordinates. The atomic forces and the stress tensor can thus be computed analytically. The force $\mathbf{F}_k$ acting

on the k-th atom is

$$\begin{aligned} \mathbf{F}_k &= -\frac{\partial E}{\partial \mathbf{R}_k} \\ &= -\sum_{i=1}^{N} \frac{\partial E_i}{\partial \mathbf{R}_k} \\ &= -\sum_{i=1}^{N} \sum_{j=1}^{M_i} \frac{\partial E_i}{\partial G_{i,j}} \frac{\partial G_{i,j}}{\partial \mathbf{R}_k} \end{aligned} \tag{2.44}$$

where i runs on atoms and j on the symmetry functions. Since the energy is a function of interatomic distances $\mathbf{R}_{kj} = \mathbf{R}_k - \mathbf{R}_j$, the stress tensor can be obtained from the virial theorem [144] as

$$\sigma_{\alpha,\beta} = \sum_{i=1}^{N} \sum_{k=1}^{N} R_{ik,\alpha} \cdot \frac{\partial E}{\partial R_{ik,\beta}} \tag{2.45}$$

where α and β are Cartesian coordinates.

Extrapolation

The NN method allows interpolation of the points in the dataset of a multi-variate function with any arbitrary functional form. However, the NN algorithm fails in predicting the value of the fitted function outside the configurational space spanned by the training dataset. This condition can be simply checked by keeping memory of the minimum and maximum values assumed by each symmetry function for the whole input dataset. In this way, the values assumed by the symmetry functions depending on the atomic positions during the simulation can be compared with the values of the G functions of the dataset. If a certain atom configuration cause one or more symmetry functions to assume values outside the range defined by the training set, a so called extrapolation occurs and the resulting NN energy could be not reliable. To fix this issue, the atomic environment that causes the extrapolation can be added to the initial dataset fitting again the potential to extend its transferability.

Neural Network potential for GeTe

The NN potential for GeTe was generated by fitting the total energy of about 30000 configurations of 64-, 96- and 216-atom supercells computed within DFT [14]. Crystalline, liquid and amorphous configurations and mixed crystalline/amorphous models were generated with the PBE functional. Configurations at different pressure, temperature and stoichiometry were also included in the dataset. The structure of the neural network employed to fit the *ab-initio* data includes three hidden layers with 20 nodes each. The local environment of each atom is described by the value of 159 radial and angular symmetry functions defined in terms of the

positions of all neighbours within a distance cut-off of 6.88 Å.
The generated NN potential well reproduce the structural features of amorphous, liquid and crystalline GeTe [14] and it has been validated in several works [80, 87, 89]. Figure 2.7 shows the comparison between the pair correlation functions calculated for amorphous GeTe models generated with DFT and with the NN potential. The agreement is very good.

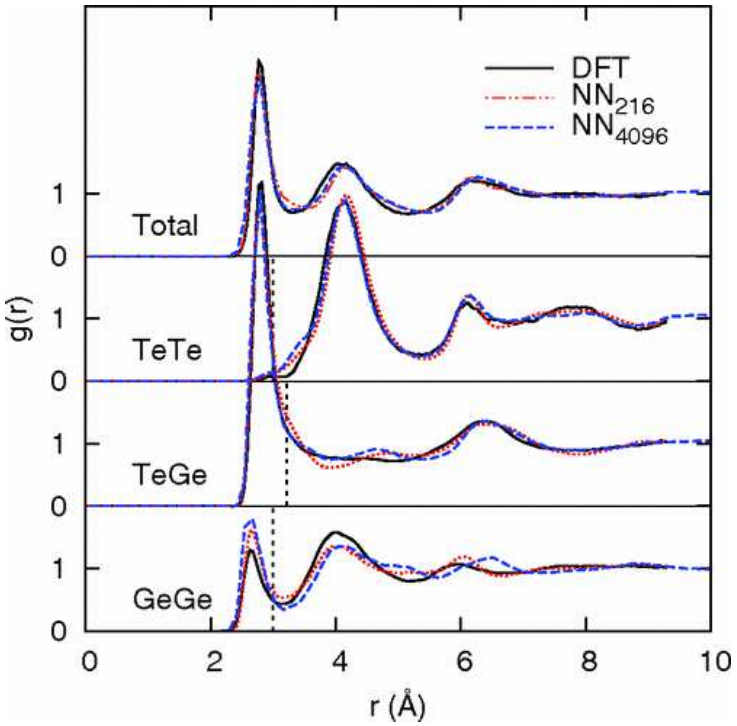

Figure 2.7.: Total and partial pair correlation functions of amorphous GeTe from a NN molecular dynamics simulation at 300 K with a 4096- and 216-atom cell, compared with results from DFT simulation at the same temperature using 216-atom cells. NN and DFT data for the small cell are averaged over 10 independent models [14].

2.8. Metadynamics

The structural relaxations responsible for the drift phenomenon occur on the time scale of minutes up to several months. To speed up the transformations and make them visible on the short time span of an atomistic molecular dynamics simulation one might increase the temperature. For phase change alloys this procedure might, however, lead to crystallization of the amorphous phase. To circumvent this problem, acceleration techniques suitable to allow overcoming large energy barriers at low temperature in an affordable simulation time must be used.

In this respect, metadynamics is a technique based on molecular dynamics that improves the sampling of the potential energy surface allowing the crossing of energy barriers higher than the thermal energy [177]. This can be done through a non-markovian dynamics in a space of few coordinates called collective variables (CV) that can discriminate between the initial and the final configurations. The dynamics spans the free energy surface, expressed as a function of the collective variables, and a biasing external, history-dependent, potential is added during the simulation. The biasing potential, built as a sum of Gaussian functions centered along the trajectory in the space of the collective variables, drives the system towards the lowest saddle point in the free energy surface.
The external biasing potential is made of intermittently added Gaussian functions that discourage the system from remaining in the region already visited and push it over the lowest energy barrier towards a new local minimum (Figure 2.8). The biasing potential V_G acting on

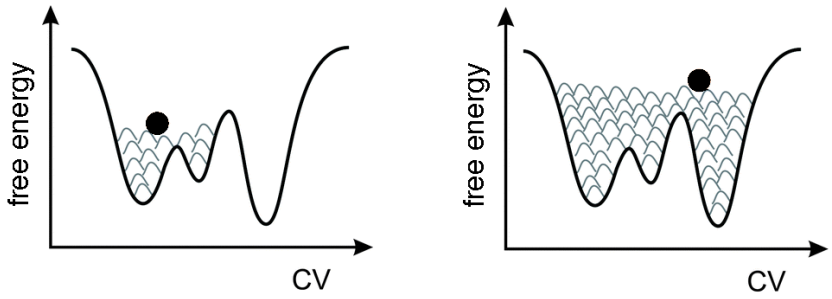

Figure 2.8.: Schematic representation of the metadynamics technique. Intermittently added Gaussian functions are introduced to discourage the system from remaining in the region already visited and to push it over the lowest energy barrier towards a new local minimum.

the system at time t is a function of the array of collective variables s at time t and at preceding times t' as

$$V_G(t) = w \sum_{t'=\tau_G,2\tau_G,\ldots}^{t'<t} e^{-\frac{(s(t)-s(t'))^2}{2\delta s^2}}. \tag{2.46}$$

The V_G potential is essentially defined by three parameters:

- the height of the Gaussian function w;
- the width of the Gaussian function δs;
- the frequency τ_G with which a new Gaussian function is added.

This procedure is applied as long as the free energy basin is filled and the system jumps into another local minimum.
The algorithm keeps memory of the positions in which the Gaussian functions were deposited

and it is thus possible to reconstruct the profile of the free energy surface in the space of the CVs:

$$\lim_{t\to\infty} V_G(s,t) = -F(s) \tag{2.47}$$

where $F(s)$ is the free energy. In order to obtain a reliable reconstruction of the free energy, the parameters that define the Gaussian functions of the bias potential should be tuned. If the Gaussian functions are too large and added with high frequency, the potential well will be filled in few steps, but free energy profile should be affected by large errors. Otherwise, when the Gaussian functions are too small, a very accurate free energy profile could be obtained but longer simulation times are needed.
A way to reconstruct rapidly and with high accuracy the free energy surface was proposed by Barducci *et al.* [178]. In this method called well-tempered metadynamics the height w of the added Gaussian varies during the dynamics as

$$w(t) = w_0 e^{-\frac{V_G(t)}{k_B \Delta T}} \tag{2.48}$$

where w_0 is the initial Gaussian height, k_B is the Boltzmann constant and ΔT is an input parameter with the dimension of a temperature. The height of the Gaussian functions becomes smaller and smaller the larger is the biasing potential already added to the same point in the phase space.
The metadynamics approach can be applied to various systems, from small molecules to proteins and solids to accelerate rare events such as chemical reactions. To this aim a careful preliminary identification of the set of CVs, able to describe the process of interest, is needed [179]. The derivative of the free energy with respect to the collective variables, in fact, corresponds to the driving force of the reaction. Once a suitable set of CVs is identified, metadynamics is able to provide very reasonable transition pathways and to discover new unpredicted stable and metastable states. In principle, the CV should satisfy three properties:

- They should clearly distinguish the initial, final and intermediate states.
- They should describe all the slow events that are relevant to the process of interest.
- Their number should not be too large, otherwise it will take a very long time to fill the free energy surface.

Typical collective variables are geometrical parameters such as distances, angles and dihedrals which are useful to study chemical reactions.
In this thesis we applied the metadynamics method to study structural relaxations in amorphous GeTe. As we would like to simulate processes in which Ge-Ge bonds break and new Ge-Te bonds are formed, we used as collective variables the partial coordination numbers of

Ge-Ge and Ge-Te pairs define as

$$S(r) = \sum_{ij} f(r_{ij}) \tag{2.49}$$

where f is a switching function [180] defined as

$$f(r_{ij}) = \frac{1 - \left(\frac{r_{ij} - d_0}{r_0}\right)^n}{1 - \left(\frac{r_{ij} - d_0}{r_0}\right)^m} \tag{2.50}$$

and r_{ij} is the distance between the i-th atom of the first subset of atoms and the j-atom of the second subset of atoms. The parameter r_0 is a measure of the steepness of the f function and d_0 is the value on which the function is centered and roughly correspond to the cut-off distance on the bond length; the parameters n and m tune the smoothness of the function. This definition ensures that the calculated coordination number is a differentiable function of the ionic coordinates.

3. Atomistic simulations of InSbTe and GaSbTe alloys

Although GST is presently the material of choice for PCM, there is a need to develop alternative phase change alloys for applications at high temperatures, e.g. for the automotive market. InSbTe and GaSbTe alloys are interesting alternatives to GST thanks to their higher crystallization temperatures. However, no structural experimental data are actually available for the amorphous phase. We have thus generated models of the amorphous phase of InSbTe and GaSbTe at different compositions by quenching from the melt within *ab-initio* simulations. The models allowed for a full characterization of the structure of the amorphous phase which also shed light on the functional properties exploited in the devices. As a preliminary work, the binary compound InSb was analysed.

3.1. InSb

In order to asses the reliability of our theoretical DFT framework for the modeling InSbTe alloys, we firstly focused on the amorphous phase of the binary compound InSb which has been already experimentally and theoretically investigated in the past.
Amorphous InSb (a-InSb) is itself an interesting material for application in micro- and optoelectronic devices, such as infrared photodetectors [181]. The binary alloy at the eutectic composition ($In_{32}Sb_{68}$) has been also proposed as phase change material in rewritable digital versatile disc [182].
InSb is a semiconductor with a zincblende crystalline structure (Figure 1.27c) with space group $F\bar{4}3m$ made of tetrahedrally coordinated In and Sb atoms. The lattice parameter obtained from x-ray powder diffraction is 6.47937(3) Å [183] corresponding to a density of 0.0294 at./Å^3 (5.775 g/cm^3) for the zincblende crystal. Under particular conditions, InSb films can crystallize in a rocksalt-like structure with lattice parameter 6.12 Å [184].
A systematic x-ray diffraction study of the structural properties of amorphous III-V semiconductors, including InSb (a-InSb), has been performed long ago by Shevchik and Paul [185] reporting for InSb a density 2 % lower than that of the crystal and a nearest neighbour distance of 2.86 $\pm$ 0.03 Å. More recently, extended x-ray absorption fine structure (EXAFS) measurements [186] on sample deposited by sputtering revealed the presence of slightly longer

In-Sb bonds in a-InSb with respect to the crystal that is accompanied by a counterintuitive increase of about 5 % in density, being 0.0311 at./Å^3 (6.1 g/cm^3). This feature has been ascribed to the presence of homopolar Sb-Sb and In-In bonds. Since pure In and pure Sb are denser than InSb, a concentration of 10 % of homopolar "wrong" bonds can lead to a higher density in the amorphous phase with respect to the crystal. A sizable fraction of homopolar bonds is indeed present in models of a-InSb generated by quenching from the melt within classical molecular dynamics simulations using empirical interatomic potentials [187, 188]. First principles simulations based on density functional theory (DFT) have been performed for the liquid phase [189]. A continuous random network model of the amorphous phase was also investigated from first principles [190]. However, an *ab-initio* model of amorphous InSb generated by quenching from the melt is still lacking.
In order to analyse the amorphous structure of InSb, we performed *ab-initio* molecular dynamics simulations generating melt-quenched models of a-InSb. The structural properties of this compound turned out to be strongly dependent on the choice of the exchange and correlation functional. Namely models generated with the Perdew-Burke-Ernzerhof (PBE) [151] functional are mainly octahedral-like in contradiction with the experimental data, while model obtained with the Becke-Lee-Yang-Parr (BLYP) [152] is mostly tetrahedral and better fits the experimental diffraction data. Here, we present a summary of the attempts we made to reproduce the experimental data on amorphous InSb which allowed us to select the best suited exchange and correlation functional. After a brief section on the computational details, we present first the results with the PBE functional and then the results with the BLYP one.

3.1.1. a-InSb with the PBE functional

Computational details

We firstly performed *ab-initio* molecular dynamics simulations at DFT-PBE level in the scheme of Kühne *et al.* [142] described in Section 2.5 as implemented in the CP2K code [157, 191]. Norm-conserving Gödecker-type (GTH) pseudopotentials [158, 159] with three valence electrons for In and five valence electrons for Sb were used. The Kohn-Sham orbitals were expanded in a double-zeta-valence plus polarization (DZVP) Gaussian-type basis set [192], while the charge density has been expanded in a plane-wave basis set with a cut-off of 100 Ry to efficiently solve the Poisson equation within periodic boundary conditions using the Quickstep scheme [157]. Brillouin zone integration was restricted to the supercell Γ point. We at first chose the PBE exchange and correlation functional because it has been demonstrated to give good results for several phase change materials [68–73, 76, 193]. In order to check the reliability of the GTH pseudopotentials, we firstly computed the equation of state of the zincblende and of the rocksalt crystals with the QUANTUM-ESPRESSO suite of programs and a $16 \times 16 \times 16$ Monkhorst-Pack mesh [194] for the integration of the Brillouin zone (Appendix

A.1). No substantial differences have been found by considering three or thirteen valence electrons for indium. The lattice parameter of the zincblende crystal is overestimated by about 2 % with respect to experiments. This somehow large discrepancy in the lattice constant is also found in other DFT-PBE calculations using different codes and pseudopotentials [195].
We generated several models of the amorphous phase of InSb by cooling the liquid at 1000 K down to 300 K with different quenching times from 50 to 300 ps at fixed density. The amorphous models were then equilibrated at 300 K for at least 20 ps. The quenching protocol adopted for the model labelled MD-L1 is reported in Figure 3.1. This scheme has been al-

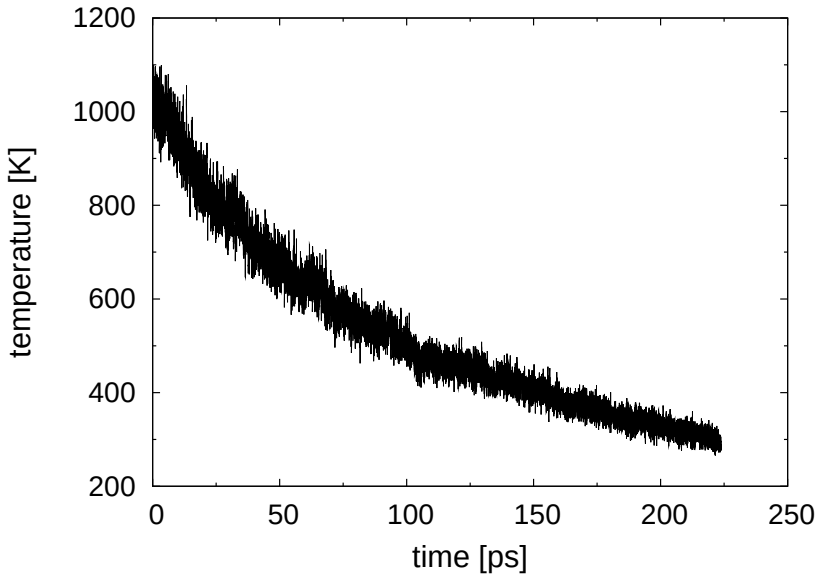

Figure 3.1.: Evolution of the temperature during the quench of a 216-atom model of amorphous InSb (MD-L1). The system has been cooled down from 1000 to 300 K in 225 ps through molecular dynamics simulations. PBE exchange and correlation functional and a DZVP basis set have been used.

ready adopted in several other works on phase change alloys giving good results [71–73, 196–200]. We used a cubic 216-atom cell. Due to the experimental uncertainty on the density of the amorphous phase, the models were generated at the crystalline density of 0.0294 at./Å^3 (5.775 g/cm^3) as already done in other classical molecular dynamics simulations [187, 188]. The resulting total energies and pressures of the amorphous models are collected in Table 3.1. Models MD-S1—MD-S4 are rapidly quenched, models MD-L1 and MD-L2 are quenched more slowly. Model MD-SZ is generated with an incomplete basis set and it will be discussed later on. Model ISA-V is generated with the ISA method (see Section 2.6) by fitting the experimental pair correlation functions discussed later on. The structures of models MD-S1—S4 and MD-L1, MD-L2 are all very similar. We thus discuss here model MD-L2 which has the lowest energy.

a-InSb models - PBE functional

model	quench. time [ps or n_{MC}]	energy [eV]	pressure [GPa]
MD-S1	50	5.394	-0.83
MD-S2	75	5.708	-0.74
MD-S3	90	5.687	-0.82
MD-S4	130	4.557	-0.46
MD-L1	225	5.263	-0.67
MD-L2	350	0.000	-0.87
MD-SZ	350	2.552	0.67
ISA-V	10000	1.548	0.30

Table 3.1.: Total DFT-PBE energy (216 atoms) and pressure of the relaxed structure at 0 K of different a-InSb models. MD-S*x* and MD-L*x* models were generated by quenching from the melt (1000 K) with a DZVP basis set, while MD-SZ with a SZV basis set [201]. ISA-V was, instead generated with the inverse simulated annealing method at constant density. In the last case the quenching time is expressed by the number of Monte-Carlo steps (n_{MC}). The reference of the energy was set to the energy of MD-L2.

Structural properties

The structural properties, calculated as averages on the 300 K trajectory of the melt-quenched models of a-InSb, were studied by computing the total and partial pair correlation functions (PCF) for the atomic species α and β defined by

$$g_{\alpha\beta}(r) = \frac{1}{N_\alpha \rho_\beta} \left\langle \sum_{i\in\alpha} \sum_{j\in\beta} \delta(\mathbf{r} + \mathbf{R}_i - \mathbf{R}_j) \right\rangle \tag{3.1}$$

where N_α is the number of atoms of species α, ρ_β the density of atoms of species β, $\mathbf{R}_i$ and $\mathbf{R}_j$ the positions of the i-th and j-th atom, respectively and δ is the Dirac delta function. The total pair correlation function can be obtained from equation (3.1):

$$g(r) = \sum_{\alpha\beta} \frac{\mathcal{N}_\alpha \mathcal{N}_\beta}{\mathcal{N}^2} g_{\alpha\beta} \tag{3.2}$$

where $\mathcal{N}_\alpha$ and $\mathcal{N}_\beta$ are the number of atoms of species α and β and $\mathcal{N}$ is the total number of atoms of the system. The partial coordination numbers for the pair of atomic species α and β were obtained from the integration of the partial pair correlation functions as

$$n_{\alpha\beta} = \int_0^{r_{cutoff}} g_{\alpha\beta}(r) \rho_\beta 4\pi r^2 dr \tag{3.3}$$

where r_{cutoff} corresponds to the first minimum position of the partial $g_{\alpha\beta}(r)$ and ρ_β is the density of atoms of species β. The total coordination number for species α is defined as

$$n_\alpha = \sum_\beta \frac{\mathcal{N}_\beta}{\mathcal{N}} n_{\alpha\beta}. \tag{3.4}$$

The plot of the total and partial PCF of Figure 3.2 shows the presence of a sizable number of homopolar In-In and Sb-Sb bonds with a particularly broaden first peak for the In-In partial PCF. The In-Sb correlation function is also very broad. The total PCF of MD-L2 shows large

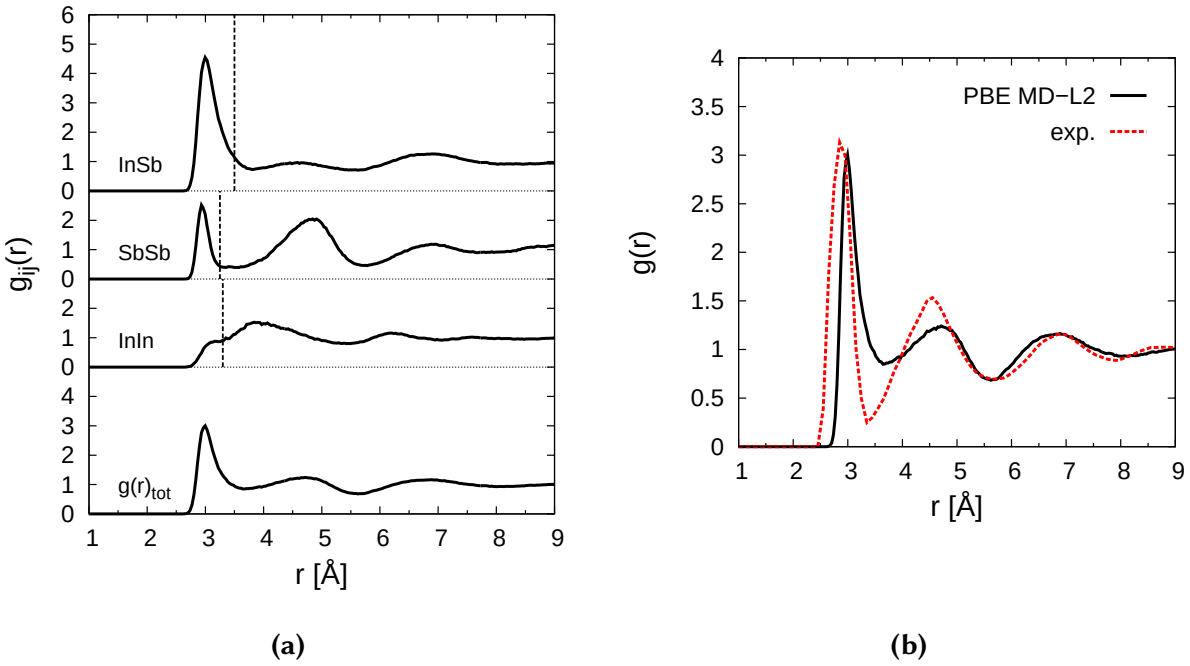

(a) **(b)**

Figure 3.2.: Total and partial correlation functions of a 216-atom model of a-InSb (MD-L2) generated with the PBE functional by quenching from the melt in 350 ps (a). The dashed vertical lines indicate the bonding cut-off distances used in the other structural analysis which are 3.30 Å, 3.25 Å and 3.50 Å for In-In, Sb-Sb and In-Sb pairs, respectively. The data were obtained by averaging over a 30 ps long trajectory at 300 K. A comparison with the total experimental $g(r)$ [185] is provided in panel (b).

discrepancy with respect to the experimental data reported in Figure 3.2b. The first peak position is shifted of about 0.15 Å. The first minimum is less defined and the second maximum is smaller compared with the experiment, indicating a lesser degree of medium-range order in the PBE model.

To analyse the geometry of the local environments in the a-InSb models, we computed the distribution of the bond angles defined by

$$P(\theta) = \frac{1}{N_{tot}} \sum_{i=1}^{N_{tot}} \sum_{k,j>k}^{N_{tot}} \delta(\theta - \theta_{jik}) \tag{3.5}$$

where N_{tot} is the total number of bonds in the structure and θ_{jik} the bond angle that the i-th atom forms with its nearest neighbours j and k. Two atoms are considered chemically bound if their interatomic distance is smaller than a given cut-off. The mean bonding cut-off distance for each pair of atomic species is usually obtained from the position of the first minimum of the partial pair correlation function. Since the first minima in the PCF are not well defined, the coordination numbers were computed by adjusting the cut-off distances in order to obtain a small fraction of zero- and over-coordinated atoms. The results are shown in the inset of Figure 3.3 reporting the distribution of coordination numbers calculated with cut-off distances of 3.30 Å, 3.25 Å and 3.50 Å for In-In, Sb-Sb and In-Sb pair, respectively. The total

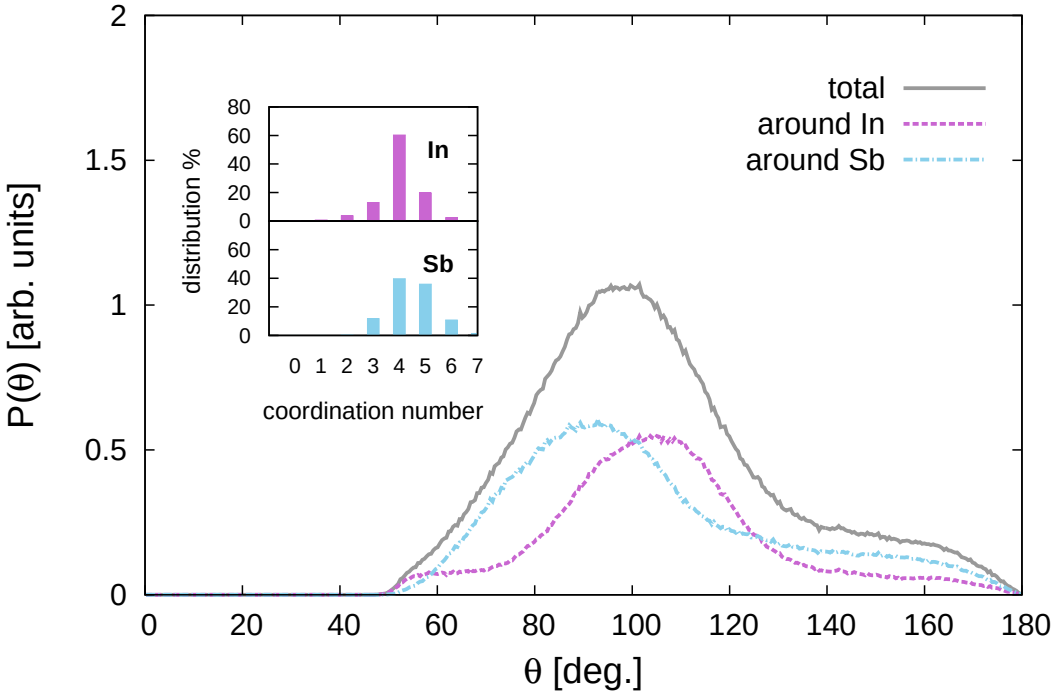

Figure 3.3.: Calculated bond angles distribution for the MD-L2 model of a-InSb obtained with the PBE functional. The total distribution (continuous grey line) was also resolved into the contributions from In (violet dashed line) and Sb species (blue dot-dashed line). The inset shows the distribution of the coordination numbers.

and partial $P(\theta)$ in Figure 3.3 show that, although the distribution for In is peaked at typical tetrahedral angles of $\sim 110^\circ$, typical bond angle of tetrahedral structures (see Figure 1.15), the curve is very broad and presents a shoulder at $\sim 90^\circ$ indicating the presence of In atoms in an octahedral-like geometry (see Figure 1.15). Sb atoms are clearly mostly in an octahedral-like coordination with bond angles of about 90° and 180°. The disagreement between the theoretical and experimental PCF (Figure 3.2b) suggest that the topology of the amorphous network resulting from model MD-L2 might differ from the real one [185].
Accidentally, we obtained a good agreement with experimental data by generating a model with an *ab-initio* MD quench 350 ps long using the PBE functional and a minimal single-zeta-valence (SZV) basis set (MD-SZ in Table 3.1) [201]. The system was initially quenched at the crystalline density, then the equation of state was calculated by relaxing the amorphous structure for different cell volumes at 0 K. The energy-volume $E-V$ points were fitted with a Murnaghan function defined by

$$E(V) = E_0 + \frac{B_0}{B_0'} V \left[\frac{(V_0/V)^{B_0'}}{B_0' - 1} + 1 \right] - \frac{B_0 V_0}{B_0' - 1} \tag{3.6}$$

where E_0 and V_0 are the equilibrium energy and the equilibrium volume, respectively, B_0 is the bulk modulus and B_0' is the first derivative of the bulk modulus with respect to the equilibrium pressure A theoretical density of 0.0286 at./Å^3 (5.61 g/cm^3) was found. The misfit of about 8 % between the experimental density of a-InSb of Ref. [186] and that of our optimized amorphous model is not surprising if we consider that the theoretical DFT-PBE equilibrium density of the crystal is 6.6 % lower than the experimental value (see Appendix A.1). In order to compare this structure with the recent EXAFS data [186], the amorphous model at the density of 5.78 g/cm^3 was compressed up to the experimental density of 6.1 g/cm^3 by isotropically shrinking the simulation cell in a few steps. This is valid under the assumption that the misfit with experiments in the density is due to an error in the bond length and not to a difference in the topology of the amorphous network. Our model scaled at the experimental density of 6.1 g/cm^3 is subject to a pressure of 1.2 GPa with a maximum off-diagonal component of the stress tensor of 0.13 GPa and a maximum anisotropy in the diagonal components of 0.26 GPa. The model at the new density was further equilibrated at 300 K.
By comparing the structural properties of the compressed and uncompressed model, it can be seen that the structure of the system is quite independent on the density change of about 5 %.
Sharp and well defined first peaks were found in the partial and total pair correlation functions (Figure 3.4) and the bond angle distributions (Figure 3.5) clearly indicate a tetrahedral coordination for both In and Sb. This has to be contrasted with the structure of model MD-L2 which is mostly octahedral.
This model generated with the minimal SZ basis set and discussed in our work of Ref. [201] was initially considered the best one since it reproduces the experiments and, once relaxed

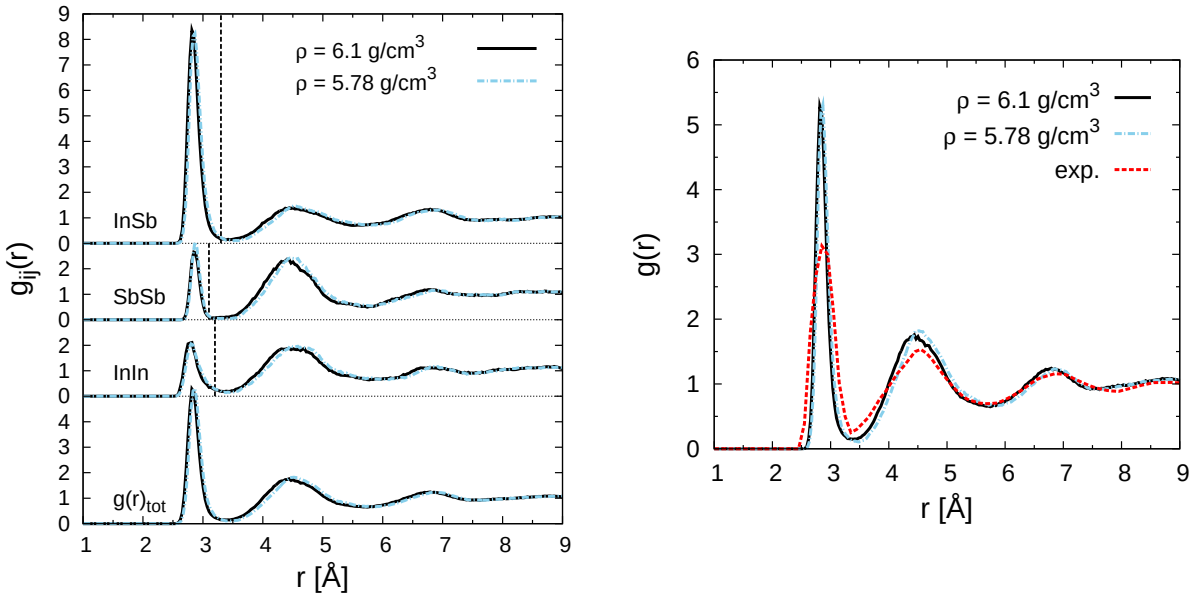

(a) **(b)**

Figure 3.4.: (a) Total and partial correlation functions of a 216-atom model of a-InSb (MD-SZ) generated with the PBE functional by quenching from the melt in 350 ps with a single-zeta-valence basis set (a). The model at the crystalline density of 5.78 g/cm^3 has been also rescaled to the experimental density of 6.1 g/cm^3 [186] and re-equilibrated at 300 K. Dashed vertical lines indicate the bonding cut-off distances used in the other structural analysis, being 3.20 Å, 3.10 Å and 3.30 Å for In-In, Sb-Sb and In-Sb pairs, respectively. The data were obtained by averaging over a 20 ps long trajectory at 300 K. A comparison with the total experimental $g(r)$ [185] is provided in panel (b).

with a DZVP basis set, it showed the lowest energy. However, further MD simulations with long quenching time ($\sim$ 300 ps) and a more accurate basis set (DZVP) allowed us to obtain a model (MD-L2) with lower energy but octahedrally coordinated (Table 3.1).

In attempting to obtain a structure that fits the experimental data by using the accurate DZVP basis set, we further generated models of the amorphous phase by imposing a constraint on the PCF forcing the system to reproduce the experimental pair correlation functions. Two different models with 216 atoms in a cubic cell were then generated with the inverse simulation annealing (ISA) method discussed in Section 2.6 at the fixed crystalline density (ISA-V) or at constant zero pressure (ISA-P) to find the theoretical equilibrium den-

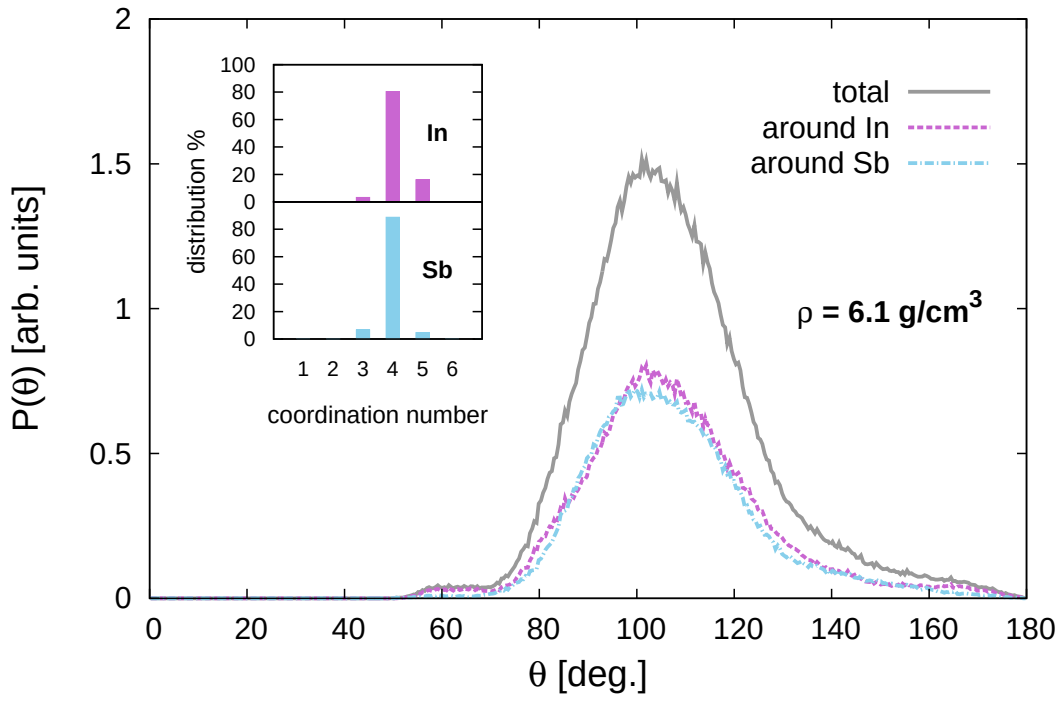

Figure 3.5.: Calculated bond angles distribution for the MD-SZ model of a-InSb rescaled at the experimental density of 6.1 g/cm^3 [186] obtained with the PBE functional and a single-zeta-valence basis set. The total distribution (continuous grey line) was also resolved into the contributions from In (violet dashed line) and Sb species (blue dot-dashed line). The inset shows the distribution of the coordination numbers.

sity. In this latter model, van der Waals interactions according to Grimme [202] were also included to better reproduce the equilibrium density. Long range van der Waals interactions are in fact non included in GGA exchange and correlation functionals such as PBE or BLYP ones. A factor w_g of 1.0 eV·Å^{-4} was used to weight the contribution of the experimental $g(r)$ to the energy (see equation (2.30)). Liquid InSb was initially equilibrated at 1000 K for 1000 Monte-Carlo (MC) steps, then the models were quenched from 1000 to 300 K in 8000 MC steps linearly lowering the temperature as a function of the number of MC steps. A more rapid quenching form 300 to 5 K followed to reach near zero temperature and the structures were then equilibrated at 300 K for 25 ps. At this last step the constraint on the PCF was removed. Figure 3.6 reports the evolution of the potential energy, the density and the pressure during the quenching of the model generated at constant pressure, ISA-P. At the end of the simulation, a density of 0.0289 at./Å^3 (5.679 g/cm^3) was reached. This value is lower than the crystal density, in contrast with EXAFS measurements [186] that predict an increase of the

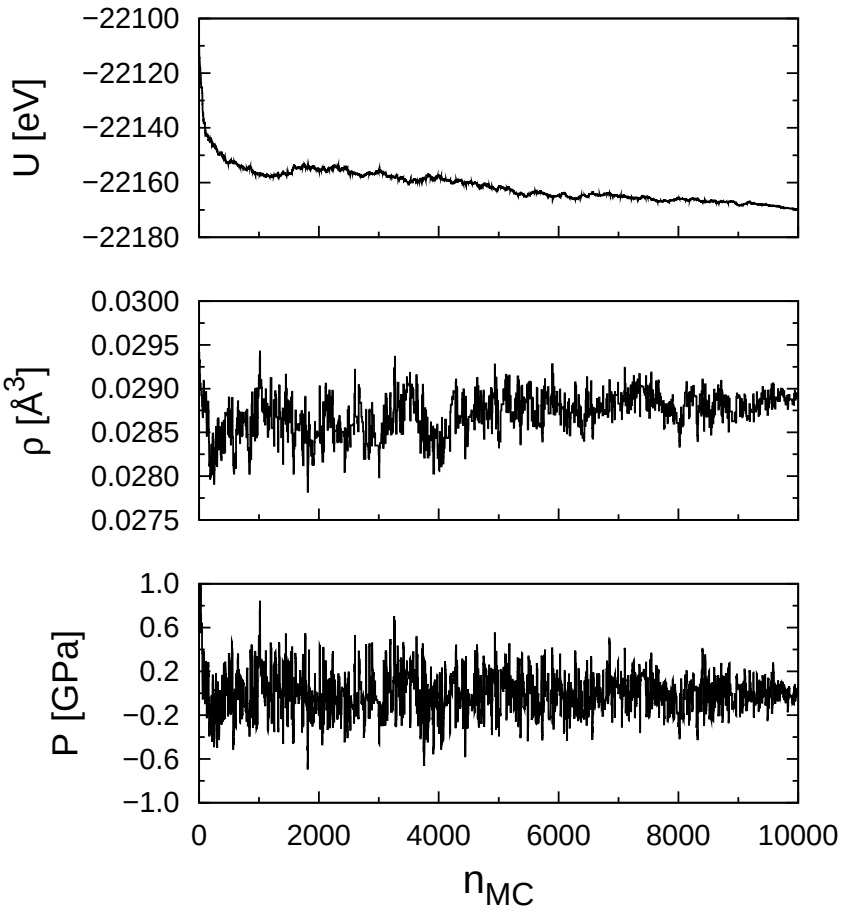

Figure 3.6.: Evolution of the potential energy U, density ρ and pressure P during the ISA quenching of a-InSb at constant pressure as a function of quenching "time" expressed by the number of Monte-Carlo steps n_{MC}.

density in the amorphous with respect to the crystal, but it is in agreement with an older work in Ref. [185]. The resulting density is similar to that obtained from the Murnaghan fit of the energy-volume points calculated for the model generated with SZV basis set.
Figure 3.7 shows the pair correlation functions of the ISA-P model just after the ISA quenching with the constraint on PCF and after an equilibration at 300 K without the constraint. A very good agreement with experiments was obtained for PCFs calculated directly after the ISA quenching before the constraint were removed. After removing the constraint and equi-

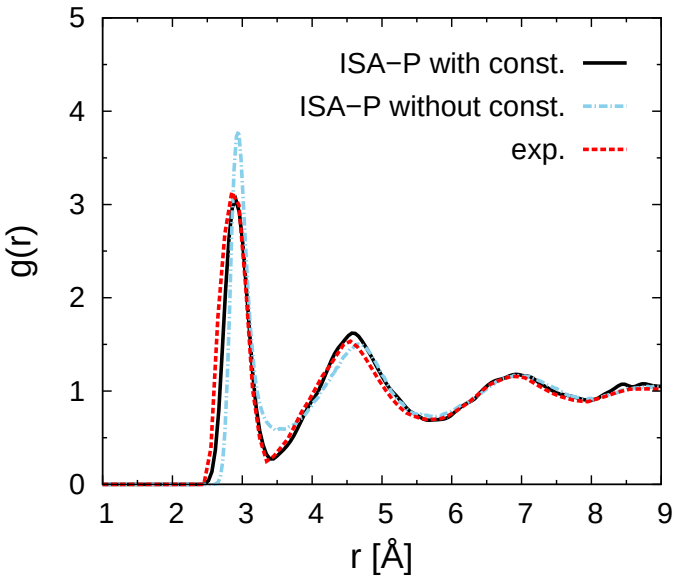

Figure 3.7.: Total pair correlation function of the ISA-P a-InSb model directly after the ISA quench with constraint on $g(r)$ and after equilibration at 300 K without constraint on $g(r)$, compared with the experimental $g(r)$ [185].

librating the amorphous at 300 K, the PCF slightly changes in the direction of the PCF found by MD quench simulations.
The comparison between PCFs of ISA-P and ISA-V models obtained by averaging on a trajectory at 300 K where the constraint on the PCF was removed is shown in Figure 3.8. Again a large amount of homopolar In-In and Sb-Sb bonds is present. However, the first peak of $g_{InIn}(r)$ and $g_{InSb}(r)$ are more sharp and well defined with respect to the structure of model MD-L2, revealing a higher degree of short-range order. The comparison with the experimental data (Figure 3.8b) shows a better agreement with respect to the previous models without the constraint on the PCF. The calculated bond angles distributions (Figure 3.9) show a tetrahedral local geometry for both In and Sb atoms displaying less broad distributions with respect to the DZVP-MD-models. The structure of these two models obtained with the ISA method is close to that of MD-SZ model and represents a reliable description of amorphous InSb. Despite the fact that these models fit the experimental PCF of a-InSb, they show a higher energy with respect to the octahedral-like MD-L2 model generated through standard MD. Thus, a mostly tetrahedral structure does not seem to be reachable by quenching from the melt within DFT-PBE with an accurate basis set and without any external constraint. These results indicate that

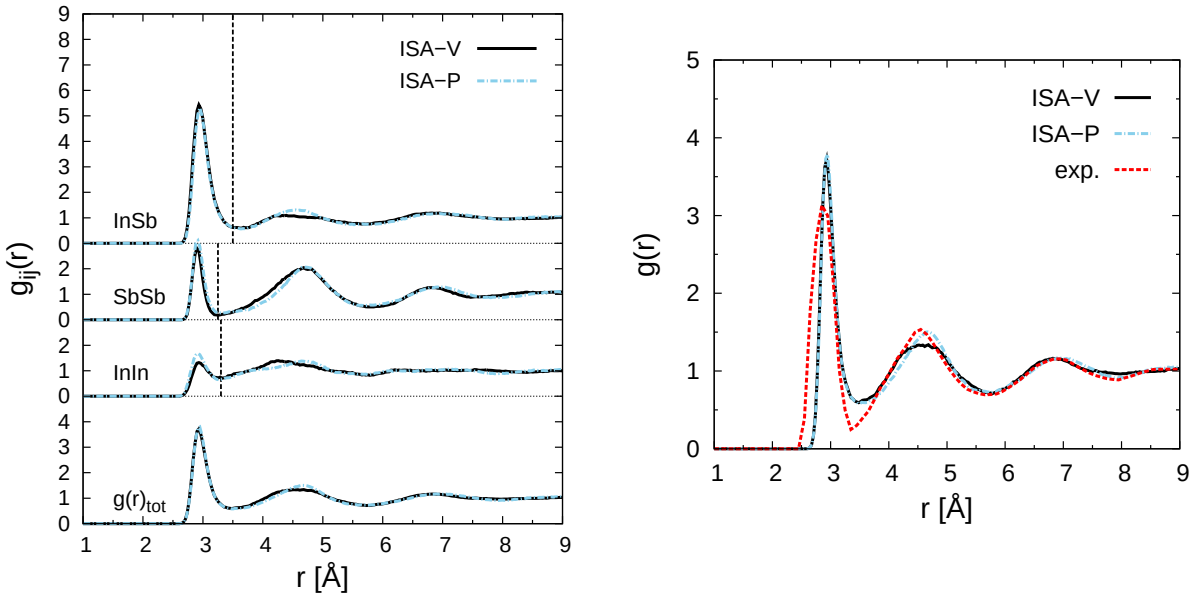

Figure 3.8.: (a) Total and partial pair correlation functions of the 216-atoms models of a-InSb generated with the PBE functional by quenching with the ISA method at fixed crystalline density 0.0294 atom/Å^3 (ISA-V) and at constant pressure (ISA-P). The dashed vertical lines indicate the bonding cut-off distances used in the other structural analysis, being 3.30 Å, 3.25 Å and 3.50 Å for In-In, Sb-Sb and In-Sb pairs, respectively. The data were obtained by averaging over a 20 ps long trajectory at 300 K. A comparison with the total experimental $g(r)$ [185] is provided in panel (b).

the most stable structure obtained with the PBE functional is mainly octahedral-like. Actually it is known experimentally that a-InSb crystallizes in a cubic rocksalt phase under moderate pressure of 1-1.3 GPa [203] which would correspond to a density increase of only 4 % by assuming a crystalline-like bulk modulus of 35 GPa [201]. It is therefore conceivable that a close competition arises between octahedral-like and tetrahedral-like local geometries and that PBE functional seems to fail in properly describing the energy hierarchy of these two structures. We then investigated whether another functional, the BLYP functional, is able to better reproduce the experimental data as discussed in the next section.

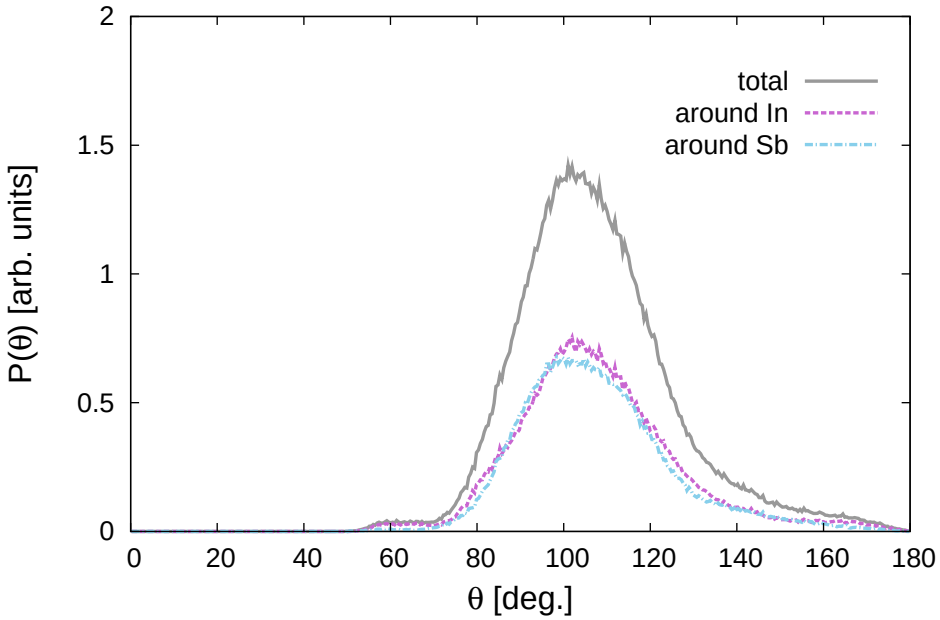

Figure 3.9.: Calculated bond angles distribution for the ISA-P model of a-InSb generated with the PBE functional. The total distribution (continuous grey line) is resolved into the contributions from In (violet dashed line) and Sb species (blue dot-dashed line).

3.1.2. a-InSb with the BLYP functional

Due to the unsatisfactory agreement between theory and experiment for a-InSb generated with the PBE functional, we performed *ab-initio* MD simulations with the BLYP [152] exchange and correlation functional that was shown to better describe other chalcogenide materials like liquid selenides [204–206].

Computational details

GTH-BLYP pseudopotentials were previously tested on the zincblende and the rocksalt phases of InSb (see Appendix A.2) and a better agreement with the experiments has been obtained for the equilibrium lattice parameter, with respect to PBE calculations. The lattice parameter of the zincblende crystal is, in fact, overestimated by only 1.5 %.

The Kohn-Sham orbitals were expanded in a Triple-Zeta-Valence plus Polarization (TZVP) Gaussian-type basis set [192]. The equilibrium density of the system was first obtained by performing an ISA quenching at constant zero pressure with BLYP functional and a DZVP basis set. The van der Waals interactions according to Grimme [202] were included. A constraint on the pair correlation functions was also added to fit the experimental data. This

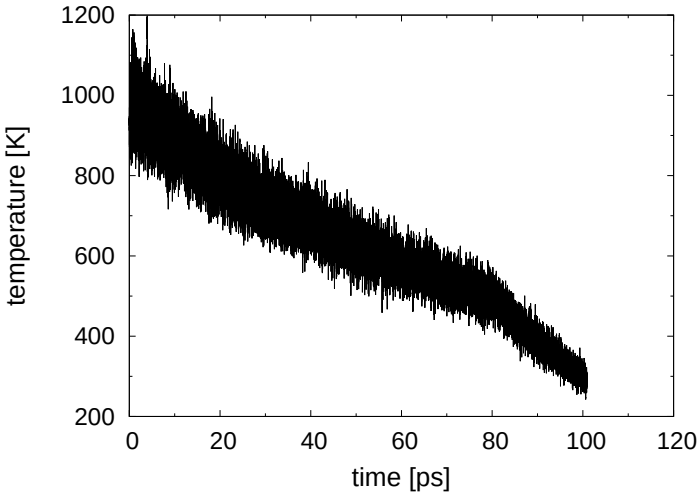

Figure 3.10.: Evolution of the temperature during the MD quench of a 216-atom model of InSb at fixed density (5.355 g/cm^3) with the BLYP functional and a TZVP basis set.

simulation assigned a density of 0.0273 atoms/Å^3 (5.355 g/cm^3) which is lower than the experimental data (5.66 g/cm^3 [185] or 6.1 g/cm^3) and lower than the PBE density (5.61 g/cm^3) calculated above. However this difference is probably due to the fact that the samples analysed in Refs. [185, 186] are as-deposited amorphous InSb, while in our case the amorphous phase was obtained by quenching from the melt. In fact, the structural properties of the amorphous chalcogenides depend on the preparation method [76]. As discussed in Section 1.2.1 GeSbTe alloys for instance have a larger fraction of tetrahedra when the amorphous phase is deposited as a thin film with respect to the glass generated by quenching from the melt [76].
An amorphous 216-atom model was then generated at the fixed density as assigned by a standard MD quenching from the melt in about 100 ps from 1000 to 300 K (Figure 3.10).

Structural properties

The structural properties of the BLYP model generated by the MD quenching from the melt were investigated by averaging on a trajectory at 300 K 10 ps long. The pair correlation functions (Figure 3.11) are sharper and less broad with respect to previous MD melt-quenched models generated with PBE functional (Figure 3.2). The agreement with experiments is good for what concerns the position of first maximum and first minimum of the total PCF (Figure 3.11b). We remark that no constraint on the structure have been applied in this case. The model shows again a sizable fraction (26 %) of homopolar In-In and Sb-Sb pairs, as highlighted also by the partial average coordination numbers in Table 3.2a and by the distribution of the different bond types in Table 3.2b. The partial PCF were integrated up to a cut-off distance shown in Figure 3.11. The distribution of coordination numbers resolved for different atomic

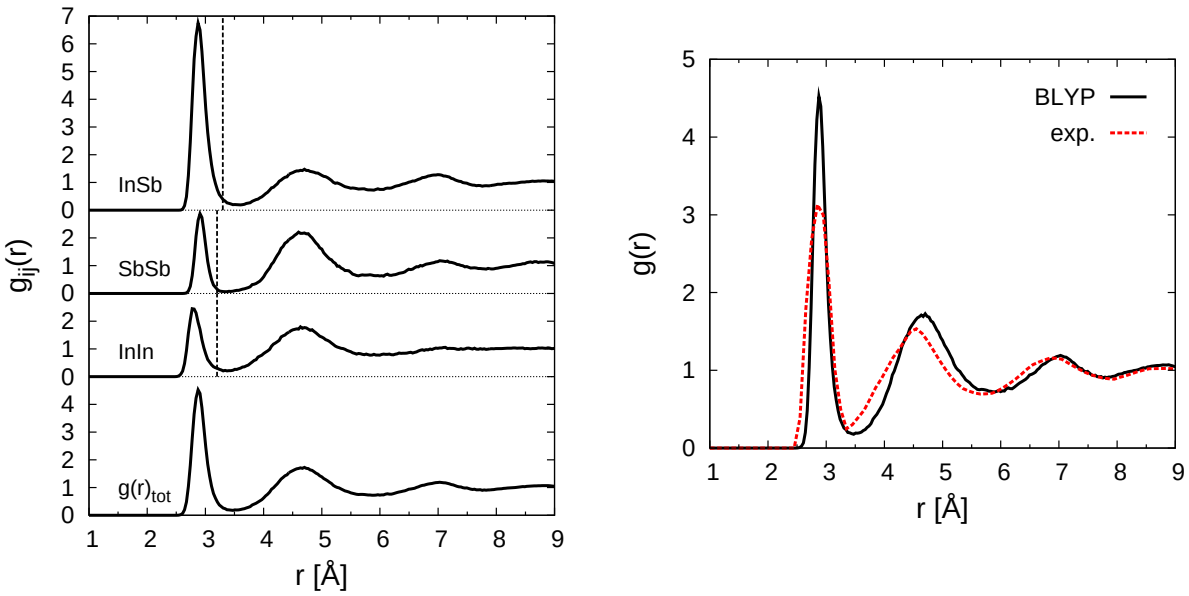

(a) **(b)**

Figure 3.11.: (a) Total and partial correlation functions of a 216-atom model of a-InSb generated with the BLYP functional by quenching from the melt in 100 ps. The dashed vertical lines indicate the bonding cut-off distances used in the other structural analysis which are 3.20 Å, 3.20 Å and 3.30 Å for In-In, Sb-Sb and In-Sb pairs, respectively. The data were obtained by averaging over a 10 ps long trajectory at 300 K. A comparison with the total experimental $g(r)$ [185] is provided in panel (b).

	Average coordination numbers		
	with In	**with Sb**	**total**
In	1.01	2.82	3.83
Sb	2.82	0.95	3.78

(a)

	Types of bonds (%)	
	with In	**with Sb**
In	13.2	74.2
Sb		12.6

(b)

Table 3.2.: (a) Partial average coordination numbers and (b) percentage of the different types of bonds in the BLYP a-InSb model calculated by using the cut-off distances shown in Figure 3.11.

species (Figure 3.12) show that both In and Sb atoms are mainly four-fold coordinated, consistently with a tetrahedral bonding geometry, while a minor fraction of three-fold coordinated atoms (about 20 %) is present.

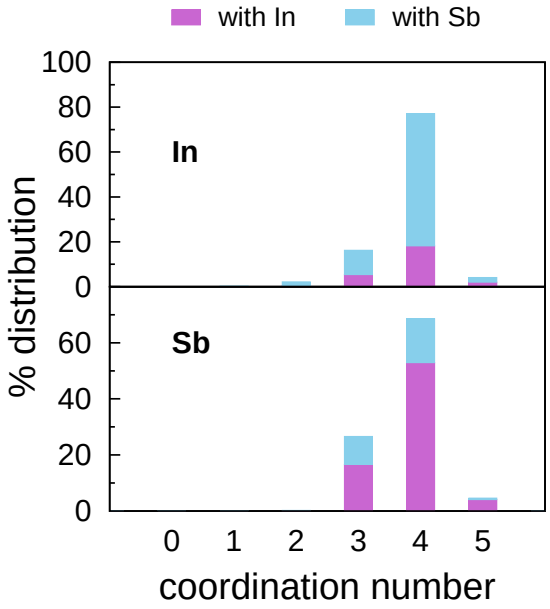

Figure 3.12.: Distribution of the coordination numbers of the a-InSb model obtained from MD quench and the BLYP functional. The contributions from the different atom pairs are indicated by different colours.

The bond angles distributions (Figure 3.13) provide information on the bonding geometry. The total distribution and the partial distribution of both In and Sb are peaked at about the tetrahedral angle of 110°. By further resolving the bond angle distributions for different coordination numbers and different environments (Figure 3.14), it can be noticed that three-fold coordinated Sb atoms present bond angles smaller than the typical tetrahedral bond angle of 110° and the peak of the distribution is closer to values typical of a defective octahedral-like environment (about 90°). The type of bonds also slightly influences the bond angles: while heteropolar triplets as SbInSb and InSbIn have distributions peaked at exactly 110°, In and Sb atoms with homopolar bonds show broader bond angle distributions. No signatures of defective octahedral-like environments for four-fold coordinated atoms with 180° bond angles are present (cf. Figure 1.15c). The statistics of the different environments present in the structure is listed in Table 3.3. Five-fold and four-fold coordinated In atoms present environments with a high indium content, while four-fold and particularly three-fold coordinated Sb atoms display a high fraction of homopolar bonds; Sb_3 environments are also present for Sb atoms.
In order to quantify the fraction of tetrahedra for In and Sb atoms, we used the order param-

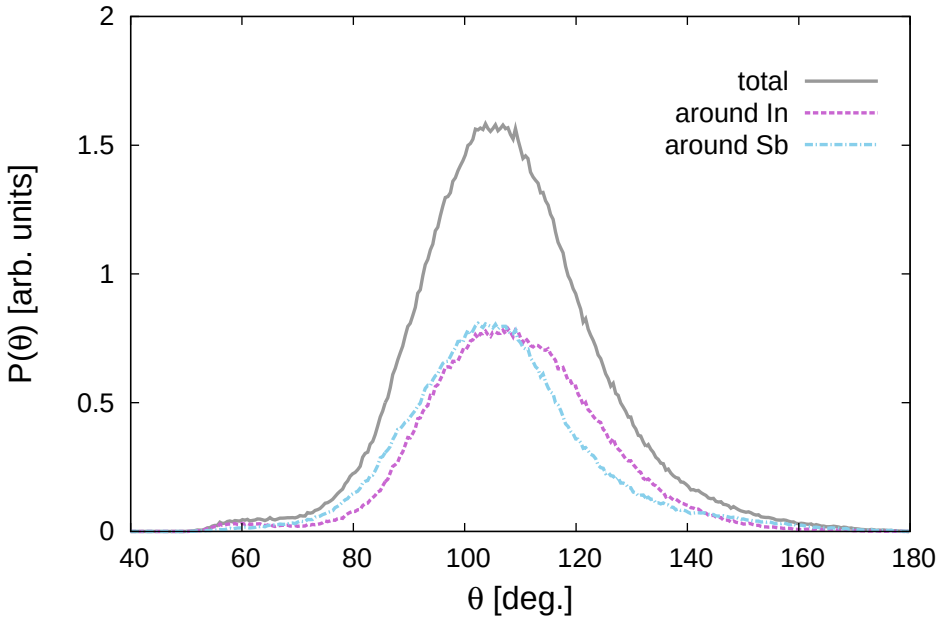

Figure 3.13.: Bond angles distribution for the model of a-InSb obtained with the BLYP functional. The total distribution (continuous grey line) is resolved into the contributions from In (violet dashed line) and Sb species (blue dot-dashed line).

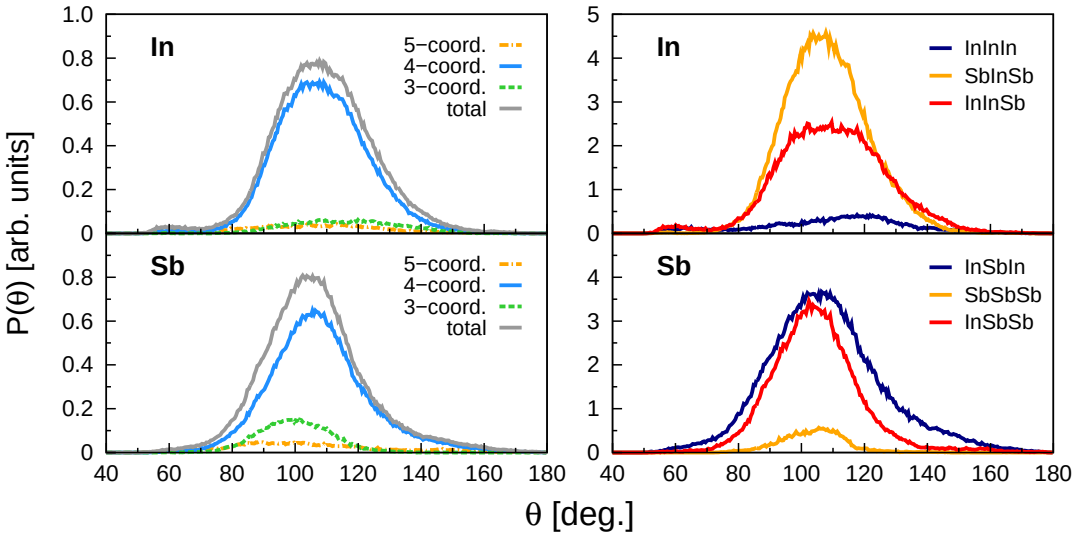

Figure 3.14.: Bond angles distribution of amorphous InSb resolved for coordination number (left panels) and for different triplets (right panels). The amorphous model was generated by quenching from the melt with the BLYP functional.

Local environments				
	2	**3**	**4**	**5**
In:	1.9%	13.0%	79.6%	5.6%
	InSb: 1% SbSb: 1%	$InSb_2$: 9.3% Sb_3: 2.7% In_2Sb: 1.0%	$InSb_3$: 34.3% Sb_4: 25.9% In_2Sb_2: 14.8% In_3Sb: 4.6%	In_3Sb_2: 4.6% In_2Sb_3: 1.0%
Sb:	—	24.1%	72.2%	3.7%
		In_2Sb: 9.3% $InSb_2$: 7.4% In_3: 5.6% Sb_3: 1.9%	In_3Sb: 38.9% In_4: 20.4% In_2Sb_2: 13.0%	In_4Sb: 1.9% In_5: 1.9%

Table 3.3.: Statistics of In and Sb coordination environments for atoms with different coordination numbers given in the first line for the a-InSb model generated with the BLYP functional. The data were obtained for the relaxed configuration at the BLYP-DFT level.

eter q introduced by De Benedetti and Errington [207] and defined by

$$q = 1 - \frac{3}{8} \sum_{i>k} \left(\frac{1}{3} + \cos\theta_{ijk} \right)^2 \tag{3.7}$$

where the sum runs over the pairs of atoms bonded to a central atom j and forming a bond angle θ_{ijk}. This local order parameter assumes different values for the different bonding geometry as:

$q = 0$: ideal octahedral (six-fold coordinated);
$q = \frac{1}{3}$: five-fold coordinated defective octahedral-like;
$q = \frac{5}{8}$: four-fold coordinated defective octahedral-like;
$q = \frac{7}{8}$: three-fold coordinated defective octahedral-like;
$q = \frac{31}{32}$: three-fold coordinated planar;
$q = 1$: tetrahedral.

Figure 3.15 reports the distribution of the q parameter for each atomic species resolved for different coordination numbers. It can be seen that the overwhelming majority of the four-fold coordinated In atoms is in a tetrahedral bonding geometry. Four-fold coordinated Sb

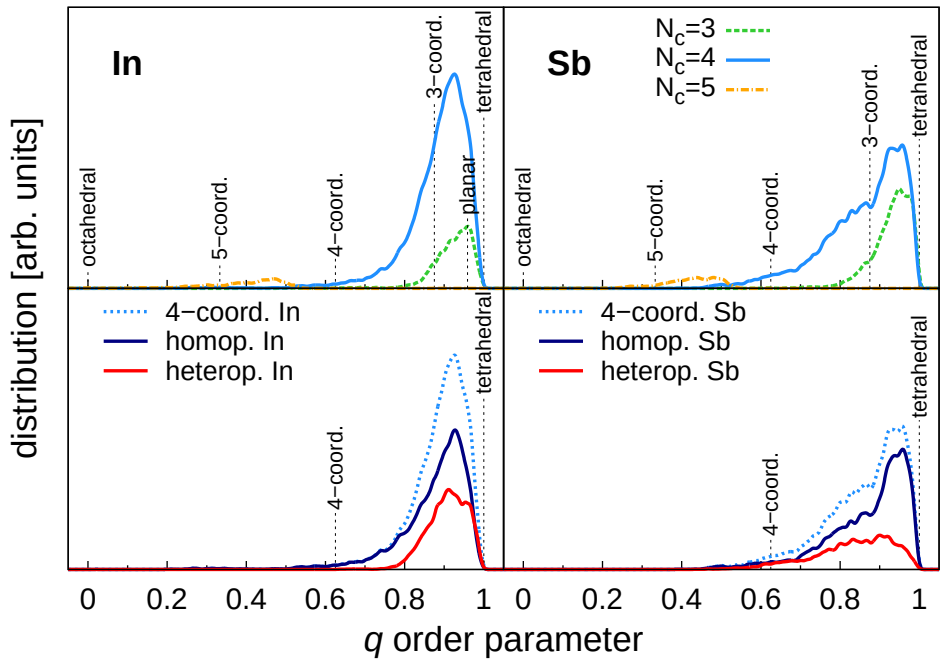

Figure 3.15.: Distribution of the local order parameter q for tetrahedricity (see text) for the model of amorphous InSb obtained from MD quenching with the BLYP functional. The distributions for In, Sb and Te atomic species are resolved for different coordination numbers. Vertical lines indicate the values of q for selected ideal geometries. The distributions for four-fold coordinated In and Sb atoms are further resolved for atoms with and without homopolar bonds (lower panels).

atoms are also mostly tetrahedral but with larger distortion.

The effects of homopolar bonds on the bonding geometry can be analysed by resolving the q distribution for four-fold coordinated atoms into the contribution of atoms which form or not form homopolar bonds (Figure 3.15, lower panels). In the case of In, the presence of In-In bonds do not influence the bonding geometry. For Sb, instead, the presence of Sb-Sb bonds slightly shifts the peak of the q parameter distribution towards lower values with respect to the ideal tetrahedral coordination leading to more distorted bonding geometries. To estimate the concentration of tetrahedral structures, the q distribution of the four-fold coordinated In and Sb atoms has been integrated in the range $0.8 - 1.0$. This method has already been applied to other Ge and In based phase change alloys [71, 199, 200] giving accurate results. The reliability of the integration range has also been checked for the InSbTe system as it will be disscussed later in Section 3.2.1.

A percentage of about 68 % (74 % in the relaxed structure) of tetrahedral In atoms and of about 52 % (61 % in the relaxed structure) of tetrahedral Sb atoms was found, confirming the tetrahedral character of the bonding network of a-InSb. Moreover, all the In tetrahedra shares

at least one corner with other tetrahedra and, among them, the 13 % of the In tetrahedra are edge-sharing.
Concerning three-fold coordinated atoms, Sb atoms are in a pyramidal geometry with bond angles of about 90° but also in a defective tetrahedral-like geometry with bond angles of 110° (for which q is equal to one).
Three-fold coordinated In atoms present, instead, a planar geometry with bond angles of about 120° corresponding to an sp^2 hybridization. To discriminate between pyramidal and planar environments we resort to the analysis of the Wannier functions (WFs) since the q values for these two geometries are too close.
The WFs are the periodic version of the Boys orbitals obtained by the unitary transformation

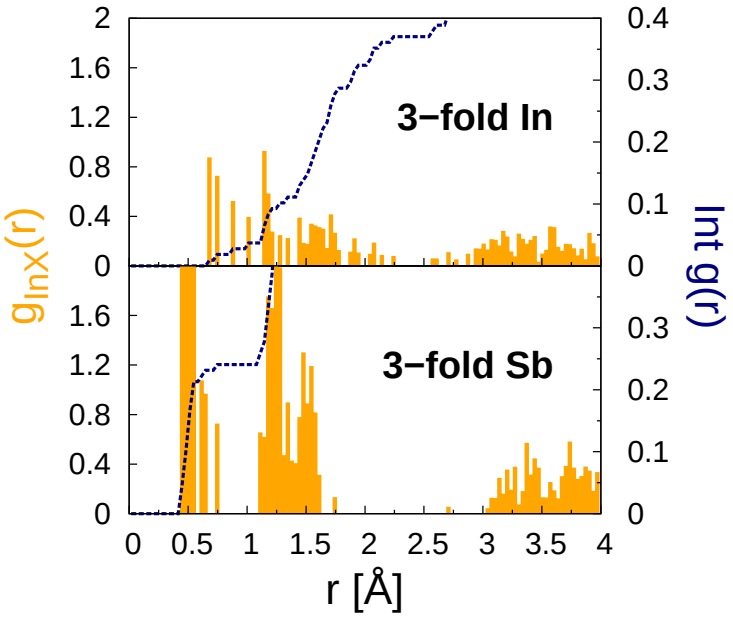

Figure 3.16.: Pair correlation functions $g(r)$ of three-fold coordinated In atoms (upper panel) and three-fold coordinated Sb atoms (lower panel) with the centers of the Wannier functions in the a-InSb model obtained with the BLYP functional. The dashed line is the running integral of $4\pi r^2 g(r)\rho$ where ρ is the density of the Wannier centers (right scale).

of the occupied KS orbitals that minimizes the quadratic spread [208–210]. An In atom with an sp^2 hybridization makes three covalent bonds giving rise to three WFs centered close to the middle of the bonds. In the case of a pyramidal configuration only the p valence electrons take part in the bonding. Thus, a lone pair remains close to the In atom in a s-type orbital and a WF with spherical shape centered on the atom can be found. As a consequence, sp^2 and not hybridized In atoms can be distinguished on the basis of the presence of an s-type WF close to the central atom. To estimate the fraction of not hybridized In atoms, we computed the pair correlation function between three-fold coordinated In atoms (13 % of the total number of In

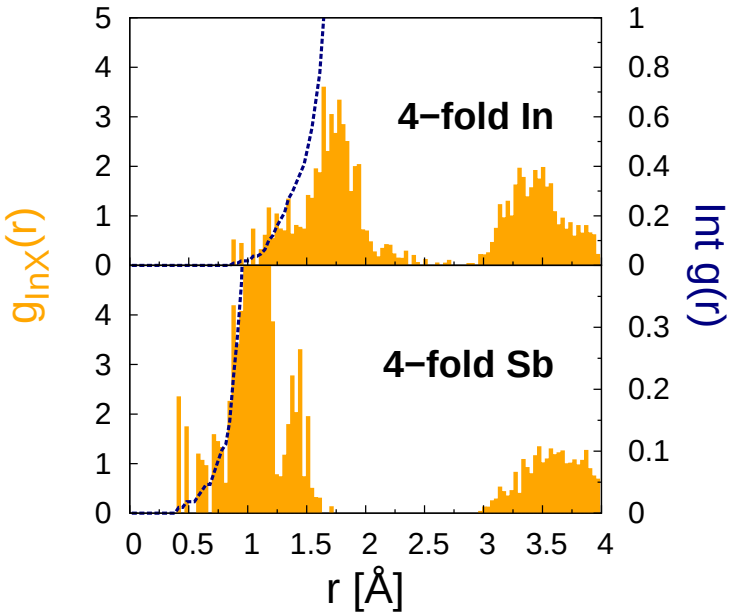

Figure 3.17.: Pair correlation functions $g(r)$ of four-fold coordinated In atoms (upper panel) and four-fold coordinated Sb atoms (lower panel) with the centers of the Wannier functions in the a-InSb model obtained with the BLYP functional. The dashed line is the running integral of $4\pi r^2 g(r)\rho$ where ρ is the density of the Wannier centers (right scale).

atoms) and the centers of the WFs of the system (Figure 3.16, upper panel). By integrating the curve up to the position of the first minimum (0.75 Å) one obtains a fraction of about 2 % of In atoms in pyramidal configurations. The remaining 11 % of three-fold coordinated In are sp^2 hybridized as also checked by visual inspection. The same procedure can be applied to antimony (Figure 3.16, lower panel). In this case, all the three-fold coordinated Sb atoms (24 %) have a pyramidal bonding geometry.
The absence of an s-type WF centered on a central atom can also identify tetrahedral four-fold coordinated atoms with sp^3 hybridization. Atoms that do not hybridize form p-type σ-bonds in an octahedral-like configuration keeping the s-type lone pair unshared. By calculating the pair correlation functions between four-fold coordinated atoms and the centers of the WFs (Figure 3.17) and integrating up to a cut-off distance of 0.7 Å, a fraction of 80 % of tetrahedral In atoms and of 67 % of Sb atoms was found, in rather good agreement with the previous estimate from the q parameter (74 % and 61 %, respectively). The CPMD code [211] was used for the WFs calculations. The main types of local environments in a-InSb are shown in Figure 3.18 together with the isosurfaces of the WFs.

The medium-range order a-InSb was analysed by computing the ring distribution according to Ref. [212]. The results are shown in Figure 3.19 and the statistics of the different types of rings is reported in Table 3.4. As typical of mostly tetrahedral networks, many five-, six-

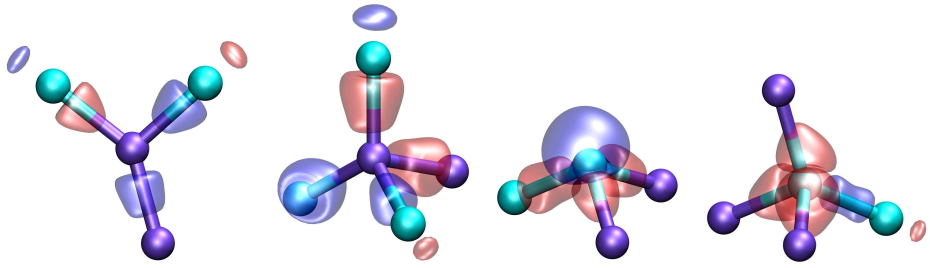

Figure 3.18.: Isosurfaces of Wannier functions for (a) three-fold coordinated planar sp^2 In, (b) tetrahedral In, (c) three-fold coordinated Sb in a pyramidal-like bonding geometry and (d) four-fold coordinated Sb in a tetrahedral environment. Atoms of In are depicted by violet spheres and Sb by cyan spheres. Isosurfaces with different colours (red and blue) have different sign. The Wannier function with spherical isosurface in (c) is an *s*-like lone pair.

and seven-membered rings are present. In particular, six-membered rings of type ABABAB, where A stands for In and B for Sb, are the building blocks of the zincblende crystal. However, the most abundant six-membered rings are of type AABABB which contains homopolar In-In and Sb-Sb bonds. Among the six-membered rings there are structures with a high In content, in particular InInInInInSb and InInInInSbSb rings. The majority of the four-membered rings are of ABAB type and about one half is formed by edge-sharing tetrahedra.

In summary, the model of a-InSb generated with the BLYP functional has a mostly tetrahedral network and reproduces well the experimental PCF. The tetrahedral bonding geometry

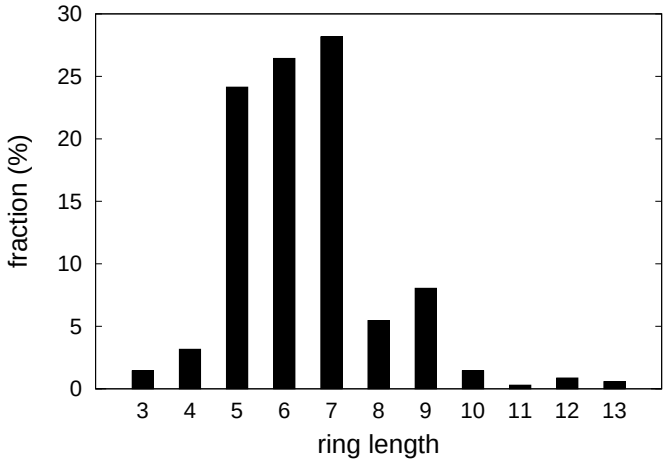

Figure 3.19.: Distribution of the ring lengths in the a-InSb model generated with the BLYP functional computed according to Ref. [212].

Rings statistics

4-membered

InSbInSb	55%	6	ABAB
InInSbSb	27%	3	AABB
InInInSb	9%	1	AAAB
InSbSbSb	9%	1	ABBB

5-membered

InSbInSbSb	51%	43	ABABB
InInSbInSb	38%	32	AABAB
InInSbSbSb	5%	4	AABBB
InSbSbSbSb	4%	3	ABBBB
InInInSbSb	2%	2	AAABB

6-membered

InInSbInSbSb	25%	23	AABABB
InSbInSbInSb	24%	22	ABABAB
InInInSbInSb	16%	15	AAABAB
InSbInSbSbSb	11%	10	ABABBB
InInSbInInSb	9%	8	AABAAB
InInInInInSb	5%	5	AAAAAB
InSbSbInSbSb	4%	4	ABBABB
InInInSbSbSb	3%	3	AAABBB
InInInInSbSb	1%	1	AAAABB
InSbSbSbSbSb	1%	1	ABBBBB

Table 3.4.: Abundance of the different types of rings of different size in the 216-atom model of a-InSb generated through an MD quench with the BLYP functional. The absolute number of rings is also given in the second column. The type of the rings is indicating by A and B letters where A stands for In and B for Sb.

is favoured with respect to the octahedral-like geometry by the BLYP functional. In fact, once relaxed with the BLYP functional, the mostly octahedral MD-L2 model generated with the PBE functional is higher in energy by about 41 meV/atom with respect to the tetrahedral-like model generated with the BLYP. The reverse is true if we optimize with the PBE functional the tetrahedral model which becomes 29 meV/atom higher in energy than MD-L2 model at PBE level.

The effect of the van der Waals interactions on the topology of the structure was also investigated by generating an amorphous model of InSb by quenching from the melt with BLYP-MD simulations and by including van der Waals interactions according to Grimme [202] (see Appendix A.3). No substantial differences can be found with respect to the BLYP model without van der Waals and the fraction of tetrahedra is about 2 % lower for In atoms and about 2 % higher for Sb atoms in the model generated with van der Waals. These results points to a deficiency of the PBE exchange-correlation functional when dealing with the close competition in energy between tetrahedral-like and octahedral-like configurations, which is probably also responsible for the tetrahedral-to-octahedral transition observed experimentally in a-InSb under moderate pressure [203].

Electronic properties

In order to study the electronic properties of the system, we used the HSE06 hybrid functional [154] which better reproduces the band gap. Since the HSE06 functional is built on the PBE functional, the structure obtained with the BLYP functional was firstly relaxed with the PBE functional and then the electronic structure was calculated with the HSE06 functional at the PBE geometry. We also computed the electronic density of states (DOS) with the BLYP exchange-correlation functional on the BLYP-relaxed structure and the PBE DOS on the PBE-relaxed structure. The DOSs were obtained from the Kohn-Sham (KS) energies at the Γ-point broadened with Gaussian functions of 27 meV width. The comparisons are shown in Figure 3.20 and do not evidence important differences in the electronic structure. The band gap is very small, if any, due to the well known deficiency of the GGA functional in reproducing band gaps.

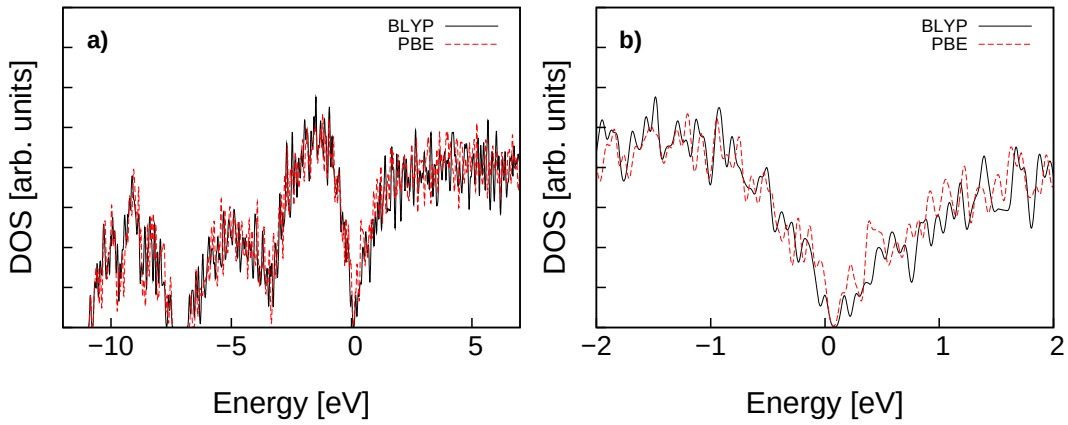

Figure 3.20.: a) Electronic density of states for the 216-atom model of a-InSb generated with the BLYP functional. The DOS is calculated either the BLYP (continuous black line) or with the PBE functional (dashed red line). The DOSs were computed on structures relaxed with the BLYP functional and with the PBE functional, respectively. The KS energies are broadened by Gaussian functions of 27 meV width. The DOSs are aligned with respect to the energy of the highest occupied orbital corresponding to zero. b) A zooming of the DOS of panel a) close to the band gap.

The DOS was then calculated with the HSE06 functional (Figure 3.21) which turns the a-InSb model into a semiconductor with a small band gap of about 0.27 eV.

To quantify the localization properties of individual KS states, we have computed the Inverse Participation Ratio (IPR), which is defined for the i-th KS state by

$$IPR_i = \frac{\sum_j c_{ij}^4}{(\sum_j c_{ij}^2)^2} \tag{3.8}$$

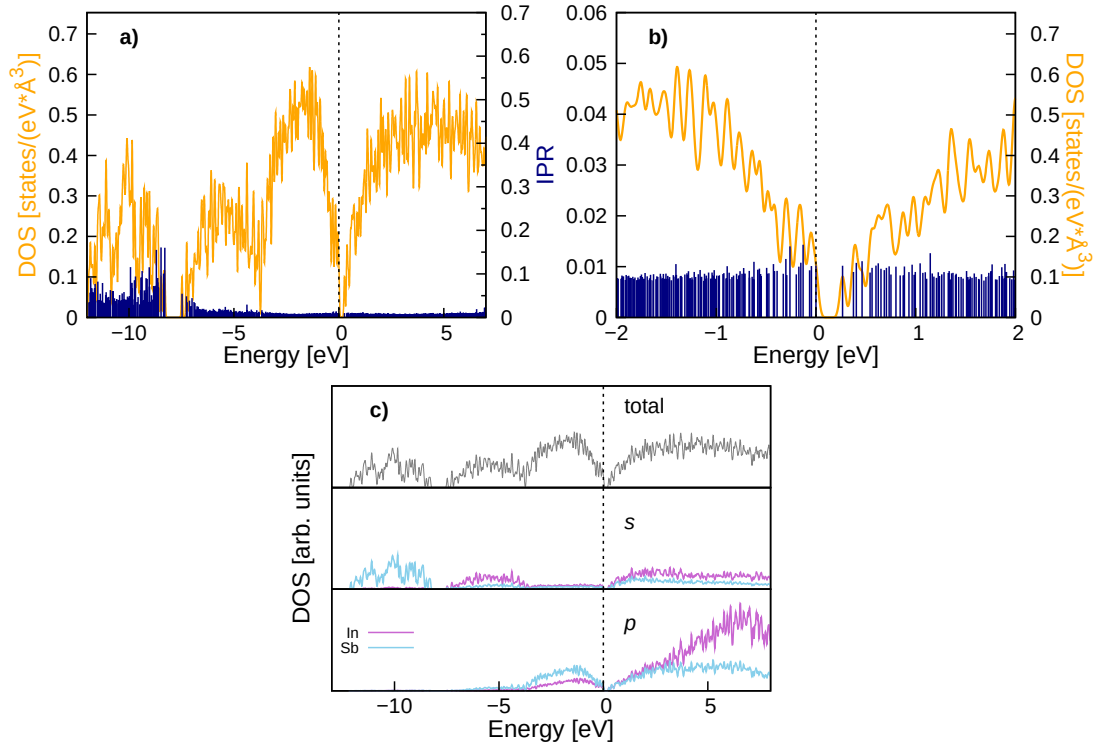

Figure 3.21.: a) Electronic density of states (HSE hybrid functional [154], see text) of the a-InSb model, generated with the BLYP functional. The KS energies are broadened by Gaussian functions of 27 meV width. The zero of energy corresponds to the top of the valence band. The Inverse Participation Ratio (IPR) is also given (blue spikes, see text for definition). b) A zooming of the DOS of panel a) close to the band gap. c) Projections on atomic *s* and *p* pseudo wavefunctions of the DOS of panel a). The contribution from *d* pseudo wavefunctions is negligible on the scale of the figure and is omitted.

where j runs over the Gaussian-Type Orbitals (GTOs) of the basis set, while c_{ij} are the expansion coefficients of the i-th KS state in GTOs. The higher the IPR value the higher is the localization of the state. The IPR is also given in Figure 3.21 and apparently, no localized states ascribed to defects can be found at the valence and conduction band edges nor in the band gap.

To investigate the atomic oxidation state, we computed the Bader ionic charges from the total electronic charge density by using the scheme of Ref. [213]. To this aim we added to the valence charge density the core charges localized on the atoms. The results reported in Figure 3.22 show a tail of the distribution towards zero due to the presence of homopolar bonds. The two In atoms with the greater (+0.4 a.u.) and the lower (−0.1 a.u.) charge are bound to each other, while positively charged Sb atoms are three-fold coordinated Sb atoms in $InSb_2$ or Sb_3 environments. No charge defects are present in the model.

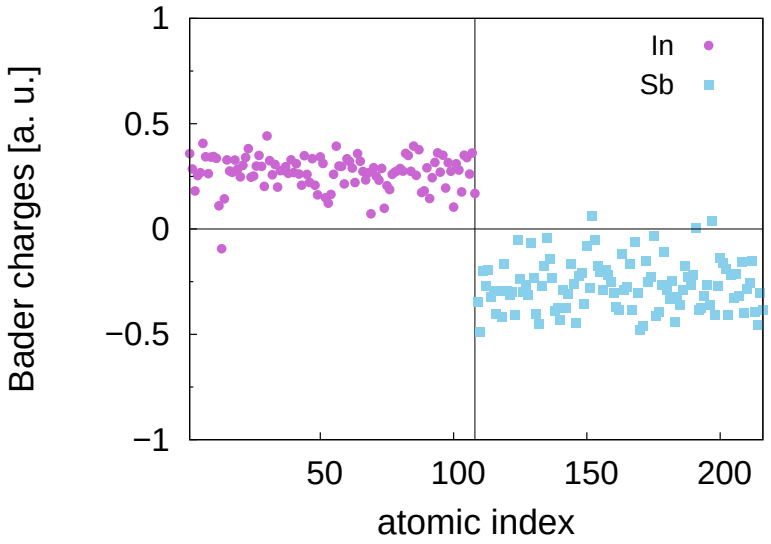

Figure 3.22.: Bader ionic charges (atomic units) of the model of a-InSb generated with the BLYP functional. Each point corresponds to an individual atom in the supercell.

Vibrational properties

Regarding the vibrational properties, the phonon frequencies of the amorphous model were computed by diagonalizing the dynamical matrix obtained in turn from the variation of atomic forces due to finite atomic displacements 0.0053 Å large. Only phonons with the periodicity of our supercell (Γ-point phonons) were considered. The phonon density of states is shown in Figure 3.23 for the model generated with the BLYP functional. In an amorphous material, phonons display localization properties that depend on the frequency. To address this issue, we have computed the inverse participation ratio (IPR) of the j-th vibrational mode defined as

$$IPR = \frac{\sum_\kappa \left| \frac{\mathbf{e}(j,\kappa)}{\sqrt{M_\kappa}} \right|^4}{\left(\sum_\kappa \frac{|\mathbf{e}(j,\kappa)|^2}{M_\kappa} \right)^2}, \tag{3.9}$$

where $\mathbf{e}(j,\kappa)$ are phonon eigenvectors, while the sum over κ runs over the N atoms in the unit cell with masses M_κ. According to this definition, the value of the IPR varies from $1/N$ for a completely delocalized phonon, to one for a mode completely localized on a single atom. The plot of the IPR in Figure 3.23 reveals the presence of phonons strongly localized on In atoms above 160 cm^{-1}.

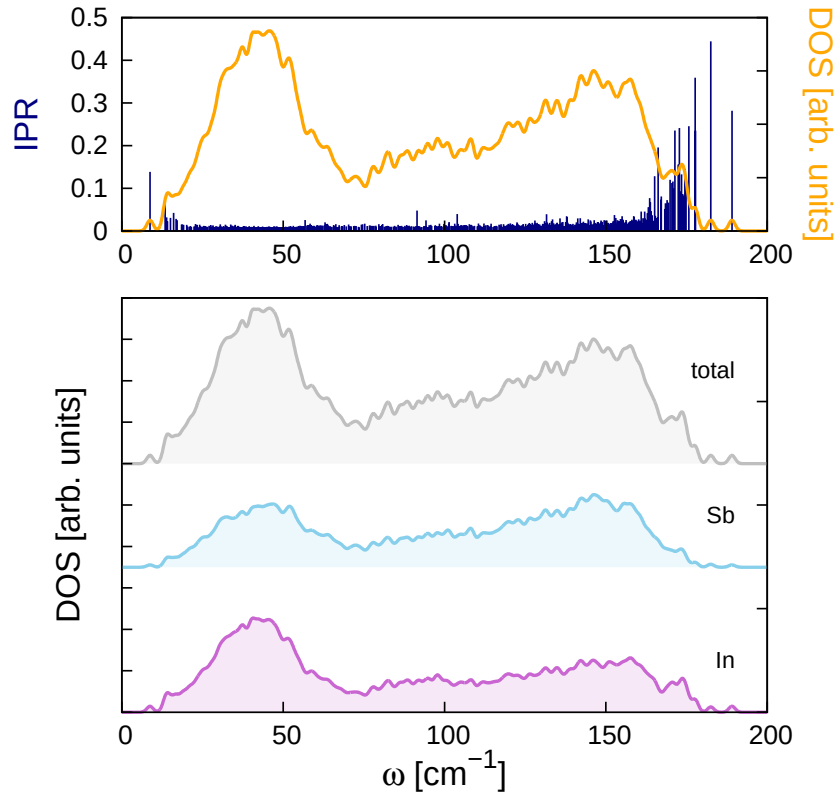

Figure 3.23.: Upper panel: phonon DOS of a-InSb and phonon IPR (blue spikes, left scale, see text for definition) superimposed to the DOS. Lower panel: projections of the phonon DOS on different species (In and Sb).

Summary

In conclusion, first principle simulations on the amorphous phase of InSb have shown that the PBE functional is not able to reproduce the experimental data on the pair correlation function. The position of the first maximum of the PCF is overestimated by about 5 % with respect to experiments. This problem can be overcome by using the BLYP exchange-correlation functional which gives an error on the position of the first maximum of the PCF below 1 %. This misfit arises because the octahedral-like structure seems to be too favoured with respect to a tetrahedral one by using the PBE functional.
The structure of a-InSb emerged from the BLYP simulations is mostly tetrahedral with a sizable fraction of homopolar bonds.

3.2. InSbTe alloys

The $In_3Sb_1Te_2$ and $In_{13}Sb_{11}Te_3$ ternary compounds were then analysed. Both these alloys have a high crystallization temperature that makes them suitable to substitute GST in PCM devices and in multi-bit memories.
The stoichiometric composition $In_3Sb_1Te_2$ can be thought of as a pseudo-binary alloy of InSb [183] and InTe [102] which both display tetrahedral environments in the crystalline phase (Figure 1.27). This composition is interesting for PCM applications since it presents a crystalline phase with cubic rocksalt structure [98], metastable at 300 K. This phase can be obtained by rapidly quenching from the melt avoiding phase separation. As opposed to the two binaries InSb and InTe, the ternary $In_3Sb_1Te_2$ crystal displays octahedral environments. Since no experimental data are available on a-$In_3Sb_1Te_2$, it is unclear whether the structure of the amorphous phase might be similar to that of the two binary crystals showing tetrahedral environments or to the structure of the ternary crystal with an octahedral-like bonding geometry. The $In_{13}Sb_{11}Te_3$ composition was also analysed being close to the alloys grown experimentally by metal-organic chemical vapour deposition (MOCVD) by Fallica *et al.* [9] for which we hope that structural data will be available in the near future.
We addressed the study of the amorphous structure of these compounds by DFT simulations as described in the next section.

3.2.1. $In_3Sb_1Te_2$

Computational details

Simulations with both PBE and BLYP exchange and correlation functionals have been carried out to model the glassy phase of the ternary compound $In_3Sb_1Te_2$. As already pointed out for InSb, also in this case PBE-models are mainly octahedrally coordinated [214], while BLYP functional predicts a much higher fraction of tetrahedral structures. Models of a-$In_3Sb_1Te_2$ were generated by quenching from the melt. A 300-atoms cubic cell was quenched from 1000 to 300 K in 250-300 ps by means of DFT simulations with the CP2K code (see Section 2.5). The quenching protocols are shown in Figure 3.24. The models were then equilibrated at 300 K for about 30 ps. Norm-conserving GTH [158, 159] pseudopotentials with three, five and six valence electrons for In, Sb and Te, respectively have been used. The Kohn-Sham orbitals were expanded in a double-zeta-valence plus polarization (DZVP) Gaussian-type basis set [192], while the charge density has been expanded in a plane-wave basis set with a cut-off of 100 Ry, Brillouin zone integration was restricted to the supercell Γ point. Since we had no information on the density of the liquid and amorphous phases, we first fixed the density of the liquid to 0.0323 atoms/Å^3 (6.448 g/cm^3) which is about 7 % lower than the density of 6.94 g/cm^3 that can be assigned to the ideal rocksalt crystal with the experimental lattice parameter of 6.126(1) Å [98]. A similar increase in density upon crystallization of the amor-

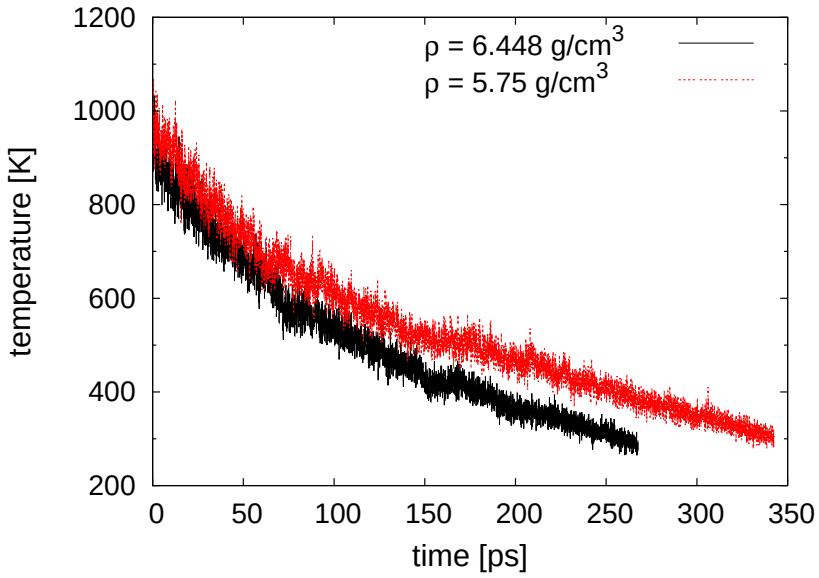

Figure 3.24.: Evolution of the temperature during the quench of 300-atoms model of amorphous $In_3Sb_1Te_2$ at high density (6.448 g/cm^3) and at low density (5.75 g/cm^3). PBE exchange and correlation functional and a DZVP basis set have been used.

phous is found in phase change GeSbTe alloys [21]. There is, however, a large uncertainty in our chosen density, as picnometric measurement of the density in the crystal gives 6.77 g/cm^3 which suggests the presence of about 2 % of vacancies [98]. A first model was thus generated at the estimated density of the liquid 6.448 g/cm^3 and the density of the amorphous was optimized by fitting the energy-volume points with a Murnaghan function (3.6), obtaining a value of 0.0288 atoms/Å^3 (5.75 g/cm^3). A second model was later generated at the fixed density of (5.75 g/cm^3) by quenching from the melt. This density is about 11 % lower than the starting density of 6.448 g/cm^3. However, an overestimation of the bond lengths using the PBE functional is actually found in the Sb-containing amorphous compounds $Ge_2Sb_2Te_5$ [71] and Sb_2Te_3 [196], as well as in InSb, as discussed before. Therefore the starting density of 6.448 g/cm^3 might be closer to the real density of the amorphous phase, that we do not know, than the theoretical one.

A third model of amorphous $In_3Sb_1Te_2$ was finally generated by quenching with the ISA method from 1000 to 300 K in 10000 Monte-Carlo steps with the BLYP exchange and correlation functional. As already done for the binary InSb system, the liquid was firstly equilibrated at 1000 K in 1000 MC steps and then linearly quenched to 300 K in 8000 MC steps. A faster quench from 300 to 5 K in 1000 MC steps followed to reach near zero temperature. The ISA simulations (Figure 3.25) were performed at constant zero pressure by including the van der Waals interactions according to Grimme [202] to better reproduce the equilibrium density. At the end of the simulation, a density of 0.0278 atoms/Å^3 (5.554 g/cm^3) was found, which is

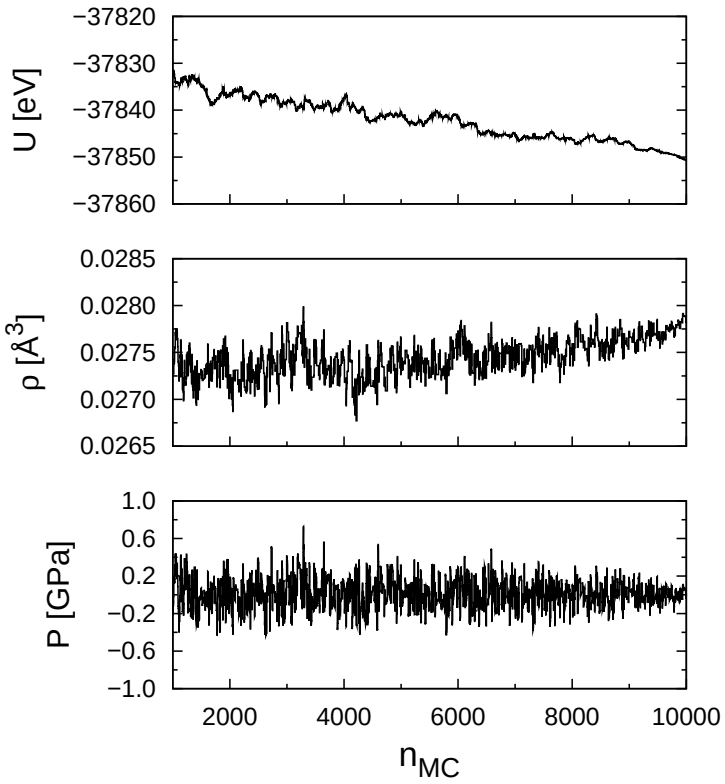

Figure 3.25.: Evolution of the potential energy U, density ρ and pressure P during the ISA quenching of a model of amorphous $In_3Sb_1Te_2$ at constant pressure with the BLYP exchange and correlation functional. These parameters are represented as function of quenching "time" expressed by the number of Monte-Carlo steps n_{MC}.

again lower than the PBE equilibrium density. The model was then equilibrated at the final fixed density at 300 K for 20 ps. The model generated with ISA and the BLYP functional is thus at the theoretical equilibrium density at zero pressure.

Structural properties

The pair correlation functions of the two PBE models of density 6.448 g/cm^3 and 5.75 g/cm^3 and of the BLYP model at density 5.554 g/cm^3 are compared in Figure 3.26. The PBE model at lower density presents sharper peaks in the total and partial PCFs and a higher degree of medium-range order with respect to the PBE model at higher density. These features are even more evident in the BLYP model at the lowest density where the second coordination shell position is well defined for all the atomic pairs. The In-In pair correlation function shows the largest differences between the three structures. Two cut-off distances were defined for the In-In bond on the basis of the position of the first minimum, being 3.35 Å for the PBE model at higher density and 3.10 Å for the PBE model at lower density and the BLYP model.

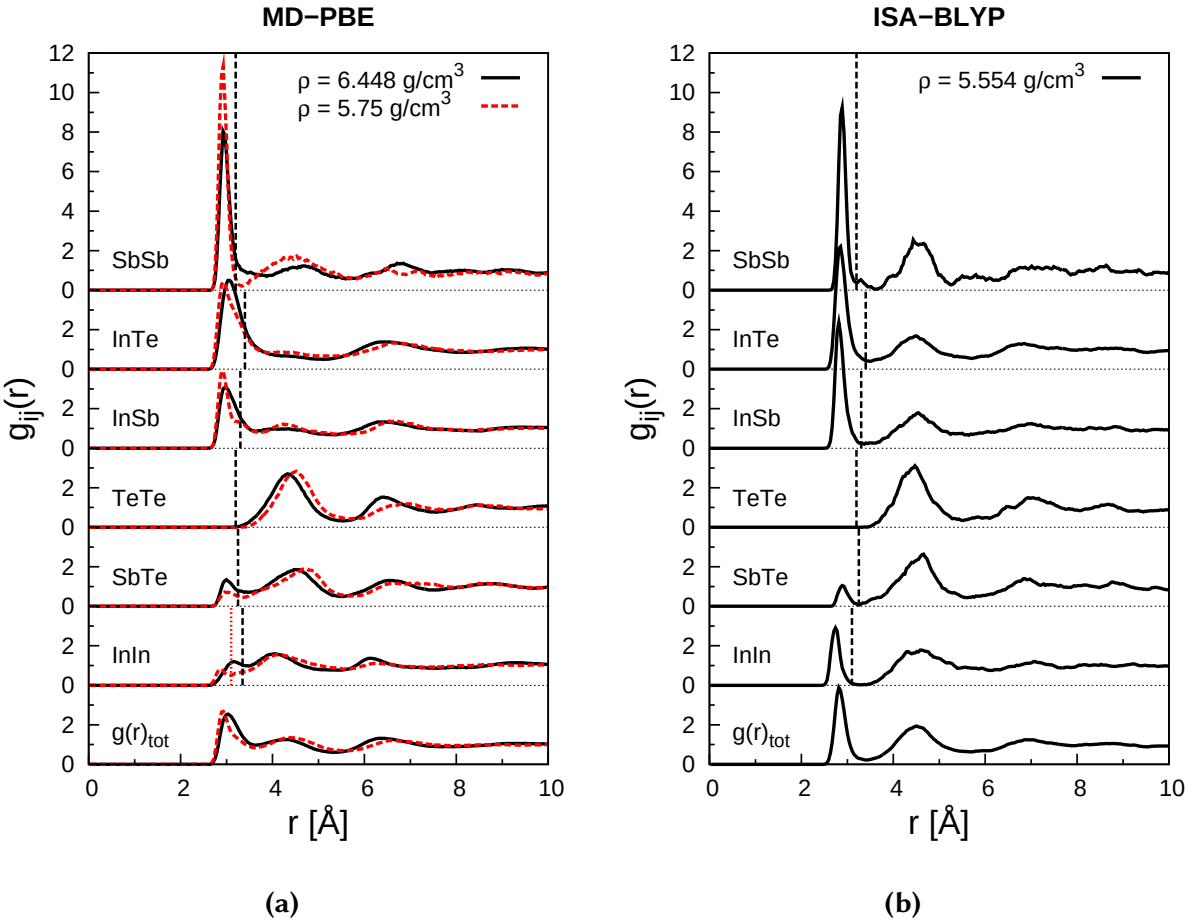

Figure 3.26.: Total and partial pair correlation functions of the 300-atom models of a-$In_3Sb_1Te_2$ generated by quenching from the melt with *ab-initio* molecular dynamics simulations. Data for (a) PBE models at the density of 6.448 g/cm^3 (continuous line) and of 5.75 g/cm^3 (dashed line) and for (b) the model generated at constant pressure with the BLYP functional which yields an equilibrium density of 5.554 g/cm^3 are reported. The vertical lines are the cut-off radii used to define the coordination numbers (3.35 or 3.10 Å, 3.30 Å, 3.40 Å, 3.25 Å, 3.20 Å and 3.20 Å for the In-In, In-Sb, In-Te, Sb-Te, Sb-Sb and Te-Te bonds, respectively). The data were obtained by averaging over a 20 ps long trajectory at 300 K for the PBE models and on a 10 ps long trajectory at 300 K for the BLYP model.

The average coordination numbers for different pairs are obtained by integrating the partial PCFs up to the bonding cut-off distances. The results reported in Table 3.5, together with the fraction of the different types of bonds (Table 3.6) show the presence of very few Sb-Te pairs against a great number of In-Sb and In-Te bonds, indicating that the amorphous phase can be mostly seen as a mixture of the InSb and InTe binary systems. Sb-Te pairs can be considered as "wrong bonds" as well as the homopolar pairs since in the rocksalt crystal Sb and Te atoms

PBE - Average coordination numbers				
	with In	**with Sb**	**with Te**	**total**
In	1.01 (0.37)	0.79 (0.68)	2.70 (2.28)	4.50 (3.32)
Sb	2.36 (2.03)	1.22 (1.31)	0.57 (0.30)	4.15 (3.64)
Te	4.04 (3.41)	0.29 (0.15)	0.01 (0.00)	4.34 (3.56)

BLYP - Average coordination numbers				
	with In	**with Sb**	**with Te**	**total**
In	0.95	0.78	1.93	3.66
Sb	2.35	0.92	0.28	3.55
Te	2.89	0.14	0.00	3.04

Table 3.5.: Average coordination numbers for different pairs of atoms computed from the partial pair correlation functions of Figure 3.26 of a-$In_3Sb_1Te_2$ obtained with the PBE functional (left table) at higher (6.448 g/cm^3) and, in parentheses, at lower density (5.75 g/cm^3). Results for the ISA-BLYP model (5.554 g/cm^3) are reported on the right.

PBE - Types of bonds (%)			
	with In	**with Sb**	**with Te**
In	11.5 (5.3)	18.0 (19.6)	61.5 (65.9)
Sb		4.6 (6.3)	4.3 (2.9)
Te			0.0 (0.0)

BLYP - Types of bonds (%)			
	with In	**with Sb**	**with Te**
In	13.8	22.8	56.2
Sb		4.5	2.7
Te			0.0

Table 3.6.: Percentage of the different type of bonds in the amorphous PBE models (left table) of $In_3Sb_1Te_2$ at high density (6.448 g/cm^3) and, in parentheses, at lower density (5.75 g/cm^3). Results for the ISA-BLYP model at the density of 5.554 g/cm^3 are reported on the right.

randomly occupy the same sublattice and do not form Sb-Te bonds. The first peak of the pair correlation functions is sharper in the models at lower density, especially for the Sb-Sb pair, resulting in lower coordination numbers for all atoms.

The model at 5.75 g/cm^3 density shows a reduction of homopolar In-In bonds and a smaller number of Sb-Te bonds with respect to the high density model, while the BLYP functional seems to slightly favour the presence of In-In and In-Sb bonds with respect to In-Te bonds. The distribution of the different types of bonds (Table 3.6) is overall very similar in the three models. However, the average atomic coordination and the distribution of the coordination numbers in Figure 3.27 are very different. Many atoms are overcoordinated, in particular in the denser model, with respect to the $8-N$ rule which states that an atomic species forms a number of bonds equal to 8 minus the number of its valence electrons ($s+p$). Antimony and tellurium can display higher coordination numbers thanks to the formation of dative bonds with In atoms. As it will be discussed later, this situation results in a defective-octahedral coordination. The PBE models show broader distributions of the coordination numbers, especially for In atoms. In the BLYP model, instead, more than 80 % of In atoms are four-fold coordinated, while about 3 % of indium is isolated with no nearest-neighbours. Antimony is also prevalently four-fold coordinated. Overall, the first coordination is much well defined

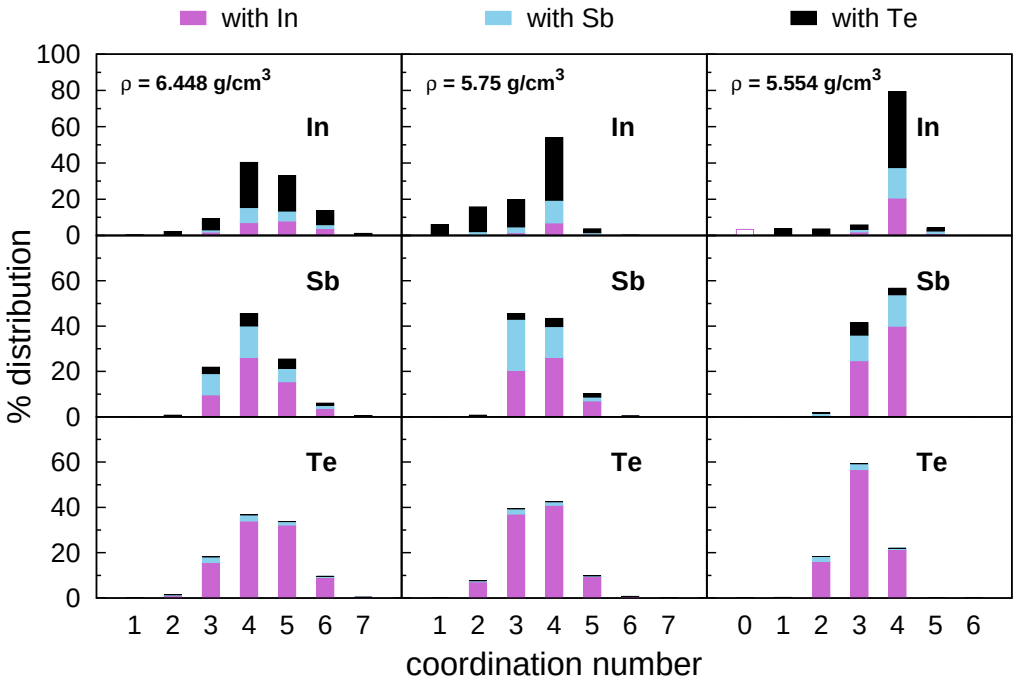

Figure 3.27.: Distribution of the coordination numbers of a-$In_3Sb_1Te_2$ models obtained by quenching from the melt at fixed volume with the PBE functional at a density of 6.448 g/cm^3 (left panel) and of 5.75 g/cm^3 (central panel) and through ISA quench and BLYP functional yielding a density of 5.554 g/cm^3 (right panel). The contributions from the different atom pairs are indicated by different colours.

with sharper minima in the PCF for the BLYP model.
Information on the local bonding geometry is provided by the bond angle distribution functions $P(\theta)$ defined by equation (3.5) (Figures 3.28 and 3.29), which highlight the structural differences among the three models. The $P(\theta)$ distribution of the denser model has a bimodal shape with two peaks at about 90° and 180° which are typical of defective-octahedral structures (Figure 1.15). The PBE model at lower density shows both tetrahedral and defective octahedral-like configurations. In fact, a bimodal shape of the $P(\theta)$ distribution can still be distinguished with peaks at $\sim 90°$ and $\sim 180°$, but also In atoms with tetrahedral sp^3 hybridization are present. The difference in bond angles corresponds to a difference in coordination numbers as shown in Figure 3.28b by the distribution functions resolved for atoms with different coordination. Three- and five-fold coordinated In atoms form bond angles of 90°, four-fold coordinated In atoms form bonds at about 100°, in between the typical values of octahedral and tetrahedral bond angles. Concerning Sb atoms, the majority is in a defective octahedral environment, but a shoulder in the distribution of the four-fold coordinated Sb atoms of the model at 5.75 g/cm^3 can be see at about 110°. The BLYP model, instead, is char-

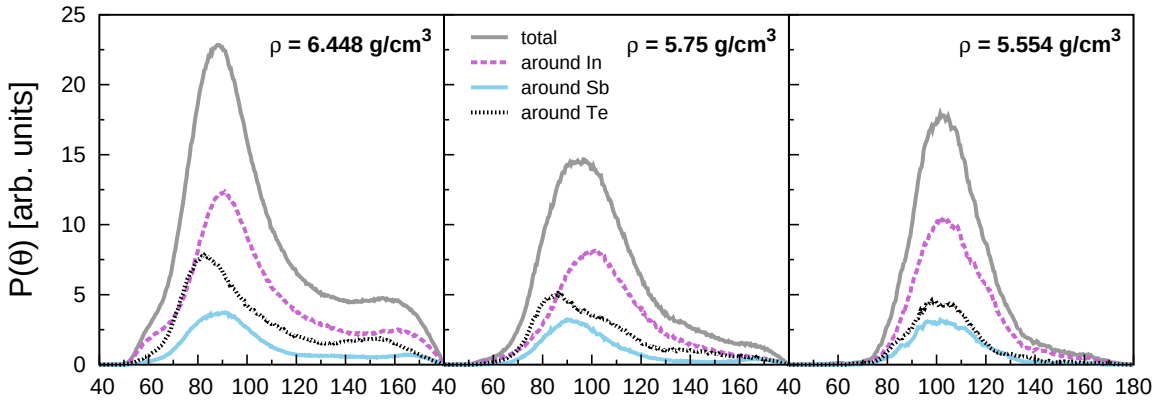

(a)

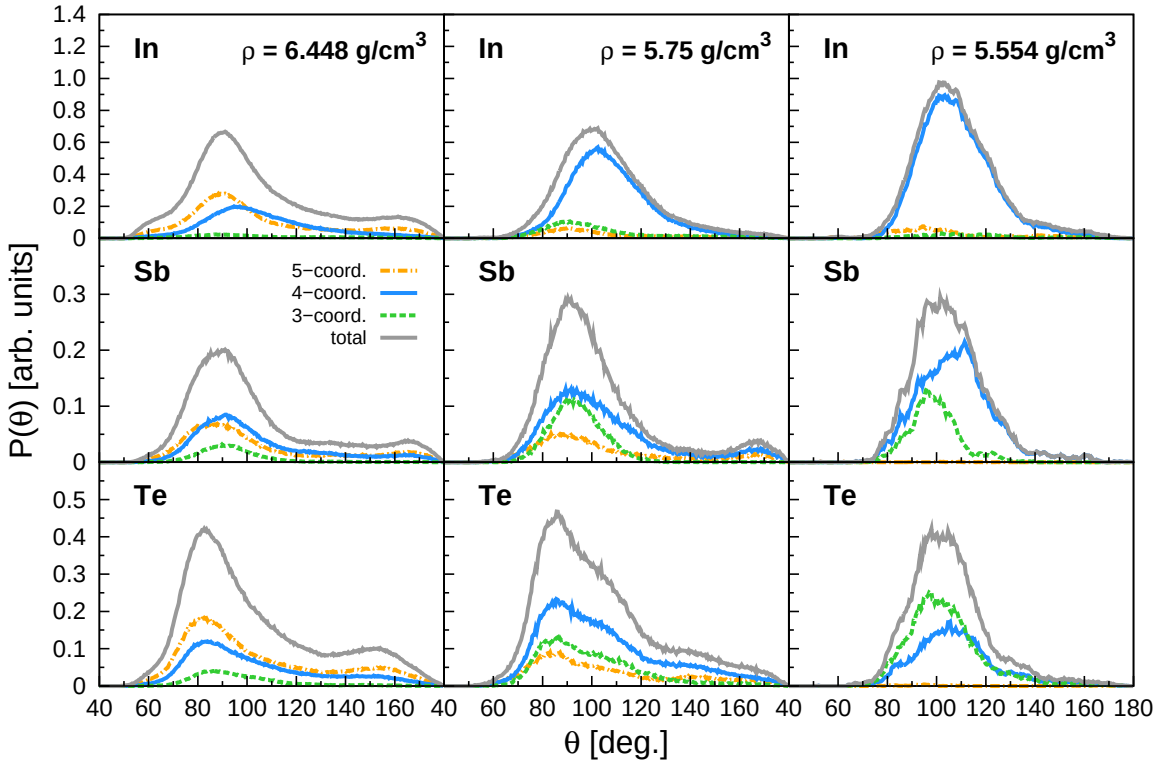

(b)

Figure 3.28.: Bond angle distribution functions resolved (a) for atomic species and (b) for different coordination numbers in a-$In_3Sb_1Te_2$. Models were with the PBE functional at a fixed density of 6.448 g/cm^3 (left panel) and of 5.75 g/cm^3 (central panel) and through ISA quench and BLYP functional at yielding a density of 5.554 g/cm^3 (right panel).

acterized by bond angles of about 110° typical of a tetrahedral coordination. Only a small tail towards high ($\sim$ 180°) bond angles is present for In atoms, indicating the presence of a very

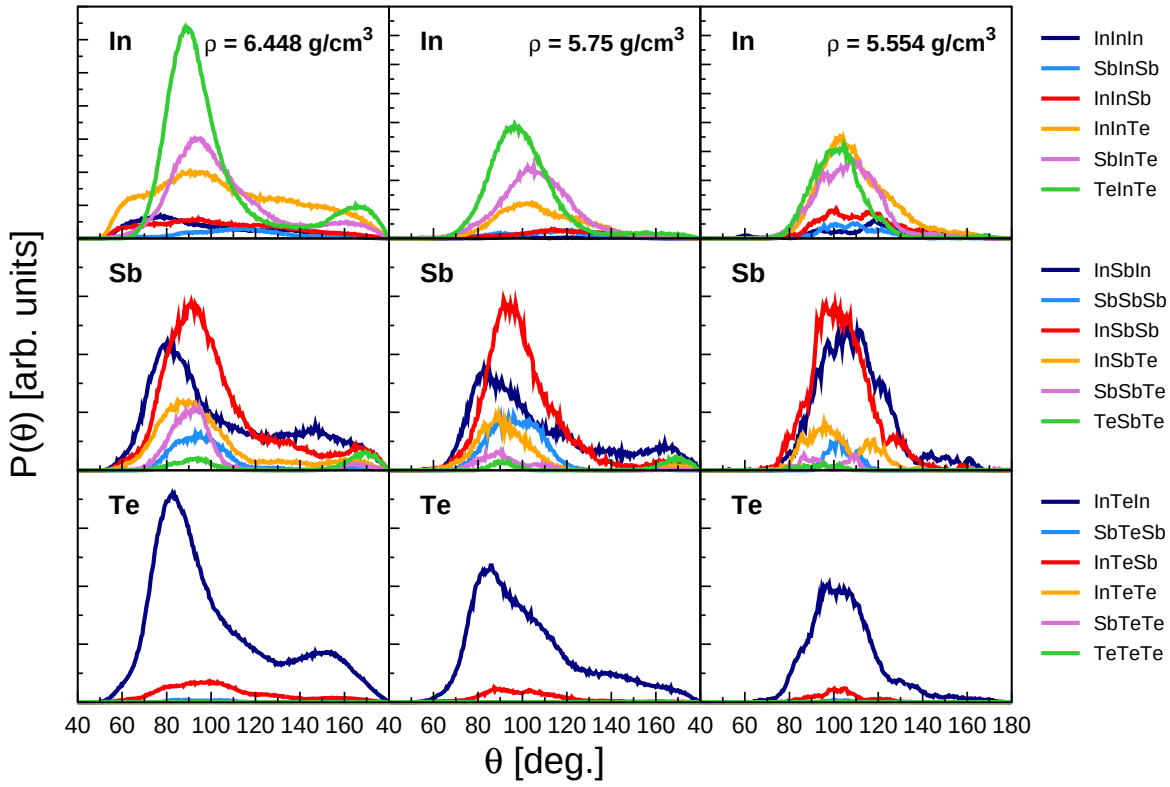

Figure 3.29.: Bond angle distribution functions resolved for different triplets in a-$In_3Sb_1Te_2$. Models were obtained with the PBE functional at a fixed density of 6.448 g/cm^3 (left panels) and of 5.75 g/cm^3 (central panels) and through ISA quench and BLYP functional yielding a density of 5.554 g/cm^3 (right panels).

small fraction of octahedral-like configurations. Four-fold coordinated Sb atoms are mostly tetrahedrally coordinated as well in the BLYP model.

By further resolving the distribution for different types of atomic triples, it is possible to note that in the BLYP model InInTe angles have a broad distribution, while InTeIn, InSbIn and SbInTe triplets form angles of $\sim 110°$. InSbTe, SbSbTe and TeSbTe angles deviate from the tetrahedral configuration recalling the octahedral structures of Sb_2Te_3.

A list of the main types of local environments and their abundance is reported in Table 3.7 for the three models. As the density decreases, the In content in the local environments of four-fold coordinated In atoms increases. Homopolar Sb-Sb bonds are, instead, present in particular in the PBE model at lower density (5.75 g/cm^3) where a not negligible fraction of Sb_3 and Sb_4 environments for Sb atoms was found. The main types of local environment of each atomic species in a-$In_3Sb_1Te_2$ models, together with the isosurfaces of the Wannier functions are reported in Figure 3.30.

PBE - Local environments

	1	2	3	4	5	6
In:	- (5.3%)	1.3% (13.3%)	1.3% (18.0%)	38.7% (59.3%)	37.3% (4.0 %)	20.0% (-)
	Te: - (4.7%)	Te_2: 1.3% (11.3%) TeSb: - (2.0%)	Te_3: - (12.7%) $SbTe_2$: 1.3% (3.3%)	$SbTe_3$: 8.7% (14.3%) Sb_2Te_2: 8.0% (8.0%) $InTe_3$: 6.7% (10.0%) $InSbTe_2$: 5.3% (12.7%) Te_4: 4.0% (6.7%) In_2SbTe: 2.0% In_2Te_2: 2.0% (3.3%) $InSb_2Te$: - (2.7%)	In_2Te_3: 9.3% $SbTe_4$: 8.0% (1.3 %) $InTe_4$: 4.7% $InSbTe_3$: 3.3% In_3SbTe: 2.7% In_2SbTe_2: 2.7% $InSb_2Te_2$: 2.0%	In_3Te_3: 3.3% $InSbTe_4$: 2.7% In_2Te_4: 2.7% $SbTe_5$: 2.0% $In_2Sb_2Te_2$: 2.0%
Sb:			22.0% (44.0%)	46.0% (46.0%)	22.0% (10.0%)	10.0% (-)
			In_2Sb: 6.0% (10.0%) InSbTe: 6.0% (2.0%) $InSb_2$: 4.0% (20.0%) Sb_2Te: 4.0% $SbTe_2$: 2.0% Sb_3: - (6.0%) In_2Te: - (4.0%) In_3: - (2.0%)	In_3Sb: 20.0% (12.0%) In_2SbTe: 12.0% In_2Sb_2: 6.0% (18.0%) $InSb_3$: 4.0% $InSbTe_2$: 2.0% (4.0%) In_4: 2.0% (6.0%) Sb_4: - (2.0%) In_3Te: - (2.0%) In_2Te_2: - (2.0%)	In_3Sb_2: 8.0% In_4Sb: 6.0% (2.0%) In_3Te_2: 4.0% In_2SbTe_2: 2.0% (2.0%) In_3SbTe: 2.0% (2.0%) $InTe_4$: - (2.0%) In_5: - (2.0%)	In_4Sb_2: 4.0% In_5Sb: 4.0% In_4SbTe: 2.0%
Te:		- (5.0%)	15.0% (29.0%)	28.0% (52.0%)	44.0% (13.0%)	12.0% (-)
		In_2: - (4.0%)	In_3: 9.0% (25.0%) In_2Sb: 4.0% (4.0%) $InSb_2$: 2.0%	In_4: 25.0% (41.0%) In_3Sb: 2.0% (11.0%)	In_5: 34.0% (12.0%) In_4Sb: 9.0% (-)	In_6: 12.0% (-)

BLYP - Local environments

	1	2	3	4	5
In:	2.7%	3.3%	5.3%	82.7%	2.0%
	Te: 2.7%	Te_2: 2.7%	InSbTe: 2.0%	$InSbTe_2$: 20.7% $InTe_3$: 16.0% In_2Te_2: 11.3% Sb_2Te_2: 9.3% $SbTe_3$: 8.0% In_2SbTe: 6.7% $InSb_2Te$: 4.7% In_3Te: 2.0%	
Sb:			48.0%	52.0%	
			In_2Sb: 22.0% InSbTe: 8.0% In_2Te: 6.0% $InSb_2$: 6.0% In_3: 4.0% $InTe_2$: 2.0%	In_3Sb: 28.0% In_2Sb_2: 10.0% In_4: 6.0% In_3Te: 4.0% In_2Te_2: 2.0% In_2SbTe: 2.0%	
Te:		18.0%	61.0%	21.0%	
		In_2: 15.0% InSb: 2.0%	In_3: 54.0% In_2Sb: 6.0%	In_4: 19.0% In_3Sb: 2.0%	

Table 3.7.: Statistics of In, Sb and Te coordination environments for atoms with different coordination numbers given in the first line for a-$In_3Sb_1Te_2$ models generated with the PBE functional at fixed density of 6.448 g/cm^3 and of 5.75 g/cm^3 (in parenthesis) and with ISA quenching and BLYP functional yielding a density of 5.554 g/cm^3. Only environments in a fraction larger than 2 % are reported.

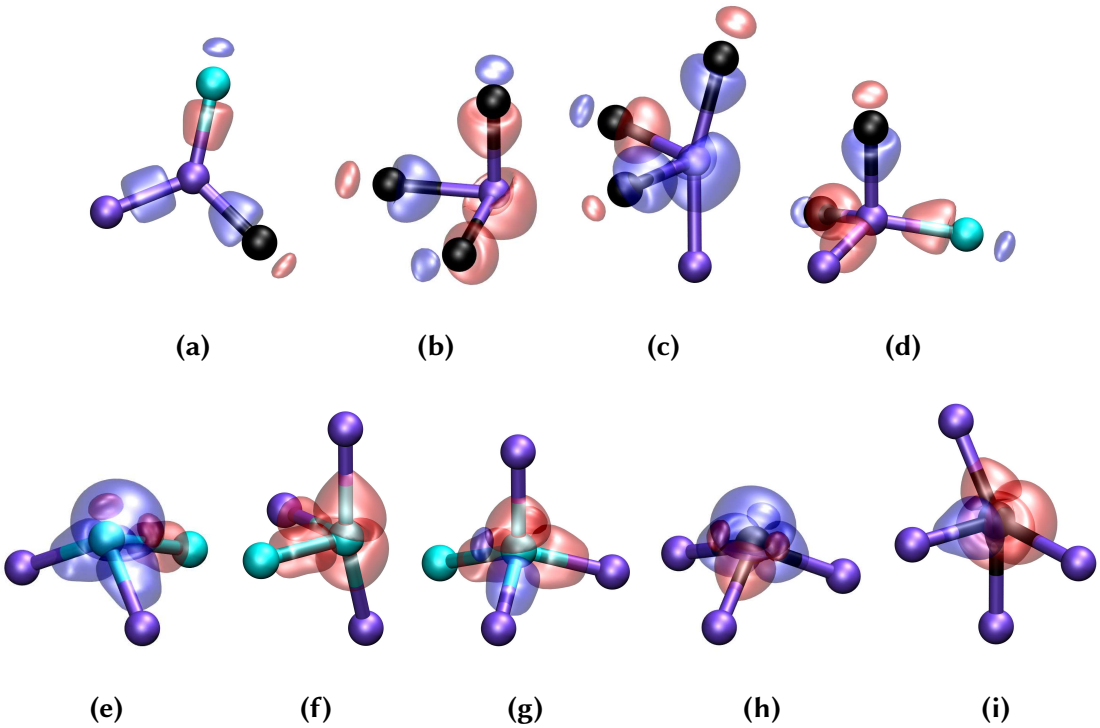

Figure 3.30.: Isosurfaces of the Wannier functions for different local environments in a-$In_3Sb_1Te_2$: three-fold coordinated In atom in (a) planar sp^2 and (b) pyramidal bonding geometry, (c) four-fold coordinated In in a defective octahedral coordination, (d) tetrahedral In, (e) three-fold coordinated pyramidal Sb, (f) defective-octahedral like four-fold coordinated Sb, (g) tetrahedral Sb, (h) three-fold coordinated pyramidal Te and (i) distorted defective-octahedral like four-fold coordinated Te. Atoms of In are depicted by violet spheres, Sb by cyan spheres and Te by black spheres. Isosurfaces with different colours have different sign. Wannier functions with spherical isosurfaces in the defective-octahedral configurations are *s*-type lone pairs.

Atoms in an octahedral-like configuration have an *s*-type WF on the central atom that corresponds to a lone pair. Three-fold coordinated In atoms in the BLYP model are mainly in a planar configuration (Figure 3.30a) with an sp^2 hybridization and bond angles of $\sim 120°$, while in the PBE models are mainly in a pyramidal geometry (Figure 3.30b) with bond angles close to 90°. To quantify the fraction of atoms in different bonding geometries, the q order parameter defined by equation (3.7) was calculated for the three models. This parameter can distinguish between octahedral and tetrahedral geometries as q is equal to 1 for a perfect tetrahedral environment and equal to 0 for an ideal octahedron. The distribution of q, resolved for different atomic species and coordination numbers is reported in Figure 3.31. Three-fold coordinated Te and Sb atoms are in a pyramidal configuration with a geometry close to that of a defective octahedron in the PBE models. In the BLYP model, these pyramidal structures

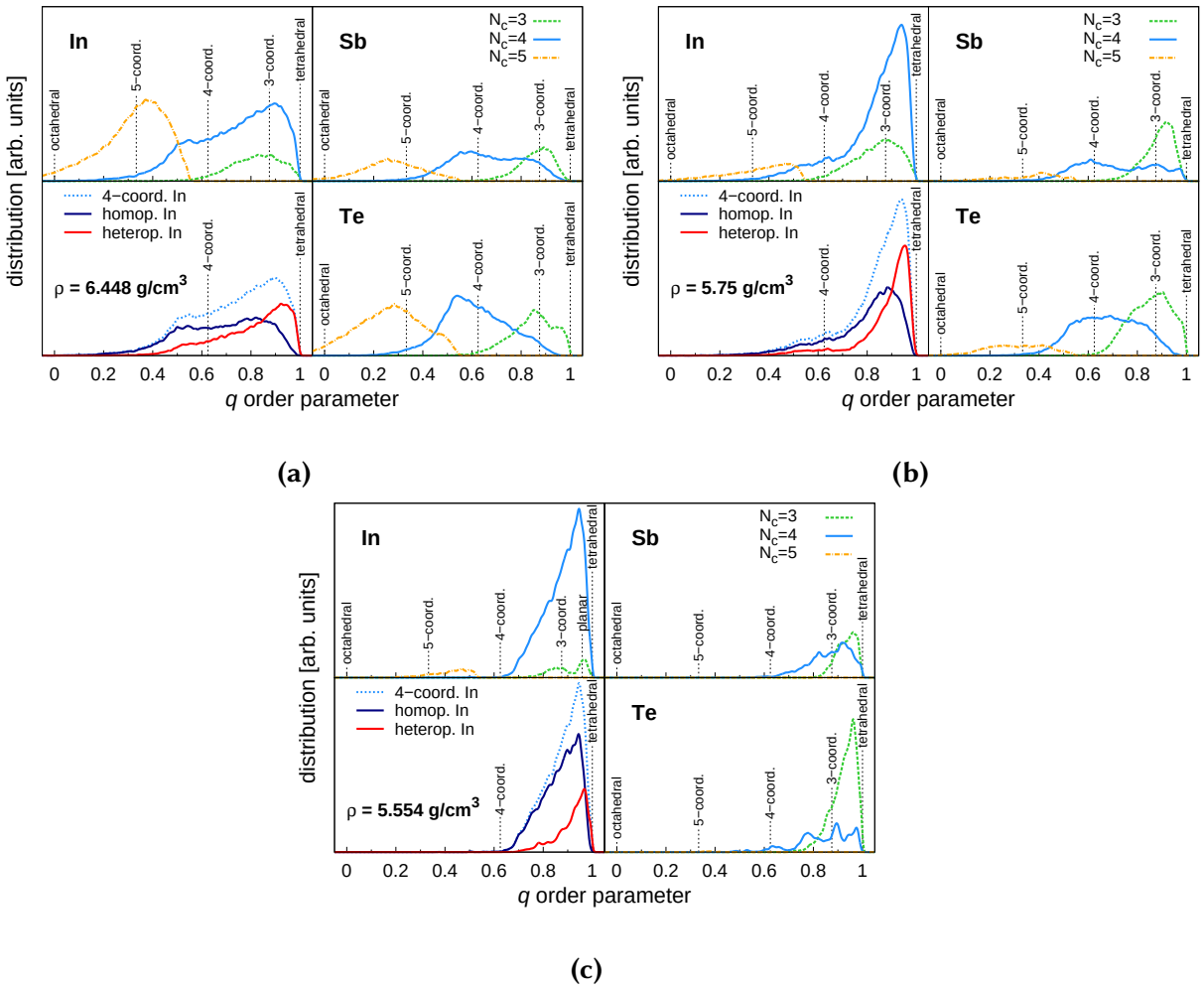

Figure 3.31.: Distribution of the local order parameter q for tetrahedricity defined by equation (3.7) for the models of a-$In_3Sb_1Te_2$ obtained with PBE functional (a) and (b) and with the BLYP functional (c). The order parameters for the In, Sb and Te species are resolved for atoms with different coordination numbers N_c. Vertical lines indicate the values of q for selected ideal geometries of defective octahedra with different coordination and tetrahedra. The distribution is further resolved for four-fold coordinated In atoms with or without homopolar bonds in the lower left panels.

are flatter and are more similar to a defective tetrahedron, rather than an octahedron. Four- and five-fold coordinated Sb and Te atoms occupy sites with a defective-octahedral geometry in the PBE models, but the very broad distribution for four-fold coordinated Sb atoms indicates the presence of many distorted structures. In the BLYP model, instead, a fraction of four-fold coordinated Sb is tetrahedral. Regarding In, there is again a prevalence of octahedral structures in the PBE models, while tetrahedral In atoms are the overwhelming majority in

the BLYP model. By resolving the q distribution of four-fold coordinated In atoms for atoms with and without In-In homopolar bonds as shown in Figure 3.31, it can be noticed that In-In bonds disfavour the tetrahedral geometry. For the model at 6.448 g/cm^3, the q distribution for four-fold coordinated In atoms is very broad and does not present a clear bimodal shape making difficult to disentangle the contribution of tetrahedra and octahedra. To identify the tetrahedral sites of In at high density, we then proceeded as follows: we first selected In atoms with $q > 0.8$ which can be safely attributed to tetrahedra in GeSbTe alloys and in $InGeTe_2$, then among those we selected atoms that have all four bonds shorter than 3.2 Å. This choice is dictated by the fact that in amorphous GeSbTe [71, 72, 74] and $InGeTe_2$ [199] the defective octahedra are made of three shorter and one or more considerably longer bond(s) in a $3+n$ coordination as discussed in Section 1.2.1. On the other hand the In-Te bonds in $InTe_4$ tetrahedra are always shorter than 3.2 Å in amorphous $InGeTe_2$ [199] and In-Sb bond lengths in $InSb_4$ tetrahedra are also shorter than 3.2 Å in amorphous InSb [201]. The angle distribution

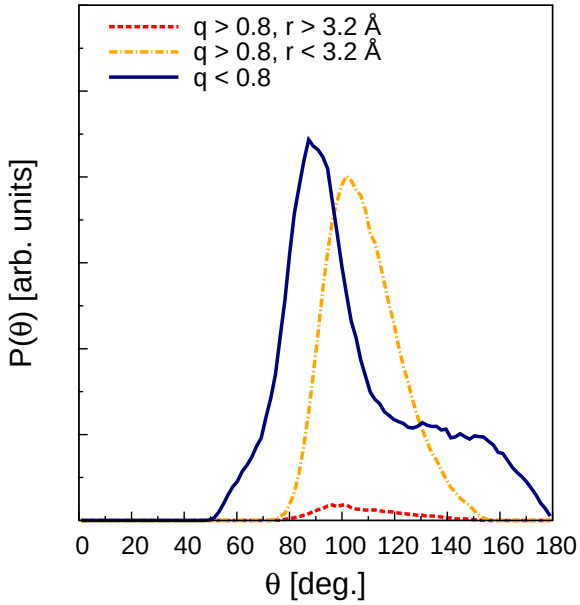

Figure 3.32.: Angle distribution function for four-coordinated In atoms with the tetrahedral order parameter $q < 0.8$ (continuous line) and $q > 0.8$ and all four bond length shorter than 3.2 Å (dot-dashed line) or with at least one bond longer than 3.2 Å (dashed line). The data refer to the model at the density of 6.448 g/cm^3.

function for In atoms with $q > 0.8$ is thus resolved for atoms with all bonds shorter than 3.2 Å and for atoms with one or more bonds longer in the model at high density (Figure 3.32). Although the angle distribution for atoms with all short bonds is peaked closer to the tetrahedral angle of 109.8°, also the very few (0.8 %) In atoms with a longer bond display bond angles compatible with the tetrahedral geometry. The fraction of In atoms with $q > 0.8$ can

thus be safely identified with tetrahedral In. The fraction of In atoms with $q > 0.8$ does not change by reducing the In-Te cut-off distance to 3.25 Å instead of 3.40 Å in the definition of the coordination number from the very beginning.
The concentration of tetrahedral In atoms can thus be estimated by integrating the q distribution for four-coordinated atoms in the range $0.8-1$ which yields a fraction of tetrahedral In of about 23 % (34 atoms among 150) at the density of 6.448 g/cm^3, of about 47 % (71 atoms among 150) at the density of 5.75 g/cm^3 and of about 77 % (116 atoms among 150) at 5.554 g/cm^3. The same procedure can be applied to Sb atoms giving a fraction of tetrahedral Sb atoms of about 10 % (5 atoms among 50) at the density of 6.448 g/cm^3, of about 18 % (9 atoms among 50) at the density of 5.75 g/cm^3 and of about 45 % (23 atoms among 50) at the density of 5.554 g/cm^3.
A further confirmation of the fraction of tetrahedral In computed above is provided by the analysis of the WFs. In fact, atoms in a defective octahedra are supposed to display a s-type WF localized on the atom since the bonding is only p-type. The fraction of four-coordinated atoms with a localized s-type WF can be obtained [199] by integrating the correlation function between four-fold coordinated In atoms and the center of WFs up to the first minimum (0.6 Å) shown in Figure 3.33a for the model at the density of 6.448 g/cm^3. The average coordination

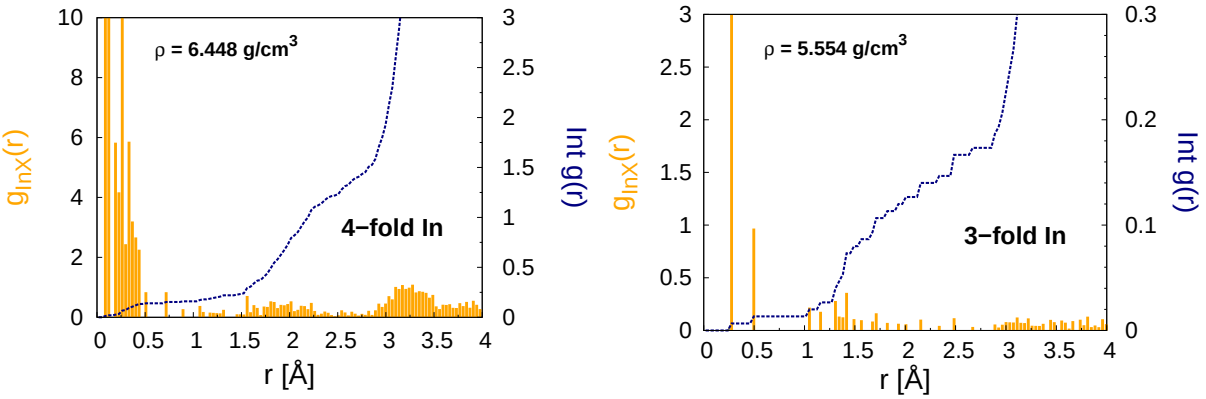

(a) (b)

Figure 3.33.: (a) Pair correlation function $g(r)$ of four-fold coordinated In atoms with the centers of the Wannier functions in the a-$In_3Sb_1Te_2$ with density of 6.448 g/cm^3. (b) Pair correlation function of three-fold coordinated In atoms with the centers of the Wannier functions in the a-$In_3Sb_1Te_2$ at the density of 5.554 g/cm^3. The dashed line is the running integral of $4\pi r^2 g(r)\rho$ where ρ is the density of Wannier centers (right scale).

number of In atoms with the s-type localized WF gives the fraction of non-tetrahedral-like atoms with coordination four. The remaining In can thus be assigned to a tetrahedral environment in a fraction (25 %) very close to that previously estimated from the analysis of the q local order parameter (23 %). The same calculation gives a fraction of 51 % of tetrahedral

structures in the model at 5.57 g/cm^3, to be compared with a value of 47 % obtained from the integration of q distribution, and a fraction of 82 % compared to 77 % for the BLYP model at 5.554 g/cm^3. As indicated by these data, the tetrahedricity of the models of a-$In_3Sb_1Te_2$ increases for decreasing density in PBE. In fact, a tetrahedral coordination gives a smaller packing factor with respect to octahedral-like coordination and is thus probably favoured in low density structures. The sharp increase in the tetrahedra content in the BLYP model can not be ascribed just to the denisty, but to a different description of the competition between tetrahedra and octahedra provided by the BLYP functional.
From the positions of the centers of the WFs it is also possible to estimate the fraction of three-fold coordinated In atoms in a planar sp^2 configuration. As discussed before for amorphous InSb, planar sp^2 In atoms do not show an s-like WF centered on the atom, while three-fold coordinated pyramidal In atoms display an s-like WF at very short distances. For the BLYP model at the lower density, by integrating the $g(r)$ between three-fold coordinated In atoms and the WF centers in Figure 3.33b up to the first minimum (0.6 Å), a fraction of 1.3 % of pyramidal three-fold coordinated In atoms was found, while the remaining 4 % of three-fold coordinated In atoms is planar sp^2. In the other two PBE models, all the three-fold coordinated In atoms have a pyramidal shape.
The medium-range order in the three models was studied by computing the rings statistics according to the method presented in Ref. [212]. As shown by the distribution of the ring

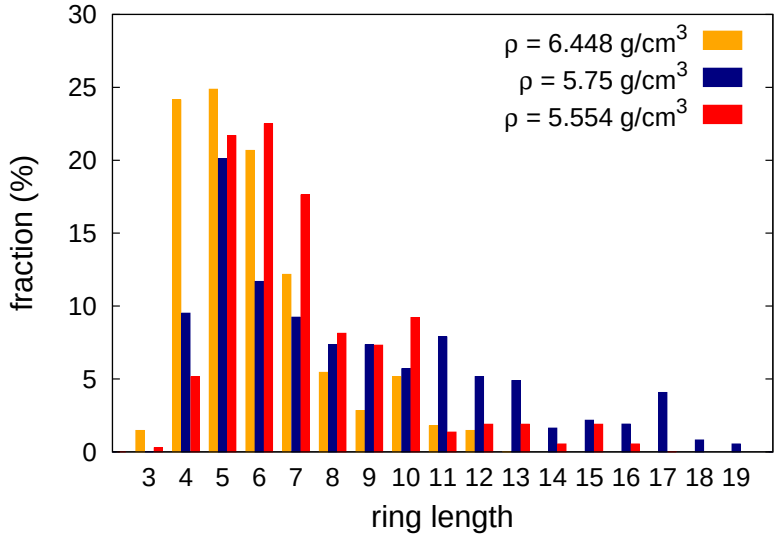

Figure 3.34.: Rings distribution function of a-$In_3Sb_1Te_2$ computed according to Ref. [212] for the three models at different densities. The two denser models were generated with the PBE functional, while the model at lower density was obtained with the BLYP functional.

lengths in Figure 3.34, the denser model present a rather broad distribution with a similar abundance of 4-, 5- and 6-membered rings, while in the model at 5.75 g/cm^3 5-membered rings dominate. The square 4-membered ring, corresponding to *p*-type σ-bonds in defective octahedra (Figure 3.36a), is the building block of the cubic rocksalt phase and is the most abundant ring in GST and GeTe [67, 68, 71, 73]. In these structures the atoms of the cationic sublattice and those of the anionic sublattice alternate forming an ABAB square ring where A and B are the atoms of the two sublattices, respectively. By considering In as atoms of type A and Sb and Te as atoms of type B, it can be seen from the rings analysis in Table 3.8 that the most abundant 4-membered rings are of ABAB type. Five- and six-membered rings are typical of a mostly tetrahedral network and have a higher concentration in the model at 5.75 g/cm^3, more tetrahedral than the denser one. Six-membered rings of type ABABAB are the building

PBE - Rings statistics

4-membered					
InTeInTe InSbInTe InSbInSb	59% (37%) 19% (31%) 1% (—)	135 (13) 44 (11) 2 (—)	ABAB	79% (69%)	181 (24)
InInInTe	13% (8%)	29 (3)	AAAB	13% (9%)	30 (3)
InSbSbTe InSbSbSb InTeSbTe	3% (6%) 1% (6%) — (6%)	7 (2) 3 (2) — (2)	ABBB	4% (17%)	10 (6)
InInSbSb InInSbTe	2% (3%) 1% (—)	4 (1) 2 (—)	AABB	3% (3%)	6 (1)
5-membered					
InInTeInTe InInSbInTe	40% (30%) 14% (14%)	94 (22) 33 (10)	AABAB	54% (43%)	128 (32)
InTeInSbSb InTeInSbTe InSbInSbSb InSbInSbTe	16% (20%) 12% (15%) 3% (7%) 2% (4%)	39 (15) 29 (11) 6 (5) 5 (3)	ABABB	33% (46%)	79 (34)
InInInInTe	6% (3%)	14 (2)	AAAAB	6% (3%)	15 (2)
InSbSbSbTe	1% (1%)	2 (1)	ABBBB	3% (3%)	6 (2)
InInSbSbSb InInSbSbTe	1% (—) 1% (1%)	3 (—) 2 (1)	AABBB	2% (1%)	5 (1)
InInInSbSb InInInSbTe	1% (—) 1% (1%)	2 (—) 2 (1)	AAABB	2% (1%)	4 (1)
SbSbSbSbSb	— (3%)	— (2)	BBBBB	— (3%)	— (2)

6-membered					
InTeInTeInTe InSbInTeInTe InSbInSbInTe	39% (23%) 22% (21%) 0.5% (5%)	76 (10) 43 (9) 1 (2)	ABABAB	61% (49%)	120 (21)
InInInTeInTe InInInSbInTe	25% (2%) — (7%)	29 (1) — (3)	AAABAB	15% (9%)	30 (4)
InInTeInSbSb InInTeInSbTe InInSbInSbTe InInTeInTeSb	6% (7%) 2% 1% (2%) 1% (2%)	11 (3) 4 2 (1) 2 (1)	AABABB	10%	19
InTeInSbSbSb InTeInSbSbTe InTeInTeSbTe	2% (7%) 2% (2%) 1% (2%)	4 (3) 3 (1) 2 (1)	ABABBB	6% (12%)	11 (5)
InInSbInInTe InInTeInInTe	2% (2%) 0.5% (9%)	4 (1) 1 (4)	AABAAB	3% (12%)	6 (5)
InInInInInTe	2% (—)	3 (—)	AAAAAB	2% (—)	3 (—)
InInInInSbTe	1% (—)	2 (—)	AAAABB	2% (—)	3 (—)
InSbSbInSbTe	0.5% (5%)	1 (2)	ABBABB	2% (5%)	3 (2)

Table 3.8.: Abundance of the different types of rings of different size in the 300-atom models of a-$In_3Sb_1Te_2$ at a density of 6.448 g/cm^3 and, in parenthesis, of 5.75 g/cm^3 obtained with the PBE functional. The absolute number of rings is also given in the second column. The type of the rings is indicated by A and B letters where A stands for In and B for Sb or Te. Rings with abundance lower than 1 % have not been considered.

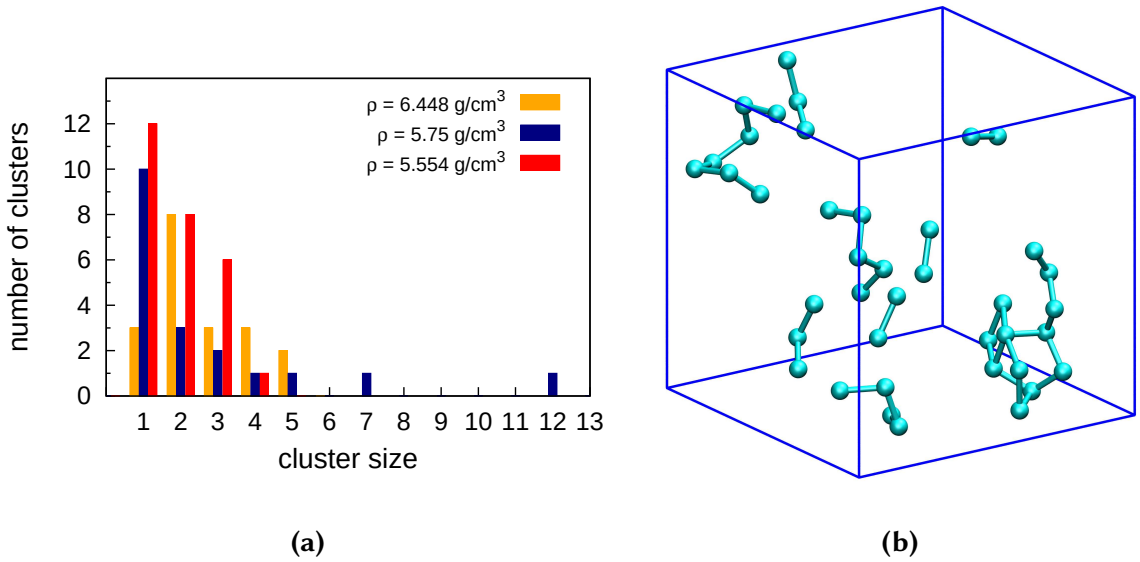

Figure 3.35.: Distribution of the size of Sb clusters (a) computed in the PBE models of a-$In_3Sb_1Te_2$ at two different densities of 6.448 g/cm^3 and 5.75 g/cm^3 and in the BLYP model at the density of 5.554 g/cm^3. (b) Representation of the clusters in the model at 5.75 g/cm^3. A cluster of 12 Sb atoms is present at the lower right corner. Sb atoms are depicted as cyan spheres and a cut-off of 3.20 Å on the Sb-Sb bond distance was used in the calculation.

units of the zincblende crystals. In the model at low density there are fewer rings because of the lower average coordination. A non negligible fraction of rings with a high Sb content as InSbSbSb, InInSbSbSb, InSbSbSbTe, InTeInSbSbSb and SbSbSbSbSb is present, in particular in the model at a density of 5.75 g/cm^3 which shows the highest fraction of Sb-Sb homopolar bonds. An analysis of the Sb structures in the PBE models (Figure 3.35) shows the presence of short chains and small clusters of Sb atoms. In particular, the denser model present a higher fraction of Sb-Sb dimers and small chains with three and four atoms. Groups composed by five Sb atoms are branched chains and cluster with four-membered rings. The model at the density of 5.75 g/cm^3 presents, instead, a cluster of medium dimension composed by twelve Sb atoms which form a four- and a six-membered ring and two five-membered rings. Other Sb groups are chains of seven, five and four Sb atoms, dimers and trimers. Despite the low Sb content (17 %) of the $In_3Sb_1Te_2$ compound, Sb shows a tendency to segregate. The BLYP model at the density of 5.554 g/cm^3 presents instead a high fraction of five-, six- and seven-membered rings with a predominance of rings with six atoms and few 4-membered rings. The most abundant four-membered rings are again of ABAB type (Table 3.9), but in this case the majority of the ABAB rings (10 over 15) does not originate from the combination of octahedral structures, but rather from the presence of edge-sharing tetrahedra of In (Figure 3.36b) as occurs in crystalline InTe [102] and in amorphous $InGeTe_2$ [199] where chains of edge-sharing

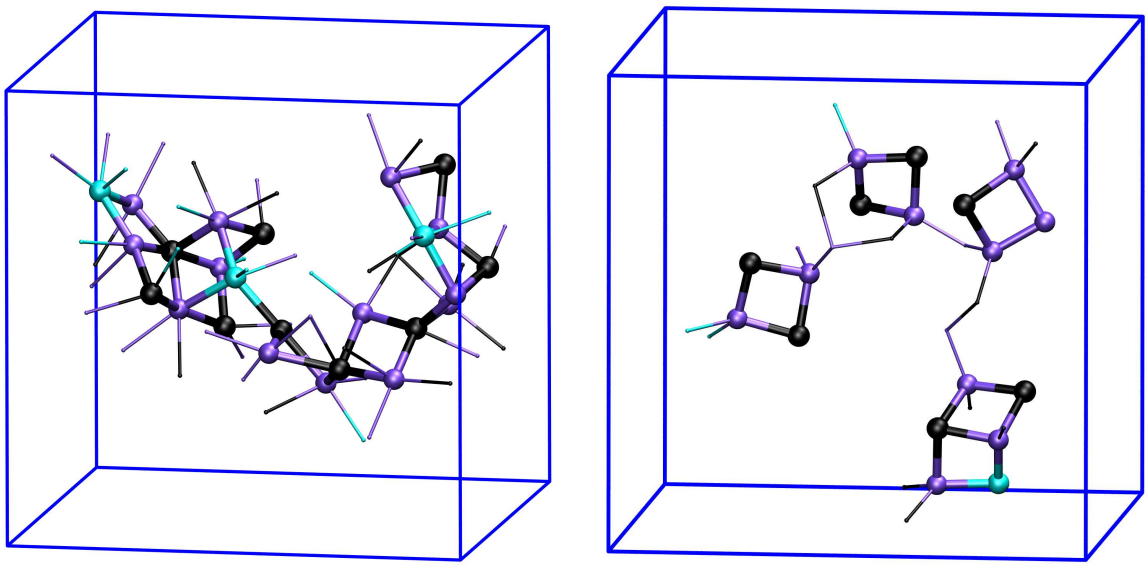

(a) (b)

Figure 3.36.: Representation of some four-membered rings in the models of a-$In_3Sb_1Te_2$ at (a) 6.448 g/cm^3 (PBE) and (b) 5.554 g/cm^3 (BLYP). In the denser model, rings are generated by octahedral-like structures, while in the other case by edge-sharing tetrahedra. In atoms are depicted by violet spheres, Sb by cyan spheres and Te by black spheres. Bonds in the four-membered rings are represented by thicker lines, while other bonds are represented by thin lines.

tetrahedra give rise to four-membered rings with two opposite bond angles smaller than 90° and two greater than 90°. In a-$In_3Sb_1Te_2$ most of the tetrahedra are corner sharing with just a minority fraction of edge-sharing tetrahedra and few or no isolated tetrahedra, as in the model at the lower density. The statistics of the different types of connectivity of the tetrahedral structures is summarized in Table 3.10. Edge-sharing tetrahedra are also corner-sharing. Since the fraction of edge-sharing tetrahedra in the model at high density is actually small, the most abundant four-membered rings are due to *p*-type σ-bonds in defective octahedra. Further discussion and summary on the structural properties and their dependence on the funcional are given at the end of Section 3.2.1.

BLYP - Rings statistics

4-membered

InTeInTe	53%	10	ABAB	79%	15
InSbInTe	26%	5			
InInSbSb	11%	2	AABB	16%	3
InInSbTe	5%	1			
InInInTe	5%	1	AAAB	5%	1

5-membered

InInTeInTe	43%	34	AABAB	59%	47
InInSbInTe	15%	12			
InInSbInSb	1%	1			
InTeInSbSb	16%	13	ABABB	34%	27
InTeInSbTe	8%	6			
InSbInSbSb	6%	5			
InSbInSbTe	4%	3			
InSbSbSbSb	1%	1	ABBBB	3%	2
InSbSbSbTe	1%	1			
InInInSbSb	3%	2	AAABB	3%	2
InInSbSbSb	1%	1	AABBB	1%	1
InInInInTe	1%	1	AAAAB	1%	1

6-membered

InSbInTeInTe	23%	19	ABABAB	46%	38
InTeInTeInTe	16%	13			
InSbInSbInTe	6%	5			
InSbInSbInSb	1%	1			
InInInSbInTe	10%	8	AAABAB	19%	16
InInInTeInTe	8%	7			
InInInSbInSb	1%	1			
InInTeInSbSb	11%	9	AABABB	16%	13
InInSbInTeSb	2%	2			
InInSbInSbSb	1%	1			
InInSbInSbTe	1%	1			
InInTeInInTe	7%	6	AABAAB	10%	8
InInSbInInSb	1%	1			
InInSbInInTe	1%	1			
InTeInSbSbSb	4%	3	ABABBB	6%	5
InTeInSbSbTe	1%	1			
InTeInSbTeSb	1%	1			
InInInInInTe	2%	2	AAAAAB	2%	2
InSbSbInSbSb	1%	1	ABBABB	1%	1

Table 3.9.: Abundance of the different types of rings of different size in the 300-atom model of a-$In_3Sb_1Te_2$ at 5.554 g/cm^3 obtained with the BLYP functional. The absolute number of rings is also given in the second column. The type of the rings is indicated by A and B letters where A stands for In and B for Sb or Te.

tetrahedra statistics

density [g/cm^3]	isolated	corner-sharing	edge-sharing
6.448	11.8% (4)	82.4% (28)	5.9% (2)
5.75	1.4% (1)	67.6% (48)	31.0% (22)
5.554	—	84.3% (91)	15.7% (17)

Table 3.10.: Statistics of the connectivity of the tetrahedral structures for the models of a-$In_3Sb_1Te_2$ at three different densities. The percentage and the number (in parenthesis) of the different types of tetrahedra are given for each model.

Electronic properties

In order to investigate the oxidation state of the different atomic species, we computed the Bader ionic charges from the total charge density by using the scheme of Ref. [213]. To this aim we added to the valence charge density the core charges localized on the atoms. Two types of differently charged In atoms are actually present in crystalline InTe [102]: In1 at the center of $InTe_4$ tetrahedra and weakly bound In2 atoms between neighbouring chains. In1-Te and In2-Te bond lengths are respectively 2.819 Å and 3.576 Å long. In a-$In_3Sb_1Te_2$, as opposed to amorphous $InGeTe_2$ [199], we find very few undercoordinated (one- and two-fold) In atoms in the models at low density that could be associated to the interstitial In2 species of crystalline InTe, but they do not show any peculiar oxidation state. The resulting Bader charges distribution in Figure 3.37 is particularly broad for In atoms due to several types of bonding geometries. It does not show a bimodal shape as opposed to what occurs in $InGeTe_2$ [199] in which isolated In2-like and tetrahedral In1-like atoms with different oxidation states were clearly visible. Note that Sb atoms may have both positive and negative Bader charges. They behave as cations in Sb_2Te_3-like environments and as anions in InSb-like ones. In spite of the amphoteric behaviour of Sb in the amorphous phase, no significant antisite disorder is found experimentally in crystalline $In_3Sb_1Te_2$ [101].
The electronic densities of states were calculated on the relaxed structure of the three models at the DFT-PBE level with the hybrid HSE06 exchange and correlation functional [154] in order to better reproduce the energy gap of the material. The relaxation with the HSE06 functional is computationally too demanding and thus we sticked to the PBE-relaxed structure because the HSE06 functional is closer to the PBE than to the BLYP functional. Concerning the model at the density of 5.554 g/cm^3 obtained with ISA simulations and BLYP functional, the amorphous structure was firstly relaxed with the BLYP functional and then with the PBE functional at zero temperature. The resulting configuration is slightly different from the BLYP geometry with a concentration of tetrahedral In atoms that decreases from 72 % in the BLYP-relaxed structure to 63 % in the PBE-relaxed structure. In fact, as demonstrated before for InSb (Section 3.1), the fraction of tetrahedra in the structure depends on the choice of the exchange-correlation functional. However, although during the PBE relaxation the system tries to reach a configuration more similar to that of the other PBE models, the network remains mainly tetrahedral.
The electronic Density of States (DOS) of a-$In_3Sb_1Te_2$ at the three densities is shown in Figure 3.38 as computed from KS orbitals at the supercell Γ-point. Projection of the DOS on atomic orbitals is also given in Figure 3.38. The structural differences between the models at the three densities result in a sizable change of the electronic band gap which measures only 0.13 eV in the denser model. The other two more tetrahedral models show a wider HOMO-LUMO gap of 0.41 eV at $\rho = 5.75$ g/cm^3 and 0.47 eV in the model at $\rho = 5.554$ g/cm^3. To quantify the localization properties of individual KS states, we computed the Inverse Partic-

ipation Ratio (*IPR*), which is defined for the *i*-th KS state by equation (3.8) The IPR is given in Figure 3.38 a)-f). No strongly localized states deep in the gap nor close to the conduction and valence bands edges are found in the model at high density, while few localized states appear at low density. By considering the four more localized states close to the band gap in the models at low density as ingap states, the resulting HSE band gap between the extended band edges turned out to be 0.77 eV for the model at the density of 5.75 g/cm^3 and 0.75 eV for the model at 5.554 g/cm^3. Snapshots of the localized states close to the band gap in the models at low density are given in Figure 3.39. All these defect states involve homopolar In-In bonds. Kohn-Sham orbitals close to the valence band edge in the model at 5-75 g/cm^3 are localized on undercoordinated or distorted In and Te atoms, while LUMO and LUMO+1 states as well as all the four defect states in the model at 5.554 g/cm^3 are localized on tetrahedral In atoms which form chains of corner-sharing tetrahedra (Figures 3.39c and 3.39g) and four-membered

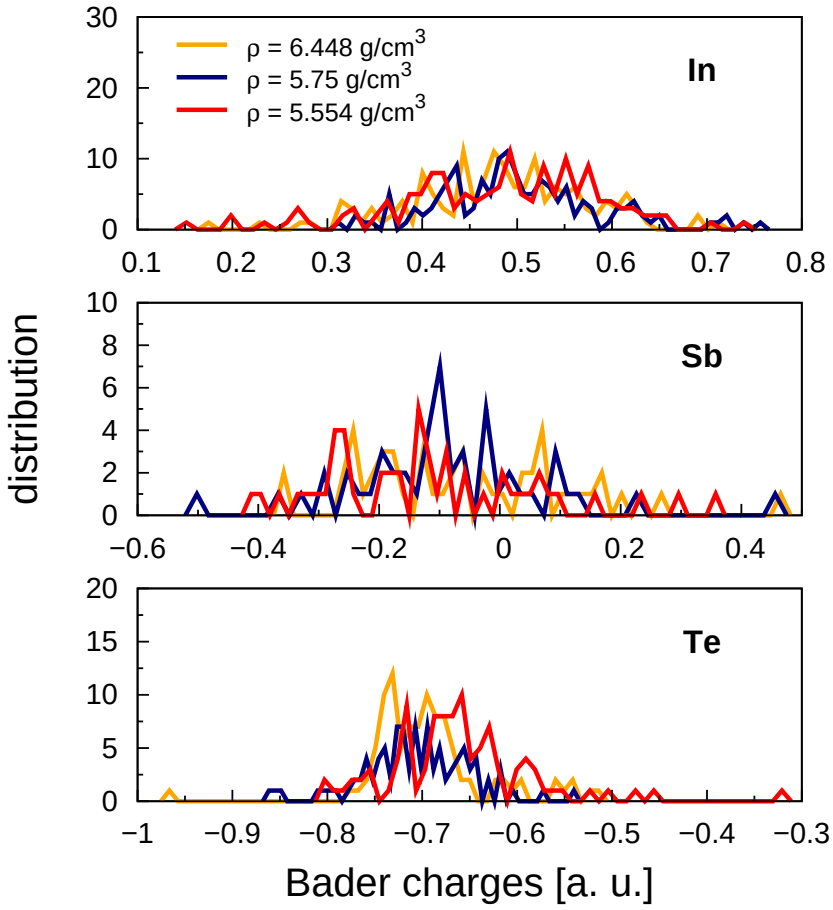

Figure 3.37.: Distribution of the Bader ionic charges (atomic units) of a-$In_3Sb_1Te_2$ for the different species and for the three models at different densities.

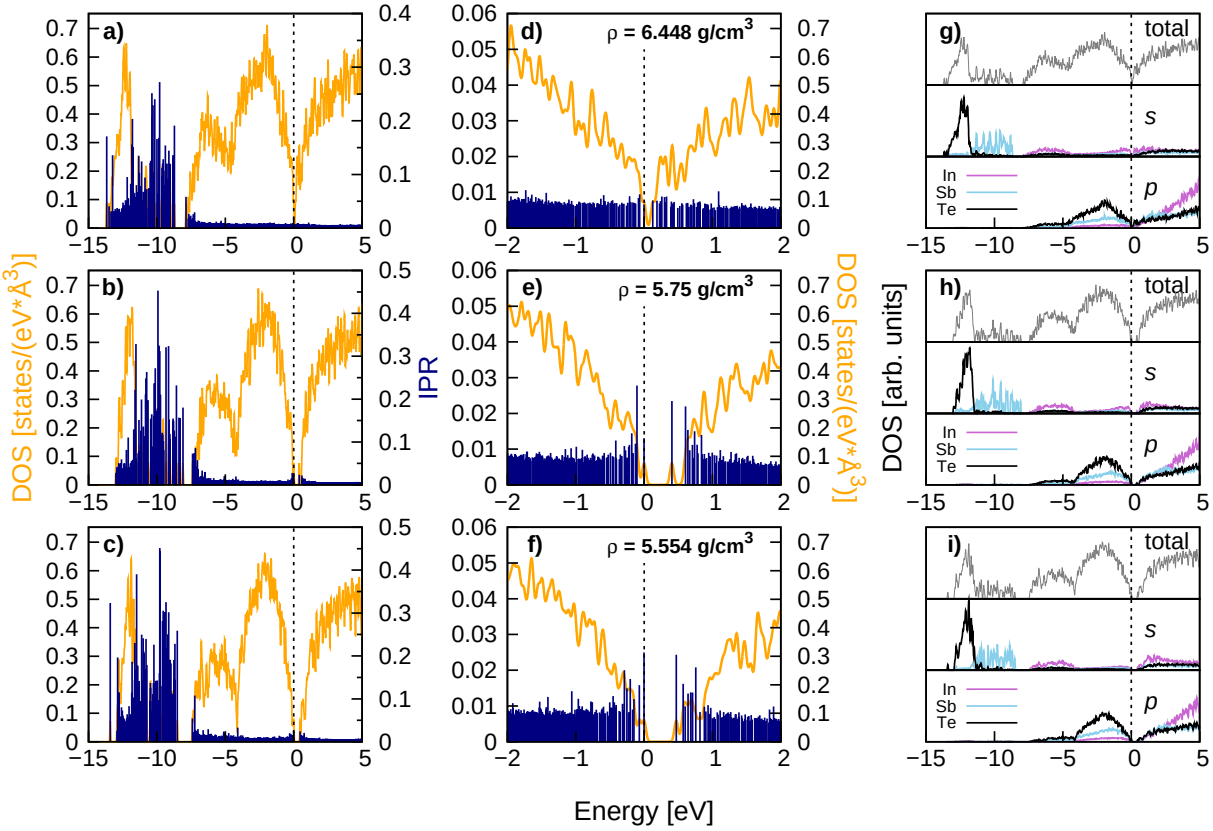

Figure 3.38.: Electronic density of states (HSE hybrid functional [154]) for the models of a-In_3Sb_1Te2 at density of a) 6.448 g/cm^3, b) 5.75 g/cm^3 and c) 5.554 g/cm^3. The KS energies are broadened by Gaussian functions of 27 meV width. The zero of energy corresponds to the top of the valence band. The Inverse Participation Ratio (*IPR*) is given on the right scale (blue spikes, see text for definition). d)-f) A zooming of the DOS of panel a)-c) close to the band gap. g)-i) Projections on atomic *s* and *p* pseudo wavefunctions of the DOS of panels a)-c). The contribution from *d* pseudo wavefunctions is negligible on the scale of the figure and is omitted.

rings (Figures 3.39f and 3.39h). The overall most localized states are *s*-like states of Sb, deep in energy, for all the three models.

To investigate the optical properties of a-$In_3Sb_1Te_2$ we computed the imaginary part of the dielectric function ε_2 in the Random Phase Approximation from KS orbitals with the HSE functional as was already done in the past for GST, GeTe and Sb_2Te_3 [215]. Neglecting local field effects has been proven to be adequate in previous calculations on GeTe [216].

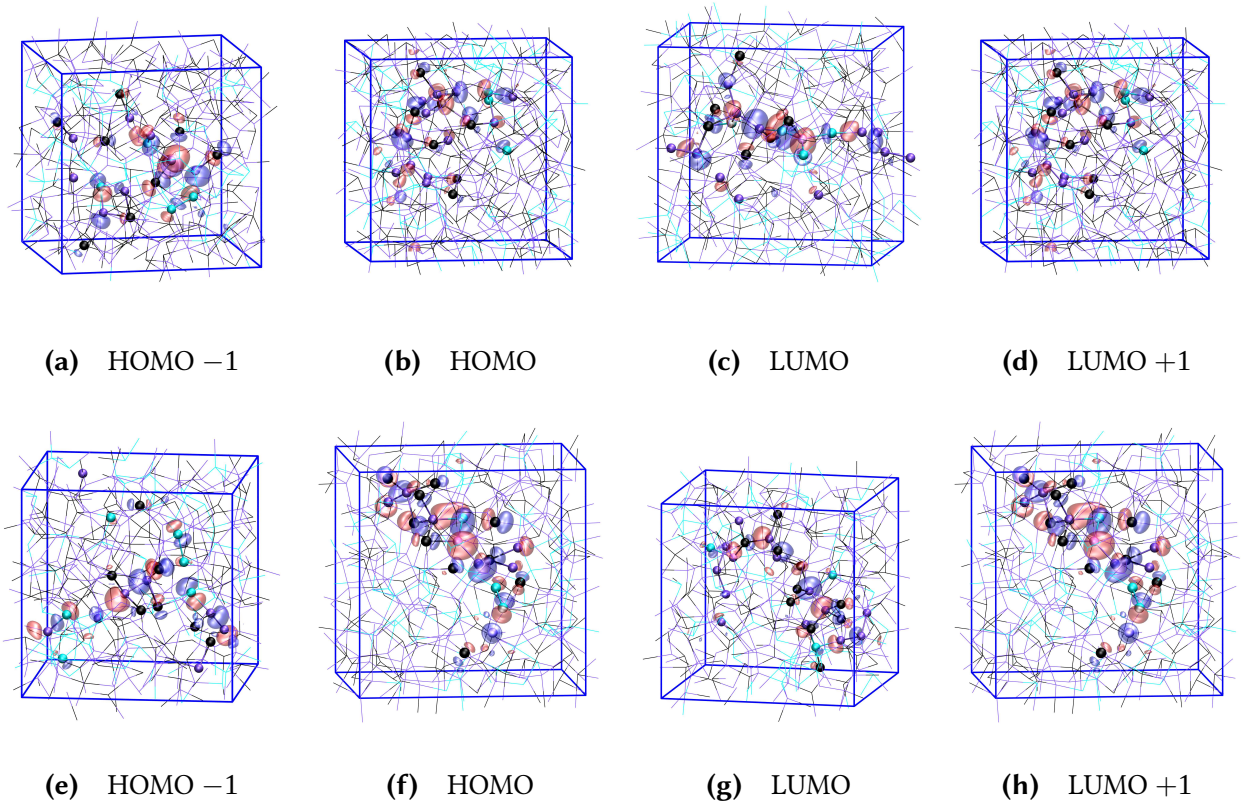

(a) HOMO −1 **(b)** HOMO **(c)** LUMO **(d)** LUMO +1

(e) HOMO −1 **(f)** HOMO **(g)** LUMO **(h)** LUMO +1

Figure 3.39.: Snapshot of the most localized Kohn-Sham states close to the band gap of the two models of a-In_3Sb_1Te2 (a)-(d) at the density of 5.75 g/cm^3 and (e)-(h) at the density of 5.554 g/cm^3. Semitransparent red and blue surfaces render an isovalue of +0.016357 a.u. and −0.016357 a.u., respectively. The whole bonding network is displayed with thin lines. The states are mostly localized on the atoms highlighted with violet, cyan and black spheres for In, Sb and Te, respectively.

The ε_2 function is computed as one third of the trace of the dielectric tensor given by

$$\varepsilon_2(\omega) = \frac{8\pi^2}{3V_0 N_{\mathbf{k}} \omega^2} \sum_{v,c,\mathbf{k}} |\langle c,\mathbf{k}|\mathbf{p}|v,\mathbf{k}\rangle|^2 \delta(\omega - E_{c,\mathbf{k}} + E_{v,\mathbf{k}}) \tag{3.10}$$

where $E_{c,\mathbf{k}}$ and $E_{v,\mathbf{k}}$ refer to the energies of conduction and valence bands at the $N_{\mathbf{k}}$ $\mathbf{k}$-points in the Brillouin zone. We actually restricted the calculation to the Γ-point of the supercell with volume V_0. The δ-functions are substituted by a Gaussian functions with variance of 0.136 eV. Decreasing the variance to 20 meV makes the spectra more noisy but does not change sizably their overall shape and values at maxima of ε_2.

The theoretical ε_2 function of a-$In_3Sb_1Te_2$ is reported in Figure 3.40 for the three models

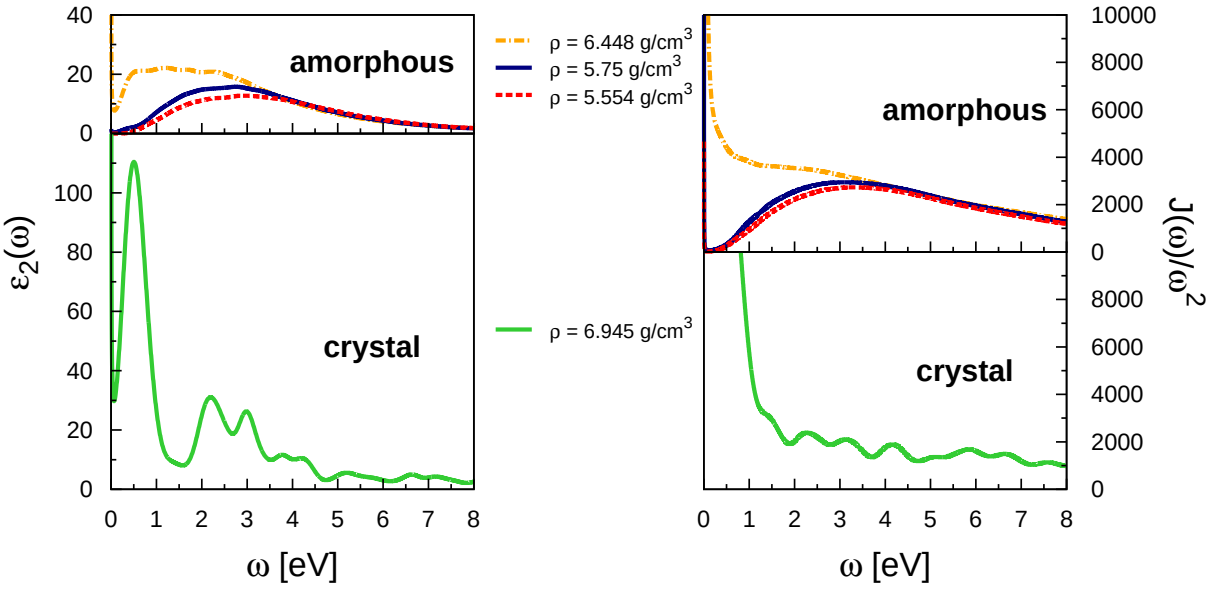

Figure 3.40.: Imaginary part of the dielectric function ε_2 of equation (3.10) in the left panels and of the Joint Density of States (JDOS) $J(\omega)/\omega^2$ of equation (3.11) in the right panels for the three models of a-$In_3Sb_1Te_2$ at different densities and for the ideal cubic crystal.

at different densities. The switch of tetrahedra into defective octahedra upon increasing the density has a large effect on the optical response. This is due both to a change in the electronic density of states and to a change in the optical matrix elements. It is in fact conceivable that the optical matrix elements between bonding and antibonding sp^3-like states in the models at low densities would be different from those involving p-type states of defective octahedra in the model at high density.

To disentangle the role of the matrix elements we computed the Joint Density of States (JDOS) $J(\omega)$ defined by

$$J(\omega) = \frac{1}{V_0} \sum_{c,v} \delta(\omega - E_c + E_v) \tag{3.11}$$

where the sum is over the valence and conduction states at the supercell Γ-point. For the sake of comparison with the ε_2 function, we report in Figure 3.40 the function $J(\omega)/\omega^2$ (see 3.10 and 3.11). The JDOS of the denser model of the amorphous phase and that of the two models at lower density are actually different in the range $0-2$ eV as one could also infer from the DOS in Figure 3.38. The densities of states of the two models at low density are very similar in the whole analysed spectral range. Larger differences arise, instead, in the imaginary part of the dielectric function of the two models at the density of 5.75 g/cm^3 and 5.554 g/cm^3, indicating that a difference in the optical matrix elements between the two models is present in the range 1-3 eV.

In order to study the optical contrast with respect to the crystal of relevance for applications in DVDs, the comparison with the ε_2 and the JDOS of the crystals is also given in Figure 3.40. The crystal has been modeled by a cubic supercell with 216 atoms with In on one sublattice and Sb and Te on the other sublattice. The experimental density was chosen with no vacancies. However, this analysis is, at this stage, problematic since the precise structure of the crystal is not fully resolved. In fact, a concentration of vacancy of about 2 % is needed to reconcile the measured lattice parameter and the picnometric density [98]. Still, it is instructive to compare ε_2 and $J(\omega)/\omega^2$ of the amorphous models with those calculated for the ideal crystal with no vacancies at the experimental lattice parameter ($a = 6.126$ Å) shown in Figure 3.40. A strong optical contrast is present between the crystal and the mostly octahedral-like amorphous model at high density (6.448 g/cm^3) although the bonding geometry is quite similar. The presence of tetrahedra is sufficient to produce a strong optical contrast with the cubic octahedral-like crystal [217], but they are not necessary. In GeSbTe alloys the loss of long range order and the misalignment of p σ-bonds is actually responsible for a reduction the optical matrix elements in the octahedral-like amorphous phase with respect to the cubic crystal [50, 120, 215]. In $In_3Sb_1Te_2$ both a change in the optical matrix elements and a change in the $J(\omega)/\omega^2$ contribute to the optical contrast between the octahedral-like crystal and the octahedral-like amorphous phase.

Vibrational properties

Regarding the vibrational properties of a-$In_3Sb_1Te_2$, we computed the phonon frequencies by diagonalizing the dynamical matrix obtained in turn from the variation of atomic forces due to finite atomic displacements 0.0053 Å large. Only phonons with the periodicity of our supercell (Γ-point phonons) were considered. The phonon density of states is shown in Figure 3.41 for the three a-$In_3Sb_1Te_2$ models at different densities.
In an amorphous material, phonons display localization properties that depend on the frequency. To address this issue, we have computed the inverse participation ratio (*IPR*) of the j-th vibrational mode defined in equation (3.9). Phonons above 140 cm^{-1} are mostly localized on tetrahedra centered on In. We further resolved the projection on tetrahedral In atoms with different environments in the model at the density of 5.554 g/cm^3, where a large fraction of tetrahedra is present. It can be seen that the modes at highest energy (above 180 cm^{-1}) can be assigned to tetrahedral In atoms with homopolar In-In bonds (Figure 3.42). From the projected DOS we also computed the Debye-Waller factor for each species defined by [218]

$$B_\kappa = \frac{8\pi^2}{3}\langle \mathbf{u}_\kappa^2 \rangle \tag{3.12}$$

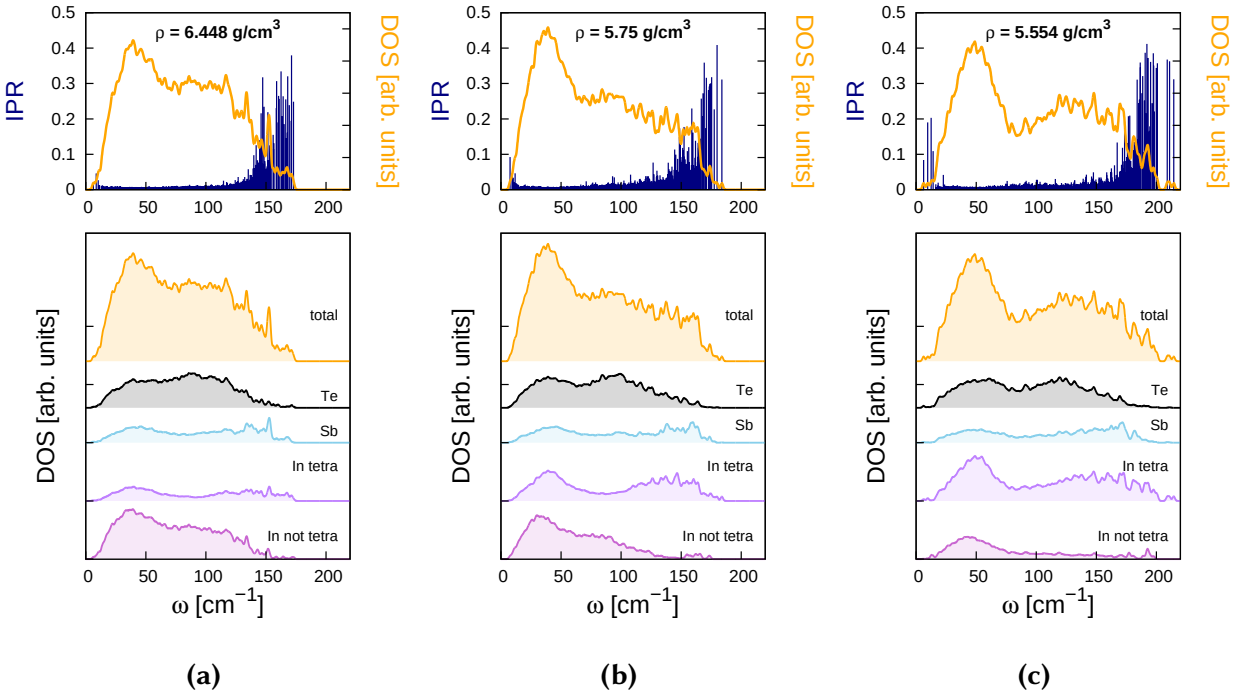

Figure 3.41.: Theoretical phonon DOS of the models of a-$In_3Sb_1Te_2$ at density of (a) 6.448 g/cm^3, (b) 5.75 g/cm^3 and (c) 5.554 g/cm^3. The phonon IPR (green spikes, see text for definition) is superimposed to the DOS in the upper panels. Projections on different species (Sb, Te, tetrahedral In and non tetrahedral In) are reported in the lower panels.

where κ runs over the three species and $\langle \mathbf{u}_\kappa^2 \rangle$ is the mean average square displacement of atoms of species κ computed from harmonic phonons as

$$\langle \mathbf{u}_\kappa^2 \rangle = \sum_{j,m} \frac{\hbar}{\omega_j} \frac{|\mathbf{e}(j,m)|^2}{M_\kappa} \left[n_B(\frac{\hbar\omega_j}{k_B T}) + \frac{1}{2} \right] \tag{3.13}$$

where m runs over atoms of species κ, ω_j and $\mathbf{e}(j,m)$ are frequency and eigenvector of the j-th harmonic phonon. The temperature dependence is introduced by the Bose factor $n_B(\frac{\hbar\omega_j}{k_B T})$. The resulting Debye-Waller factors as a function of temperature are reported in Figure 3.43. The Debye-Waller factor of In is larger than for the other two species as occurs in amorphous $InGeTe_2$ as well [199]. However, in the most tetrahedral model at the density of 5.554 g/cm^3, the average square displacement of In atoms is lower with respect to the other two models. Tetrahedral In atoms are, in fact, characterized by a high energy phononic modes and can move less freely with respect to In atoms in an octahedral configuration.

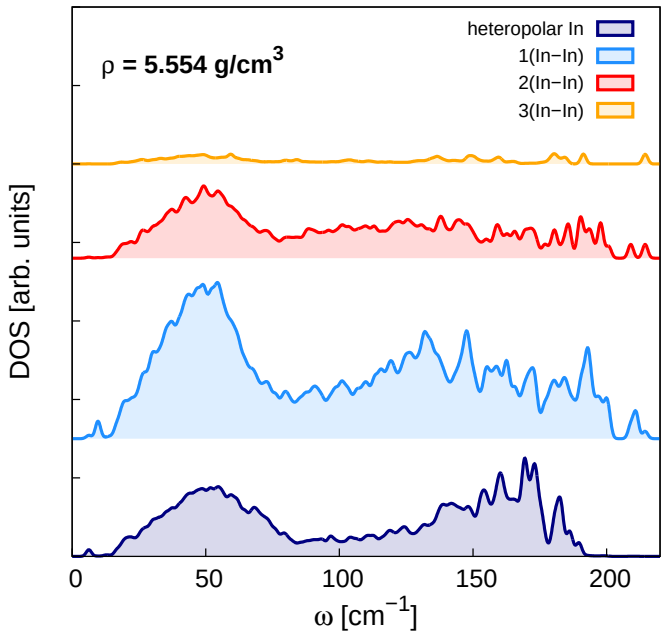

Figure 3.42.: Phononic DOS of a-$In_3Sb_1Te_2$ at the density of 5.554 g/cm^3 projected on tetrahedral In atoms in different environments with no homopolar bonds and with one, two or three homopolar In-In bonds.

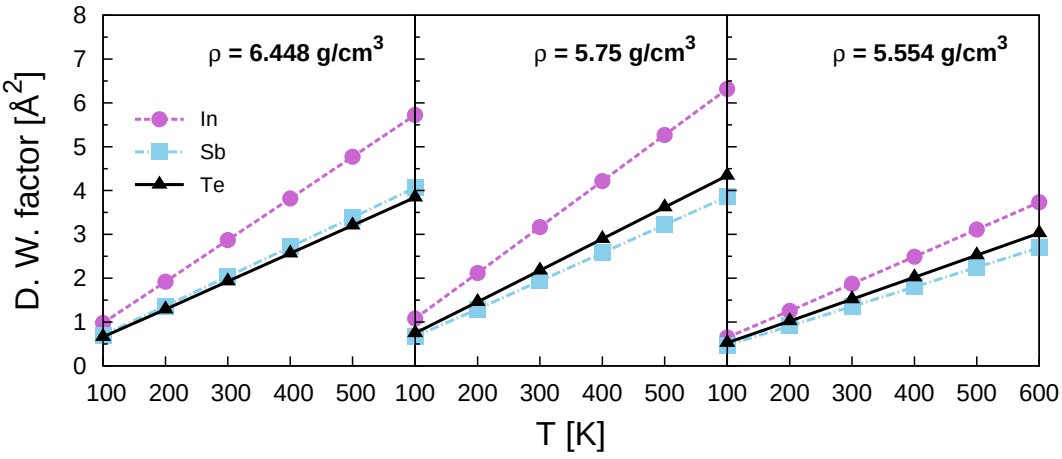

Figure 3.43.: Debye-Waller factor B_κ (see text) of In, Sb and Te atoms as a function of temperature in the models of a-$In_3Sb_1Te_2$ at density of 6.448 g/cm^3, 5.75 g/cm^3 and 5.554 g/cm^3.

Discussion and summary

As already found for the binary InSb system, also for InSbTe a strong dependence of the structural properties on the exchange and correlation functional has been found. The PBE functional leads to prevalently octahedral-like structures, while BLYP functional favours a

tetrahedral geometry for both In and Sb atoms with a lower equilibrium density with respect to PBE, even when van der Waals interactions are included.
In a-InSbTe a strong competition is indeed present between octahedral and tetrahedral structures. In fact, at the $In_3Sb_1Te_2$ composition the system crystallizes in an octahedral rocksalt structure, while the two binary alloys InSb and InTe forming $In_3Sb_1Te_2$ have a tetrahedral bonding geometry. The question that arises is whether the topology of the amorphous network of $In_3Sb_1Te_2$ is more similar to that of the crystalline phase of the ternary compound, as occurs for $Ge_2Sb_2Te_5$ or whether it is closer to the binary systems InTe and InSb the ternary compound is made of.
Note that to compare to experiments, it is better to analyse the structure at the theoretical equilibrium density where the bond lengths are in equilibrium. The models at low density (5.75 g/cm^3 and 5.554 g/cm^3) with large fraction of tetrahedral-like sites are therefore probably more similar to the real experimental system at equilibrium. Moreover, since previous analysis on the binary alloy showed that BLYP functional better describes the structure of amorphous InSb with respect to PBE functional, the mostly tetrahedral model at the density of 5.554 g/cm^3 is probably closer to the real structure.
Still the analysis of the model at high density is important because in the PCM devices the amorphous is not free to relax to its equilibrium density but experience instead a compressive stress because of the embedding within the denser crystalline matrix. Therefore, we can not exclude that the octahedral-like model at 6.448 g/cm^3 might be instead closer to the structure of the melt-quenched $In_3Sb_1Te_2$ phase formed during the reset process in PCM. The larger fraction of tetrahedra have fingerprints in the optical response and in the vibrational spectra as discussed in previous sections. In particular, since the bond lengths in tetrahedra are shorter than the bond lengths in defective octahedra, phonons localized on tetrahedra have frequencies in the higher region of the vibrational spectrum which thus acquires a larger weight in the model at low density.
A link between the structure of the amorphous phase and the easy of the phase transformation, either the crystallization of the amorphous [67] or the amorphization of the crystal [197, 219], has been proposed in previous theoretical works on $Ge_2Sb_2Te_5$. The fast crystallization of the amorphous phase has been ascribed to the predominance of four-membered ABAB rings in both the amorphous and the crystalline phases [67]. On the contrary the presence of tetrahedra, absent in the crystal, is supposed to hinder the crystallization [200]. These features would surely have an impact on the crystallization at low temperatures, below the glass transition, of relevance for data retention. Therefore one might suggest that data retention in a-$In_3Sb_1Te_2$ would be better for the model at low density which features a larger content of tetrahedra and of five-membered rings, both absent in the crystal. On the other hand, the compressive stress experienced by the amorphous region in PCM would reduce data retention by bringing the system closer to our model at high density with a larger content of octahedra and the four-membered rings. Regarding the crystallization in set operation PCM, we remark

that the amorphous is brought to high temperatures just below the melting point [18]. The amorphous region thus turns into a supercooled liquid whose crystallization properties are mostly controlled by the atomic mobility as discussed in other works on the GeSbTe system [79, 80]. Therefore, it is not clear how the density would impact on the crystallization speed at high temperature where the structure of the supercooled liquid is of relevance.

3.2.2. $In_{13}Sb_{11}Te_3$

Films of InSbTe ternary alloys with low Te content have been grown experimentally by MOCVD. In particular, the compositions $In_3Sb_{2.7}Te_{0.8}$ and $In_3Sb_{2.5}Te_{1.1}$ have been investigated by measuring electrical and thermal conductivity [9] and by realizing PCM cells which show good switching properties [9]. However, experimental data on the structure of the amorphous phase are not available yet. To gain insights on the structure of these alloys, we performed simulations of the $In_{13}Sb_{11}Te_3$ ($In_3Sb_{2.5}Te_{0.7}$) composition which is close to the experimental ones, by generating a model of the amorphous phase with the inverse simulation annealing method (ISA). Since no experimental data on the density are available, we used the ISA method at constant pressure to generate a model at the theoretical equilibrium density. The ISA method was used with no constraints on the experimental data. The $In_{13}Sb_{11}Te_3$ alloy can be thought as a pseudo-binary compound formed by the two binary systems InSb and In_2Te_3 in the ratio $(InSb)_{11}(In_2Te_3)_1$. Since it is almost entirely constituted by InSb with only a small percentage of In_2Te_3, we expect that the amorphous structure of the ternary compound should be close to that of a-InSb. As discussed before, crystalline InSb has a zincblende structure and a-InSb shows as well a mainly tetrahedral network. In_2Te_3, instead, has two crystalline phases. The high temperature phase is stable above 523 K and it corresponds to a defect zincblende structure with $F\bar{4}3m$ space group [220] where two thirds of the tetrahedral sites of the cationic sublattice are randomly occupied by In atoms. The low temperature phase has a defective anti-fluorite structure and space group $F\bar{4}3m$ [221] where only one third of the cationic tetrahedral sites are occupied by In atoms.
Measurements on thin films of $In_3Sb_{2.7}Te_{0.8}$ and $In_3Sb_{2.5}Te_{1.1}$ [9] have shown that a polycrystalline face centered cubic *fcc* phase with composition $InSb_{0.8}Te_{0.2}$ can be obtained by heating above 260 °C, while by annealing at about 500 °C the formation of the stoichiometric crystalline phase $In_3Sb_1Te_2$ with rocksalt structure occurs.

Computational details

To characterize the structure of amorphous $In_{13}Sb_{11}Te_3$, a 324-atom model was generated by quenching from the liquid phase from 1000 K to 300 K in 8000 MC steps and from 300 K to 5 K in 1000 MC steps. Simulations were performed with the ISA method at constant pressure to reach the equilibrium density at near zero temperature. Van der Waals interactions in the scheme of Grimme [202] were included (Figure 3.44). Energies and forces during the quenching have been calculated from first principles with the CP2K code by using BLYP functional. A triple-zeta-valence plus polarization (TZVP) basis set was used to expand the Kohn-Sham orbitals while the electronic density was expanded on plane-waves with a cut-off of 100 Ry. The resulting amorphous structure at the BLYP theoretical equilibrium density of 0.0283 atoms/Å^3 (5.60 g/cm^3) was then equilibrated for 12 ps at 300 K.

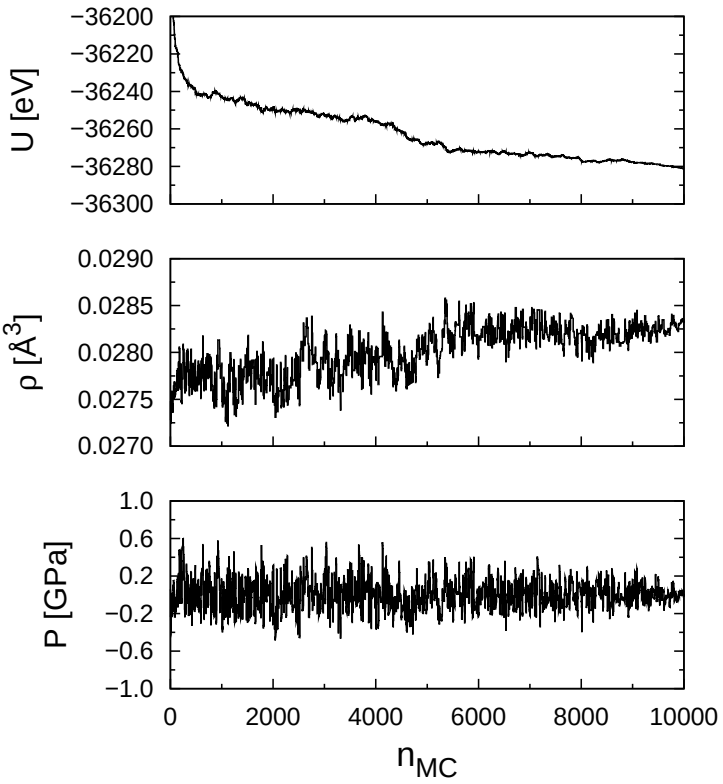

Figure 3.44.: Evolution of the potential energy U, density ρ and pressure P during the ISA quenching of a model of amorphous $In_{13}Sb_{11}Te_3$ at constant pressure with the BLYP functional. The quenching "time" is expressed by the number of Monte-Carlo steps n_{MC}.

Structural properties

The total and partial pair correlation functions shown in Figure 3.45a were obtained by averaging over a 10 ps long trajectory at 300 K. As already found for InSb, there are many homopolar In-In and Sb-Sb bonds while, as in a-$In_3Sb_1Te_2$, very few Sb-Te bonds are present. The partial average coordination numbers and the percentage of the different bond types are listed in Table 3.11a and 3.11b. As for a-$In_3Sb_1Te_2$, the a-$In_{13}Sb_{11}Te_3$ alloy appears as a solid solution of InSb and InTe with a predominance of InSb due to the low Te concentration. The coordination numbers distributions in Figure 3.45b show that both In and Sb atoms are mainly four-fold coordinated, consistently with a mainly tetrahedral network, while the majority of Te atoms is three-fold coordinated. This is confirmed by the bond angles distributions (Figure 3.46a) which are peaked at about 110° for In and Sb atoms. The $P(\theta)$ function of Te, instead, is broader and typical of pyramidal environments. By resolving the distributions with respect to the coordination number (Figure 3.46b), it can be noticed that four-fold coordinated Sb atoms

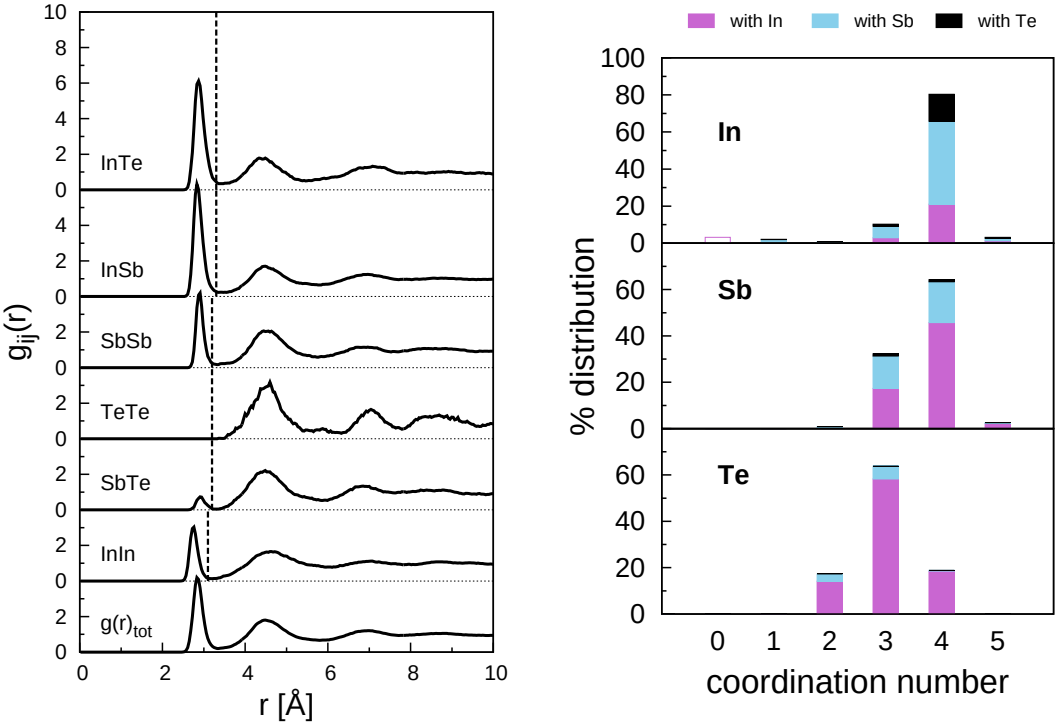

(a) (b)

Figure 3.45.: (a) Total and partial pair correlation functions of a-$In_{13}Sb_{11}Te_3$. The vertical lines are the cut-off radii used to define the coordination numbers (3.10 Å, 3.30 Å, 3.30 Å, 3.20 Å, 3.20 Å and 3.20 Å for the In-In, In-Sb, In-Te, Sb-Te, Sb-Sb and Te-Te bonds, respectively). (b) Distributions of the coordination numbers. The contribution from the different atom pairs are represented with different colours.

Average coordination numbers

	with In	with Sb	with Te	total
In	1.00	2.08	0.64	3.72
Sb	2.46	1.16	0.07	3.69
Te	2.77	0.24	0.00	3.01

(a)

Types of bonds (%)

	with In	with Sb	with Te
In	13.2	55.3	17.0
Sb		13.0	1.5
Te			0.0

(b)

Table 3.11.: (a) Partial average coordination numbers and (b) percentage of the different types of bonds in a-$In_{13}Sb_{11}Te_3$ calculated by using the cut-off distances given in Figure 3.45a.

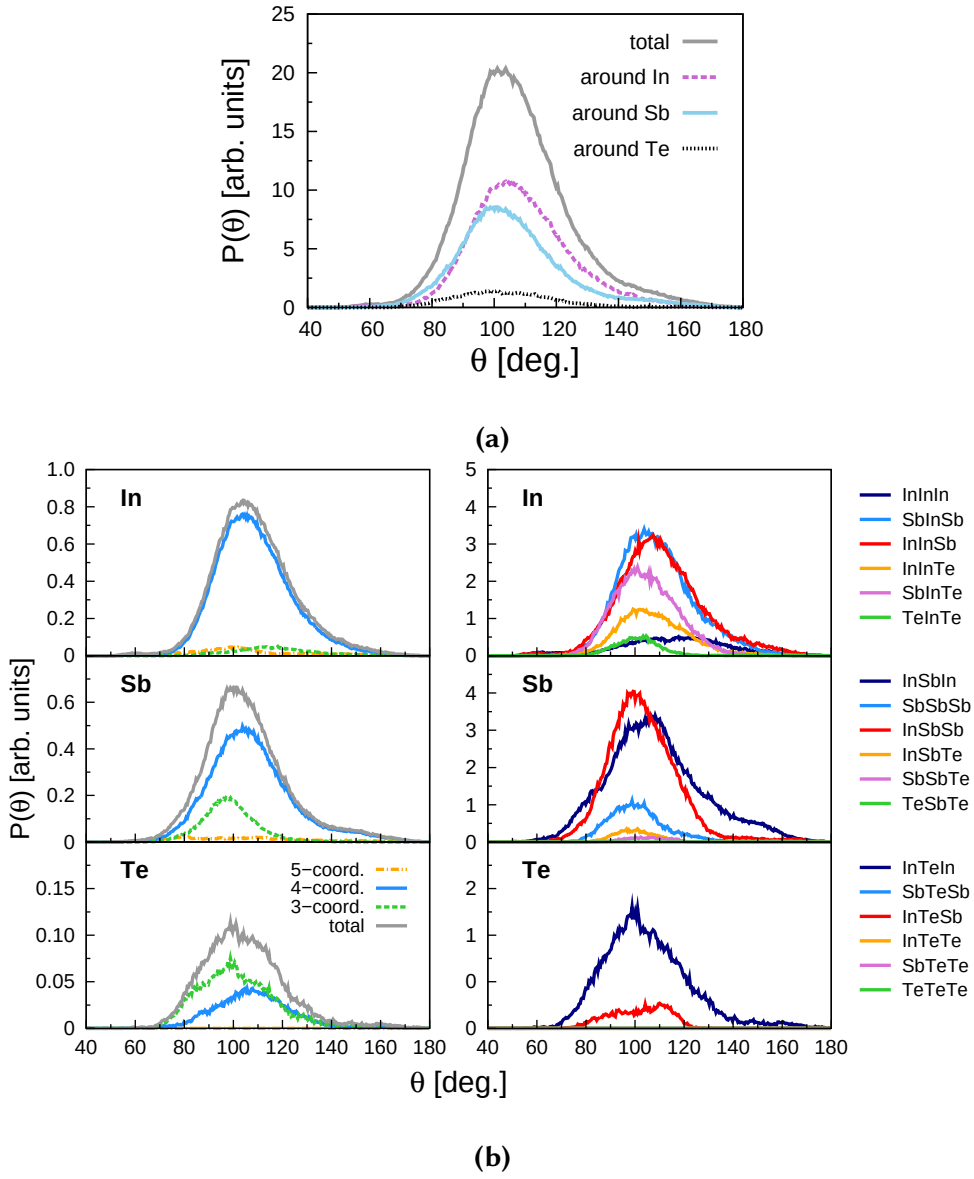

Figure 3.46.: (a) Total distribution of the bond angles in amorphous $In_{13}Sb_{11}Te_3$ and distributions resolved for different atomic species and (b) bond angles distributions resolved for coordination number (left panels) and for different triplets (right panels).

form bond angles of about 110° typical of tetrahedra, while the bond angles distribution for three-fold coordinated Sb atoms is peaked at $\sim 95°$, indicating the presence of pyramidal structures. The presence of this two types of environments for Sb might arise from the high fraction of homopolar Sb-Sb bonds in three-fold coordinated Sb atoms. In fact, about 40 % of the bonds formed by three-fold coordinated Sb is a homopolar bond and the local geometry of Sb is similar to that of elemental Sb, which presents a "3+3" coordination with bond angles at

90°. Thus Sb-Sb bonds favour octahedral-like environments for Sb, while Sb-In bonds favour the tetrahedral geometry.
Table 3.12 reports the statistics of the different types of local environments. Three-fold coordinated Sb presents a high fraction of homopolar bonds with a small percentage of $Sb\text{-}Sb_3$ structures containing only antimony. The majority of the local environments of In contains homopolar In-In bonds but, as it will be discussed later, this does not affect the bonding geometry for In. Both the type and the abundance of Te environments are very close to those of a-$In_3Sb_1Te_2$.
In order to quantify the fraction of tetrahedral structures, the q order parameter defined by equation (3.7) was computed. Figure 3.47 shows the q-distributions resolved for different

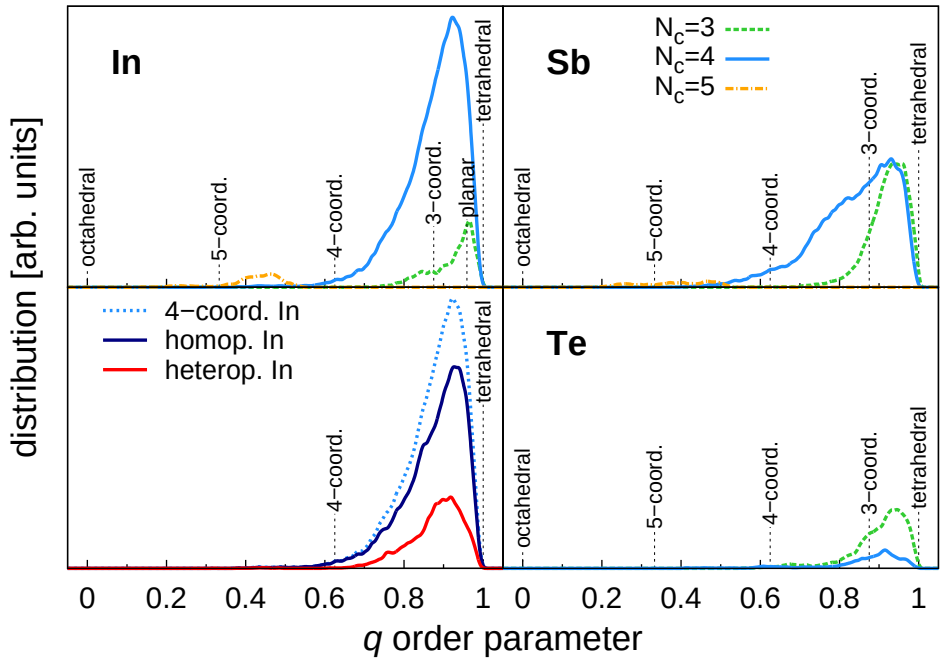

Figure 3.47.: Distribution of the local order parameter q for tetrahedricity (see text) for the model of amorphous $In_{13}Sb_{11}Te_3$. The distributions for In, Sb and Te atomic species are resolved for different coordination numbers. Vertical lines indicate the values of q for selected ideal geometries. The distribution for four-fold coordinated In atoms is further resolved for atoms with and without In-In homopolar bonds (lower left panel).

atomic species and coordination numbers. By integrating the distribution of four-fold coordinated In and Sb atoms in the range $0.8 - 1.0$ as already discussed for amorphous $In_3Sb_1Te_2$, a fraction of 68 % (106 atoms among 156) of In atoms and of 44 % (58 atoms among 132) of Sb atoms in tetrahedral environments was found. A fraction of 14 % (15 atoms among 106) of tetrahedral In atoms are in edge-sharing tetrahedra and among them, three tetrahedra shares two edges with other tetrahedral In atoms. The remaining tetrahedra with a central In atom

	Local environments				
	1	**2**	**3**	**4**	**5**
In:			8.3%	82.7%	3.2%
	Sb: 1.3%	—	$InSb_2$: 3.2% Sb_3: 1.9% InSbTe: 1.3%	$InSb_2Te$: 17.9% $InSb_3$: 16.7% Sb_3Te: 9.6% In_2Sb_2: 9.0% Sb_4: 7.1% $InSbTe_2$: 6.4% In_2SbTe: 5.1% Sb_2Te_2: 4.5% In_3Sb: 3.2% $InTe_3$: 1.3% In_2Te_2: 1.3%	
Sb:		—	31.8%	65.9%	1.5%
			In_2Sb: 12.1% $InSb_2$: 9.1% Sb_3: 3.8% In_3: 3.8% In_2Te: 2.3%	In_3Sb: 30.3% In_4: 16.7% In_2Sb_2: 10.6% $InSb_3$: 4.5% In_2SbTe: 3.0%	In_5: 1.5%
Te:		13.8%	61.1%	25.0%	—
		In_2: 8.3% InSb: 5.6%	In_3: 41.7% In_2Sb: 19.4%	In_4: 25.0%	

Table 3.12.: Statistics of In, Sb and Te coordination environments for atoms with different coordination numbers given in the first line for the a-$In_{13}Sb_{11}Te_3$ model generated with ISA simulations and BLYP functional The data were obtained for the relaxed configuration at the BLYP-DFT level and only environments in a fraction larger than 1 % are reported.

are corner-sharing. By further resolving the q-distribution for four-fold coordinated In atoms with and without homopolar In-In bonds (Figure 3.47) it can be seen that, as opposed to a-$In_3Sb_1Te_2$, the presence of homopolar bonds has no effect on the position of the peak of the q-distribution and hence it does not cause a change in the bonding geometry. A similar situation was found for a-InSb. Three-fold coordinated In atoms are in a pyramidal geometry or in a planar configuration with an sp^2 hybridization.
The concentration of tetrahedral structures in the amorphous phase can be obtained also from the integration of the pair correlation functions of four-fold coordinated atoms with the centers of the WFs (Figure 3.48) as discussed before. Similarly, the fraction of planar sp^2 indium

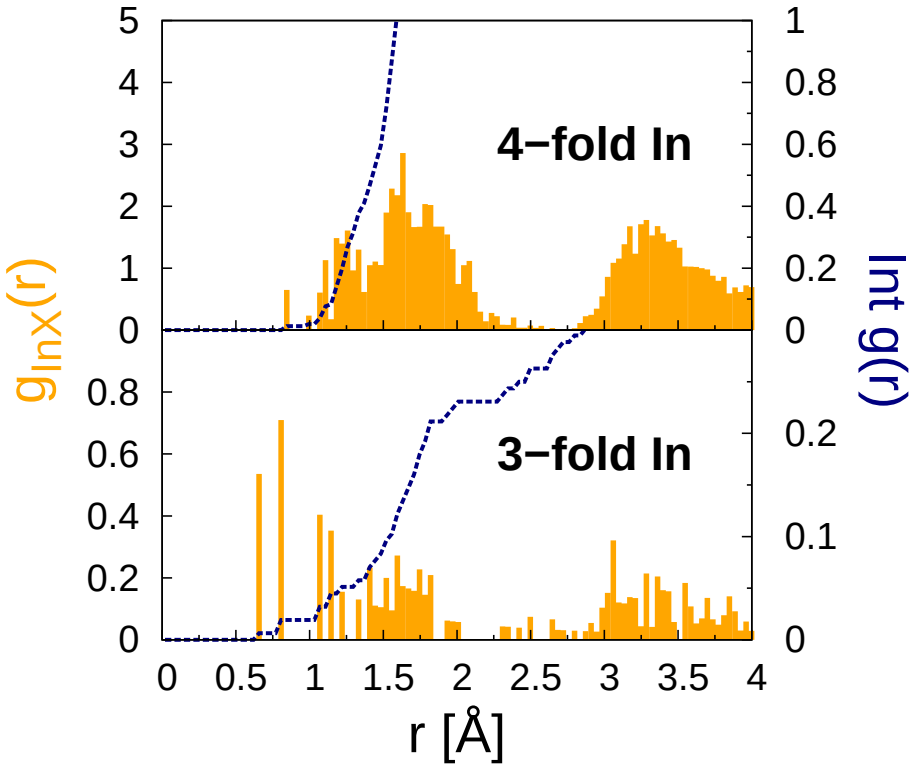

Figure 3.48.: Pair correlation functions $g(r)$ of three-fold (lower panel) and four-fold coordinated In atoms with the centers of the Wannier functions in a-$In_{13}Sb_{11}Te_3$. The dashed line is the running integral of $4\pi r^2 g(r)\rho$ where ρ is the density of the Wannier centers (right scale).

atoms can be calculated by integrating the pair correlation functions of three-fold coordinated atoms with the WFs centers (Figure 3.48). By integrating the PCF up to the first minimum (0.8 Å, see Figure 3.48), we obtained a fraction of 1.3 % of four-fold coordinated In atoms in defective octahedral-like environments which results in a concentration of 71 % of tetrahedral indium atoms, in good agreement with the estimate obtained from the q parameter. Regarding three-fold coordinated In atoms, the integration of the PCF from 0 to 0.85 Å (first minimum

position) gives a fraction of pyramidal In atoms of 2 % and the concentration of planar sp^2 In atoms is 6.4 %.
Concerning the medium-range order, the distribution of the rings lengths reported in Figure 3.49 shows a predominance of five- and six-membered rings which are typical of tetrahedral networks. Four-membered rings are mainly of type ABAB, where A is In and B in Sb or Te (Table 3.13) and present a couple of opposite bond angles smaller than 90° and a couple of bond angles greater than 90° since originate from edge-sharing tetrahedral structures as found in a-$In_3Sb_1Te_2$ and in a-InSb. The majority of the five-membered rings (54 %)

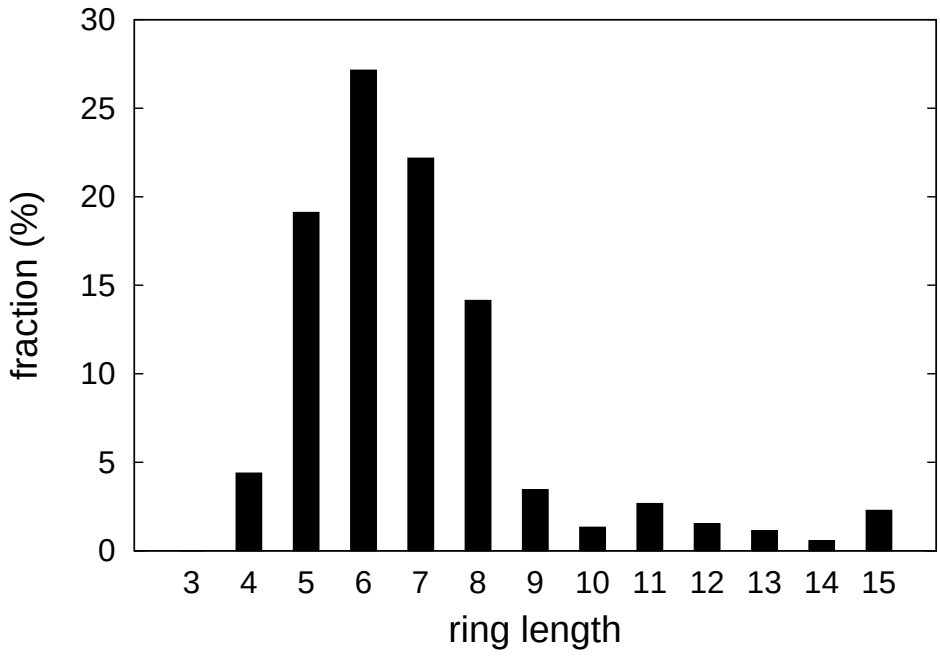

Figure 3.49.: Distribution of the ring lengths in a-$In_{13}Sb_{11}Te_3$ computed according to Ref. [212].

presents In-In homopolar bonds, while the most abundant type of six-membered rings is the AABABB sequence showing again In-In couples. The 26 % of six-membered rings is, instead, of type ABABAB as can be found in the zincblende phase of InSb. Very similar percentages of AABABB and ABABAB rings were found in a-InSb confirming that a-$In_{13}Sb_{11}Te_3$ can be seen essentially as a-InSb with a small amount of Te. Rings with a high concentration of Sb-Sb bonds are also present, in particular the model shows InSbSbSb, SbSbSbSb, InSbSbSbSb, InSbSbSbTe, InInSbSbSb, InInSbSbSbSb and InSbSbSbSbSb rings. The distribution of the dimensions of Sb clusters, Sb chains and branched chains in Figure 3.50 shows the presence of a 15-atom and of a 17-atom cluster. The first one is a branched chain with a four-membered rings while the second is a branched chain.

BLYP - Rings statistics

4-membered

InSbInSb	35%	8	ABAB	65%	15
InSbInTe	26%	6			
InTeInTe	4%	1			
InInInSb	13%	3	AAAB	17%	4
InInInTe	4%	1			
InSbSbSb	13%	3	ABBB	13%	3
SbSbSbSb	4%	1	BBBB	4%	1

5-membered

InInSbInSb	19%	19	AABAB	45%	45
InInSbInTe	19%	19			
InInTeInTe	7%	7			
InSbInSbSb	23%	23	ABABB	39%	39
InTeInSbSb	12%	12			
InSbInSbTe	2%	2			
InTeInSbTe	2%	2			
InSbSbSbSb	5%	5	ABBBB	7%	7
InSbSbSbTe	2%	2			
InInInInSb	5%	5	AAAAB	5%	5
InInInSbSb	2%	2	AAABB	2%	2
InInSbSbSb	1%	1	AABBB	2%	2
InInSbSbTe	1%	1			

6-membered

InInSbInSbSb	18%	25	AABABB	31%	44
InInTeInSbSb	8%	11			
InInSbInSbTe	4%	5			
InInSbInTeSb	1%	2			
InInTeInTeSb	1%	1			
InSbInSbInSb	15%	21	ABABAB	26%	37
InSbInSbInTe	9%	13			
InSbInTeInTe	2%	3			
InInInSbInSb	8%	12	AAABAB	16%	23
InInInSbInTe	6%	9			
InInInTeInTe	1%	2			
InInSbInInSb	6%	9	AABAAB	8%	11
InInTeInInTe	1%	2			
InSbInSbSbSb	5%	7	ABABBB	7%	10
InTeInSbSbSb	1%	2			
InSbInSbSbTe	1%	1			
InSbSbInSbSb	5%	7	ABBABB	6%	9
InSbSbInSbTe	1%	2			
InInSbSbSbSb	2%	3	AABBBB	3%	4
InInSbSbSbTe	1%	1			
InInInSbSbSb	1%	2	AAABBB	1%	2
InInInInSbSb	1%	1	AAAABB	1%	1
InSbSbSbSbSb	1%	1	ABBBBB	1%	1

Table 3.13.: Abundance of the different types of rings of different size in the 324-atom model of a-$In_{13}Sb_{11}Te_3$ The absolute number of rings is also given in the second column. The type of the rings is indicating by A and B letters where A stands for In and B for Sb or Te.

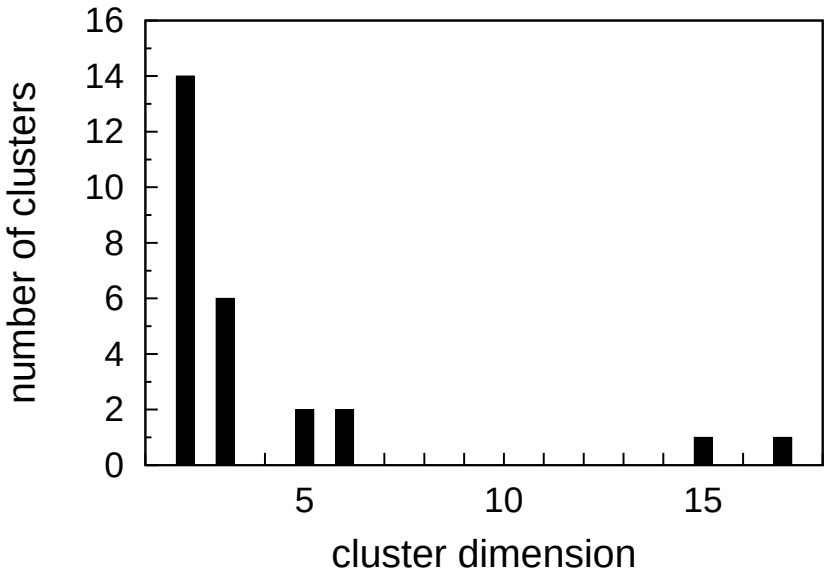

Figure 3.50.: Distribution of dimensions of the Sb clusters in the model of a-$In_{13}Sb_{11}Te_3$. Linear and branched chains are also included.

Electronic properties

The electronic properties of a-$In_{13}Sb_{11}Te_3$ were calculated with the HSE06 hybrid exchange and correlation functional [154] on the structure relaxed with the PBE functional. Figure 3.51 reports the electronic DOS and the IPR value for each electronic state defined by equation (3.8). The model has a small gap of about 0.32 eV and shows few more localized states at

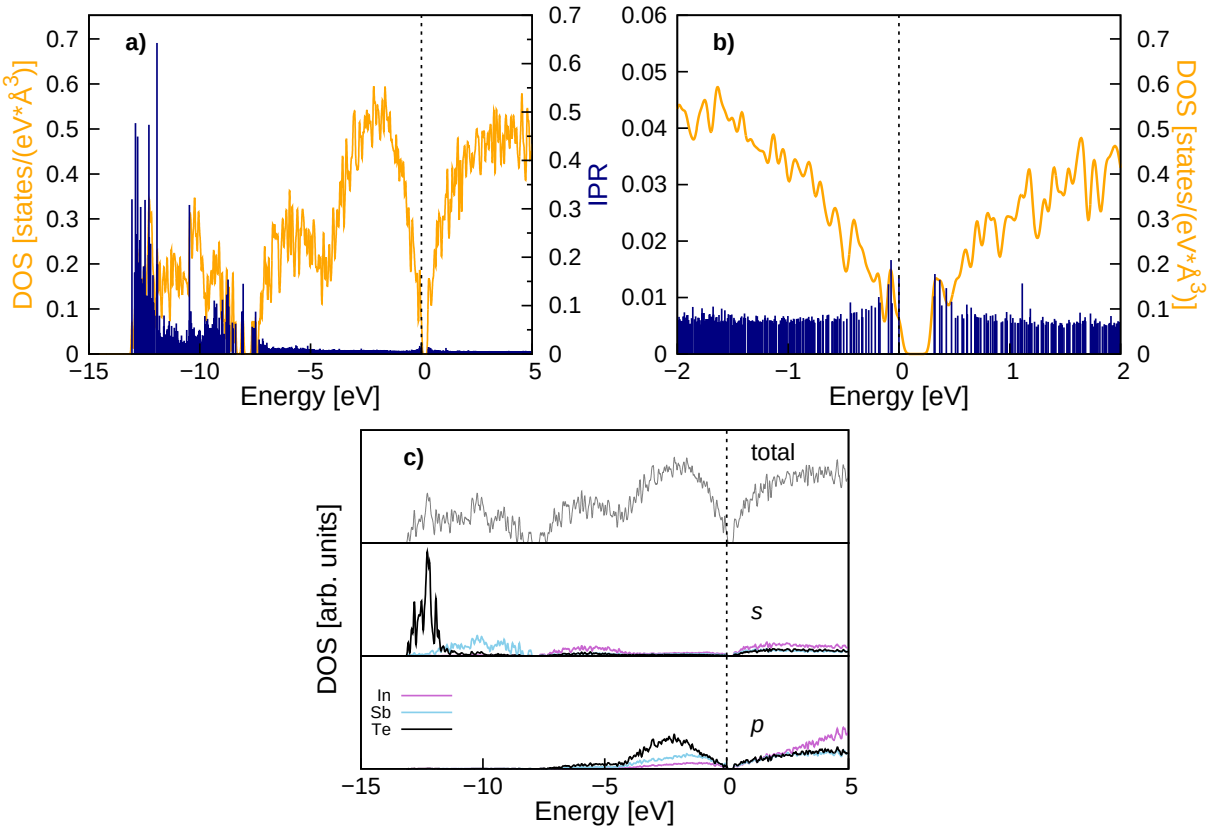

Figure 3.51.: a)Electronic density of states (HSE hybrid functional [154]) of a-$In_{13}Sb_{11}Te_3$ with KS energies broadened by Gaussian functions of 27 meV width. The zero of energy corresponds to the top of the valence band. The Inverse Participation Ratio (*IPR*) is also given (blue spikes, see text for definition). b) A zooming of the DOS of panel a) close to the band gap. c) Projections on atomic *s* and *p* pseudo wavefunctions of the DOS of panel a). The contribution from *d* pseudo wavefunctions is negligible on the scale of the figure and it is omitted.

the edge of the valence and conduction bands. States close to the valence edge are mainly localized on Sb atoms with homopolar bonds, while states at the conduction band edge are formed by three-fold coordinated In and Sb atoms. By considering the localized states at band edges with IPR value greater than 0.012 as defect states, the band gap turns out to be about 0.56 eV. From the projection of the total DOS on different atomic species resolved for different

channels of angular momentum (Figure 3.51), the very localized deep states can be ascribed to *s*-type orbitals of Te while the contribution to the DOS at the band edges is almost the same for all the three atomic species.

Vibrational properties

The phonon DOS was computed from the diagonalization of the dynamical matrix obtained in turn from the variation of atomic forces due to finite atomic displacements 0.0053 Å large. Only phonons with the periodicity of our supercell (Γ-point phonons) were considered. The phonon DOS of a-$In_{13}Sb_{11}Te_3$ is reported in Figure 3.52a together with the phonon Inverse Participation Ratio defined by equation (3.9) which gives a measure of the localization of each phonon.

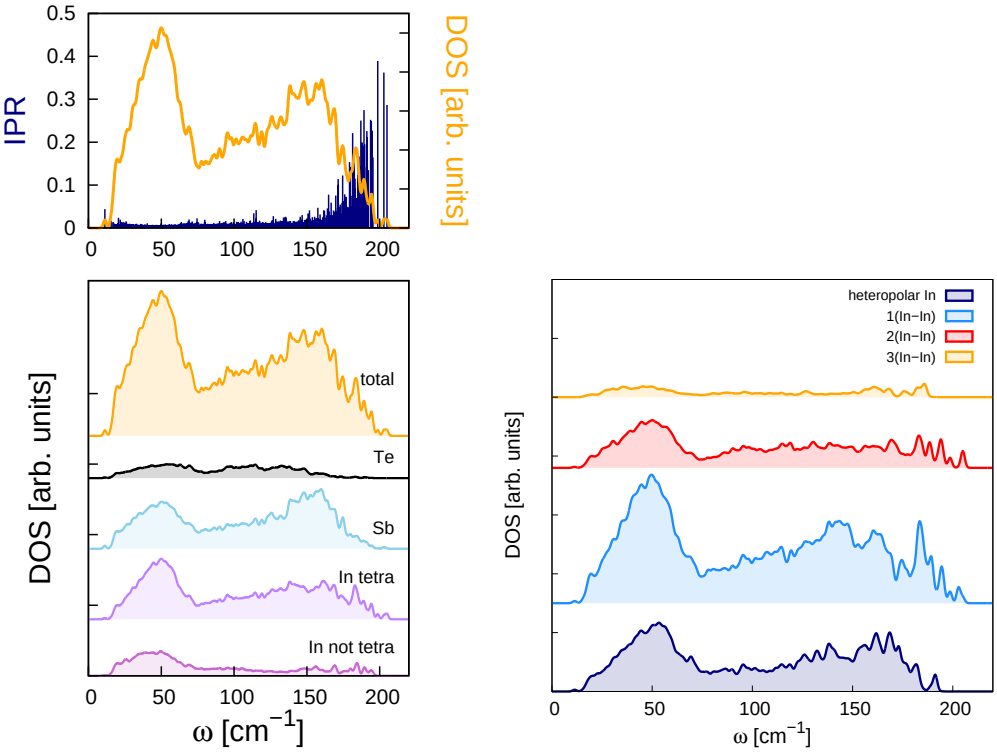

Figure 3.52.: (a) Theoretical phonon DOS of the model of a-$In_{13}Sb_{11}Te_3$. The phonon IPR (green spikes, see text for definition) is superimposed to the DOS in the upper panel. Projections on different species (Sb, Te, tetrahedral In and non tetrahedral In) of the phonon DOS of the upper panel are reported in the lower panel. (b) Projection of the phonon DOS on tetrahedral In atoms in different environments with no homopolar bonds and with one, two or three homopolar In-In bonds.

As already found for a-$In_3Sb_1Te_2$, phonons with frequency above 180 cm^{-1} are strongly localized on tetrahedral In atoms and, in particular, phonons with energy at about 200 cm^{-1} are due to tetrahedral In atoms with homopolar bonds, as it can be noticed from the projection of the phonon DOS on different types of tetrahedral In atoms in Figure 3.52b.
The Debye-Waller factor B_κ for each atomic species was then calculated according to (3.12) and the resulting temperature dependence of B_κ is shown in Figure 3.53 for each species. The results are very close to those obtained for a-$In_3Sb_1Te_2$ at the lowest density.

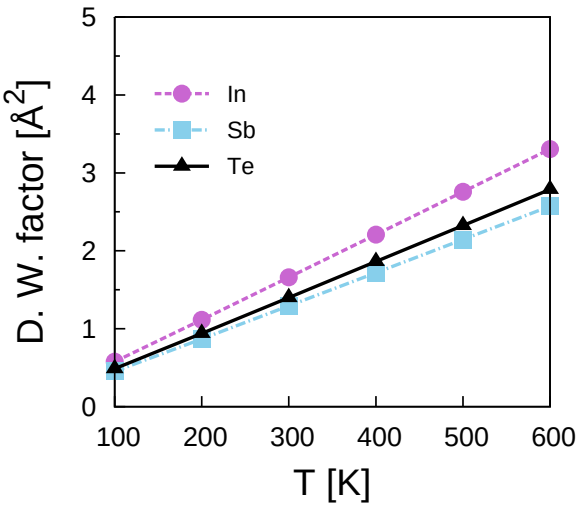

Figure 3.53.: Debye-Waller factor B_κ defined by equation (3.12) of In, Sb and Te atoms as a function of temperature in the model of a-$In_{13}Sb_{11}Te_3$.

Summary

The amorphous phase of $In_{13}Sb_{11}Te_3$ shows features very similar to the other previously discussed alloys, InSb and $In_3Sb_1Te_2$. The $In_{13}Sb_{11}Te_3$ alloy can be seen as composed mainly by InSb with a small amount of InTe. The structural properties of a-$In_{13}Sb_{11}Te_3$ are, in fact, very close to those of a-InSb with similar coordination numbers and fractions of homopolar In-In and Sb-Sb bonds. Also the geometry of local environments and the medium-range order are very similar in the two compounds.
Both a-$In_{13}Sb_{11}Te_3$ and a-$In_3Sb_1Te_2$ appear as mixtures of the binary compounds InSb and InTe and present a mostly tetrahedral network.

3.3. $Ga_4Sb_6Te_3$

The $Ga_4Sb_6Te_3$ alloy is a phase change material characterized by a particularly high crystallization temperature (271 °C [37]) which guarantees a high stability of the amorphous phase and thus a high data retention. This compound is a pseudobinary alloy of the binaries GaSb and Sb_2Te_3, in the ratio $(GaSb)_4(Sb_2Te_3)_1$. In the crystalline phase GaSb has a zincblende structure with tetrahedral environments, while Sb_2Te_3 has a rhombohedral lamellar structure formed by layers of six-fold coordinated Sb atoms in an octahedral arrangement (Figure 3.54). The ternary crystal with composition $Ga_4Sb_6Te_3$ has also a rhombohedral phase,

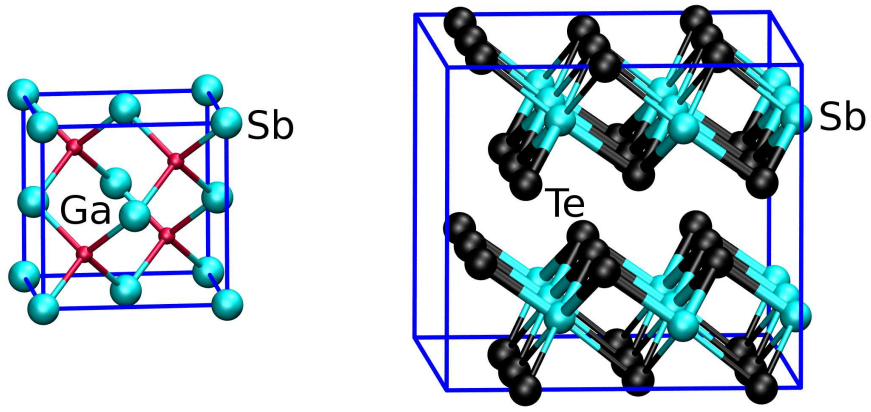

Figure 3.54.: Representation of the crystalline structure of (a) GaSb in the zincblende phase and of (b) Sb_2Te_3 in the rhombohedral phase. Ga atoms are depicted by red spheres, Sb atoms by cyan spheres and Te atoms by black spheres.

but the atomic arrangement inside the structure is still unknown. However, octahedral-like environments are probably present. Thus, as already found for InSbTe alloys, there is again a competition between tetrahedral and octahedral-like structures that makes the short-range geometry of the amorphous phase very difficult to be predicted.

Computational details

We studied the $Ga_4Sb_6Te_3$ alloy by means of DFT simulations. We generated models of the amorphous phase by quenching from the melt. We used two different MD approaches: Car-Parrinello (CP) [161] MD, as implemented in the CPMD code [211] with a plane waves basis set, and the scheme of Kühne *et al.* [142] (see Section 2.5) implemented in the CP2K suite of

programs [157, 191] with a Gaussian-type basis set for KS orbitals. All the simulations were performed with the BLYP exchange and correlation functional which was shown to provide a good description of the structural properties of amorphous and liquid selenides [204–206] and to better describe the amorphous phase of In-based phase change alloys as discussed before in Section 3.1. Brillouin Zone integration was restricted to the supercell Γ-point. Norm conserving pseudopotentials were used with three, five and six valence electrons for Ga, Sb and Te, respectively. Norm-conserving pseudopotentials of the Troullier-Martins (TM) type [222] were used in all CPMD simulations with the inclusion of non-linear core correction (NLCC) [223] for Ga. In the CP2K simulations, instead, we used Gödecker-Teter-Hutter (GTH) pseudopotentials [158, 159] not including any NLCC. The influence of the different choice of pseudopotentials, especially in the case of the first peak in the Ga-Ga pair correlation function will be discussed later. In all CPMD simulations the valence electrons are represented in a plane-wave basis set with an energy cut-off of 60 Ry, assessed on the basis of the accuracy of the stress tensor in constant pressure simulations. Temperature was controlled with a Nosé-Hoover [224–226] thermostat chain [227]. An integration step of 0.12 fs ensured a good control of the conserved quantities all along the simulations. The CP2K simulations employ a Triple-Zeta-Valence plus Polarization (TZVP) Gaussian-type basis set, while the charge density is expanded in a planewave basis set with a cut-off of 100 Ry to efficiently solve the Poisson equation within periodic boundary conditions by using the Quickstep scheme [157, 191]. The completeness of the TZVP basis set was demonstrated by comparing the structural properties of a 117-atom model of a-GaSbTe equilibrated at 300 K with CP2K and CPMD with the same pseudopotentials without NLCC. In the CP2K simulations we used a time step of 2 fs, the Langevin thermostat of Ref. [142] for temperature control, and the GTH pseudopotentials mentioned above. The resulting model was also further equilibrated at fixed volume with CPMD to assess the dependence of the structure on the choices of pseudopotentials which differ in the two codes.

Benchmark simulations

In the lack of experimental data on the density of the amorphous and liquid phases, we performed CPMD constant pressure simulations of a 117-atom liquid model at 900 K which yielded an equilibrium density of 0.03076 atom/Å^3. The energy cut-off of 60 Ry is large enough to neglect Pulay contributions to the stress tensor. Starting from the melted phase at the liquid density, the system was rapidly quenched at constant volume from 900 K to 300 K by varying the temperature according to two cooling protocols summarized in Figure 3.55. The resulting amorphous models at 300 K were then further optimized by releasing the internal stress yielding an equilibrium density of 0.0278 atom/Å^3. The analysis of the structural properties revealed some differences between the two models obtained from the short (100 ps)

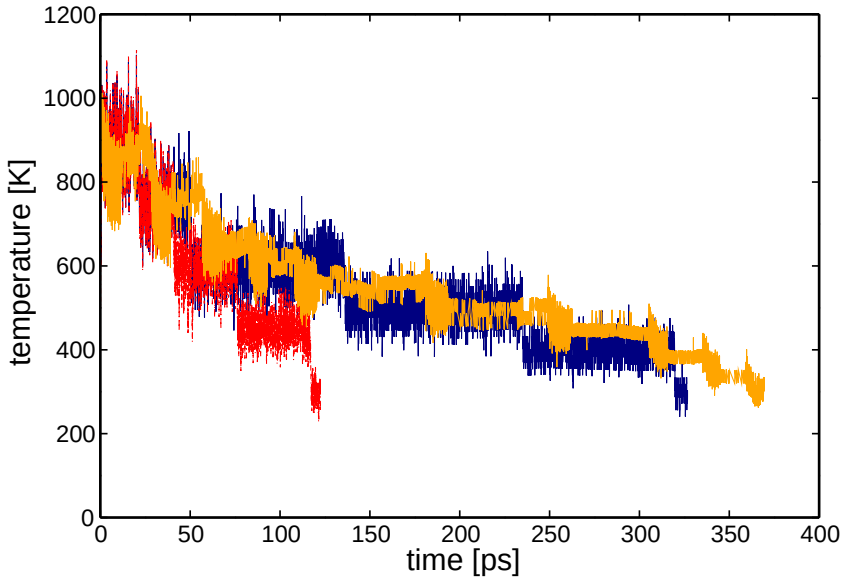

Figure 3.55.: Temperature as a function of time in the quenching protocol used to generate the 117-atom amorphous models with a short (red line) and long quenches (blue line) with the CPMD code and the larger 299-atom model with the CP2K code (orange line).

and long (300 ps) quenching schedules. The partial and total pair correlation functions of the 117-atoms models were computed according to equations (3.1) and (3.2) and the resulting curves in Figure 3.56 show slightly different peak shapes and positions of the first minimum. The coordination numbers are also somehow affected by changes in the quenching schedule. Overall, they appear to increase for the longer quench (Table 3.14).

We then generated a larger 299-atom amorphous model by quenching from the melt in about 350 ps at the theoretical equilibrium density of 0.0278 atom/$Å^3$ discussed above in NVT sim-

Average coordination numbers

	with Ga	with Sb	with Te	total
Ga	0.22 (0.18)	1.83 (1.71)	1.59 (1.24)	3.64 (3.13)
Sb	1.22 (1.14)	1.76 (1.66)	0.25 (0.33)	3.23 (3.13)
Te	2.12 (1.66)	0.49 (0.66)	0.00 (0.00)	2.61 (2.32)

Table 3.14.: Average coordination numbers for different pairs of atoms computed from the partial pair correlation functions of Figure 3.56 of the amorphous 117-atom models of $Ga_4Sb_6Te_3$ obtained by quenching from the melt in 300 ps and, in parentheses, in 100 ps with the CPMD code.

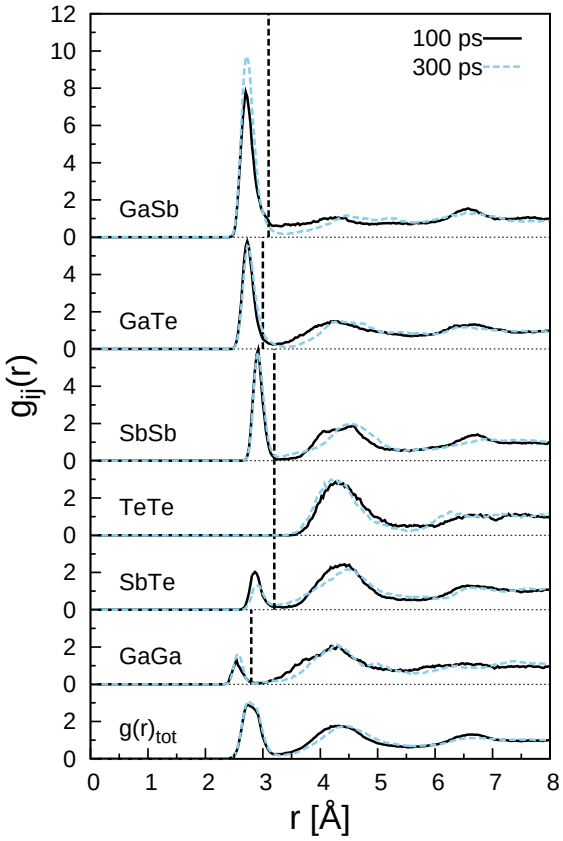

Figure 3.56.: Comparison of the partial and total pair correlation functions of the two 117-atom large models of a-$Ga_4Sb_6Te_3$ quenched from 900 K to 300 K in 100 or 300 ps.

ulations with the CP2K code according to the cooling protocol reported in Figure 3.54. The resulting model was then equilibrated with CPMD to asses the dependence of the structure on the choice of the pseudopotentials. The structural properties of the 299-atom amorphous models equilibrated with either CP2K or CPMD turn out to be very similar. Some differences are found only in the position of the first peak in the Ga-Ga pair correlation function, which changes from 2.45 Å to 2.54 Å in the cases of CP2K and CPMD, respectively, as reported in Table 3.15. This discrepancy is clearly due to the inclusion of NLCC in the pseudopotential for Ga used in CPMD simulations. Indeed, when the same pseudopotentials, namely GTH, were used in both codes the pair correlation functions of the models of a-GaSbTe are the same. To assess which pseudopotential is in fact better transferable for the description of a-GaSbTe, we optimized the internal positions of a 240-atom supercell of cystalline GaTe with CPMD, with the GTH pseupotentials or with the TM pseudopotentials including NLCC for Ga. We chose this system since the crystal presents Ga-Ga dimers. Crystalline GaTe, in fact, has a monoclinic lamellar structure (space group $B2/m$) with weak interactions between Te atoms of different planes (Figure 3.57). During the simulations, the lattice parameters were fixed to

PCF first peak position [Å]		
	CPMD-NLCC	CP2k
Ga-Ga	2.54	2.45
Ga-Sb	2.73	2.70
Ga-Te	2.69	2.70
Sb-Sb	2.91	2.92
Sb-Te	2.88	2.89
Te-Te	—	—

Table 3.15.: Position [Å] of the first peak of the partial pair correlation functions of the 299-atom amorphous model of a-$Ga_4Sb_6Te_3$ equilibrated at 300 K with CPMD and the NLCC pseudopotential (CPMD-NLCC) for Ga and with CP2K and GTH pseudopotentials without NLCC (CP2K).

the experimental values of a =17.404 Å, b =10.456 Å, c =4.077 Å and β =104.44° [228]. The main distances between atoms independent by symmetry are compared in Table 3.16 with experimental data. As a further check, the GTH results were also reproduced by relaxing the

c-GaTe - Interatomic distances			
	NLCC	GTH	exp.
Ga(1)-Ga(2)	2.506	2.376	2.431
Ga(1)-Te(1)	2.677	2.639	2.638
Ga(1)-Te(2)	2.701	2.666	2.669
Ga(2)-Te(1)	2.692	2.658	2.660
Ga(2)-Te(3)	2.695	2.653	2.656
Ga(3)-Ga(3)	2.475	2.379	2.437
Ga(3)-Te(2)	2.727	2.690	2.686
Ga(3)-Te(3)	2.710	2.674	2.678

Table 3.16.: Interatomic distances [Å] in a 240-atom supercell of monoclinic GaTe optimized with GTH pseudopotentials and with pseudopotentials including NLCC for Ga. Experimental values from Ref. [228] are reported in the last column. The atoms independent by symmetry are labeled according to Ref. [228] (cfr. Figure 3.57).

12-atom unit cell of crystalline GaTe, with the same pseudopotentials, a plane waves expansion of KS orbitals with an energy cut-off of 80 Ry and a k-point $8 \times 8 \times 8$ mesh using the QUANTUM ESPRESSO package [229]. It can be seen that the Ga-Te distances are in good agreement with the experimental data, while the Ga-Ga distances are slightly underestimated in the GTH calculations and slightly overestimated in the TM-NLCC calculations. The agreement with experiments for crystalline GaTe seems, however, marginally better for the GTH

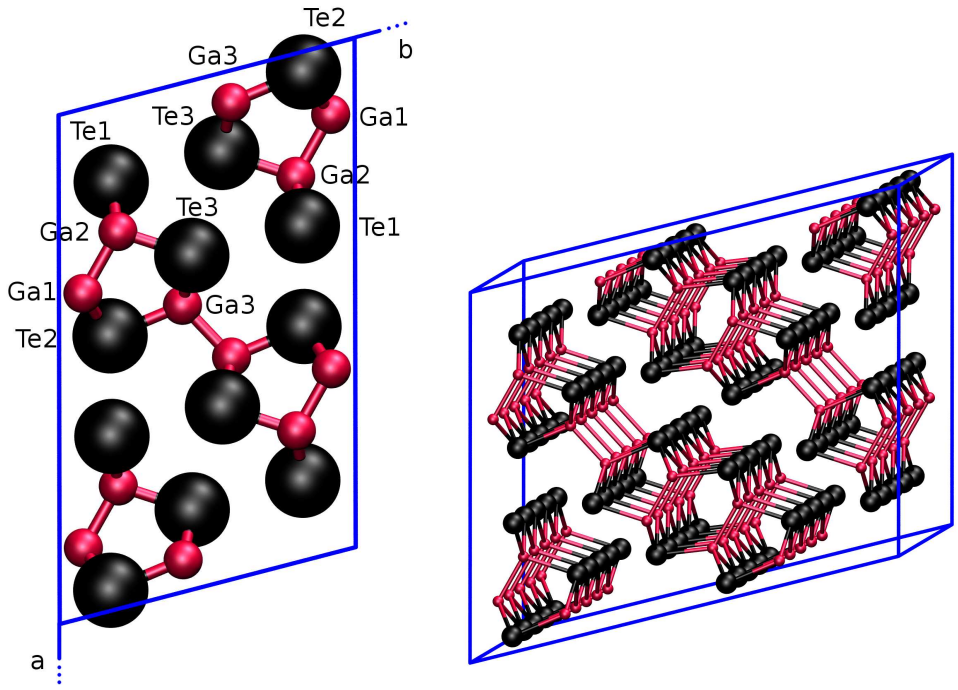

Figure 3.57.: Monoclinic crystal structure of GaTe. (a) The atoms independent by symmetry are labeled according to Ref. [228]. (b) Representation of the 240-atoms supercell of monoclinic GaTe used in the simulations. Ga and Te atoms are depicted by red and black spheres, respectively.

pseudopotentials without NLCC. Hereafter, only the analysis of the 299-atom model obtained with the CP2K code and the GTH pseudopotentials without NLCC will be reported.

Structural properties

To investigate the structural properties of amorphous $Ga_4Sb_6Te_3$, we firstly computed the total and partial pair correlation functions (PCF) shown in Figure 3.58a. The correlation functions are averaged over a trajectory 45 ps long at 300 K. Table 3.17a shows the average coordination numbers for the different species obtained by integrating the pair correlation function up to the position of the first minimum chosen as cut-off for the bonding distance or to slightly lower values (see Figure 3.58a). As can be seen from Figure 3.59, which shows the dependence of the coordination numbers on the cut-off distance, no significant changes arise in the coordination number if the cut-off distance is taken within a small range around the first minimum position of the PCF. The abundance of the different types of bonds in the structure is listed in

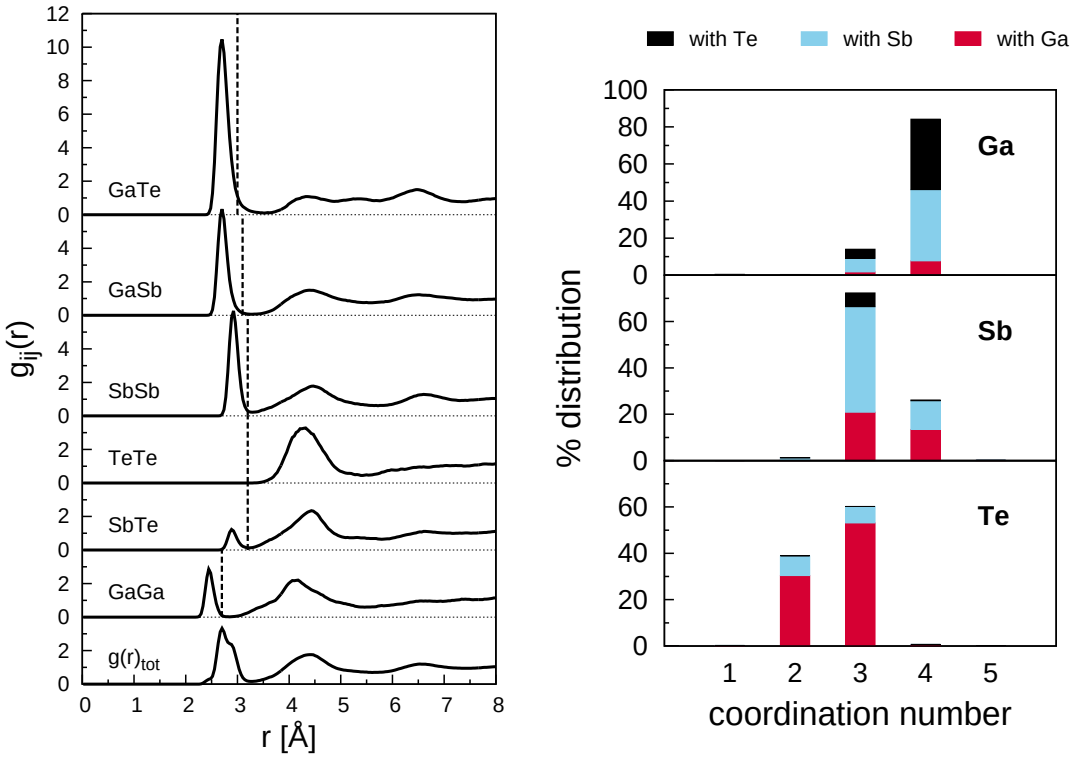

(a) (b)

Figure 3.58.: (a) Total and partial pair correlation functions of a-$Ga_4Sb_6Te_3$ at 300 K averaged over a simulation 45 ps long. The vertical dashed lines are the cut-off radii used to define the coordination numbers (2.70 , 3.10 , 3.00 , 3.20 , 3.20 and 3.20 for the Ga-Ga, Ga-Sb, Ga-Te, Sb-Te, Sb-Sb and Te-Te bonds, respectively). (b) Distributions of the coordination numbers. The contribution from the different atom pairs are represented with different colours.

Table 3.17b. As can be seen from PCFs and from coordination numbers, in the system there is a predominance of Ga-Sb and Ga-Te bonds, and just very few Sb-Te bonds. Thus, as previously found for InSbTe alloys (see Section 3.2.1), amorphous $Ga_4Sb_6Te_3$ can be considered a mixture of the GaSb and GaTe binary compounds, in spite of the fact that the composition of this ternary alloy lies on the GaSb-Sb_2Te_3 pseudobinary tie-lie. A very high concentration of Sb-Sb homopolar bonds was found and some Ga-Ga bonds are present as in crystalline GaTe. The distribution of coordination numbers and the distribution of coordination environments are reported in Figure 3.58b and Table 3.18. Gallium atoms are mainly four-fold coordinated with only a minor fraction of three-fold coordinated atoms. Some four-fold coordinated Ga atoms form Ga-Ga dimers displaying different environments of type GaX_3, in particular $GaSbTe_2$ is one of the most abundant. The majority of Sb atoms is, instead, three-fold coordinated where more than one half of the neighbours are Sb atoms forming homopolar bonds and

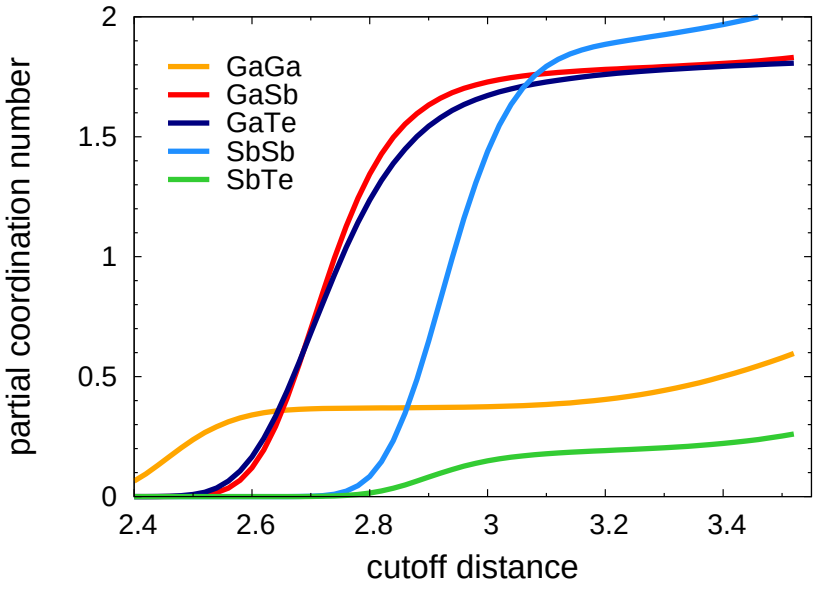

Figure 3.59.: Partial coordination numbers as a function of the cut-off distance on the bonding length in the 299-atom model of a-$Ga_4Sb_6Te_3$.

	Average coordination numbers			
	with Ga	**with Sb**	**with Te**	**total**
Ga	0.37 (0.37)	1.76 (1.83)	1.67 (1.77)	3.80 (3.97)
Sb	1.16 (1.22)	1.89 (1.92)	0.19 (0.19)	3.25 (3.33)
Te	2.23 (2.36)	0.38 (0.39)	0.00 (0.00)	2.61 (2.75)

(a)

	Types of bonds (%)		
	with Ga	**with Sb**	**with Te**
Ga	3.4	33.2	31.4
Sb		26.6	5.4
Te			0.0

(b)

Table 3.17.: Partial average coordination numbers (a) and percentage of the different types of bonds (b) in the 299-atom model of a-$Ga_4Sb_6Te_3$ calculated by using the cut-off distances given in Figure 3.58a. The values in parenthesis refer to the cut-off chosen as the minima of the pair correlation functions.

about the 17 % of three-fold coordinated Sb has an Sb_3 environment. Tellurium atoms are mainly three-fold coordinated.

Information on the local bonding geometry is gained from the bond angle distribution functions shown in Figure 3.60. The total bond angle distribution is peaked at about 100° as a result of the contribution of Sb atoms which form bond angles of about 90° and In atoms with bond angles of about 110°. All these structural information point to many similarities between the amorphous $Ga_4Sb_6Te_3$ and the two compounds GaSb and GaTe. The majority of

	Local environments		
	2	**3**	**4**
Ga:	—	5.4%	93.5%
		Sb_2Te: 2.2%	Sb_2Te_2: 27.2% $GaSbTe_2$: 16.3% $SbTe_3$: 14.1% Sb_3Te: 14.1% $GaSb_2Te$: 6.5 % Sb_4: 4.3% $GaSb_3$: 3.3% Te_4: 3.3% Ga_2Sb_2: 2.2%
Sb:	—	71.7%	27.5%
		$GaSb_2$: 28.3% Sb_3: 17.4% Ga_2Sb: 10.9% GaSbTe: 7.2% Sb_2Te: 3.6% $SbTe_2$: 2.2%	Ga_3Sb: 9.4% Ga_2Sb_2: 8.7% $GaSb_3$: 5.1% Sb_4: 2.2%
Te:	29.0%	71.0%	
	Ga_2: 14.5% GaSb: 13.0%	Ga_3: 50.7% Ga_2Sb: 17.4% $GaSb_2$: 2.9%	

Table 3.18.: Distribution of Ga, Sb and Te coordination environments for atoms with different coordination numbers given in the first line for a-$Ga_4Sb_6Te_3$ (299 atoms). Only environments in a fraction larger than 2 % are reported.

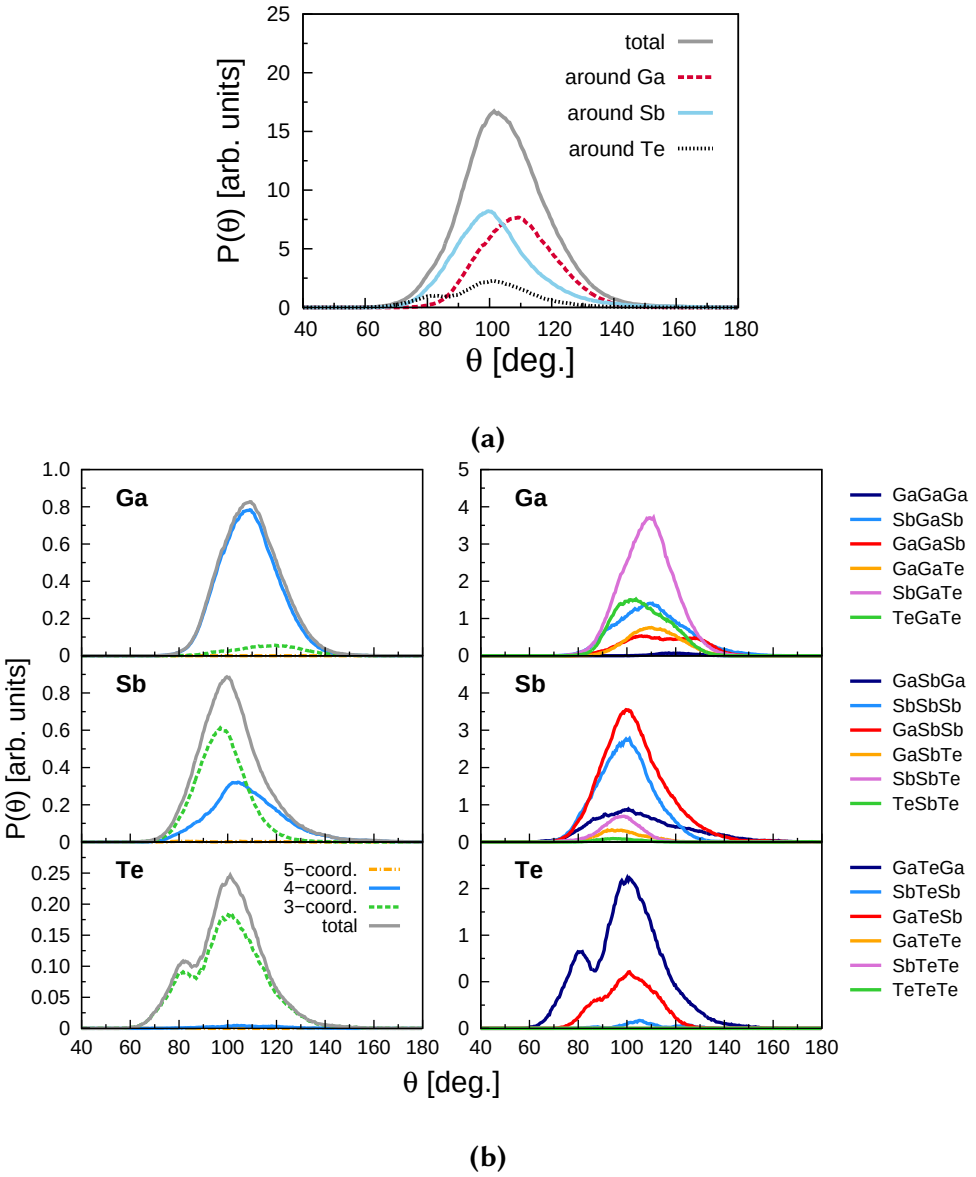

Figure 3.60.: (a) Total distribution of the bond angles in the 299-atom a-$Ga_4Sb_6Te_3$ model and distributions resolved for different atomic species and (b) bond angles distributions resolved for coordination number (left panels) and for different triplets (right panels).

the Ga atoms in the amorphous phase of the ternary compound displays, in fact, a tetrahedral coordination as in both the binary crystals. This can be seen in the projection of the bond angle distributions on atoms with different coordination number (Figure 3.60b). By resolving the distribution for the contributions of different triplets of atomic species (Figure 3.60b, right panel) one finds that SbGaSb and SbGaTe triplets form angles of about 110°, typical of tetrahedral structures, like in zincblende-GaSb and in monoclinic GaTe. The TeGaTe and

GaGaTe triplets show a broader distribution in agreement with the spread of bonding angles in the range $100° - 120°$ of crystalline GaTe. Antimony atoms show, instead, two different geometries for three-fold and four-fold coordination. Three-fold coordinated Sb atoms have bond angles compatible with a pyramidal geometry as in elemental metallic Sb. Three-fold coordinated Sb atoms form, in fact, a high fraction of homopolar bonds, indicating a partial segregation of Sb (see below). Four-fold coordinated Sb are tetrahedral. The bond angle distribution of Te atoms has a bimodal shape with a peak at about 100° as can be found in crystalline GaTe, and a peak at smaller bond angles ($\sim 80°$) which is due to GaTeGa triplets and originates from the presence of edge-sharing tetrahedra with Te atoms at the vertices and Ga atoms at the center. A graphic representation of the most common local environments in a-$Ga_4Sb_6Te_3$ is given in Figure 3.61 reporting the isosurfaces of the Wannier functions (WFs) which provide a simple description of the different bondings. We clearly identify four WFs along the four bonds in sp^3 hybridization of four-fold coordinated Sb, while three-fold coordinated Sb atoms show three p-type σ-bonds with the spherical s-like WF on the central Sb atom, typical of a pyramidal-like bonding geometry. For all the WFs calculations discussed here the CPMD code [211] was used.

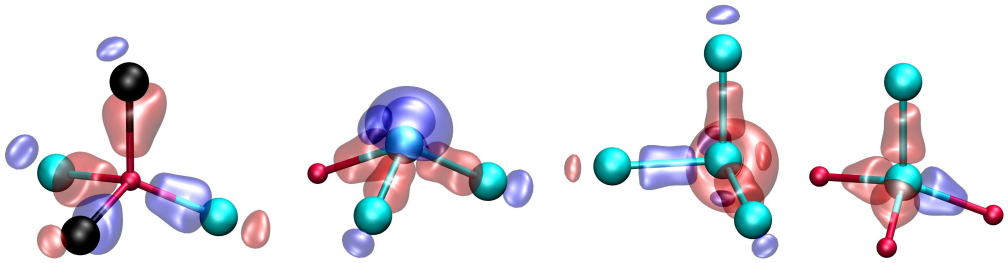

Figure 3.61.: Isosurfaces of Wannier functions for (a) Ga in a tetrahedral site, (b) and (c) three-fold coordinated Sb in a pyramidal-like bonding geometry and (d) four-fold coordinated Sb in a tetrahedral environment. Atoms of Ga are depicted by red spheres, Sb by cyan spheres and Te by black spheres. Isosurfaces with different colours (red and blue) have different sign. Wannier functions with spherical isosurfaces in (b) and (c) are s-like lone pairs.

The percentage of tetrahedra in a-$Ga_4Sb_6Te_3$ has been quantified by computing the q order parameter introduced in Ref. [207] as a measure of the tetrahedricity of the atomic environments and defined by equation (3.7). As discussed before, the q order parameter can discriminate between different atomic geometries (see equation 3.7 and the related discussion in Section 3.1.2) [71]. The distribution of the q order parameter for three and four-fold coordinated atoms of the three atomic species is shown in Figure 3.62. It can be seen that both four-fold coordinated Ga and Sb atoms are mainly in a tetrahedral environments. As shown by the q parameter distribution resolved for four-fold coordinated Ga atoms which form at least one

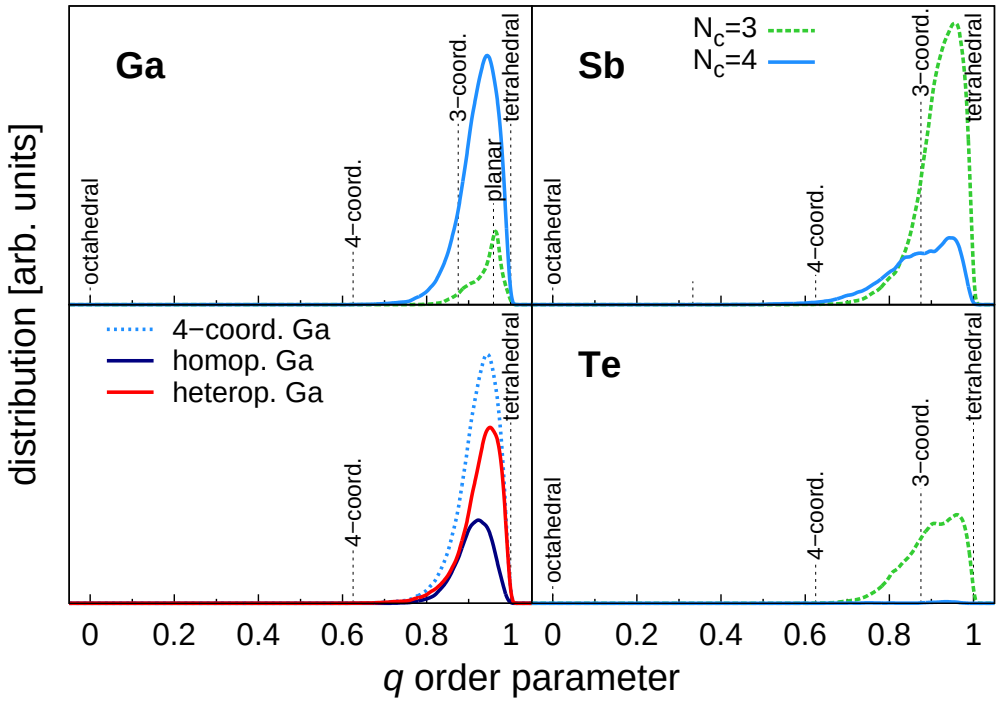

Figure 3.62.: Distribution of the local order parameter q for tetrahedricity (see text) for a-$Ga_4Sb_6Te_3$. The order parameters for the Ga, Sb and Te species are resolved for atoms with different coordination numbers. Vertical lines indicate the values of q for ideal geometries in defective octahedral sites with N_c coordination, tetrahedral and three-fold coordinated planar sites. The distribution is further resolved for four-fold coordinated Ga atoms with or without homopolar bonds in the lower left panels.

Ga-Ga bond (homopolar Ga), Ga atoms without homopolar bonds have a higher degree of tetrahedricity as the corresponding peak of the q-distribution is closer to one. The fraction of atoms in tetrahedral coordination is obtained by integrating the q-distribution for four-fold coordinated atoms from 0.8 to 1. This threshold in the q parameter was shown to be a good choice to identify the tetrahedra in the GeSbTe, $InGeTe_2$ and InSbTe alloys [74, 199, 214]. We obtained a fraction of tetrahedral Ga atoms of about 82.6 % (76 atoms among 92) and a fraction of about 21.0 % (29 atoms among 138) of tetrahedral Sb atoms. To quantify by a different mean the complementary fraction of Sb in pyramidal-like geometry, we calculated the partial pair correlation function between Sb atoms and the centers of the Wannier functions as already done for InSbTe alloys (see Sections 3.1 and 3.2.1). The pair correlation function for Sb-WF was resolved into the contributions from three-fold coordinated and four-coordinated atoms

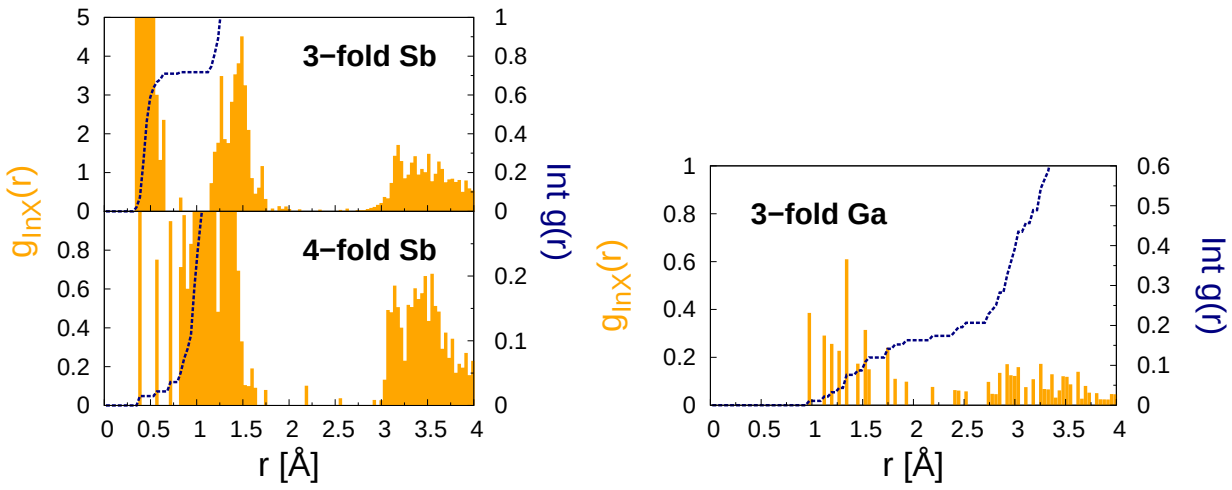

Figure 3.63.: (a) Pair correlation function $g(r)$ of three-fold and four-fold coordinated Sb atoms and (b) of three-fold cooordinated Ga atoms with the centers of the Wannier functions in a-$Ga_4Sb_6Te_3$. The dashed line is the running integral of $4\pi r^2 g(r)\rho$ where ρ is the number density of Wannier centers (right scale).

in Figure 3.63a. The pair correlation function for four-fold coordinated Sb atoms shows a very small peak for short distances, while this first peak is much more evident for three-fold coordinated Sb atoms. By integrating the pair correlation function of four-fold coordinated atoms up to the position of the first minimum (0.7 Å) we obtain that 3 % of all the Sb atoms are in a defective-octahedral environment with four neighbours and the remaining four-fold coordinated Sb atoms are tetrahedrally coordinated (24 % of the total number of Ga). The whole fraction of three-fold coordinated Sb (72 %) is in a pyramidal-like bonding geometry.
As already found for In atoms in InSbTe alloys, the q parameter distribution for three-fold coordinated Ga atoms evidences the presence of planar Ga atoms with an sp^2 hybridization. To quantify the planar structures in the model, we computed the pair correlation functions between three-fold coordinated Ga atoms with the centers of the WFs. As can be seen from Figure 3.63b, no peak is present at small distances indicating that all the three-fold coordinated Ga atoms are in a sp^2 hybridization with no s-like WFs.
The medium range order has been studied by analysing the distribution of the rings length reported in Figure 3.64 and computed according to Ref. [212]. The abundance of the different types of rings is reported in Table 3.19. There is a predominance of five- and six-membered

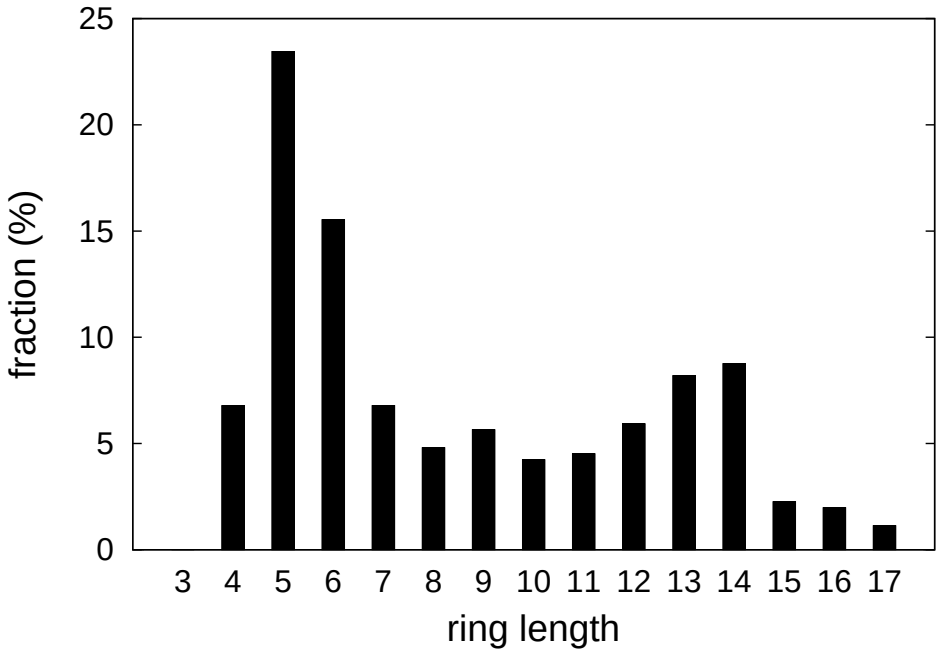

Figure 3.64.: Ring distribution function of a-$Ga_4Sb_6Te_3$ computed according to Ref. [212].

rings that are typical of a mostly tetrahedral network. Five-membered rings of type GaGaTe-GaTe are present in the monoclinic phase of GaTe and appear also in a-$Ga_4Sb_6Te_3$. Due to the large amount of Sb, the most common five-membered rings in a-$Ga_4Sb_6Te_3$ contain homopolar Sb-Sb bonds (GaTeGaSbSb, GaSbSbSbSb and GaSbGaSbSb). All the four-membered rings of type ABAB are due to the presence of edge-sharing Ga tetrahedra, where A stands for Ga and B for Sb or Te. The most abundant six-membered ring is of the type ABABAB which is the building block of both crystalline GaSb and crystalline GaTe. In the latter crystal, AABAAB rings are also present. A large fraction of Sb-Sb bonds is present in six-membered rings as well, with up to 13 % of six-membered rings of the type GaSbSbSbSbSb. This feature indicates a somehow partial segregation of Sb as crystalline Sb is also made of a network of six-membered rings. In fact, the composition $Ga_4Sb_6Te_3$ once seen as a mixture of GaSb and GaTe binaries would ideally contain a fraction of 5/6 of Sb atoms in an elemental state. To quantify the segregation of antimony, we identified clusters of Sb atoms bound continuously to other Sb atoms via linear chains, branched chains or rings. The distribution of the size of these clusters is shown in Figure 3.65a. Actually, in the model of a-$Ga_4Sb_6Te_3$ only 4 % of Sb atoms (5 atoms over 138) form only heteropolar bonds while 17 % of Sb atoms (23 atoms over 138) forms Sb-Sb dimers and chains 4-, 5- and 6-atoms long. The majority (80 %) of the Sb atoms belong to two clusters of 13 and 97 Sb atoms. The 13-atoms cluster is constituted by a 9-atom long branched chain, while the biggest cluster presents five- and six-membered rings.

Rings statistics

4-membered					
GaTeGaTe	42%	10	ABAB	83%	20
GaSbGaTe	33%	8			
GaSbGaSb	8%	2			
GaSbSbSb	8%	2	ABBB	13%	3
GaSbSbTe	4%	1			
SbSbSbSb	4%	1	BBBB	4%	1

5-membered					
GaTeGaSbSb	30%	25	ABABB	55%	46
GaSbGaSbSb	13%	11			
GaTeGaSbTe	7%	6			
GaSbGaSbTe	5%	4			
GaSbSbSbSb	17%	14	ABBBB	23%	19
GaSbSbSbTe	6%	5			
GaGaSbGaTe	7%	6	AABAB	11%	9
GaGaTeGaTe	2%	2			
GaGaSbGaSb	1%	1			
SbSbSbSbSb	5%	4	BBBBB	6%	5
SbSbSbSbTe	1%	1			
GaGaSbSbSb	4%	3	AABBB	5%	4
GaGaSbSbTe	1%	1			

6-membered					
GaSbGaSbGaTe	13%	7	ABABAB	35%	19
GaSbGaTeGaTe	13%	7			
GaTeGaTeGaTe	5%	3			
GaSbGaSbGaSb	4%	2			
GaSbGaSbSbSb	9%	5	ABABBB	29%	16
GaTeGaSbSbTe	9%	5			
GaTeGaSbSbSb	5%	3			
GaSbGaSbSbTe	4%	2			
GaSbGaTeSbTe	2%	1			
GaSbSbSbSbSb	13%	7	ABBBBB	13%	7
GaGaSbGaSbSb	4%	2	AABABB	7%	4
GaGaTeGaSbSb	4%	2			
GaGaTeGaGaTe	4%	2	AABAAB	5%	3
GaGaSbGaGaTe	2%	1			
GaSbSbGaSbSb	4%	2	ABBABB	4%	2
GaGaGaSbGaTe	2%	1	AAABAB	2%	1
GaGaGaSbSbSb	2%	1	AAABBB	2%	1
GaGaSbSbSbSb	2%	1	AABBBB	2%	1
SbSbSbSbSbSb	2%	1	BBBBBB	2%	1

Table 3.19.: Abundance of the different types of rings of different size in the 299-atom model of a-$Ga_4Sb_6Te_3$. The absolute number of rings is also given in the second column. The type of the rings is indicated by A and B letters where A stands for Ga and B for Sb or Te.

The volume occupied by the 97-atom cluster was identified by computing the Voronoi polyhedra centered on each Sb atom of the cluster (Figure 3.65b). Nanoscale segregation of Sb has been found also in DFT models of amorphous $GaSb_7$ [230] close to to the eutectic composition of the GaSb alloy.

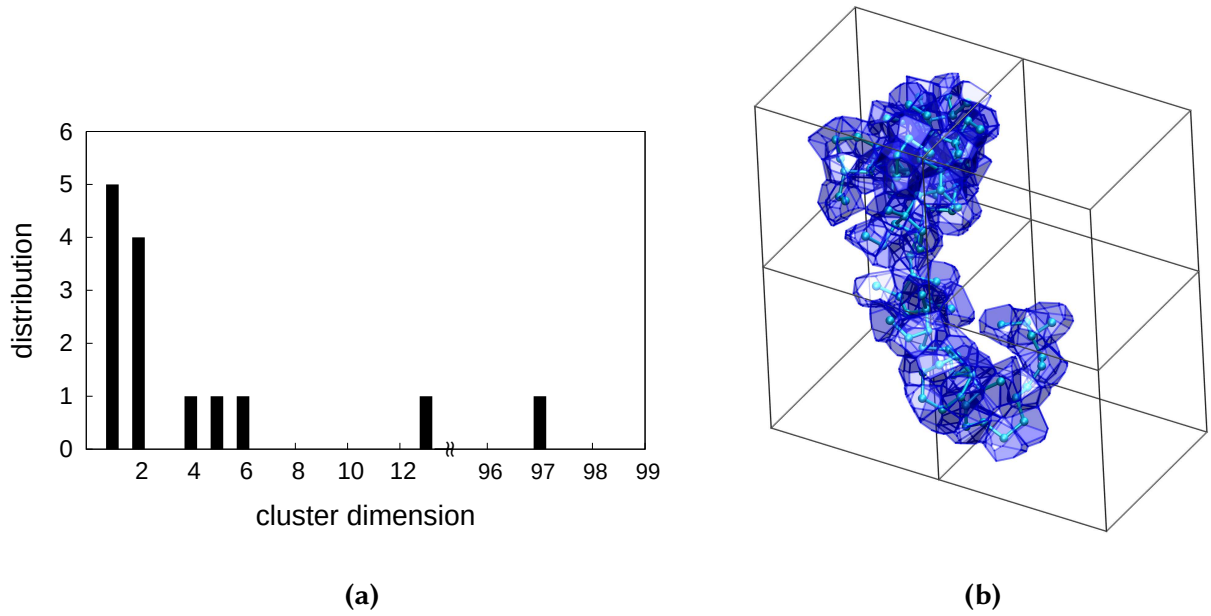

(a) **(b)**

Figure 3.65.: (a) Distribution of the size of the cluster of connected Sb-Sb bonds in the 299-atom a-$Ga_4Sb_6Te_3$ model. The horizontal scale indicates the number of atoms each cluster is made of. (b) Snapshot of the 97-atom Sb-cluster. The atoms of the cluster are shown as cyan spheres. The shape of the cluster is depicted by the blue transparent surfaces of the Voronoi poliedra built around the Sb atoms of the cluster. Four 299-atoms supercells are shown but the periodic boundary conditions are not applied to the atoms of the Sb cluster to highlight its shape and connectivity.

Electronic properties

We analyzed the electronic properties of the amorphous model by using the hybrid HSE06 functional of Ref. [154] to better estimate the band gap. A geometry optimization with the HSE06 functional is computationally too demanding therefore, since the HSE06 functional is built on the PBE functional, we firstly relaxed the model with the PBE functional which yields a geometry very close to the structure relaxed with the BLYP functional. The electronic density of states (DOS) is also very similar for PBE and BLYP (Figure 3.66). The electronic DOS

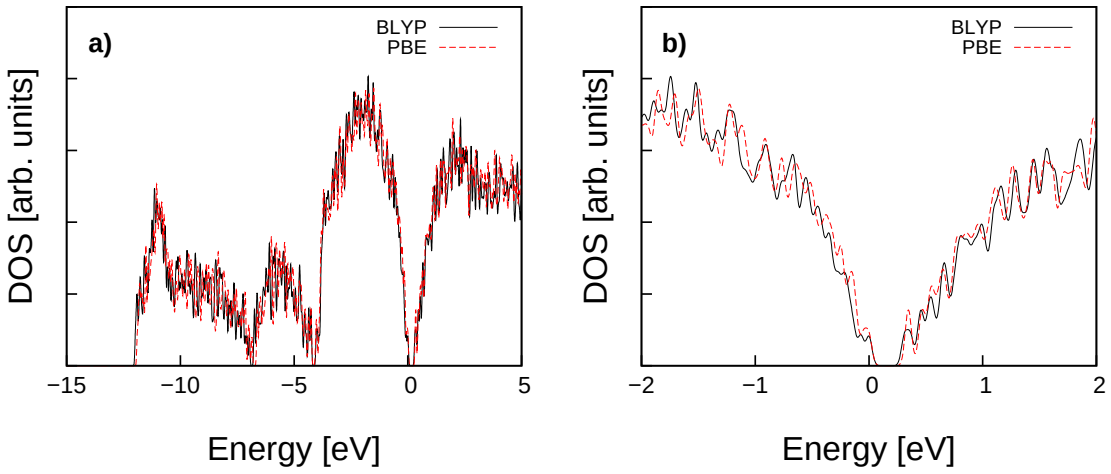

Figure 3.66.: Electronic density of states for the 299-atoms model of a-$Ga_4Sb_6Te_3$ calculated with the BLYP functional (continuous black line) and with the PBE functional (dashed red line). The DOSs were computed on structures relaxed with the BLYP functional and with the PBE functional, respectively. The KS energies are broadened by Gaussian functions of 27 meV width. The DOSs are aligned with respect to the energy of the highest occupied orbital corresponding to zero. b) A zooming of the DOS of panel a) close to the band gap.

of a-$Ga_4Sb_6Te_3$ from Kohn-Sham (KS) energies at the Γ-point with the HSE06 functional and the geometry optimized at the DFT-PBE level of theory is reported in Figure 3.67. The projections of the DOS on the three atomic species are also reported in Figure 3.67. To quantify the localization of the KS orbitals, the value of the Inverse Participation Ratio (IPR), defined for the i-th KS state by equation (3.8), is provided for each state in Figure 3.67. The higher the IPR value the higher is the localization of the state. The zoom of the DOS in Figure 3.67b shows the presence of two localized states in the band gap at ~ 0.15 eV above the top of the valence band. Both states are localized on small clusters of Sb atoms and some surrounding tetrahedral Ga atoms as illustrated in Figure 3.68. By neglecting these very localized states near the edge of the valence band, a-$Ga_4Sb_6Te_3$ turns out to be a semiconductor with a band

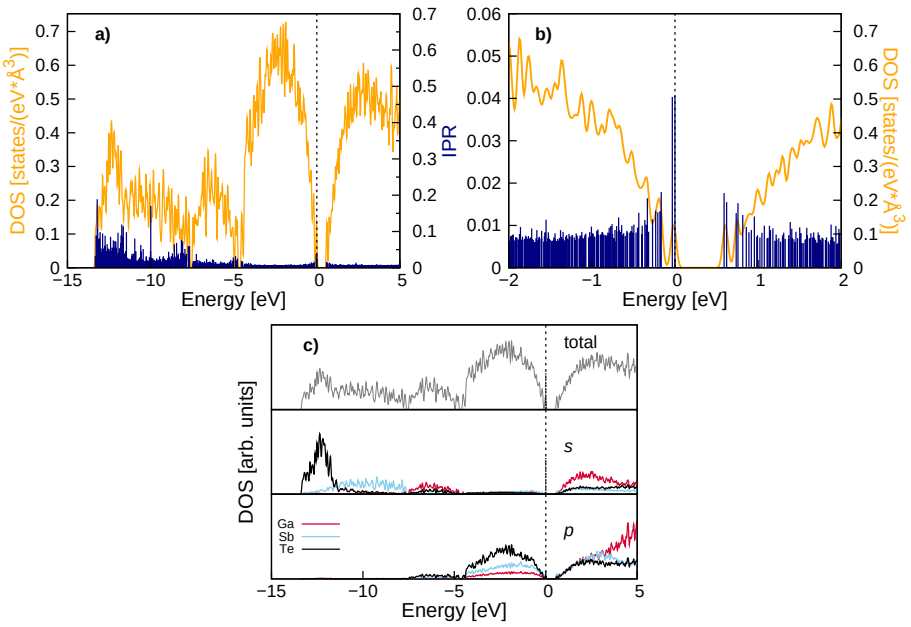

Figure 3.67.: Electronic density of states (HSE hybrid functional [154]) for the 299-atoms model of a-$Ga_4Sb_6Te_3$. The KS energies are broadened by Gaussian functions of 27 meV width. The zero of energy corresponds to the highest occupied orbital. The Inverse Participation Ratio (IPR) is given on the right scale (blue spikes, see text for definition). b) A zooming of the DOS of panel a) close to the band gap. c) Projections on atomic *s* and *p* pseudo wavefunctions of the DOS of panel a). The contribution from *d* pseudo wavefunctions is negligible on the scale of the figure and it is omitted.

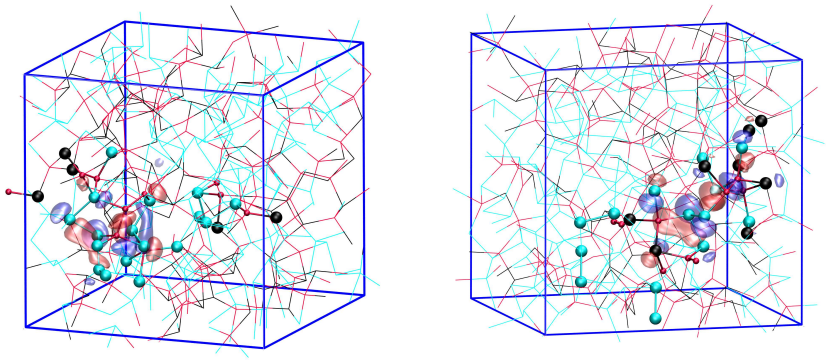

(a) HOMO -1 **(b)** HOMO

Figure 3.68.: Snapshots of the most localized Kohn-Sham states close to the band gap of the 299-atoms model of a-$Ga_4Sb_6Te_3$. Semitransparent red and blue surfaces render an isosurfaces with a value of $+0.022398$ a.u. and -0.022398 a.u. , respectively. The whole bonding network is displayed by thin lines. The states are mostly localized on the Ga, Sb and Te atoms highlighted with red, cyan and black spheres, respectively.

gap of 0.76 eV. Note that the edge of the valence band is mostly due to Sb and Te *p* states while the edge of the conduction band has also a similar contribution from *p* states of Ga.
We also computed the ionic charges from the total electronic charge density according to Bader [231] (Figure 3.69) by using the scheme of Ref. [213] and adding to the valence charge density the core charges localized on the atoms. Ga and Sb atoms shows a very broad distribution of the Bader charges due to the presence of homopolar bonds. Many Sb atoms have nearly zero charge due to the very large fraction of Sb-Sb bonds. Sb atoms have an amphoteric character as they are more positively charged when bound mostly to Te and negatively charged when bound to Ga.

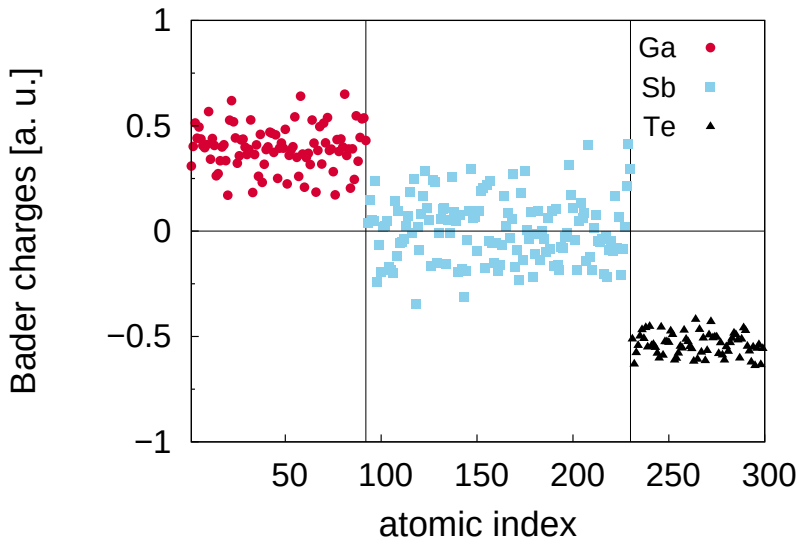

Figure 3.69.: Bader ionic charges (atomic units) of a-$Ga_4Sb_6Te_3$ for each atom of the different species of the 299-atoms model.

Vibrational properties

We computed the phonon frequencies of the amorphous model with the BLYP functional by diagonalizing the dynamical matrix obtained in turn from the variation of atomic forces due to finite atomic displacements 0.0053 Å large. Only phonons with the periodicity of our supercell (Γ-point phonons) were considered. The phononic DOS and its projection on the different atomic species are reported in Figure 3.70. In order to analyse the localization properties of the vibrational modes, we computed the phononic inverse participation ratio for each phononic state *j* defined by the equation (3.9). The plot of the IPR in Figure 3.70 shows the presence of very localized phononic states above 170 cm^{-1} that mainly involve Ga atoms. As found for other phase change alloys as InSbTe, InGeTe and GeSbTe [72, 199, 214], the strongly localized

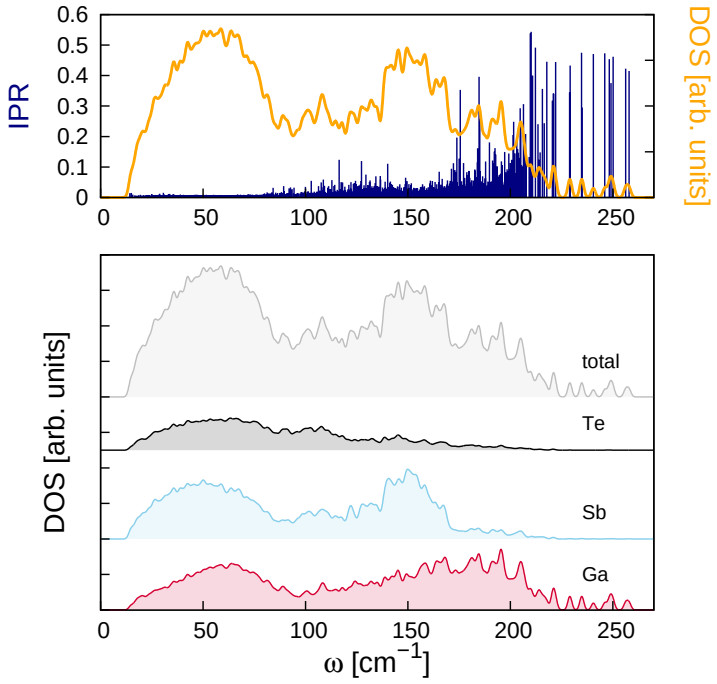

Figure 3.70.: Theoretical phonon DOS of the 299-atoms model of a-$Ga_4Sb_6Te_3$. a) The phonon IPR (blue spikes, see text for definition) is superimposed to the DOS. b) Projections on different species (Sb, Te and Ga) of the phonon DOS of panels a).

high energy modes are due to vibrations of atoms in a tetrahedral environment; in particular, the modes in the range $230 - 260$ cm^{-1} are due to vibrations of Ga-Ga homopolar bonds.

Summary

In conclusion, our atomistic simulations on the a-$Ga_4Sb_6Te_3$ alloy have pointed out that in spite of the fact that the $Ga_4Sb_6Te_3$ composition lies on the GaSb-Sb_2Te_3 pseudobinary tie-lie, very few Sb-Te bonds are present in the amorphous models which appear instead as a mixture of the two binary tetrahedral-like compounds GaTe and GaSb and elemental Sb ($Ga_4Sb_6Te_3 = (GaSb)_1(GaTe)_3$-$Sb_5$). Gallium atoms are in fact mostly in a tetrahedral environment, forming also Ga-Ga dimers typical of the crystal structure of GaTe. Antimony presents instead two different types of local environments, pyramidal-like for three-fold coordinated atoms and tetrahedral-like for four-fold coordinated atoms. The high concentration of Sb with respect to the pseudobinary GaSb−GaTe leads to a partial segregation of Sb forming clusters with structures that recall the metallic phase of crystalline Sb. These features are similar to those found in amorphous models of $In_3Sb_1Te_2$ (see Section 3.2.1) which show as well very few Sb-Te bonds and local structures similar to those present in the binary compounds InTe and InSb.

4. Simulations of resistance drift in amorphous GeTe

The resistance drift, as discussed in Section 1.4, is a phenomenon that occurs in the amorphous phase of chalcogenide materials resulting in an increase of the electrical resistivity with time that affects the reliability of PCM devices and hinders the realization of multilevel cells. The metastable amorphous phase is, in fact, subject to aging which leads to an increase in the resistance. The drift phenomenon is ubiquitous in chalcogenide alloys investigated for PCM applications. Since in PCM the amorphous phase is under compressive stress due to the embedding in the denser crystalline matrix, it was proposed that the drift arises from stress relief upon time leading to an increase in the band gap [126]. This scenario seemed to be confirmed by the measurement of a lower drift in eventually stress-free GST nanowires [12]. However, since later measurements of both PCM and stress-free, as-deposited amorphous GST films gave the same drift exponent [128], an alternative scenario seemed more viable in which the drift was actually resulting from relaxations of local defective structures of the amorphous phase toward a more stable configuration [127]. This aging process would not lead to a more crystalline-like material, but to a less defective, more ideal glass. In fact, the crystal actually displays a lower resistivity than the amorphous while the drift leads to an increase of resistance over time.

As discussed in Section 1.4.3 optical ellipsometry measurements of GST upon drift have indeed shown a widening of the band gap and a reduction of Urbach tails [137]. Extended Urbach tails and a large density of deep defect states in the gap have actually been detected in amorphous GeTe by modulated photocurrent experiments [118]. Widening of the band gap and reduction of Urbach tails both concur to increase the resistivity of the amorphous phase [121] as both these effects lead to an increase of the activation energy for carriers generation (see Section 1.4). In fact, the conductivity of the amorphous phase is believed to be due to carriers injected in valence (holes) or conduction (electrons) bands from states inside the mobility gap by the electric field according to the Poole-Frenkel mechanism [121] (see Section 1.4.2). The role of deep defect states in the conduction mechanism and then in the drift phenomenon is instead more controversial [139].

The structural, atomistic origin of the localized states inside the mobility gap either in Urbach tails or deep in the gap is, however, unknown. The first result linking structural features of the amorphous phase with the resistance drift came recently from Ge K-edge x-ray absorp-

tion near-edge structure (XANES) spectra of $Ge_2Sb_2Te_5$ [140]. It was shown that the drift is correlated with the reduction of a step-like feature in the pre-edge XANES spectra [140] previously ascribed to the presence of tetrahedrally coordinated Ge from [141]. The results seem thus to suggest that the drift is correlated with a reduction of Ge in tetrahedral sites. How the conversion of tetrahedral sites into defective octahedral/pyramidal sites would affect the electronic states of the amorphous is still an open issue which has to be addressed by electronic structure calculations.

In order to study the atomistic origin of drift and to provide a link between electronic states and the specific structural features whose relaxation leads to an increase of the resistance, large models (1728 atoms) of amorphous GeTe were generated through molecular dynamics simulations based on the Neural Network (NN) potential (see Section 2.7). The electronic properties were then analysed at the DFT level. We discuss first the structure of the amorphous models, then their electronic properties and finally the simulations that we performed to mimic the drift which provided a microscopic insight on the nature of the structural relaxation leading to the increase of the resistance.

4.1. Structural properties of a-GeTe

We firstly generated two models of a-GeTe by quenching from the melt at fixed density from 1000 to 300 K in 100 ps (Figure 4.1) with the NN potential (see Section 2.7). The simulations were performed with the NN code RuNNer [232] by using the DL_POLY code as MD driver [233]. Time step was set to 2 fs and temperature was enforced by a stochastic thermostat [234]. In one model (model 1) the density was equal to the theoretical equilibrium density of 0.03351 atoms/Å^3, while in the second model (model 2), a higher density of 0.03565 atoms/Å^3 was chosen aiming at generating a larger concentration of defect states in the gap according to the suggestion of Ref. [132]. This second model was then rescaled at the former density of 0.03351 atoms/Å^3. The two models were then equilibrated at 300 K. The structural properties of our models were analysed by averaging over the last 200 ps of the trajectory at 300 K and very similar pair correlation functions (PCF) were obtained (Figure 4.2) By integrating the pair correlation functions up to a cut-off distance (see Figure 4.2), the partial coordination numbers of Table 4.1a were obtained. Model 2 shows a slightly larger fraction of homopolar bonds with respect to model 1. The distribution of the coordination numbers is reported in Figure 4.3 showing a prevalence of four-fold coordinated Ge atoms and of three-fold coordinated

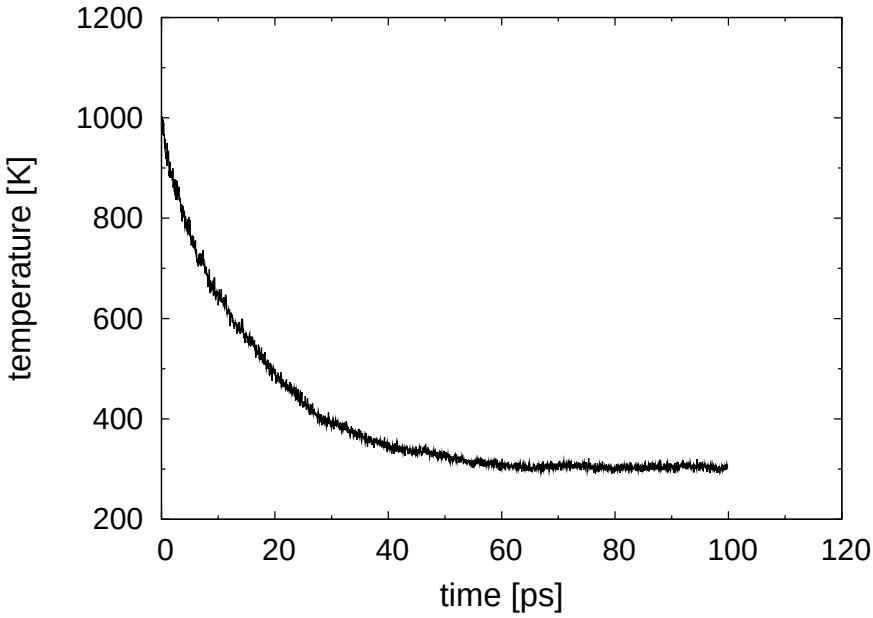

Figure 4.1.: Evolution of the temperature during the quench of 1728-atom models of amorphous GeTe at the density of 0.03351 atoms/Å^3. The systems have been cooled down from 1000 to 300 K in about 100 ps through classical molecular dynamics simulations by using a Neural-Network potential.

Average coordination numbers			
	with Ge	**with Te**	**total**
Ge	1.16 (1.19)	3.19 (3.09)	4.35 (4.29)
Te	3.19 (3.09)	0.09 (0.11)	3.28 (3.20)

(a)

Types of bonds (%)		
	with Ge	**with Te**
Ge	15.2 (15.9)	83.7 (82.6)
Te		1.1 (1.5)

(b)

Table 4.1.: Partial average coordination numbers (a) and percentage of the different types of bonds (b) of model 1 and, in parentheses, of model 2 of a-GeTe. The data were calculated by using the cut-off distances listed above in the text.

Te atoms. The bond angles distribution in Figure 4.4 computed according to equation (3.5), shows the presence of both tetrahedral and octahedral structures for Ge atoms, in agreement with previous calculations on GeTe and GST amorphous models [67–72]. The distribution of bond angles formed by Ge atoms in both models presents, in fact, peaks at about 90° and 180°, typical of defective octahedral environments, (see Figure 1.15) and a shoulder at about 110° indicating the presence of tetrahedrally coordinated Ge atoms. The concentration of

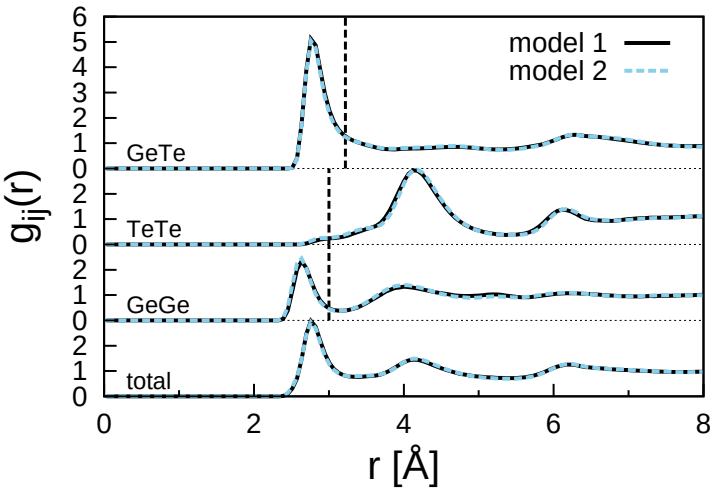

Figure 4.2.: Total and partial correlation functions of the 1728-atom models of a-GeTe generated with NN-MD simulations by quenching from the melt in 100 ps. Model 1 was generated at the theoretical density of 0.03351 atoms/Å^3, while model 2 was generated at a higher density (0.03565 atoms/Å^3) and then rescaled at the theoretical density. The dashed vertical lines indicate the bonding cut-off distances used in the other structural analysis which are 3.20 Å, 3.20 Å and 3.22 Å for Ge-Ge, Te-Te and Ge-Te pair, respectively. The data were obtained by averaging over a 200 ps long trajectory at 300 K.

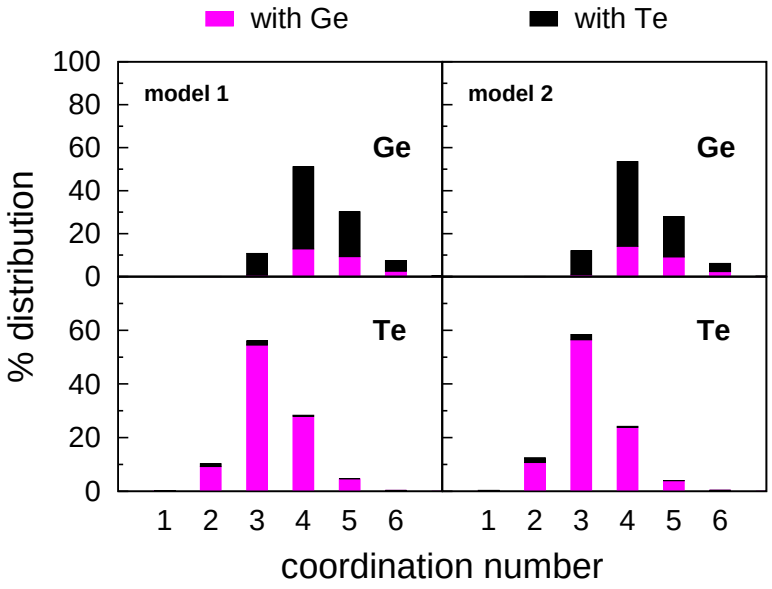

Figure 4.3.: Distribution of the coordination numbers of a-GeTe models. The contributions from the different atom pairs are indicated by different colours.

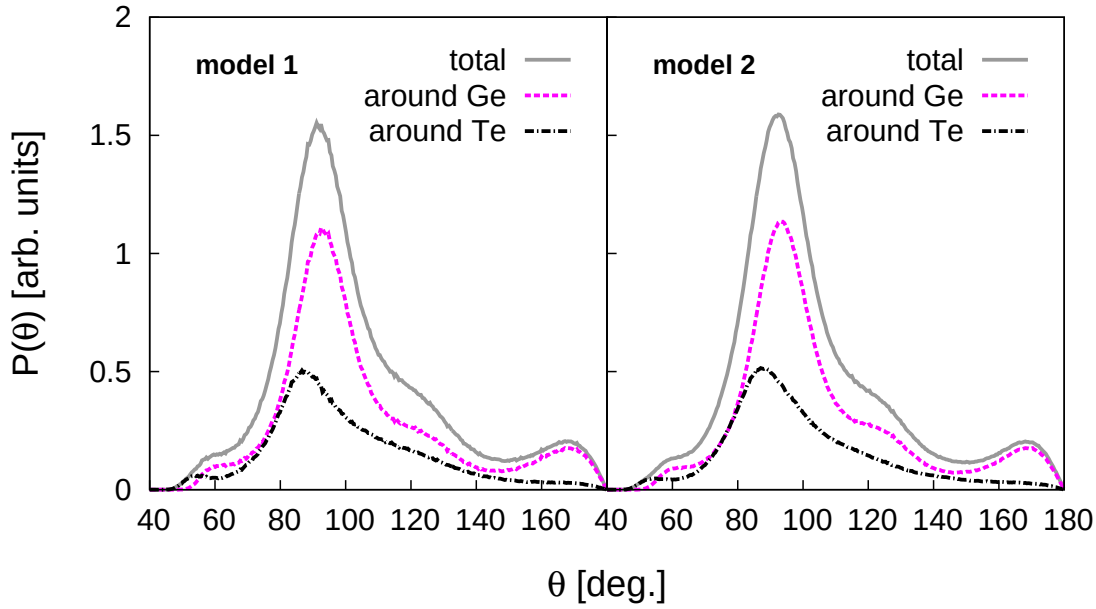

Figure 4.4.: Calculated bond angles distribution for the two models of a-GeTe. The total distribution (continuous grey line) was also resolved into two contribution form Ge species (red dashed line) and Te species (black dot-dashed line).

tetrahedral Ge atoms can be estimated from the calculation of the q order parameter, defined by equation (3.7), reported in Figure 4.5. The distribution for four-fold coordinated Ge atoms shows a clear bimodal shape for both the models with two peaks corresponding to defective octahedral-like geometries for $q = 0.625$ and to tetrahedral geometries for $q = 1$. By resolving the distribution of four-fold coordinated Ge atoms for atoms with (homopolar Ge) and without (heteropolar Ge) homopolar Ge-Ge bonds, it can be seen that homopolar bonds favour a tetrahedral coordination, as found in other previous works on GST and GeTe [67–69, 71, 72]. By integrating the q distribution of four-fold coordinated Ge atoms in the range $0.8 - 1$, the concentration of tetrahedral Ge atoms can be obtained. This procedure for the estimation of the fraction of tetrahedra was already applied to Ge-based phase change alloys in previous theoretical works [71, 72] giving reliable results. We obtained a concentration of tetrahedral Ge atoms of 24 % for the model 1 and of 28 % for model 2 after density rescaling. Before the rescaling the fraction of tetrahedra in model 2 is only 17 %, consistently with the fact that pressure favours octahedra with respect to tetrahedra.

The two models were then relaxed at the DFT-PBE level by solving the Kohn-Sham (KS) equation with the Quickstep scheme as implemented in the CP2K suite of programs [157, 191]. In this approach the KS orbitals are expanded in Gaussian type orbitals (GTOs) and the charge density is represented with an auxiliary plane waves basis with a cut-off of 100 Ry to efficiently solve the Poisson equation. Gaussian-type pseudopotentials [158, 159] with four and

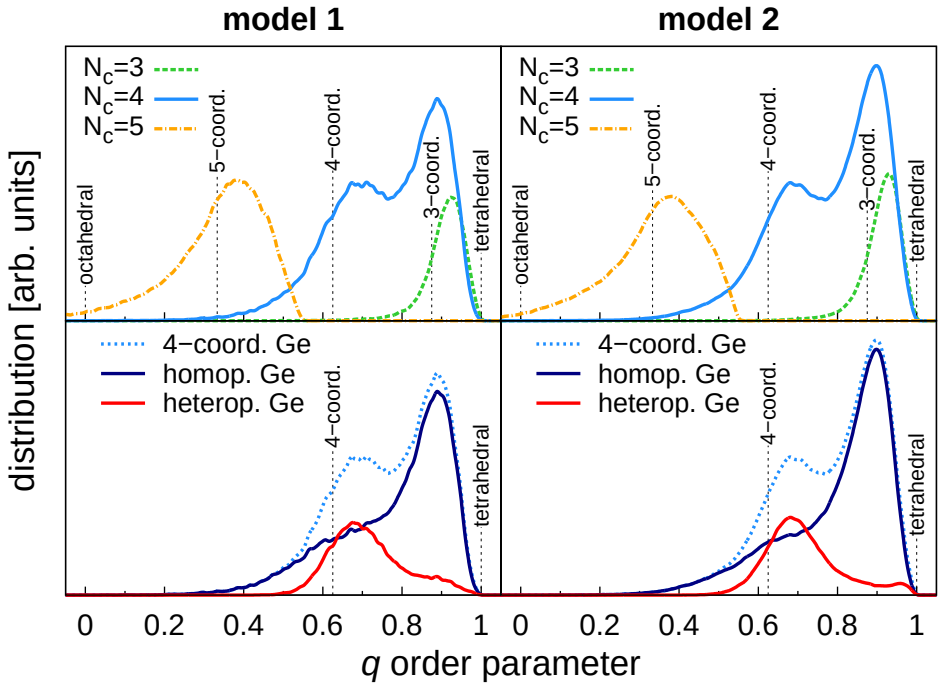

Figure 4.5.: Distribution of the local order parameter q for tetrahedricity (see text) for Ge atoms in the two models of a-GeTe. The distributions for Ge atomic species are resolved for different coordination numbers. Vertical lines indicate the values of q for ideal geometries in defective octahedral sites with N_c coordination and tetrahedral sites. The distributions for four-fold coordinated Ge atoms are further resolved for atoms with and without homopolar bonds (lower panels).

six valence electrons were adopted for Ge and Te. The KS orbitals were expanded in a Triple-Zeta-Valence plus Polarization (TZVP) GTOs. Brillouin zone integration was restricted to the supercell Γ point.

The *ab-initio* relaxation of the two models does not induce relevant changes in the structure. The comparison of the pair correlation functions of the systems before and after the relaxation is shown in Figure 4.6. The pair correlation functions of the models before the relaxation were calculated by averaging on a trajectory at 300 K according to equations (3.1) and (3.2), while for the relaxed models the PCF were computed from the optimized positions at the DFT-PBE level and the harmonic phonons calculated with the NN potential. In this case, the thermal average of equation (3.1) was restricted to the harmonic approximation by replacing the δ function with a Gaussian function of variance σ [235] defined as

$$\sigma^2 = \left\langle [\mathbf{d} \cdot (\mathbf{u}_I - \mathbf{u}_J)]^2 \right\rangle \tag{4.1}$$

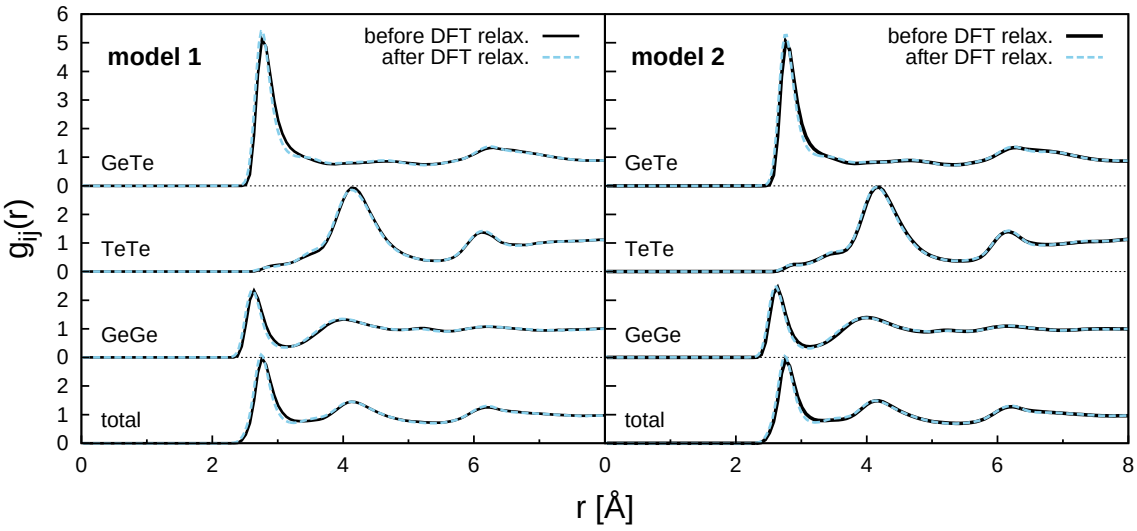

Figure 4.6.: Total and partial correlation functions of the two models of a-GeTe before and after an *ab-initio* relaxation. Correlation functions before the relaxation were calculated by averaging on a 200 ps long trajectory at 300 K, while correlation functions after the relaxation were computed with harmonic phonons (see text).

where $\mathbf{u}_I$ is the displacement of the I-th atom with respect to the equilibrium position $\mathbf{R}_I$, and $\mathbf{d}$ is a unitary vector along the direction of $\mathbf{R}_I - \mathbf{R}_J$. The thermal average $\langle .. \rangle$ is then computed from harmonic phonons as

$$\langle \mathbf{u}_I \mathbf{u}_J \rangle = \sum_n \frac{\hbar}{\omega_n} \frac{\mathbf{e}(n,I)}{\sqrt{M_I}} \frac{\mathbf{e}(j,J)}{\sqrt{M_J}} \left[n_B(\omega_n) + \frac{1}{2} \right], \tag{4.2}$$

where M_I is the mass of I-th atom, ω_n and $\mathbf{e}(n,I)$ are frequencies and eigenvector of the n-th harmonic phonon. The temperature dependence is introduced by the Bose factor $n_B(\omega_n) + \frac{1}{2}$ whose classical limit is $k_B T/(\hbar\omega_n)$. Since the NN potential reproduces well the phonon density of states of a-GeTe [236] we did not compute phonons by DFT in our large (1728 atoms) cell.

Table 4.2a and Table 4.2b report the partial coordination numbers and the abundance of the different bond types in the structures after the *ab-initio* relaxation. The data were obtained by integrating the pair correlation functions obtained from harmonic phonons up to the cut-off distances of Figure 4.2. The fraction of tetrahedral Ge atoms of the DFT-PBE relaxed models obtained from the q parameter integration turned out to be 31 % for model 1 and 29 % for model 2.

The rings distribution in the two models of a-GeTe, that gives information on the medium-range order, was computed according to Ref. [212]. The results in Figure 4.7 show a predom-

Average coordination numbers			
	with Ge	**with Te**	**total**
Ge	1.02 (1.07)	3.15 (3.10)	4.16 (4.17)
Te	3.15 (3.10)	0.07 (0.09)	3.22 (3.19)

(a)

Types of bonds (%)		
	with Ge	**with Te**
Ge	13.8 (14.5)	85.2 (84.3)
Te		1.0 (1.2)

(b)

Table 4.2.: Partial average coordination numbers (a) and percentage of the different types of bonds (b) of model 1 and, in parentheses, of model 2 of a-GeTe after the DFT-PBE relaxation. The data were calculated by integrating the partial pair correlation functions obtained from harmonic phonons up to the cut-off distances given in Figure 4.2.

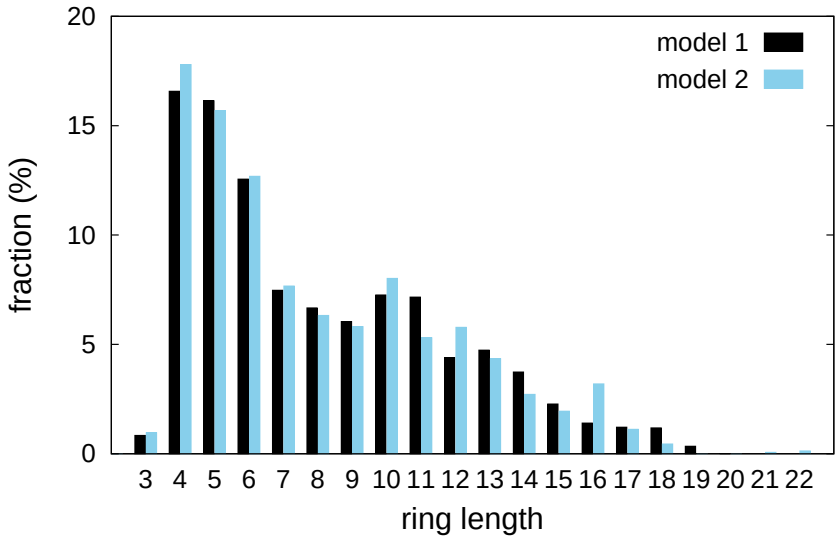

Figure 4.7.: Rings distribution function of the two models of a-GeTe computed according to Ref. [212].

inance of four-membered rings and a high fraction of five-membered rings. Four-membered rings are the building blocks of the cubic rocksalt crystal.
The structural properties of our models of a-GeTe are overall very similar to models generated previously either with the NN potential [14] or by fully DFT simulations [73].

4.2. Electronic structure of a-GeTe

In order to analyse the electronic properties of the models, the electronic DOS was computed from KS orbitals at the supercell Γ-point broadened with a Gaussian function with variance of 27 meV. In order to study the Urbach tails and the defect states in the gap, the Kohn-Sham energies have been computed with the exchange-correlation potential proposed by Engel and Vosko (EV) [237] that it is known to better reproduce the band gap with respect to PBE-GGA functionals and it is less computationally demanding than the hybrid functionals used previously to study electronic states in small models of InSbTe and GaSbTe alloys. The KS energies are obtained by diagonalizing the Kohn-Sham Hamiltonian with the self-consistent density at the PBE level. The energetics and the structural properties are in fact much better described by the PBE than by the EV functional. We verified that the individual KS states are very similar in PBE and EV calculations, but for the fact that the larger gap in EV enhances the localization of defect states in the gap and at the band edges (see Appendix B).
The total and projected DOSs on the different atomic species are reported in Figure 4.8 where

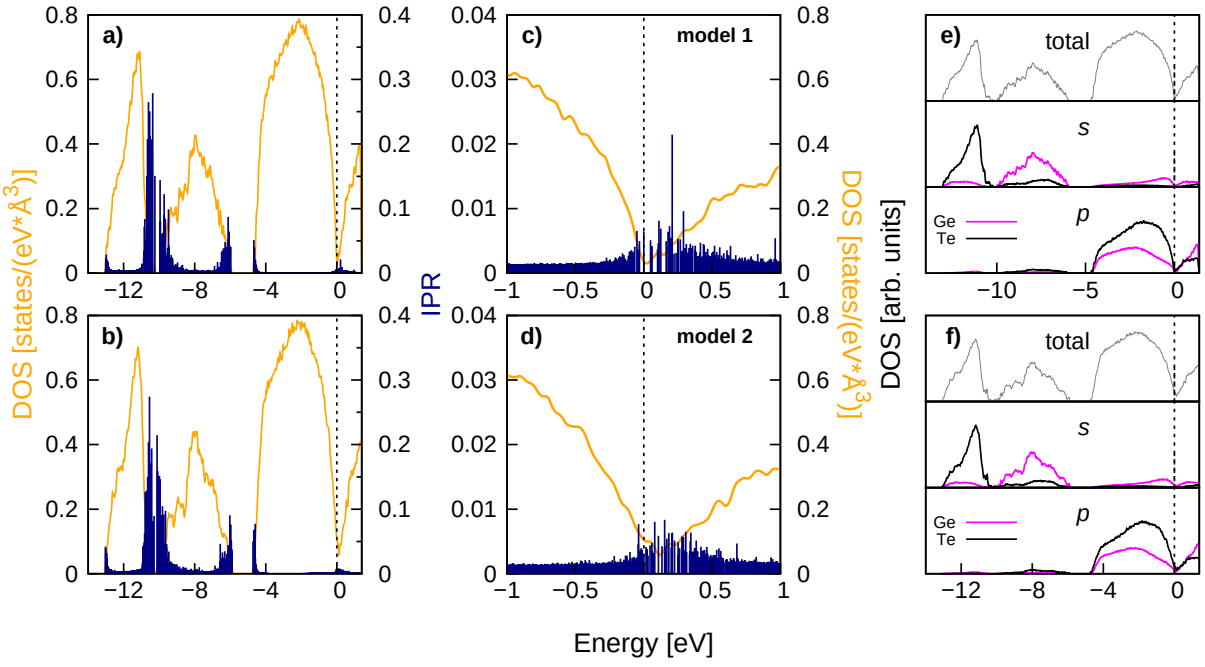

Figure 4.8.: Electronic density of states (Engel-Vosko functional [237]) for the two models of a-GeTe. The KS energies are broadened by Gaussian functions of 27 meV width. The zero of energy corresponds to the top of the valence band. The Inverse Participation Ratio (IPR) is given on the right scale (blue spikes, see text for definition). c)-d) A zooming of the DOS of panel a)-b) close to the band gap. e)-f) Projections on atomic *s* and *p* pseudo wavefunctions of the DOS of panels a)-b). The contribution from *d* pseudo wavefunctions is negligible on the scale of the figure and is omitted.

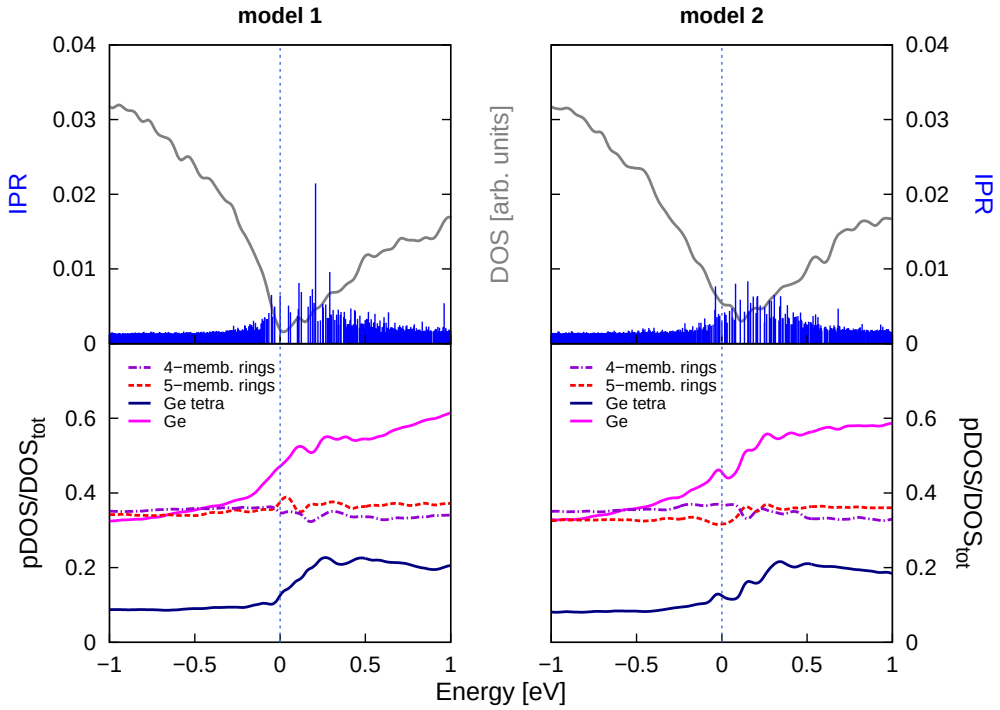

Figure 4.9.: Upper panels: electronic density of states (DOS) around the band gap of a-GeTe models and inverse participation ratio values (IPR, see text). Lower panels: projection of the totals DOS on different types of atoms: tetrahedral Ge atoms, atoms forming four- and five-membered rings. All the projected DOS are normalized with respect to the total DOS. The vertical dashed line indicates the highest occupied KS state which coincides with the zero of energy. The DOS was computed from KS orbitals at the supercell Γ-point broadened with a Gaussian function with variance of 27 meV.

also the IPR value of each electronic state is shown as a measure of the localization (see equation (3.8) for definition). A broad distribution of defect states was found around a pseudogap in the DOS with localization (IPR) decreasing toward the band edges. The number of deep states is larger in the model generated at higher density (model 2). The concentration of defect states in the gap might be overestimated due to the use of the NN potential for the generation of the amorphous models which, albeit very good, is still an approximation to the real DFT-PBE potential energy surface. Still we can gain important information on the nature of defect states in the gap thanks to the good statistics provided by the large size of the simulation cell.
In attempting to find a correlation between the localized states and several possible structural features, we projected the total DOS on different types of atoms such as tetrahedral Ge atoms, atoms in four- and five-membered rings and Ge atoms that form chain of homopolar Ge-Ge bonds. In order to identify which of these structures contribute to the DOS in the region around the band gap, we plotted the projected DOS on different types of atoms divided by the total DOS. Tetrahedral Ge atoms and atoms in rings of different lengths (Figure 4.9) seem not

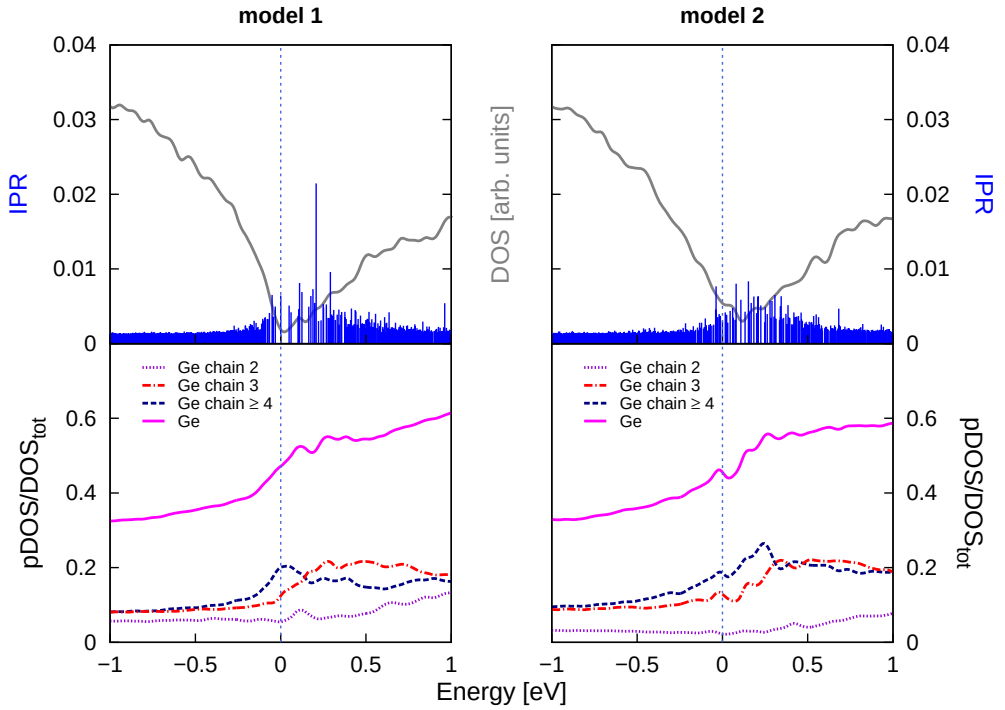

Figure 4.10.: Upper panels: electronic density of states (DOS) around the band gap of a-GeTe models and inverse participation ratio values (IPR, see text). Lower panels: projection of the totals DOS on Ge atoms belonging to chains of Ge-Ge homopolar bonds of different lengths. All the projected DOS are normalized with respect to the total DOS. The vertical dashed line indicates the highest occupied KS state which coincide with the zero of energy. The DOS was computed from KS orbitals at the supercell Γ-point broadened with a Gaussian function with variance of 27 meV.

to give any particular contribution to the electronic states near the valence band edge, while a clear correlation was found instead with chains of Ge-Ge homopolar bonds. Figure 4.10 reports the DOS projected on atoms belonging to Ge-Ge chains of different length showing an increase of the contribution to the total DOS of Ge atoms in chains of four or more Ge atoms in the region around the valence band edge. A Ge atom is considered part of a chain if it is bound to at least an other Ge atom of the chain within a cut-off distance of 3.00 Å. Thus also branched chains and dimers are taken into account. The fraction of Ge atoms forming long chains of four or more atoms is of 43 % in model 1 and 48 % in model 2. Figure 4.11 shows the two most localized Kohn-Sham states of model 2 which are localized on chains of Ge atoms five- and seven-atom long and on other atoms in the neighbourhood of the chain. Note that Ge-Ge chains are also found in models of amorphous GeTe generated by quenching from the melt in DFT-PBE simulations [73] and they are not an artifact of the NN potential. The length of such chains is limited below nine atoms by the size of the DFT simulation cell containing 216 atoms. Still the fraction of Ge atoms in chains with four or more Ge atoms is 30 % in the

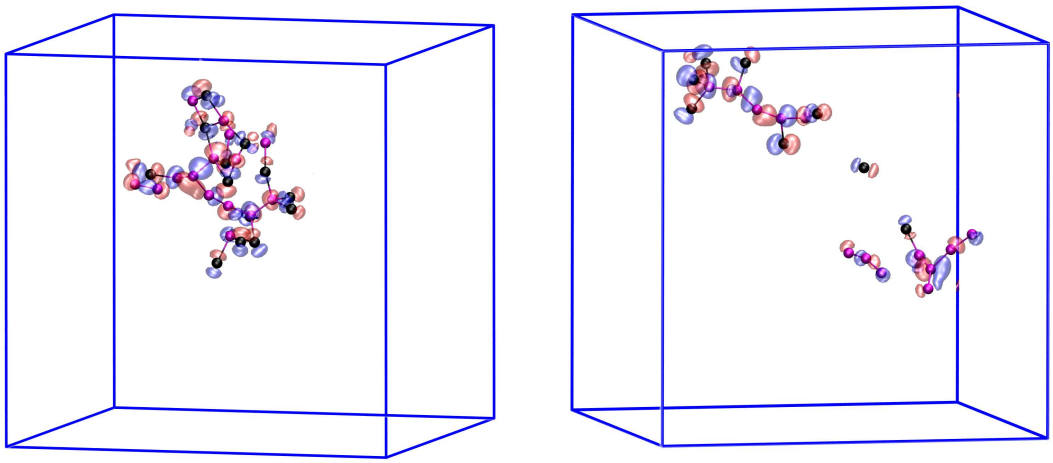

(a) LUMO +7 **(b)** LUMO +10

Figure 4.11.: Visualization of the two most localized Kohn-Sham states with IPR values of (a) 0.0080 and (b) 0.0083 inside the band gap of the a-GeTe model 2 after quenching from the melt. The two states are at energy 0.08 eV and 0.15 eV, respectively. Semitransparent red and blue surfaces render an isosurface with a value of $+0.012357$ a.u. and -0.012357 a.u., respectively. The states are mostly localized on the Ge atoms of Ge-Ge chains highlighted with red spheres, while Te atoms are depicted with black spheres.

216-atom cell. We remark that the chains of Ge-Ge bonds are not isolated from the rest of the amorphous network as Ge atoms belonging to the chains are mostly four-fold coordinated and bonded with Ge atoms and Te atoms as well.

4.3. Structural relaxation and resistance drift

To accelerate the structural relaxations that are supposed to lead to the drift in the electrical resistance, we annealed the two models at 500 K for 1.5 ns in NN-MD simulations and we then optimized the geometry of the resulting model at the DFT-PBE level. The electronic DOS were calculated again with the EV functional The alignment of the DOSs of the two models before and after annealing with respect to lowest energy state at about -14 eV (Figure 4.12), gives and alignment also of the lower edges of the *p*-like bands at about -4.5 eV. From Figure 4.12 it

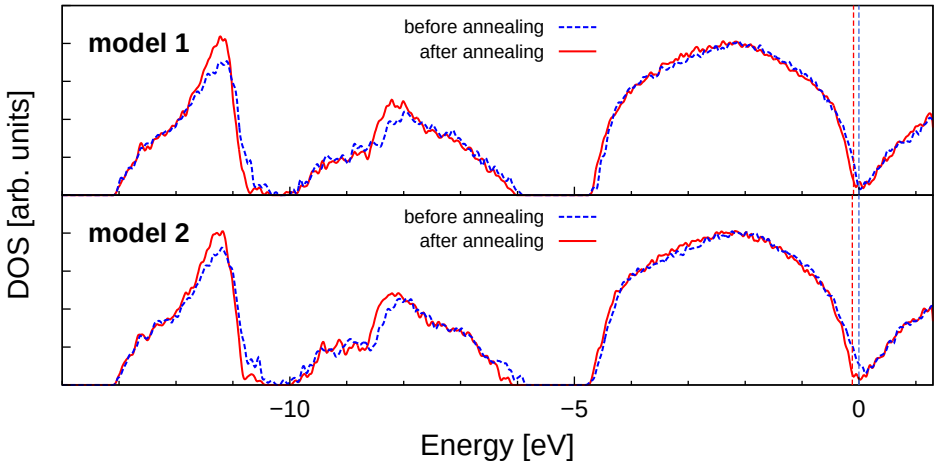

Figure 4.12.: Electronic density of states (DOS) of the two models before (dashed blue line) and after (continuous red line) annealing in the full energy range. The Engel-Vosko functional was used. The same plots for the PBE functional are shown in Figure B.1 of Appendix B. The DOS before and after annealing are aligned at the lowest energy states at about -14 eV which also leads to an alignment of the lower edges of the *p*-like bands at about -4.5 eV. The vertical dashed line indicates the highest occupied Kohn-Sham (KS) state which coincides with the zero of energy before annealing. The DOS was computed from KS orbitals at the supercell Γ-point broadened with a Gaussian function with variance of 27 meV.

can be seen that the position of the highest occupied orbital (HOMO) and of the valence band edge shift towards lower energies after annealing for both models. The redshift of the valence band edge is more evident for the model generated under compressive stress (model 2) which presented a higher number of in-gap defect states before annealing. As shown by the calculated IPR of each electronic state in Figure 4.13, the annealing procedure led to a decrease of the number of in-gap states, in particular in model 2, and to an increase of the localization. The remaining defect states in the band gap are still localized on long chains of homopolar Ge atoms, as demonstrated by the projected DOS in Figure 4.13. Due to the reduction of the Urbach tails, the band gap of a-GeTe widens after the annealing procedure.
Figure 4.14 reports the comparison between the pair correlation functions before and after the annealing of the two models of a-GeTe. The curves were obtained from the relaxed atomic

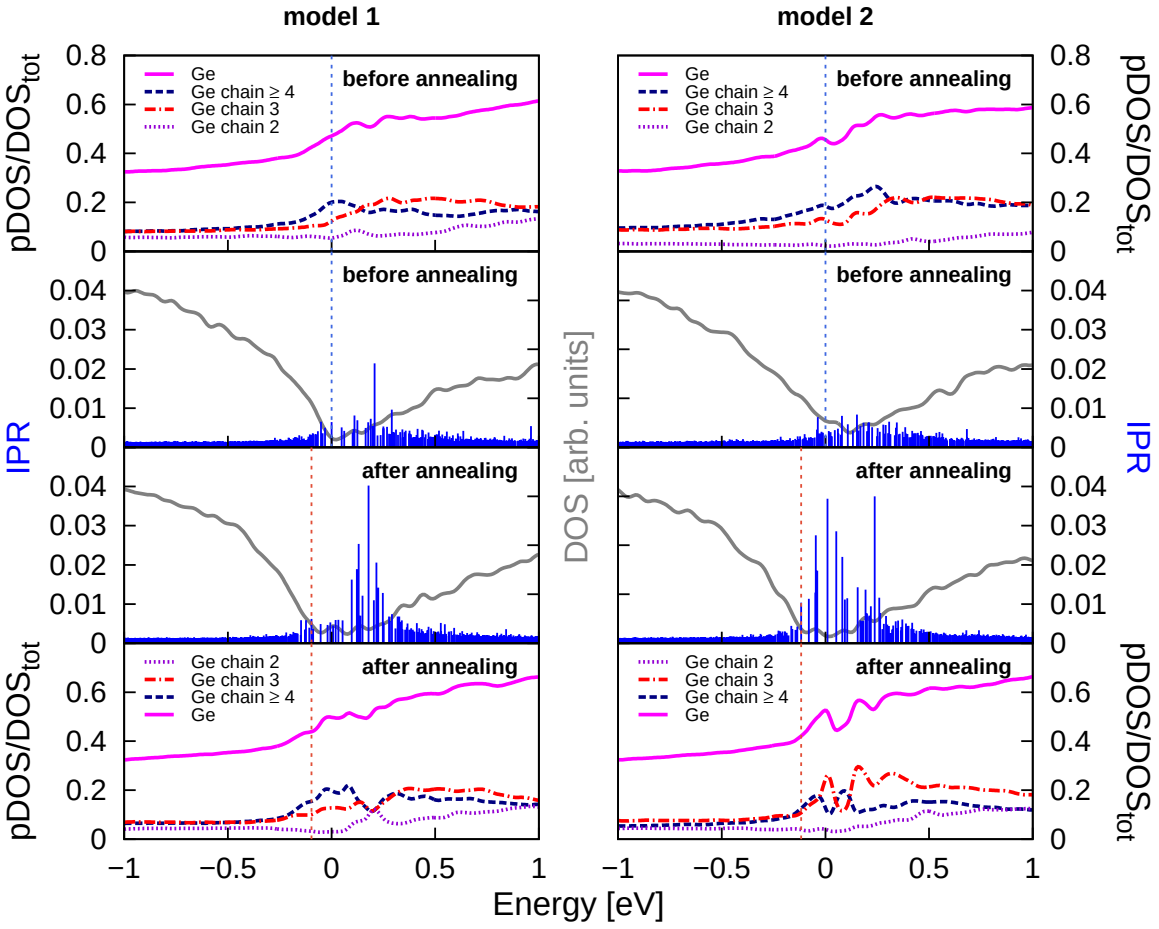

Figure 4.13.: Projection of the electronic density of states (DOS) on Ge atoms belonging to Ge chains of different lengths normalized to the total DOS (model 1 and model 2 in the left and right panels), total DOS and the Inverse Participation Ratio (IPR, see text) for the two models of a-GeTe before annealing (upper panels) and after annealing at 500 K (lower panels). The Engel-Vosko functional was used, the corresponding plots for the PBE functionals are given in Figure B.2 of Appendix B. The DOS before and after annealing are aligned at the lowest energy states at about -14 eV as shown in Figure 4.12 which also leads to an alignment of the lower edges of the *p*-like bands at about -4.5 eV. The vertical dashed line indicates the highest occupied KS state which coincide with the zero of energy before annealing. The DOS was computed from KS orbitals at the supercell Γ-point broadened with a Gaussian function with variance of 27 meV.

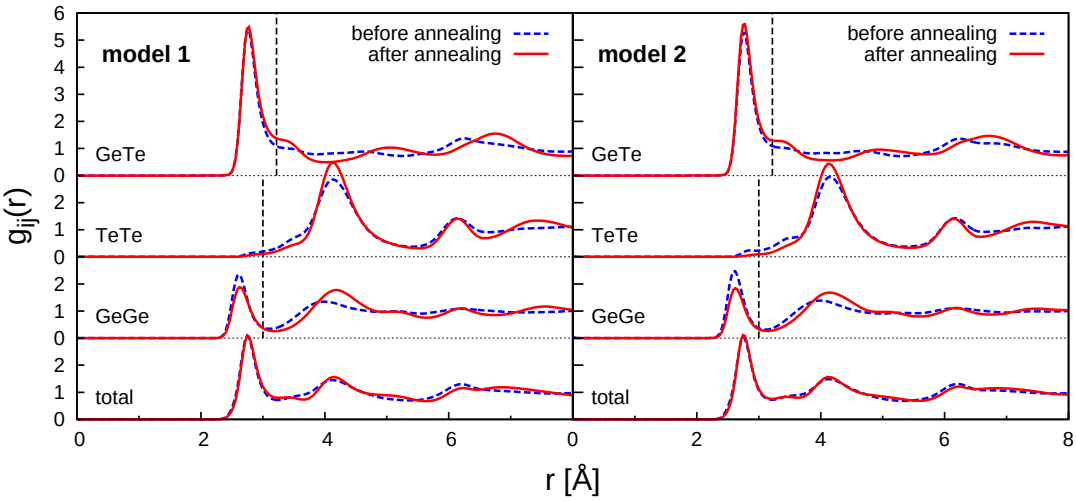

Figure 4.14.: Partial pair correlation functions of a-GeTe before and after annealing simulations computed for model 1 and model 2 optimized at the DFT-PBE level with harmonic phonons (see text). Vertical lines are the cut-off used to define the bonds. The shoulder at about 3.2 Å in $g_{GeTe}(r)$ is due to partial crystallization.

positions at the DFT-PBE level and harmonic phonons as described above. The plots clearly show a decrease of Ge-Ge homopolar bonds. The radial distribution of Ge-Te and Te-Te pairs remain almost unchanged, but for a shoulder at about 3.2 Å in the Ge-Te pair correlation function due to partial crystallization of the models. In fact, the annealing the a-GeTe at 500 K also induced the formation of small crystallites, similarly to what was observed in previous simulations of the homogeneous crystallization [87]. In the two models after annealing, an overall fraction of crystalline atoms of about 10 % and 13 % was found for model 1 and model 2, respectively. Although a fraction of our models crystallized after annealing, a reduction of atoms belonging to longer chains (at least four Ge atoms) was still observed also by considering the subset of atoms that do not crystallize as shown in Table 4.3. Overall, the length of Ge chains reduces after annealing, the number of long chains decreases, while shorter chains increase in number (Figure 4.15).

We mention that the fraction of crystalline atoms was found from the local order parameter Q_6 for crystallinity introduced in Refs. [238, 239]. For the i-th atom, the $Q_6(i)$ parameter is defined by

$$
\begin{aligned}
Q_6(i) &= \sum_{j=1}^{N_b(i)} \frac{\sum_{m=-6}^{6} q_{6m}(i)\, q_{6m}^{*}(j)}{(\sum_{m=-6}^{6} |q_{6m}(i)|^2)^{1/2} (\sum_{m=-6}^{6} |q_{6m}(j)|^2)^{1/2}}, \\
q_{6m}(i) &= \frac{1}{N_b(i)} \sum_{j=1}^{N_b(i)} Y_{6m}(\hat{\mathbf{r}}_{ij})
\end{aligned}
\tag{4.3}
$$

Ge-Ge structures in a-GeTe

	Ge-Ge bonds (%)	Ge in chains ($\geq$ 4) (%)
model 1	13.9	43.2
model 1 annealed	10.2	34.3
model 2	14.5	48.5
model 2 annealed	10.3	31.6
model 2 metadyn.	12.6	39.6

Table 4.3.: Fraction of Ge-Ge bonds (%) over the total number of bonds and fraction of Ge atoms in Ge-Ge chains with four or more Ge atoms for the two models of a-GeTe (model 1 and model 2) before and after annealing at 500 K and for model 2 after a metadynamics simulation.

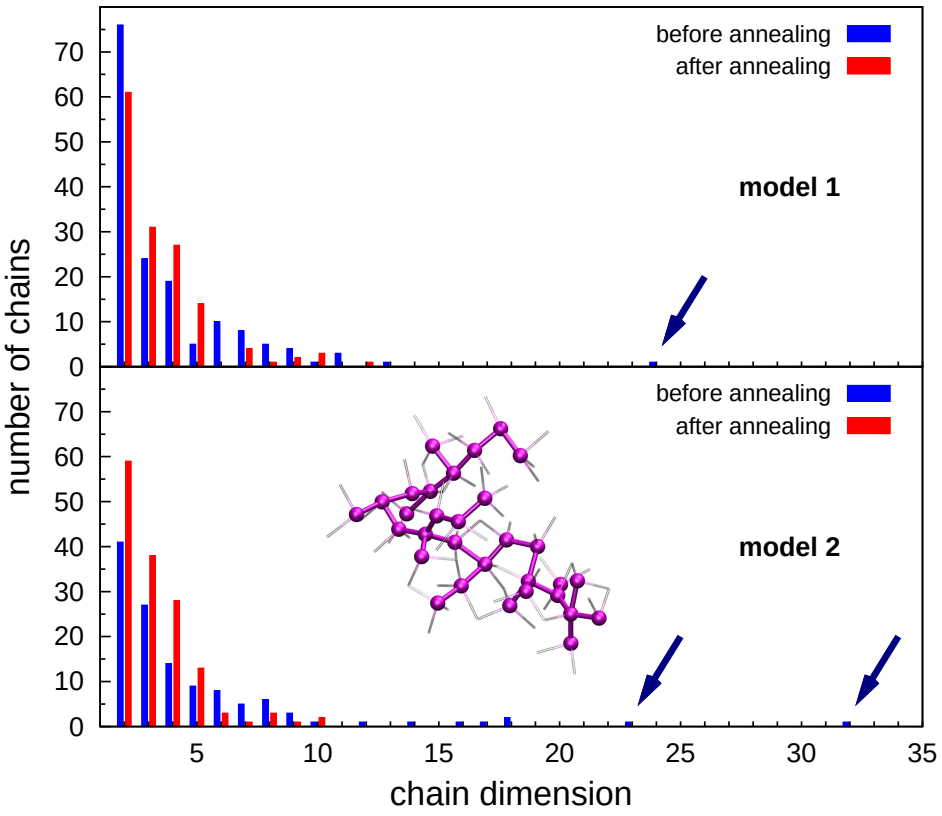

Figure 4.15.: Distribution of the number of Ge-Ge chains as a function of the number of atoms in the (also branched) chain for the two models of a-GeTe before and after annealing. The Ge atoms are considered bonded when their distance is shorter than 3.0 Å as assigned from the Ge-Ge pair correlation function of the amorphous phase (cf. Figure 4.2). A chain of homopolar Ge-Ge bonds is shown in the inset. Long chains are indicated by arrows.

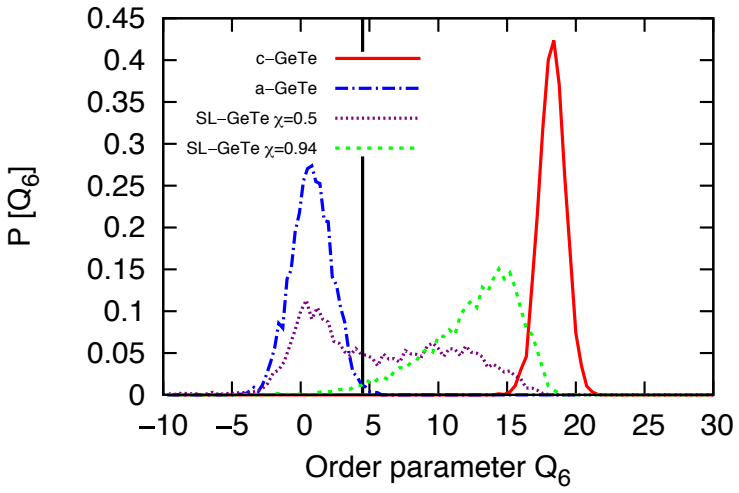

Figure 4.16.: Distribution of the order parameter for crystallinity Q_6 for a snapshot of a crystalline and amorphous models (4096-atom large) in a 300 K simulation at their theoretical equilibrium densities and two snapshots of previous simulations at 675 K in which a fraction ($\chi = 0.5$ and $\chi = 0.94$) of atoms is crystallized (from Ref. [87]).

where $Y_{6m}(\hat{\mathbf{r}}_{ij})$ are the spherical harmonics of the polar angles defined by the versor $\hat{\mathbf{r}}_{ij}$ which links atoms i and j. The index j runs over the $N_b(i)$ neighbouring atoms which include the third coordination shell of crystalline GeTe at its theoretical equilibrium density (5.3 Å cut-off). We define as crystalline an atom with $Q_6 > 4.5$. These choices ensure that atoms at the interface between the crystalline nuclei and the disordered phase are also considered as crystalline as shown in Figure 4.16.

In order to obtain an independent, compelling demonstration that the removal of Ge-Ge chains leads to a reduction of gap states we performed NN metadynamics simulations [177]. This technique, described in Section 2.8 allows breaking the Ge-Ge bonds in an affordable simulation time even at lower temperatures where crystal nucleation does not occur. This method has been applied to study several chemical reactions and structural transformations at surfaces, in the gas phase and in the bulk [179, 240]. The method is based on a coarse-grained, non-Markovian dynamics in the manifold spanned by few reaction coordinates named collective variables, biased by a history-dependent potential, which drives the system towards the lowest saddle point. In our case, we chose two collective variables defined by the partial coordination numbers Ge-Ge and Ge-Te for atoms in Ge-Ge chains. We performed a chain of subsequent simulations by changing the subset of atoms included in the definition of the collective variables in order to progressively remove different Ge-Ge chains. The isotropic Gaussian functions of height 0.124 eV and width of 50 meV was added every 100 MD steps. After a well-tempered [179, 240] metadynamics simulation 4 ps long at 300 K, the geometry of the resulting model was optimized at the DFT-PBE level. The final configuration was about 10.8 eV (1728-atom) lower in energy than the initial one optimized at DFT-PBE level before

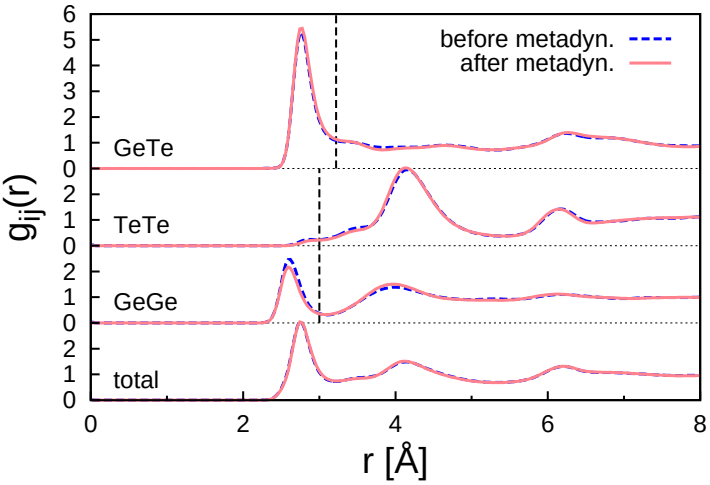

Figure 4.17.: Partial pair correlation functions of a-GeTe before and after metadynamics simulations (model 2) computed for the model optimized at the DFT-PBE level and with harmonic phonons (see text). Vertical lines are the cut-off distances used to define the bonds.

the metadynamics was applied (model 2). In the final state after metadynamics, a sizable fraction of long Ge-Ge chains were indeed removed as shown in Table 4.3 and no crystallites were formed. The reduction of homopolar Ge-Ge bonds can be seen also from the comparison of the pair and correlation functions before and after the metadynamics run (Figure 4.17). The distribution of the homopolar Ge chain lengths before and after metadynamics is shown in Figure 4.18. The number of long chains clearly reduces after metadynamics simulations, while the number of short chains increases. Overall, the number of Ge atoms involved in homopolar chains of four or more Ge atoms decreases after the metadynamics run as shown in Table 4.3.
The electronic DOS of model 2 after metadynamics was calculated with the EV functional on the relaxed structure at DFT-PBE level. The results, compared with the electronic properties of model 2 before metadynamics are reported in Figure 4.19. A shift of the HOMO state towards lower energies occurred after metadynamics simulations, although it is less evident with respect to the annealed models. A zooming of the gap region of model 2 before and after metadynamics is provided in Figure 4.20 where a shift of the valence band edge towards lower energy and a gap widening due to the reduction of Urbach tails is visible for the model after metadynamics simulations. From the calculation of the IPR (Figure 4.20) it is possible to see that the decrease in the number of Ge-Ge chains obtained from metadynamics clearly reduces the states in the gap and enhances their localization. The remaining states in the gap are still localized mostly on Ge-Ge chains. The removal of Ge-Ge chains thus leads to an overall widening of the band gap and reduction of Urbach tail which can explain the drift in electrical resistance.
After the annealing process the concentration of tetrahedral Ge atoms decreases from 31 %

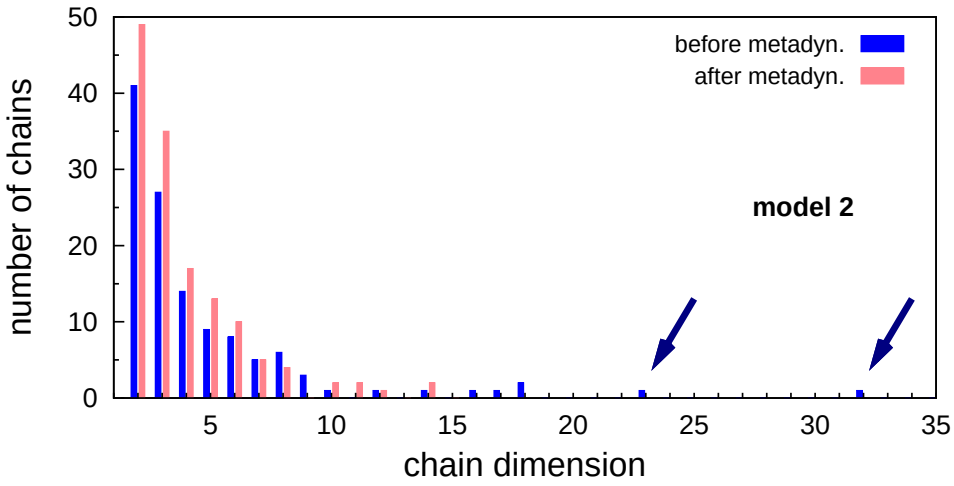

Figure 4.18.: Distribution of the number of Ge-Ge chains as a function of the number of atoms in the (also branched) chain for the model 2 of a-GeTe before and after metadynamics. The Ge atoms are considered bonded when their distance is shorter than 3.0 Å as assigned from the Ge-Ge pair correlation function of the amorphous phase (cf. Figure 4.2 and 4.17).

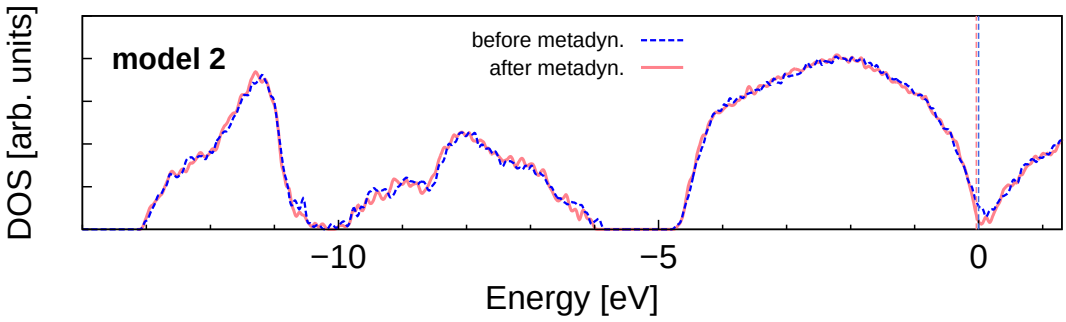

Figure 4.19.: Electronic density of states (DOS) of model 2 of a-GeTe before (dashed line) and after (continuous line) metadynamics simulations in the full energy range. The Engel-Vosko functional was used. The DOS before and after annealing are aligned at the lowest energy states at about -14 eV which also leads to an alignment of the lower edges of the *p*-like bands at about -4.5 eV. The vertical dashed line indicates the highest occupied Kohn-Sham (KS) state which coincides with the zero of energy before annealing. The DOS was computed from KS orbitals at the supercell Γ-point broadened with a Gaussian function with variance of 27 meV.

to 25 % in model 1 and from 29 % to 26 % in model 2. After metadynamics simulations, the fraction of tetrahedral Ge atoms only slightly reduces from 29 % to 28 %. Possibly due to the still small size of our simulation cell, we have thus not found a clear correlation between a reduction of tetrahedra and a reduction of states in the gap. However, since Ge-Ge homopolar bonds favour a tetrahedral coordination for germanium (see Figure 4.5), the reduction of homopolar bonds is probably linked to the reduction of tetrahedral structures. Our results are

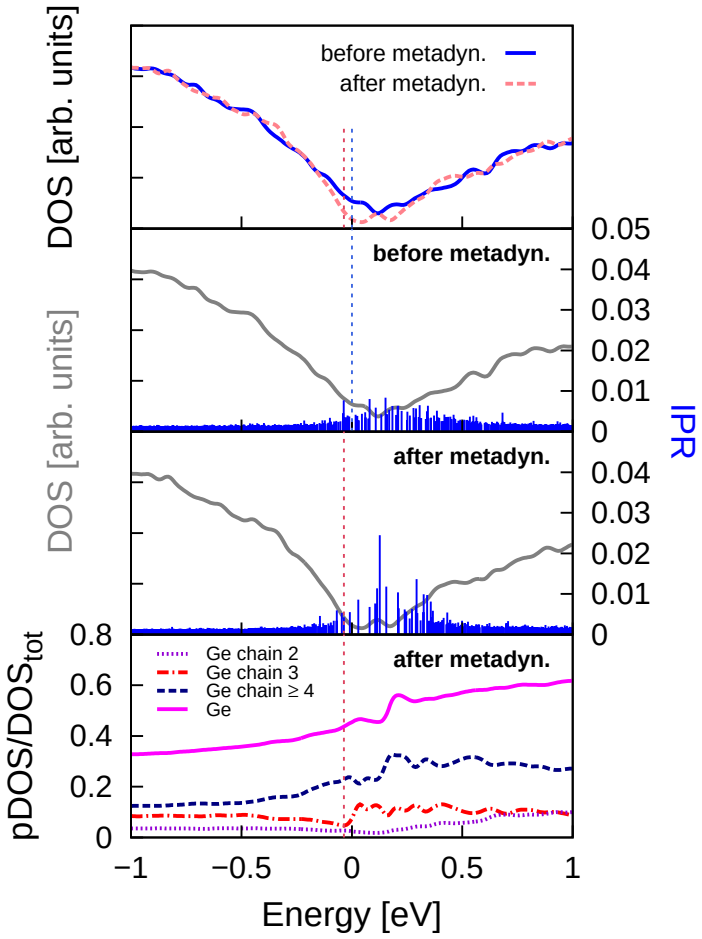

Figure 4.20.: Upper panel: electronic density of states (DOS) close to the band gap of model 2 of a-GeTe before (dashed line) and after (continuous line) metadynamics simulations (zooming of Figure 4.19). Lower panels: inverse participation ratio (IPR) superimposed to the DOS for the model before and after metadynamics simulations and projection of the electronic DOS on Ge atoms belonging to Ge chains of different lengths normalized to the total DOS for the model after metadynamics simulations; the corresponding plot before metadynamics is shown in the upper right panel of Figure 4.13. The Engel-Vosko functional was used, the corresponding plots for the PBE functional are given in Figure B.3 in Appendix B. The DOS are aligned with respect to the lowest energy states of the model before and after metadynamics. The zero of the energy corresponds to the highest occupied orbital (HOMO) of the model before metadynamics. The dashed vertical lines indicate the position of the HOMO state for the two models. The DOS were computed from KS orbitals at the supercell Γ-point broadened with a Gaussian function with variance of 27 meV.

thus in agreement with recent XANES measurements showing a decrease of the fraction of tetrahedra in aged GST models [140, 141].
It is interesting to note that the same structural features (Ge-Ge chains), identified here as the source of the resistance drift in the amorphous phase below the glass transition T_g, have also been shown to be involved in the dynamics of the supercooled liquid above T_g [89]. As discussed in Section 1.2.2, recent NN-MD simulations on large GeTe models have shown the emergence of dynamical heterogeneities in supercooled liquid GeTe, responsible for the breakdown of the Stokes-Einstein relation between viscosity and diffusivity [89] (see Section 1.2.1). Such a feature is actually the ultimate source of the high crystallization speed of phase change chalcogenides exploited in PCM [79]. The NN-MD simulations revealed that dynamical heterogeneities in supercooled liquid GeTe originate from structural heterogeneities in the form of chains of homopolar bonds. The outcomes reported here further demonstrate at the atomistic level a connection between the fragility of the supercooled liquid and the extent of structural relaxations in the glass. This connection has been recently discussed for GeAsSe alloys in Ref. [90] on the basis of the Adam-Gibbs model of the fragility. The Adam-Gibbs theory states that the viscosity η of a liquid is related to the configurational entropy S_c by the relation

$$\eta = \eta_0 e^{\frac{C}{TS_c}} \tag{4.4}$$

where C is a constant. The plot of Figure 4.21 represents the behaviour of the configurational entropy with respect to temperature extrapolated for temperatures below T_g for three hypothetical glasses with different fragility. The configurational entropy $S_c(T)$ scaled to its value at T_g $S_c(T_g)$, is reported sketched as a function of temperature in Figure 4.21. The dashed hor-

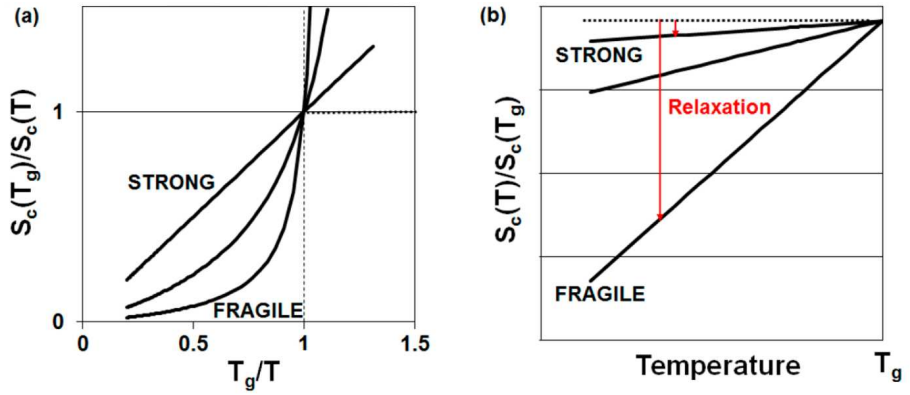

Figure 4.21.: Schematic representation of the ratio between the configurational entropy S_c at temperatures T_g and T for three hypothetical glass formers with fragility ranging from 16 to 200. In panel a) the ratio $S_c(T_g)/S_c(T)$ mimic a modified Vogel-Tamman-Fulcher equation (1.1). The reciprocal quantity in panel b) highlights the driving force for structural relaxations below T_g. From Ref. [90].

izontal line is the value of the frozen configurational entropy of a glass cooled down to T_g, while the solid lines represent the equilibrium entropy of the corresponding liquids cooled infinitely slowly.
Below T_g, the difference between $S_c(T_g)$ and $S_c(T)$ is the driving force for structural relaxations. This model predicts that a larger fragility of the supercooled liquid would correlate with a larger propensity for structural relaxations as the temperature drops below T_g.
Our NN simulations on amorphous GeTe demonstrate indeed that the same structural features responsible for the high mobility close to T_g, typical of fragile liquids, are also responsible for the structural relaxations in the glass that generate the drift in the electrical resistance. These results suggest that, in the search of better performing materials for PCM, a compromise must be reached between the requests of minimization of the resistance drift and of maximization of the crystallization speed in the SET operation. These two properties in fact originate from the same structural features that control both the mobility in the supercooled liquid (where crystallization takes place) and the structural relaxations in the glass responsible for the resistance drift.

Conclusions

In this thesis, we presented a study of the structural and electronic properties of different phase change alloys proposed for PCM applications. In particular, we addressed two different problems by means of atomistic simulations: *i*) the structural analysis of InSbTe and GaSbTe alloys, in order to find a correlation between the structural features of the amorphous phase and the high crystallization temperature and *ii*) the study of the drift phenomenon in amorphous models of GeTe aiming at uncovering the atomistic origin of this process.
Concerning the first issue, the amorphous phase of alloys with composition $In_3Sb_1Te_2$, $In_{13}Sb_{11}Te_3$ and $Ga_4Sb_6Te_3$ have been studied by Density Functional (DFT) molecular dynamics simulations. These alloys have been proposed for high temperature applications because of their high crystallization temperature that ensures a good thermal stability of the amorphous phase at temperatures above 100 °C. Preliminary simulations on the InSb binary system were initially performed by generating 216-atom models of the amorphous phase by quenching from the melt with both the PBE and the BLYP exchange and correlation functionals. The structural properties of a-InSb turned out to be strongly dependent on the choice of the functional. In particular, the model generated with the BLYP functional has a mainly tetrahedral coordination, similar to crystalline InSb in the zincblende phase, while with the PBE functional a mainly octahedral-like structure is obtained. By comparing the results with experimental diffraction data available for a-InSb, the BLYP functional well reproduces the experimental pair correlation functions with an error on the bond lengths less than 1 %, while PBE functional overestimate the bond lengths by about 5 %. These results seem to indicate that the PBE functional does not reproduce well the structure of this system because of a close competition between tetrahedral and octahedral structures. In fact, the zincblende crystal of InSb, stable at normal pressure, transforms into a cubic rocksalt structure under moderate pressure.
A competition between octahedral-like and tetrahedral structures is present also in the ternary compound $In_3Sb_1Te_2$. $In_3Sb_1Te_2$ crystallizes in a cubic rocksalt phase with octahedral environments, while the two binary compounds InSb and InTe of which the ternary alloy is made of have a tetrahedral bonding geometry in the crystalline phase.
We generated models about 300 atoms large of amorphous $In_3Sb_1Te_2$ by quenching from the melt with either the PBE or the BLYP functional. Models obtained with the PBE functional are mainly octahedral-like with a minority fraction of tetrahedral sites which increases by decreasing the density. The model obtained with the BLYP functional is instead mainly tetrahedral. In view of the results obtained on the binary InSb compound we must consider

more reliable the models obtained with the BLYP functional. Unfortunately, no experimental data on the structure of amorphous InSbTe alloys are available yet. The amorphous phase of $In_3Sb_1Te_2$ turns out to be a nanoscale mixture of InTe and InSb binary systems with very few Sb-Te bonds.

A similar competition between octahedra and tetrahedra is present in the $Ga_4Sb_6Te_3$ alloy. The $Ga_4Sb_6Te_3$ composition actually lies on the pseudo-binary GaSb-Sb_2Te_3 tie-line. The ternary system crystallizes in a rhombohedral structure which has not been fully resolved experimentally, but which is believed to present octahedral environments similarly to the Sb_2Te_3 crystal. The GaSb binary compound crystallizes instead in a zincblende (tetrahedral-like) geometry. In spite of this, the models of the amorphous phase of $Ga_4Sb_6Te_3$ that we generated from the melt (with the BLYP functional) show very few Sb-Te bonds. The amorphous network should actually be better seen as a nanoscale mixture of the two binaries GaSb and GaTe which both have a tetrahedral-like bonding geometry. In fact, the bonding in amorphous $Ga_4Sb_6Te_3$ turns out to be mostly tetrahedral as well. A partial, nanoscale segregation of Sb is also found at this composition.

The predominance of tetrahedral structures in a-$In_3Sb_1Te_2$ and a-$Ga_4Sb_6Te_3$, which are absent in the ternary crystals, might hinder the crystallization process concurring in the enhancement of the thermal stability of the amorphous phase with respect, for instance, to $Ge_2Sb_2Te_5$ where the crystal and the amorphous are both mostly octahedral-like.

Regarding the resistance drift, we studied the evolution in time of the electronic states of models of a-GeTe. In-gap states and defect states close to the band edges (Urbach tails) actually control the conductivity of the amorphous phase. In order to have a sufficiently good statistics on the distribution of in-gap states, we generated large, 1728-atom models of a-GeTe by quenching from the melt within classical molecular dynamics simulations by using a Neural Network potential. After a DFT relaxation, the models revealed several defect states in the band gap and at band edges mainly localized on chains of homopolar Ge-Ge bonds. By annealing the models at 500 K in order to accelerate the drift process, a reduction in the number of Ge-Ge bonds and of the length of Ge-Ge chains was found, resulting in a reduction of the size of Urbach tails and in the number in-gap states. As a consequence, the band gap widens, resulting in an increase of the resistance. These results allowed us to propose a drift mechanism based on the removal of Ge-Ge bonds due to the structural relaxation process that occurs during the aging of the amorphous phase. To further support this argument, we performed metadynamics simulations in order to reduce the number of Ge-Ge bonds at 300 K in an affordable simulation time. The model obtained after metadynamics simulations presents a lower fraction of Ge-Ge bonds, a smaller number of in-gap states and a larger band gap, confirming our proposed mechanism for the drift.

Actually, previous NN-MD simulations revealed that chains of homopolar Ge-Ge bonds are present also in supercooled liquid GeTe and that they are responsible for the high atomic mobility close to the glass transition temperature T_g which is the ultimate origin of the very high

crystallization speed exploited in the device. Our results show that the same structural features are responsible both for the high crystallization speed in the supercooled liquid above T_g and for the structural relaxations leading to the resistance drift below T_g. In the search of new materials for PCMs, a compromise should then be found between fast switching and low drift coefficients.

A. InSb

A.1. Test for PBE pseudopotentials

We started the analysis of InSb by testing the pseudopotentials for In and Sb. To this end we computed the equation of state of crystalline InSb in the zincblende and rocksalt phases. We used the general gradient approximation (GGA) Perdew-Burke-Ernzerhof PBE [151] exchange and correlation functional and GTH [158, 159] pseudopotentials with five valence electrons for Sb and with three or thirteen electrons for In used in the CP2K MD simulations. The calculations were performed with the QUANTUM-ESPRESSO suite of programs with a $16 \times 16 \times 16$ Monkhorst-Pack mesh [194] for the integration of the Brillouin zone and a plane-wave cut-off of 60 Ry in the case of three valence electrons for In and of 80 Ry when the semi-core electrons are included in the valence.
The calculated equations of state of crystalline InSb are reported in Figure A.1, where the energy-volume points has been fitted with a Murnaghan function that express the energy E as a function of the volume V as

$$E(V) = E_0 + \frac{B_0}{B_0'} V \left[\frac{(V_0/V)^{B_0'}}{B_0' - 1} + 1 \right] - \frac{B_0 V_0}{B_0' - 1} \tag{A.1}$$

where E_0 and V_0 are the energy and volume at equilibrium, B_0 is the bulk modulus at V_0 and B_0' is the first derivative of the bulk modulus with respect to pressure at V_0. The results of the fitting are listed in Table A.1 where a comparison with experimental data is also provided. The inclusion of semicore d states of In does not change the structural properties sizably. The error with respect to the experimental value on the lattice parameter is about 2 %.

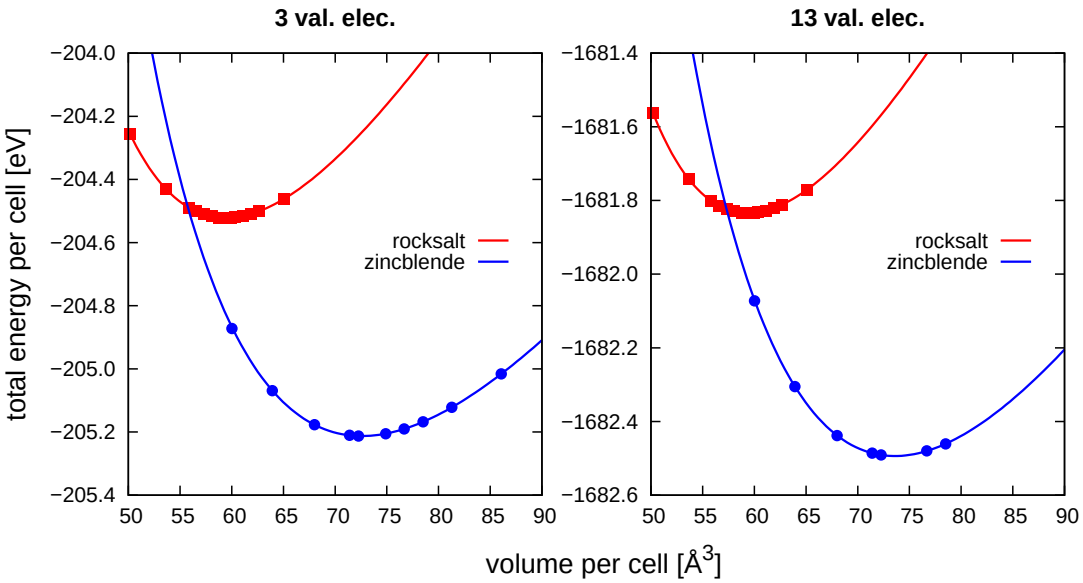

Figure A.1.: Equation of state of crystalline InSb in the zincblende (blue, circles) and in the rocksalt (red, squares) phase. The data were obtained with the PBE functional and fitted with a Murnaghan function (equation A.1). Three (left panel) or thirteen (right panel) valence electrons were considered for In.

c-InSb equation of state (PBE)

	3 val. elec.			13 val. elec.			exp.	
	E_0 [eV]	a [Å]	B_0 [GPa]	E_0 [eV]	a [Å]	B_0 [GPa]	a [Å]	B_0 [GPa]
Zincblende	-205.213	6.622	34.6	-1682.49	6.652	36.3	6.47937(3) [183]	46.50 [183]
Rocksalt	-204.521	6.195	42.5	-1681.83	6.193	43.8	6.12 [184]	–

Table A.1.: Equation of state data of crystalline InSb in the zincblende and rocksalt phases obtained from the Murnaghan fitting of the energy-volume plot of Figure A.1 calculated with PBE functional. E_0 represents the total energy of the unit cell containing two atoms, a is the lattice parameter and B_0 the bulk modulus. Experimental values are also given for comparison. The rocksalt phase can be experimentally recovered at normal conditions.

A.2. Test for BLYP pseudopotentials

In Section 3.1 it has been shown that the PBE exchange and correlation functional generate mainly octahedral-like amorphous models of InSb, in contrast with the experimental data. A new model with the GGA BLYP [152] exchange and correlation functional was then generated. In order to test the BLYP pseudopotentials for In and Sb, we repeated the calculation of the equation of state of the zincblende and the rocksalt phase. We used GTH [158, 159]

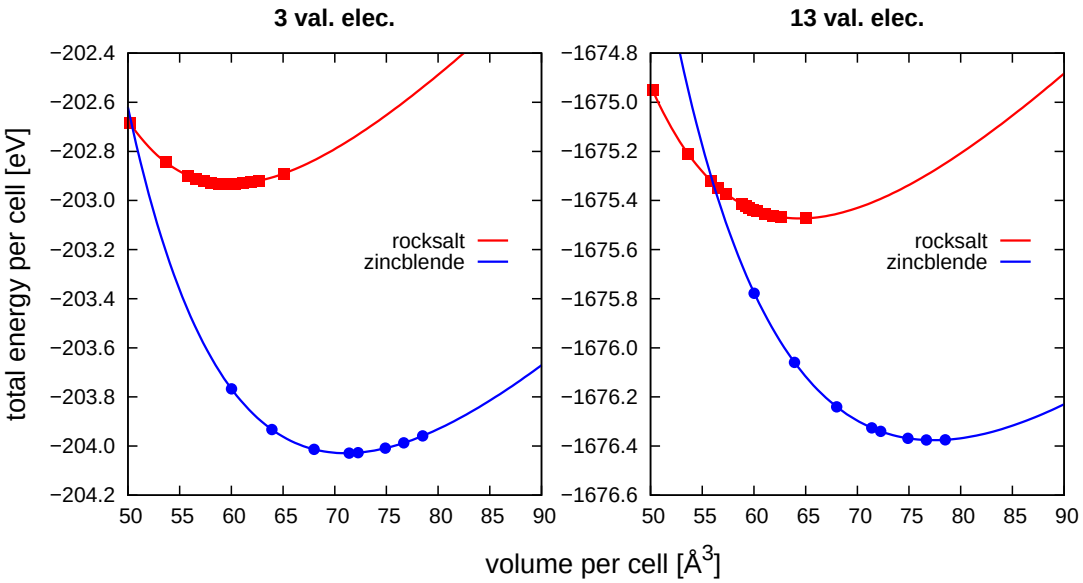

Figure A.2.: Calculated equation of state of crystalline InSb in the zincblende (blue, circles) and in the rocksalt (red, squares) phase. The data were obtained with the BLYP functional and fitted with a Murnaghan function A.1. Three (left panel) or thirteen (right panel) valence electrons were considered for In.

pseudopotentials with three or thirteen valence electrons for In and with five valence electrons for Sb. The other details are the same of the PBE calculations in the previous section. The BLYP equations of state of crystalline InSb are reported in Figure A.2, The parameters of the corresponding Murnaghan fit are listed in Table A.2. By including the semicore electrons

c-InSb equation of state (BLYP)

	3 val. elec.			**13 val. elec.**			**exp.**	
	E_0 [eV]	a [Å]	B_0 [GPa]	E_0 [eV]	a [Å]	B_0 [GPa]	a [Å]	B_0 [GPa]
Zincblende	-204.029	6.575	34.9	-1676.38	6.764	29.9	6.47937(3) [183]	46.50 [183]
Rocksalt	-202.933	6.210	35.7	-1675.47	6.364	33.0	6.12 [184]	–

Table A.2.: Equation of state data of crystalline InSb in the zincblende and rocksalt phases obtained from the Murnaghan fitting of the energy-volume plot of Figure A.2 calculated with BLYP functional (see Table A.1).

of In among valence electrons, one obtains worse results with respect to considering only three valence electrons. Compared to PBE, the BLYP functional better describes the zincblende structure giving an error of 1.5 % in the lattice constant with respect to experiments.

A.3. Effect of the van der Waals interactions on the structure of a-InSb

We generated an amorphous model of InSb by quenching from the melt from 1000 to 300 K in 100 ps through *ab-initio* molecular dynamics simulations at the fixed density of 0.0273 atom/Å^3 (5.355 g/cm^3) by using the BLYP functional supplemented by the van der Waals (vdW) interactions according to Grimme [202]. The density and the other parameters used in the dynamics were the same employed for the model presented in Section 3.1. The

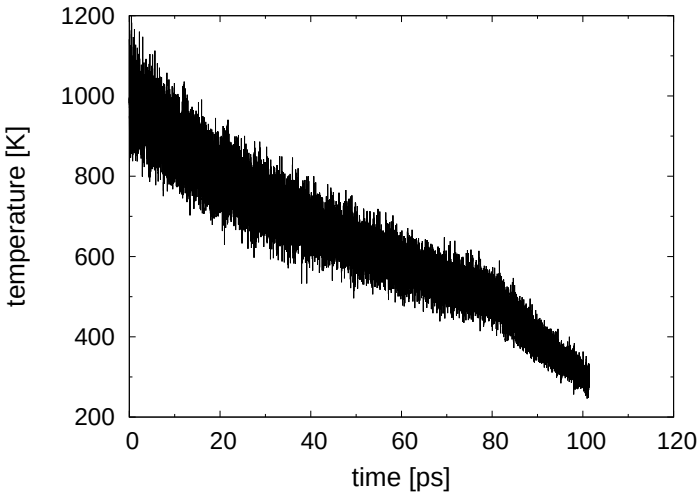

Figure A.3.: Evolution of the temperature during the quench of a 216-atom model of amorphous InSb. The system has been cooled down from 1000 to 300 K in about 100 ps. The BLYP functional and a TZVP basis set have been used supplemented by van der Waals interactions.

quenching protocol is shown in Figure A.3.

The partial and total pair correlation functions are compared in Figure A.4 with those obtained for the BLYP model without vdW interactions. The total PCF is very similar between the two models, but for a slight increase in the In-In and Sb-Sb bonds. This effect can be quantified by computing the partial pair correlation numbers (Table A.3a) of the system by integrating the partial pair correlation functions up to the cut-off distances of 3.20 Å, 3.20 Å and 3.30 Å for In-In, Sb-Sb and In-Sb pairs, respectively. An increase of about 3 % of the In-In and Sb-Sb homopolar bonds was found when the vdW interactions are considered. However, the coordination numbers distributions of the two systems are very similar (Figure A.5). The change in the fraction of homopolar bonds is, however, within the size of the fluctuations we expect due to the finite size of the simulation cell as it has been quantified for Ge-Ge bonds in a-GeTe in Ref. [14].

The bond angle distribution functions and the distribution of the q order parameter are shown in Figure A.6 and A.7 to be compared with the corresponding data for the BLYP model with-

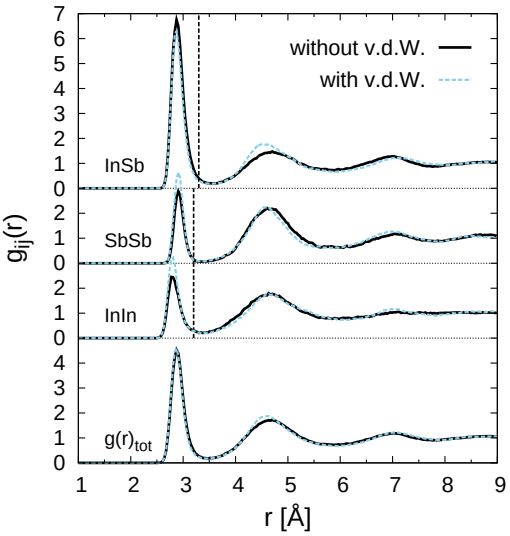

Figure A.4.: Total and partial correlation functions of 216-atom models of a-InSb generated with (dashed blue line) and without (black continuous line) van der Waals interactions. The models were obtained by quenching from the melt in 100 ps with the BLYP functional. The dashed vertical lines indicate the bonding cut-off distances used in the other structural analysis which are 3.20 Å, 3.20 Å and 3.30 Å for In-In, Sb-Sb and In-Sb pair, respectively. The data were obtained by averaging over a 10 ps long trajectory at 300 K.

Average coordination numbers

	with In	with Sb	total
In	1.19 (1.01)	2.53 (2.82)	3.72 (3.83)
Sb	2.53 (2.82)	1.16 (0.95)	3.69 (3.78)

(a)

Types of bonds (%)

	with In	with Sb
In	16.0 (13.2)	68.3 (74.2)
Sb		15.6 (12.6)

(b)

Table A.3.: (a) Partial average coordination numbers and (b) percentage of the different types of bonds in the BLYP a-InSb models generated with and, in parentheses, without van der Waals interactions. The data were calculated by using the cut-off distances given in Figure A.4.

out vdW correction. By integrating the distributions for four-fold coordinated In and Sb atoms from 0.8 to 1.0 as discussed in Section 3.1, the fraction of tetrahedral In and Sb atoms turned out to be about 66 % and 54 %, respectively, which are very close to the values of 68 % and 52 % obtained for In and Sb atoms, respectively, in the BLYP model of a-InSb generated without vdW.

In summary, we can conclude that the inclusion of the vdW correction does not affect sizably the structure of the amorphous phase of InSb.

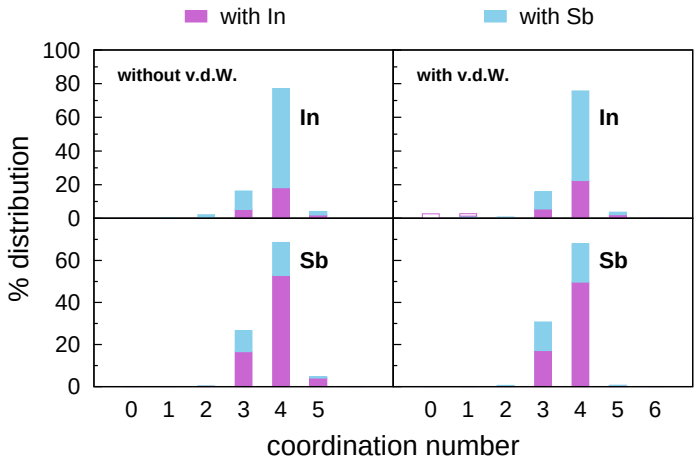

Figure A.5.: Distribution of the coordination numbers of a-InSb models obtained with the BLYP functional with or without van der Waals interactions. The contributions from the different atom pairs are indicated by different colours.

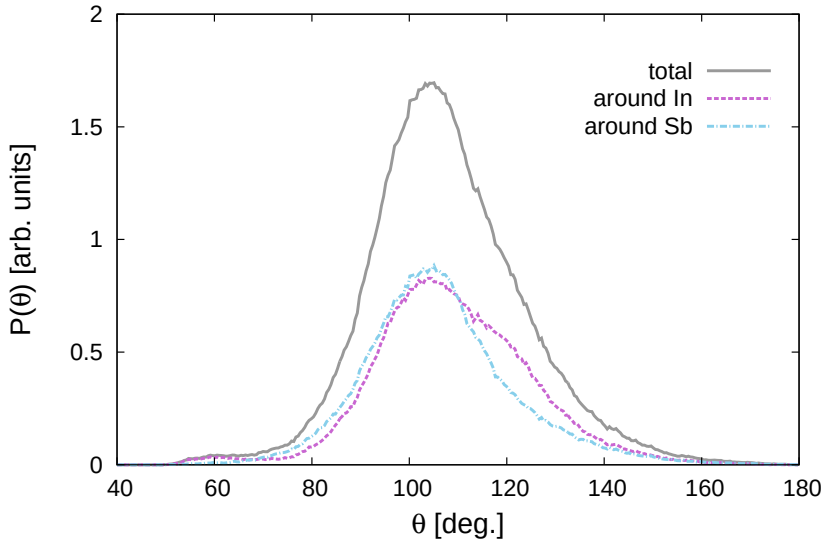

Figure A.6.: Bond angles distribution for the model of a-InSb obtained with the BLYP functional and with van der Waals interactions. The total distribution (continuous grey line) was also resolved into two contribution form In species (violet dashed line) and Sb species (blue dot-dashed line).

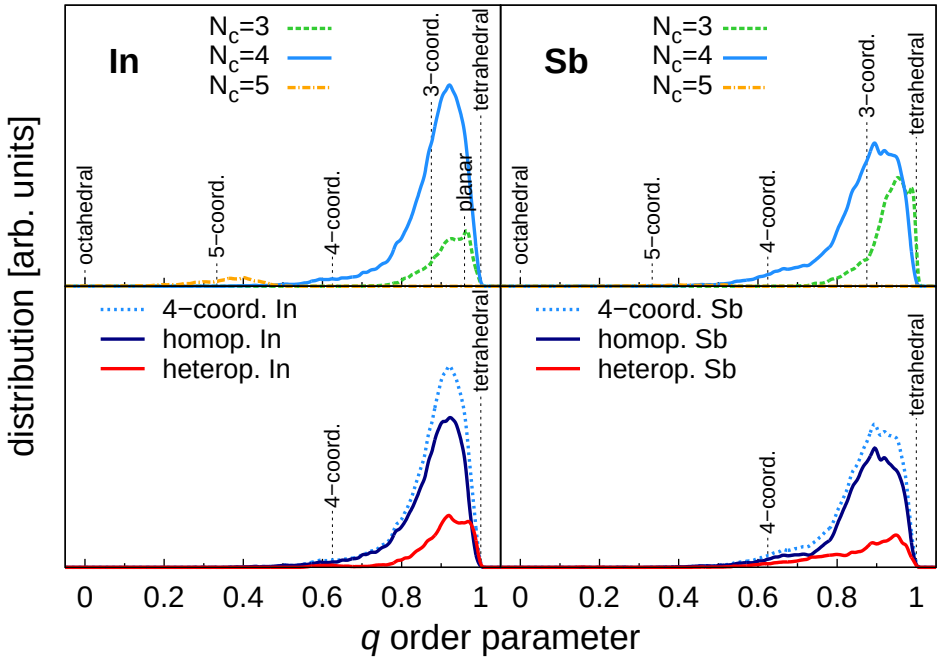

Figure A.7.: Distribution of the local order parameter q for tetrahedricity (see text) for the model of amorphous InSb obtained from an MD quenching with the BLYP functional and van der Waals interactions. The distributions for In, Sb and Te atomic species are resolved for different coordination numbers. Vertical lines indicate the values of q for ideal geometries in defective octahedral sites with N_c coordination, tetrahedral and three-fold coordinated planar sites. The distributions for four-fold coordinated In and Sb atoms are further resolved for atoms with and without homopolar bonds (lower panels).

B. Resistance drift

The electronic properties of the models of a-GeTe, generated by quenching from the melt through NN-MD simulations, were calculated on the relaxed structures at the DFT-PBE level with the Engel-Vosko (EV) functional to better reproduce the band gap (see Section 4). Here we report the same calculations of Section 4 performed with the PBE exchange and correlation functional. The Kohn-Sham states are very similar in PBE and EV calculations. However, the larger gap in the EV simulations leads to a stronger localization of defect states with respect to PBE calculations.

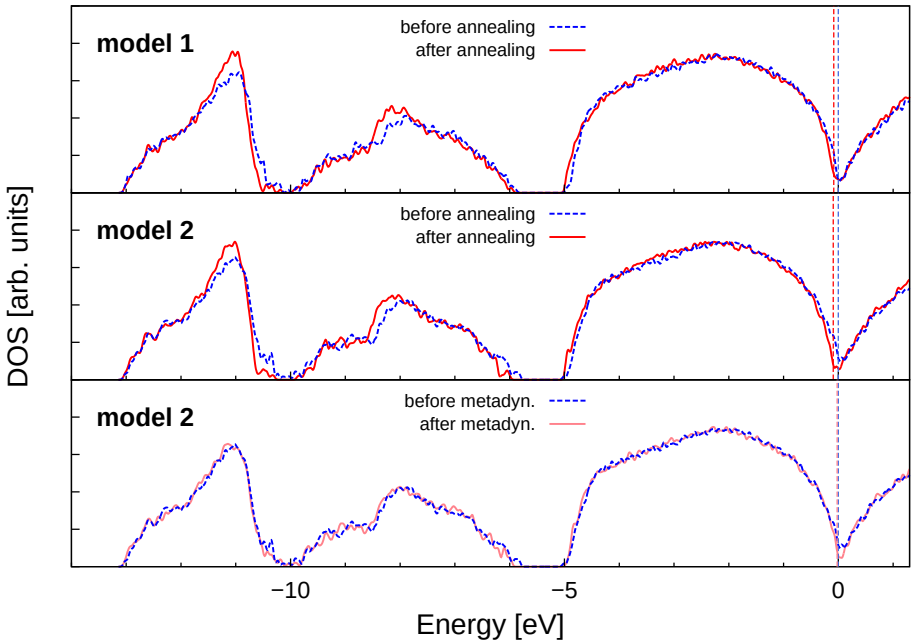

Figure B.1.: Electronic density of states (DOS) of the two models before (dashed blue line) and after (continuous red line) annealing (upper panels) and for model 2 before and after metadynamics (lower panel) in the full energy range. The PBE functional was used. The DOS before and after annealing/metadynamics are aligned at the lowest energy states at about -14 eV which also leads to an alignment of the lower edges of the *p*-like bands at about -4.5 eV. The vertical dashed line indicates the highest occupied Kohn-Sham (KS) state which coincides with the zero of energy before annealing/metadynamics. The DOS was computed from KS orbitals at the supercell Γ-point broadened with a Gaussian function with variance of 27 meV.

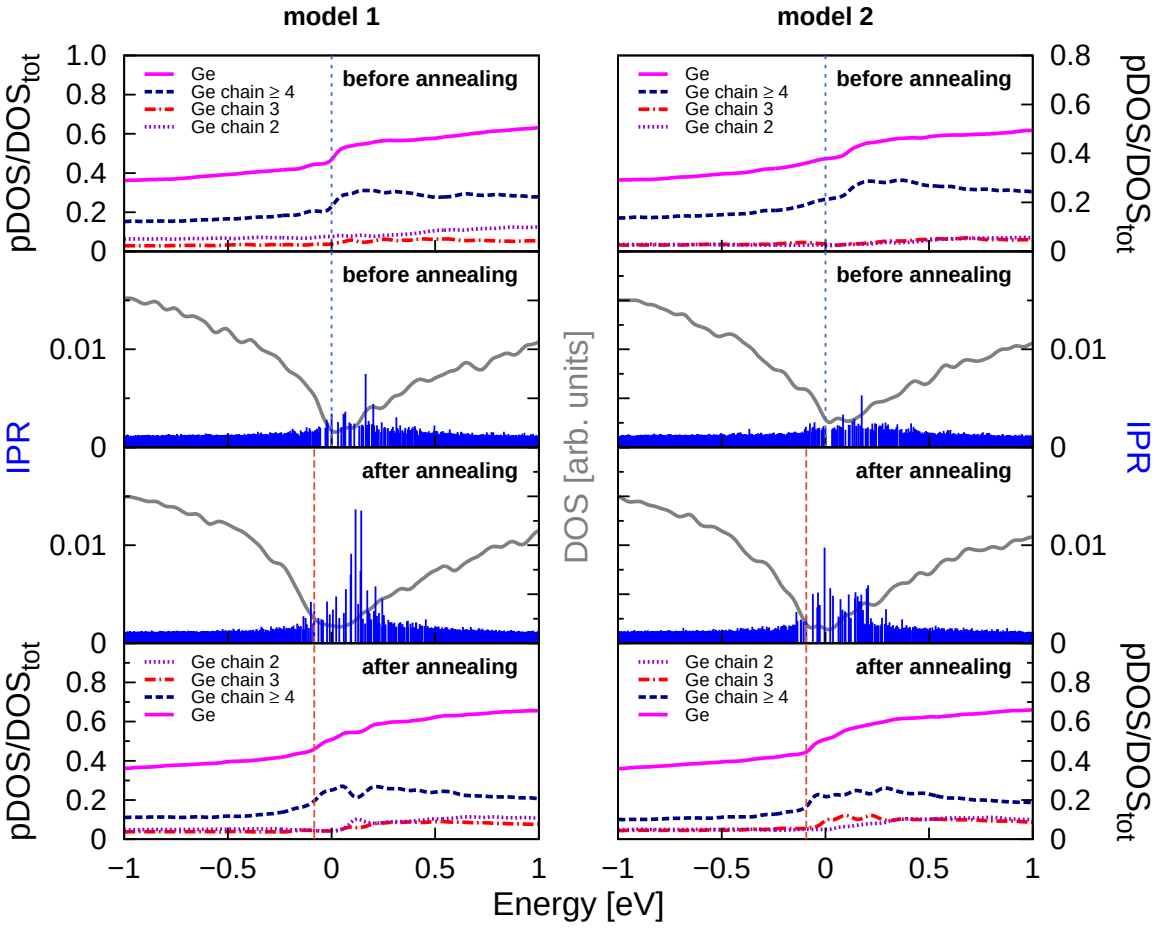

Figure B.2.: Projection of the electronic density of states (DOS) on Ge atoms belonging to Ge chains of different lengths normalized to the total DOS (model 1 and model 2 in the left and right panels), total DOS and the Inverse Participation Ratio (IPR, see text) for the two models of a-GeTe before annealing (upper panels) and after annealing at 500 K (lower panels). The PBE functional was used, the corresponding plots for the EV functional are given in Figure 4.13. The DOS before and after annealing are aligned at the lowest energy states at about -14 eV as shown in Figure B.1 which also leads to an alignment of the lower edges of the *p*-like bands at about -4.5 eV. The vertical dashed line indicates the highest occupied KS state which coincide with the zero of energy before annealing. The DOS was computed from KS orbitals at the supercell Γ-point broadened with a Gaussian function with variance of 27 meV.

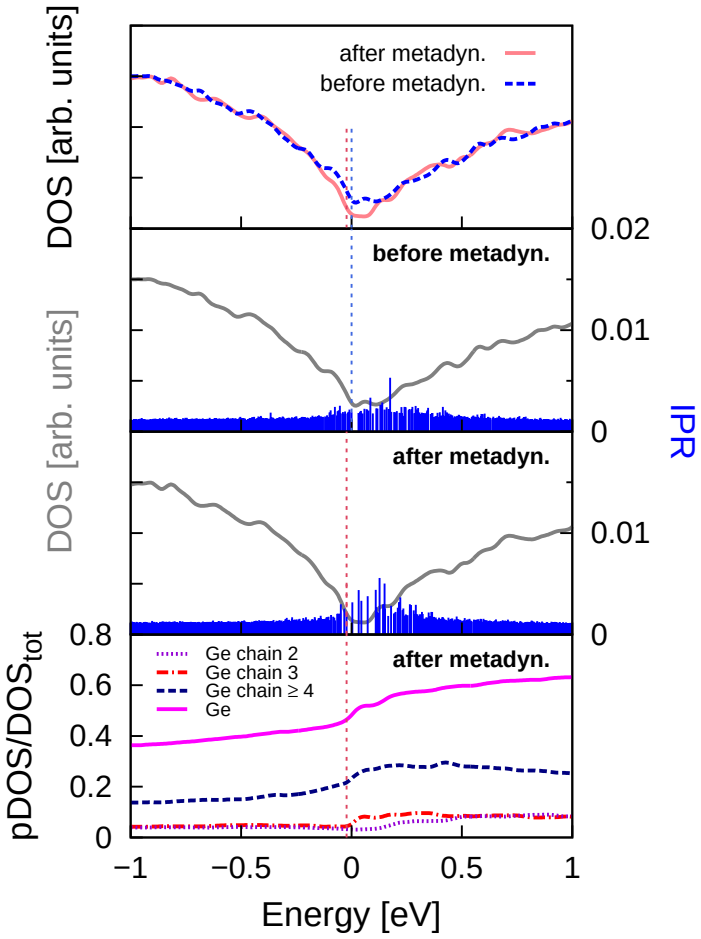

Figure B.3.: Upper panel: electronic density of states (DOS) close to the band gap of model 2 of a-GeTe before (dashed line) and after (continuous line) metadynamics simulations (zooming of Figure B.1, lower panel). Lower panels: inverse participation ratio (IPR) superimposed to the DOS for the model before and after metadynamics simulations and projection of the electronic DOS on Ge atoms belonging to Ge chains of different lengths normalized to the total DOS for the model after metadynamics simulations; the corresponding plot before metadynamics is shown in the upper right panel of Figure B.2. The PBE functional was used, the corresponding plots for the EV functional are given in Figure 4.20. The DOS are aligned with respect to the lowest energy states of the model before and after metadynamics. The zero of the energy corresponds to the highest occupied orbital (HOMO) of the model before metadynamics. The dashed vertical lines indicate the position of the HOMO state for the two models. The DOS were computed from KS orbitals at the supercell Γ-point broadened with a Gaussian function with variance of 27 meV.

Publications

Works related to this thesis

- J. H. Los, T. D. Kühne, S. Gabardi and M. Bernasconi,
"First principles simulation of amorphous InSb", Phys. Rev. B **87**, 184201 (2013)

- J. H. Los, T. D. Kühne, S. Gabardi and M. Bernasconi,
"First-principles study of the amorphous In_3SbTe_2 phase change compound", Phys. Rev. B **88**, 174203 (2013)

- A. Bouzid, M. Boero, C. Massobrio, S. Gabardi and M. Bernasconi,
"First principles study of amorphous $Ga_4Sb_6Te_3$ phase change alloy", Phys. Rev. B; in press

- J. H. Los, S. Gabardi, M. Bernasconi and T. D. Kühne,
"Inverse simulated annealing: Improvements and application to amorphous InSb"; submitted

- S. Gabardi, S. Caravati, G. C. Sosso, J. Behler and M. Bernasconi,
"Microscopic origin of resistance drift in the amorphous state of the phase change compound GeTe"; submitted

- S. Gabardi, S. Caravati, J. H. Los, T. D. Kühne and M. Bernasconi,
"Influence of exchange and correlation functional on the structure of amorphous InSbTe alloys"; in preparation

Other publications

- S. Gabardi, S. Caravati, M. Bernasconi, M. Parrinello,
"*Density functional simulations of Sb-rich GeSbTe phase change alloys*" J. Phys.: Condens. Matter **24**, 385803 (2012)

Bibliography

[1] A. L. Lacaita, *Sol. Stat. Elec.* **50**, 24 (2006).

[2] A. L. Lacaita and D. J. Wonters, *Phys. Stat. Sol. (a)* **205**, 2281 (2008).

[3] M. Wuttig and N. Yamada, *Nat. Mater.* **6**, 824–832 (2007).

[4] R. Bez and A. Pirovano, *Materials science in semiconductor processing* **7**, 349 (2004).

[5] Y. Maeda, H. Andoh, I. Ikuta and H. Minemura, *J. Appl. Phys.* **64**, 1715 (1988).

[6] E. T. Kim, J. Y. Lee and Y. T. Kim, *Phys. Status Solidi RRL* **3**, 103 (2009).

[7] S. Raoux, A. K. König, H.-Y. Cheng, D. Garbin, R. W. Cheek, J. L. Jordan-Sweet and M. Wuttig, *Phys. Stat. Sol.* **249**, 1999 (2012).

[8] H.-Y. Cheng, S. Raoux and J. L. Jordan-Sweet, *Appl. Phys. Lett.* **98**, 121911 (2011).

[9] R. Fallica, T. Stoycheva, C. Wiemer and M. Longo, *Phys. Status Solidi RRL* **11**, 1009 (2013).

[10] Y. Jung, S.-H. Lee, A. T. Jennings and R. Agarwal, *Nano Lett. 8*, 2056 (2008).

[11] H.-S. P. Wong, S. Raoux, S.-B. Kim , J. Liang, J. P. Reifenberg, B. Rajendran, M. Asheghi and K. E. Goodson, *IEEE Proc.* **98**, 2201 (2010).

[12] M. Mitra, Y. Jung, D. S. Gianola and R. Agarwal, *Appl. Phys. Lett.* **96**, 222111 (2010).

[13] A. Pirovano, A. L. Lacaita, F. Pellizzer, S. A. Kostylev, A. Benvenuti and R. Bez, *IEEE Trans. Elec. Dev.* **51**, 714 (2004).

[14] G. C. Sosso, G. Miceli, S. Caravati, J. Behler and M. Bernasconi, *Phys. Rev. B* **85**, 174103 (2012).

[15] J. F. Dewald, A. D. Pearson, W. R. Northover and W. F. Peck, *J. Electrochem. Soc.* **109**, 243C (1962).

[16] S. R. Ovshinsky, *Phys. Rev. Lett.* **21**, 1450–3 (1968).

[17] A. Redaelli and A. Pirovano, *Nanotechnology* **22**, 254021 (2011).

[18] A. L. Lacaita and A. Redaelli, *Microelectron. Eng.* **109**, 351 (2013).

[19] G. W. Burr, B. N. Kurdi, J. C. Scott, C. H. Lam, K. Gopalakrishnan and R. S. Shenoy, *IBM J. Res. Dev.* **52**, 449 (2008).

[20] M. H. R. Lankhorst, B. W. S. M. M. Ketelaars and R. A. M. Wolters, *Nat. Mater.* **4**, 347 (2005).

[21] D. Lencer, M. Salinga and M. Wuttig, *Adv. Mater.* **23**, 2030–2058 (2011).

[22] S. R. Ovshinsky, Q. Ye, D. A. Strand, W. Czubatyj, "Electrically erasable directly overwritable multibit single cell memory elements and arrays fabricated therefrom" *U.S. Patent Editor* (1995).

[23] S. Raoux, C. T. Rettner, J. L. Jordan-Sweet, A. J. Kellock, T. Topuria, P. M. Rice and D. C. Miller, *J. Appl. Phys.* **102**, 094305 (2007).

[24] T. Nirschl, J. B. Philipp, T. D. Happ, G. W. Burr, B. Rajendran, M.-H. Lee, A. Schrott, M. Yang, M. Breitwisch, C.-F. Chen, E. Joseph, M. Lamorey, R. Cheek, S.-H. Chen, S. Zaidi, S. Raoux, Y. C. Chen, Y. Zhu, R. Bergmann, H.-L. Lung and C. Lam, *IEEE Int. Elec. Dev. Meet.*, 461 (2007).

[25] Y. F. Lai, J. Feng, B. W. Qiao, Y. F. Cai, Y. Y. Lin, T. A. Tang, B. C. Cai and B. Chen, *Appl. Phys. A, Mater. Sci. Process.* **84**, 21 (2006).

[26] F. Rao, Z. Song, M. Zhong, L. Wu, G. Feng, B. Liu, S. Feng and B. Chen, *Jpn. J. Appl. Phys.* **46**, L25 (2007).

[27] Y. Zhang, J. Feng, Y. Zhang, Z. Zhang, Y. Lin, T. Tang, B. Cai and B. Chen, *Phys. Stat. Sol., Rapid Res. Lett.* **1**, R28 (2007).

[28] B. Liu, T. Zhang, J. Xia, Z. Song, S. Feng and B. Chen, *Semicond. Sci. Technol.* **19**, L61 (2004).

[29] K. Nakayama, M. Takata, T. Kasai, A. Kitagawa and J. Akita, *J. Phys. D, Appl. Phys.* **40**, 5061 (2007).

[30] F. Bedeschi, R. Fackenthal, C. Resta, E. M. Donze, M. Jagasivamani, E. C. Buda, F. Pellizzer, D. W. Chow, A. Cabrini, G. Calvi, R. Faravelli, A. Fantini, G. Torelli, D. Mills, R. Gastaldi and G. Casagrande, *IEEE J. Sol.-Stat. Circ.* **44**, 217 (2009).

[31] B. Yu, X. Sun, S. Ju, D. B. Janes and M. Meyyappan, *IEEE Trans. Nanotech.* **7**, 496 (2008).

[32] M. Chen, K. A. Rubin and R. W. Barton, *Appl. Phys. Lett.* **49**, 502–504 (1986).

[33] Y. K. Kim, U. Hwang, Y. J. Cho, H. M. Park, M. H. Cho, P. S. Cho and J. H. Lee, *Appl. Phys. Lett.* **90**, 021908 (2007).

[34] N. Matsuzaki, K. Kurotsuchi, Y. Matsui, O. Tonomura, N. Yamamoto, Y. Fujisaki, N. Kitai, R. Takemura, K. Osada, S. Hanzawa, H. Moriya, T. Iwasaki, T. Kawahara, N. Takaura, M. Terao, M. Matsuoka and M. Moniwa, IDEM Tech. Dig. 738 (2005).

[35] T. Morikawa, K. Kurotsuchi, M. Kinoshita, M. Matsuzaki, Y. Matsui, Y. Fujisaki, S. Hanzawa, A. Kotabe, M.Terao, H. Moriya, T. Iwasaki, M. Matsuoka, F. Nitta, M. Moniwa, T. Koga and N. Takaura, *Electron Devices Meeting, 2007. IEDM 2007. IEEE International*, 307-310 (2007).

[36] E. T. Kim, J. Y. Lee and Y. T. Kim, *Phys. Status Solidi RRL* **3**, 103 (2009).

[37] H. Y. Cheng, S. Raoux and J. L. Jordan-Sweet, *Appl. Phys. Lett.* **98**, 121911 (2011).

[38] M. Boniardi, D. Ielmini, I. Tortorelli, A. Redaelli, A. Pirovano, M. Allegra, M. Magistretti, C. Bresolin, D. Erbetta, A. Mondelli, E. Varesi, F. Pellizzer, A. L. Lacaita, R. Bez, *Solid-State Electronics* **58**, 11-16 (2011).

[39] G. Betti Beneventi, E. Gourvest, A. Fantini, L. Perniola, V. Sousa, S. Maitrejean, J. C. Bastien, A. Bastard, A. Fargeix, B. Hyot, C. Jahan, J.F. Nodin, A. Persico, D. Blachier, A. Toffoli, S. Loubriat, A. Roule, S. Lhostis, H. Feldis, G. Reimbold, T. Billon, B. De Salvo, L. Larcher, P. Pavan, D. Bensahel, P. Mazoyer, R. Annunziata and F. Boulanger, *IEEE International Memory Workshop* (2010).

[40] G. E. Ghezzi, J. Y. Raty, S. Maitrejean, A. Roule, E. Elkaim and F. Hippert, *Appl. Phys. Lett.* **99**, 151906 (2011).

[41] C.-C. Chang, T.-R. Yew and T.-S. Chin, *Cryst. Eng. Comm.* **13**, 5642 (2011).

[42] M. Chen, K. A. Rubin and R. W. Barton, *Appl. Phys. Lett.* **49**, 502 (1986).

[43] G. Burns, P. Merkelbach, C. Schlockermann, M. Salinga, M. Wuttig, T. D. Happ, J. B. Philipp and M. Kund, *Appl. Phys. Lett.* **95**, 043108 (2009).

[44] K. Schubert and H. Fricke, *Z. Naturforsch* **6a**, 781 (1951).

[45] J. Goldak, C. S. Barrett, D. Innes and W. Youdelis, *J. Chem. Phys.* **44**, 3323 (1966)

[46] P. Fons, A. V. Kolobov, M. Krbal, J. Tominaga, K. S. Andrikopoulos, S. N. Yannopoulos, G. A. Voyiatzis and T. Uruga, *Phys. Rev. B* **82**, 155209 (2010).

[47] D. I. Bletskan, *Journal of Ovonic Research* **1**, 53 (2005).

[48] J. Y. Raty, V. V. Godlevsky, J. P. Gaspard, C. Bichiara, M. Bionducci, R. Bellissent, R. Ceolin, J. R. Chelikowsky and Ph. Ghosez, *Phys. Rev. B* **65**, 115205 (2002).

[49] J. L. F. Da Silva, A. Walsh and H. Lee, *Phys. Rev. B* **78**, 224111 (2008).

[50] K. Shportko, S. Kremers, M. Woda, D. Lencer, J. Robertson and M. Wuttig, *Nat. Mat.* **7**, 653 (2008).

[51] I. I. Petrov, R. M. Imamov and Z. G. Pinsker, *Sov. Phys. Cryst.* **13**, 339 (1968).

[52] B. J. J. Kooi and J. Th. M. De Hosson, *J. Appl. Phys.* **92**, 3584 (2002).

[53] T. Matsunaga N. Yamada and Y. Kubota, *Acta Cryst.* **B60**, 685 (2004).

[54] Z. Sun, J. Zhou and R. Ahuja, *Phys. Rev. Lett.* **96**, 055507 (2006).

[55] G. C. Sosso, S. Caravati, C. Gatti, S. Assoni and M. Bernasconi, *J. Phys.: Condens. Matter.* **21**, 245401 (2009).

[56] E. Rotunno, L. Lazzarini, M. Longo and V. Grillo, *Nanoscale* **5**, 1557 (2013).

[57] N. Yamada, E. Ohno, K. Nishiuchi, N. Akahira and M. Takao, *J. Appl. Phys.* **69**, 2849 (1991).

[58] N. Yamada and T. Matsunaga, *J. Appl. Phys.*, **88**, 12 (2000).

[59] T. Nonaka, G. Ohbayashi, Y. Toriumi, Y. Mori and H. Hashimoto , *Thin Solid Films* **370**, 258 (2000).

[60] S. Shamoto, N. Yamada, T. Matsunaga, Th. Proffen, J. W. Richardson, J. H. Chung and T. Egami, *Appl. Phys. Lett.* **86**, 081904 (2005).

[61] A. V. Kolobov, P. Fons, J. Tominaga, A. L. Ankudinov, S. N. Yannopouls and K. S. Andrikopoulos, *J. Phys.: Condens. Matter* **16**, S5103–S5108 (2004).

[62] Y. Maeda and M. Wakagi, *Jpn. J. Appl. Phys.* **30**, 101 (1991).

[63] K. Hirota, K. Nagino and G. Ohbayashi, *J. Appl. Phys.* **82**, 65 (1997).

[64] K. S. Andrikopoulos, S. N. Yannopoulos, G. A. Voyiatzis, A. V. Kolobov, M. Ribes and J. Tominaga, *J. Phys.: Condens. Matter* **18**, 965–979 (2006).

[65] A. V. Kolobov, P. Fons, A. I. Frenkel, A. L. Ankudinov, J. Tominaga and T. Uruga, *Nat. Mater.* **3**, 703–708 (2004).

[66] S. Kohara, K. Kato, S. Kimura, H. Tanaka, T. Usuki, K. Suzuya, H. Tanaka, Y. Moritomo, T. Matsunaga, N. Yamada, Y. Tanaka, H. Suematsu and M. Takata, *Appl. Phys. Lett.* **89**, 201910 (2006).

[67] J. Hegedüs and S. R. Elliott, *Nat. Mater.* **7**, 399 (2008).

[68] J. Akola and R. O. Jones, *Phys. Rev. B* **76**, 235201 (2007).

[69] J. Akola and R. O. Jones, *J. Phys.: Condens. Matter* **20**, 465103 (2008).

[70] J. Akola and R. O. Jones, *Phys. Rev. Lett.* **100**, 205502 (2008).

[71] S. Caravati, M. Bernasconi, T. D. Kühne, M. Krack and M. Parrinello, *Appl. Phys. Lett.* **91**, 171906 (2007).

[72] S. Caravati, M. Bernasconi, T. D. Kühne, M. Krack and M. Parrinello, *J. Phys.: Condens. Matter* **21**, 255501 (2009); **21**, 499803(E) (2009); **22**, 399801(E) (2010).

[73] R. Mazzarello, S. Caravati, S. Angioletti-Uberti, M. Bernasconi and M. Parrinello, *Phys. Rev. Lett.* **104**, 085503 (2010); **107**, 039902(E) (2011).

[74] G. C. Sosso, S. Caravati, R. Mazzarello and M. Bernasconi, *Phys. Rev. B* **83**, 134201 (2011).

[75] K. S. Andrikopoulos, S. N. Yannopoulos, A. V. Kolobov, P. Fons and J. Tominaga, *J. Phys. Chem. Sol.* **68**, 1074 (2007).

[76] J. Akola, J. Larrucea and R. O. Jones, *Phys. Rev. B* **83**, 094113 (2011).

[77] V. L. Deringer, W. Zhang, M. Lumeij, S. Maintz, M. Wuttig, R. Mazzarello and R. Dronskowsk, *Angew. Chem. Int. Ed.* **53**, 10817 (2014).

[78] T. H. Lee and S. R. Elliott, *Phys. Rev. Lett.* **107**, 145702 (2011).

[79] J. Orava, A. L. Greer, B. Gholipour, D. W. Hewak and C. E. Smith, *Nat. Mater.* **11**, 279 (2012).

[80] G. C. Sosso, J. Behler and M. Bernasconi, *Phys. Status Solidi B* **249**, 1880 (2012).

[81] J. Akola and R. O. Jones, *Phys. Stat. Sol. B* **249**, 1851 (2012).

[82] C. A. Angell, *Science* **267**, 1924 (1995); P. G. Debenedetti and F. H. Stillinger, *Nature* **410**, 259 (2001).

[83] N. Ciocchini, M. Cassinerio, D. Fugazza and D. Ielmini, *IEEE Trans. Electron. Dev.* **60**, 3767 (2013).

[84] J. A. Kalb, C. Y. Wen, F. Spaepen, H. Dieker and M. Wuttig, *J. Appl. Phys.* **98**, 054902 (2005).

[85] S. Privitera, S. Lombardo, C. Bongiorno, E. Rimini and A. Pirovano, *J. Appl. Phys.* **102**, 013516 (2007).

[86] A. Redaelli, D. Ielmini, U. Russo and A. L. Lacaita, *IEEE Trans. Electron. Dev.* **53**, 3040 (2006).

[87] G. C. Sosso, G. Miceli, S. Caravati, F. Giberti, J. Behler and M. Bernasconi, *J. Phys. Chem. Lett. 4*, 4241 (2013).

[88] E. R. Weeks, J. C. Crocker, A. C. Levitt, A. Schonfield and D. A. Weitz, *Science* **287**, 627 (2000).

[89] G. C. Sosso, J. Colombo, E. Del Gado, J. Behler and M. Bernasconi, *J. Phys. Chem. B* **118**, 13621 (2014).

[90] T. Wang, O. Gulbiten, R. Wang, Z. Yang, A. Smith, B. Luther-Davies and P. Lucas, *J. Phys. Chem. B* **118**, 1436 (2014).

[91] H. Iwasaki, M. Harigaya, O. Nonoyama, Y. Kageyama, M. Takahashi, K. Yamada, H. Deguchi and Y. Ide, *Jpn. J. Appl. Phys.* **32**, 5241 (1993).

[92] H. J. Shin, Y. S. Kang, A. Benayad, K. H. Kim, Y. M. Lee, M. C. Jung, T. Y. Lee, D. S. Suh, K. H. P. Kim, C. K. Kim and Y. Khang, *Appl. Phys. Lett.* **93**, 021905 (2008).

[93] X.-R. Zhang and M. Wuttig, *Chin. Phys. Lett.* **21**, 1096 (2004).

[94] Y. I. Kim, E. T. Kim, J. Y. Lee and Y. T. Kim, *Appl. Phys. Lett.* **98**, 091915 (2011).

[95] Y. T. Kim, E. T. Kim, C. S. Kim and J. Y. Lee, *Phys. Status Solidi RRL* **5**, 98 (2011).

[96] J.-K. Ahn, H.-J. Cho, K.-W. Park and S.-G. Yoon, *J. Electrochem. Soc.* **157**, D353 (2010).

[97] J.-K. Ahn, K.-W. Park, H.-J. Jung and S.-G. Yoon, *Nanolett.* **10**, 472 (2010).

[98] von K. Denker and A. Rabenua, *Z. Anorg. Allg. Chemie* **333**, 201 (1964).

[99] L. Men, F. Jiang and F. Gan, *Mater. Sci. Eng. B* **47**, 18 (1997).

[100] B. Legendre, B. Gather and R. Blachnik, *Zeitschrift für Metallkunde* **71**, 588 (1980).

[101] T. Schröder, T. Rosenthal, S. Grott, C. Stiewe, J. de Boor and O. Öckler, *Z. Anorg. Allg. Chemie* **639**, 2536 (2013).

[102] J. H. C. Hogg and H. H. Sutherland, *Acta Cryst.* **32**, 2689 (1976).

[103] K.-F. Kao, C.-C. Chang, F. T. Chen, M.-J. Tsai and T.-S. Chin, *Script. Mater.* **63**, 855 (2010).

[104] Y. Lu, S. Song, Z. Song and B. Liu, *J. Appl. Lett.* **109**, 064503 (2011).

[105] J. A. Dixon and S. R. Elliott, *Appl. Phys. Lett.* **104**, 141905 (2014).

[106] C.-M. Lee, W.-S. Yen, J.-P. Chen and T.-S. Chin, *IEEE Trans. Magn.*, **41**, 1022 (2005).

[107] H.-Y. Cheng, K.-F. Kao, C.-M. Lee and T.-S. Chin, *IEEE Trans. Magn.* **43**, 927 (2007).

[108] Y.-C. Chu, P.-C. Chang, K.-F. Kao, S.-C. Chang, T.-S. Chin, *Thin Solid Films* **518**, 7316 (2010).

[109] A. T. H. Chuang, Y.-C. Chen, Y.-C. Chu, P.-C. Chang, K.-F. Kao, C.-C. Chang, K.-Y. Hsieh, T.-S. Chin and C.-Y. Lu, *IEEE Internat. Mem. Wor.* (2011).

[110] K. P. Chik, *Sol. Stat. Commumn.* **33**, 1019 (1980).

[111] L. L. Snead and S. J. Zinkle, *Nucl. Instrum. Methods Phys. Res. B* **191**, 497 (2002).

[112] N. M. J. Conway, A. Ilie, J. Robertson, W. I. Milne and A. Tagliaferro, *Appl. Phys. Lett.* **73**, 2456 (1998).

[113] J. Luckas, A. Piarristeguy, G. Bruns, P. Jost, S. Grothe, R. Schmidt, C. Longeaud and M. Wuttig, *J. Appl. Phys.* **113**, 023704 (2013).

[114] M. Boniardi, A. Redaelli, A. Pirovano, I. Tortorelli, D. Ielimini and F. Pellizzer, *J. Appl. Phys.* **105**, 084506 (2009).

[115] D. Ielmini, S. Lavizzari, D. Sharma and A. L. Lacaita, *Appl. Phys. Lett.* **92**, 193511 (2008).

[116] S. Kasap and P. Capper, *Springer Handbook of Electronic and Photonic Materials* pag. 566 (2006).

[117] J. Luckas, D. Krebs, S. Grothe, J. Klomfaß, R. Carius, C. Longeaud and M. Wuttig, *J. Mater. Res.* **28**, 1139 (2013).

[118] C. Longeaud, J. Luckas, D. Krebs, R. Carius, J. Klomfaßand M. Wuttig, J. Appl. Phys. 112, 113714 (2012).

[119] H. Fritzsche, *J. Phys. Chem. Sol.* **68**, 878 (2007).

[120] B. Huang and J. Robertson, *Phys. Rev. B* **81**, 081204(R) (2010).

[121] D. Ielmini and Y. Zhang, *Appl. Phys. Lett.* **90**, 192102 (2007).

[122] D. Ielmini and Y. Zhang, *J. Appl. Phys.* **102**, 054517 (2007).

[123] A. Calderoni, M. Ferro, D. Ielmini and P. Fantini, *IEEE Elec. Dev. Lett.* **31**, 1023 (2010).

[124] D. Ielmini, D. Sharma, S. Lavizzari and A. L. Lacaita, *IEEE Trans. Elec. Dev.* **56** 1070 (2009).

[125] D. Ielmini, A. L. Lacaita and D. Mantegazza, *IEEE Trans. Elec. Dev.* **54**, 308 (2007).

[126] I. V. Karpov, M. Mitra, D. Kau, G. Spadini, Y. A. Kryukov and V. G. Karpov, *J. Appl. Phys.* **102**, 124503 (2007).

[127] M. Boniardi and D. Ielmini, *Appl. Phys. Lett.* **98**, 243506 (2011).

[128] M. Rizzi, A. Spessot, P. Fantini and D. Ielmini, *Appl. Phys. Lett.* **99**, 223513 (2011).

[129] W. Njoroge, H.-W. Wöltegens and M. Wuttig, *J. Vac. Sci. Technol. A* **20**, 230 (2002).

[130] M. Kastner, *Phys. Rev. B*, **7**, 5237 (1973).

[131] S. Braga, A. Cabrini and G. Torelli, *Appl. Phys. Lett.* **94**, 092112 (2009).

[132] J. Im, E. Cho, D. Kim, H. Horii, J. Ihm and S. Han, *Phys. Rev. B* **81**, 245211 (2010).

[133] E. P. Donovan, F.Spaepen, D. Turnbull, J. M. Poate and D. C. Jacobson, *J. Appl. Phys.* **57**, 1795 (1985).

[134] S. Roorda, W. C. Sinke, J. M. Poate, D. C. Jacobson, S. Dierker, B. S. Dennis, D. J. Eaglesham, F. Spaepen and P. Fuoss, *Phys. Rev. B* **44**, 3702 (1991).

[135] D. B. Miracle, T. Egami, K. M. Flores and K. F. Kelton, *MRS Bull.* **32**, 629 (2007).

[136] J. A. Kalb, M. Wuttig and F. Spaepen, *J. Mater. Res.* **22**, 748 (2007).

[137] P. Fantini, S. Brazzelli, E. Cazzini and A. Mani, *Appl. Phys. Lett.* **100**, 013505 (2012).

[138] P. Fantini, M. Ferro, A. Calderoni and S. Brazzelli, *Appl. Phys. Lett.* **100**, 213506 (2012).

[139] D. Krebs, T. Bachmann, P. Jonnalagadda, L. Dellmann and S. Raoux, *New J. Phys.* **16**, 043015 (2014).

[140] K. V. Mitrofanov, A. V. Kolobov, P. Fons, X. Wang, J. Tominaga, Y. Tamenori, T. Uruga, N. Ciocchini and D. Ielmini, *J. Appl. Phys.* **115**, 173501 (2014).

[141] M. Krbal, A. V. Kolobov, P. Fons, K. V. Mitrofanov, Y. Tamenori, J. Hegedüs, S. R. Elliott and J. Tominaga, *Appl. Phys. Lett.* **102**, 111904 (2013).

[142] T. D. Kühne, M. Krack, F. R. Mohamed and M. Parrinello, *Phys. Rev. Lett.* **98**, 066401 (2007).

[143] D. Frenkel and B. Smit, *Understanding molecular simulation*, Academic Press.

[144] M. Allen and D. Tildesley, *Computer Simulation of Liquids*, Clarendon Press – Oxford (1989).

[145] L. Verlet, *Phys. Rev.* **159**, 98 (1967).

[146] L. Verlet, *Phys. Rev.* **165**, 201 (1967).

[147] T. Schneider and E. Stoll, *Phys. Rev. B* **17**, 1302 (1978).

[148] H. B. Callen, T. A. Welton, *Phys. Rev.* **83**, 34–40 (1951).

[149] P. Hohenberg and W. Kohn, *Phys. Rev.* **136**, B864 (1964).

[150] W. Kohn and L. J. Sham, *Phys. Rev.* **140**, A1133 (1965).

[151] J. P. Perdew, K. Burke, M. Ernzerhof, *Phys. Rev. Lett.* **77**, 3865 (1996).

[152] A. D. Becke, *Phys. Rev. A* **38**, 3098 (1988); C. Lee, W. Yang and R. G. Parr, *Phys. Rev. B* **37**, 785 (1988).

[153] A. D. Becke, *J. Chem. Phys.* **98**, 1372 (1993).

[154] A. V. Krukau, O. A. Vydrov, A. F. Izmaylov and G. E. Scuseria, *J. Chem. Phys.* **125**, 224106 (2006).

[155] M. Ernzerhof and G. E. Scuseria, *J. Chem. Phys* **110**, 5029 (1999).

[156] G. Lippert, J. Hutter and M. Parrinello, *Mol. Phys.* **92**, 477 (1997).

[157] J. VandeVondele, M. Krack, F. Mohamed, M. Parrinello, T. Chassaing and J. Hutter, *Comput. Phys. Comm.* **167**, 103-128 (2005).

[158] S. Goedecker, M. Teter and J. Hutter, *Phys. Rev. B* **54**, 1703 (1996).

[159] M. Krack, *Theor. Chem. Acc.* **114**, 145 (2005).

[160] R. Martin, *Electronic Structure – Basic Theory and Pratical Methods*, Cambridge University Press (2004) pg. 56.

[161] R. Car and M. Parrinello, *Phys. Rev. Lett.* **55**, 2471 (1985).

[162] J. Kolafa, *J. Comput. Chem.* **25**, 335 (2004).

[163] J. H. Los and T. D. Kuehne, *Phys. Rev. B* **87**, 214202 (2013).

[164] D. Frenkel and B. Smit, *Understanding Molecular Simulation*, Academic Press, San Diego, CA (2002).

[165] J. Behler and M. Parrinello, *Phys. Rev. Lett.* **98**, 146401 (2007).

[166] A. Waibel, *Neural Comp.* **1**, 39 (2008).

[167] A. Rajavelu, M. Musavi and M. Shirvaikar, *Neural Networks* **2**, 387 (1989).

[168] A. Chen and M. Leung, *J. Forecasting* **24**, 403 (2005).

[169] C. Marzban and A. Witt, *Weather and Forecasting* **16**, 600 (2001).

[170] K. Funahashi, *Neural Networks* **2**, 183 (1989).

[171] G. Cybenko, *Math. Contr. Sign. Sys.* **2**, 303 (1989).

[172] H. Gassner, M. Probst, A. Lauenstein and K. Hermansson, **J. Phys. Chem. A** *102*, 4596 (1998).

[173] J. Behler, K. Reuter and M. Scheffler, *Phys. Rev. B* **77**, 115421 (2008).

[174] S. Hobday, R. Smith and J. Belbruno, *Model. Simul. Mater. Sci. Eng.* **7**, 397 (1999).

[175] A. Bholoa, S. Kenny and R. Smith, *Nucl. Instrum. Methods Phys. Res. Sect. B* **255**, 1 (2006).

[176] E. Sanville, A. Bholoa, R. Smith and S. Kenny, *J. Phys. Cond. Matt.* **20**, 285219 (2008).

[177] A. Laio and M. Parrinello, *Proc. Nat. Acad. Sci.* **99**, 12562 (2002).

[178] A. Barducci, G. Bussi and M. Parrinello, *Phys. Rev. Lett.* **100**, 020603 (2008).

[179] A. Laio and F. L. Gervasio, *Rep. Prog. Phys.* **71**, 126601 (2008).

[180] M. Bonomi, D. Branduardi, G. Bussi, C. Camilloni, D. Provasi, P. Raiteri, D. Donadio, F. Marinelli, F. Pietrucci, R. A. Broglia and M. Parrinello, PLUMED: a portable plugin for free energy calculations with molecular dynamics, *Comp. Phys. Comm.* **180** 1961 (2009); http://www.plumed-code.org/documentation

[181] T. Zens, P. Becla, A. M. Agarwal, L. C. Kimerling and A. Drehman, *J. Cryst. Growth* **334**, 84 (2011).

[182] E. Suzuki, H. Miura, M. Harigaya, K. Ito, N. Iwata and A. Watada, *Jpn. J. Appl. Phys.* **44**, 3598 (2005).

[183] O. Madelung, *Semiconductors: Data Handbook*, Springer, Berlin pp. 154-161 (2004).

[184] S. Minomura, O. Shimomura, K. Asaumi, H. Oyanagi and K. Takemura, *Proceedings of 7th International Conference on Amorphous and Liquid Semiconductors*, University of Edinburgh, pp. 53-57 (1977).

[185] N. J. Shevchik and W. Paul, *J. Non-Cryst. Solids* **13**, 55 (1974).

[186] M. Krbal, A. V. Kolobov, B. Hyot, B. André, P. Fons, R. E. Simpson, T. Uruga, H. Tanida and J. Tominaga, *J. Appl. Phys.* **108**, 023506 (2010).

[187] J. P. Rino, D. S. Borges and S. C. Costa, *J. Non-Cryst. Solids* **348**, 17 (2004).

[188] J. P. Rino, P. S. Pizani and S. C. Costa, *Braz. J. Phys.* **34**, 347 (2004).

[189] T. Gu, X. Bian, J. Qin and C. Xu, *Phys. Rev. B* **71**, 104206 (2005).

[190] L. Wang, X. S. Chen, Y. Huang, W. Lu and J. J. Zhao, *Physica B* **405**, 2481 (2010).

[191] M. Krack and M. Parrinello, in *High Performance Computing in Chemistry* (J. Grotendorst ed.), NIC vol. **25**, 29-51 (2004); http://cp2k.berlios.de.

[192] J. VandeVondele and J. Hutter, *J. Chem. Phys.* **127**, 114105 (2007).

[193] J. Akola and R. O. Jones, *Phys. Rev. B* **87**, 184201 (2013).

[194] H. J. Monkhorst and J. D. Pack, *Phys. Rev. B* **13**, 5188 (1976).

[195] D. Toton, J. He, G. Gory, J. J. Kolodziej, S. Godlewski, L. Kantorovich and M. Szymonski, *J. Phys.: Condens. Matter* **22**, 265001 (2010).

[196] S. Caravati, M. Bernasconi, M. Parrinello, *Phys. Rev. B* **81**, 014201 (2010).

[197] S. Caravati, M. Bernasconi, T. D. Kuhne, M. Krack and M. Parrinello, *Phys. Rev. Lett.* **102**, 205502 (2009).

[198] S. Caravati, D. Colleoni, R. Mazzarello, T. D. Kühne, M. Krack, M. Bernasconi and M. Parrinello, *J. Phys.: Condens. Matter* **23**, 265801 (2011).

[199] E. Spreafico, S. Caravati and M. Bernasconi, *Phys. Rev. B* **83**, 144205 (2011).

[200] S. Gabardi, S. Caravati, M. Bernasconi and M. Parrinello, *J. Phys.: Condens. Matter* **24**, 385803 (2012).

[201] J. H. Los, T. D. Kühne, S. Gabardi and M. Bernasconi, *Phys. Rev. B* **87**, 184201 (2013).

[202] S. Grimme, *J. Comput. Chem.* **27**, 1787 (2006).

[203] O. Shimomurka, A. Saumin, N. Sakai and S. Minomura, *Phil. Mag.* **34**, 839 (1976).

[204] K. Wezka, A. Bouzid, K. J. Pizzey, P. S. Salmon, A. Zeidler, S. Klotz, H. E. Fischer, C. L. Bull, M. G. Tucker, M. Boero, S. Le Roux, C. Tugène and C. Massobrio, *Phys. Rev. B* **90**, 054206 (2014).

[205] S. Le Roux, A. Bouzid, M. Boero and C. Massobrio, *Phys. Rev. B* **86**, 224201 (2012).

[206] S. Le Roux, A. Bouzid, M. Boero and C. Massobrio, *J. Chem. Phys.* **138**, 174505 (2013).

[207] J. R. Errington and P. G. Debenedetti, *Nature* **409**, 318 (2001).

[208] N. Marzari and D. Vanderbilt, *Phys. Rev. B* **56**, 12847 (1997).

[209] P. L. Silvestrelli, N. Marzari, D. Vanderbilt and M. Parrinello, *Solid State Commun.* **107**, 7 (1998).

[210] G. Berghold, C. J. Mundy, A. H. Romero, J. Hutter and M. Parrinello, *Phys. Rev. B* **61**, 10040 (2000).

[211] http://www.cpmd.org/, Copyright IBM Corp 1990-2013, Copyright MPI für Festkörperforschung Stuttgart (1997-2001).

[212] D. S. Franzblau, *Phys. Rev. B* **44**, 4925 (1991).

[213] G. Henkelman, A. Arnaldsson and H. Jonsson, *Comp. Mat. Sci. 36*, 354 (2006).

[214] J. H. Los, T. D. Kuehne, S. Gabardi and M. Bernasconi, *Phys. Rev. B* **88**, 174203 (2013).

[215] S. Caravati, M. Bernasconi and M. Parrinello, *J. Phys.: Condens. Matter* **22**, 315801 (2010).

[216] W. Wełnic, S. Botti, M. Wuttig and L. Reining, *C. R. Physique* **10**, 514 (2009).

[217] W. Wełnic, S. Botti, L. Reining and M. Wuttig, *Phys. Rev. Lett.* **98**, 236403 (2007).

[218] L.-M. Peng, S. L. Dudarev and M. J. Whelan, *High Energy Electron Diffraction and Microscopy*.

[219] J. L. F. Da Silva, A. Walsh, S.-H. Wei and H. Lee, *J. Appl. Phys.* **106**, 113509 (2009).

[220] H. Hahn and W. Klinger, *Z. Anorg. Chem.* **97**, 260 (1979).

[221] H. Inuzuka and S. Sugaike, *Proc. Japan Acad.* **30**, 383, (1954).

[222] N. Troullier and J. L. Martins, *Phys. Rev. B* **43**, 1993 (1991).

[223] S. G. Louie, S. Froyen and M. L. Cohen, *Phys. Rev. B* **26**, 1738 (1982).

[224] S. Nosé, *Mol. Phys.* **52**, 255 (1984).

[225] S. Nosé, *J. Chem. Phys.* **81**, 511 (1984).

[226] W. G. Hoover, *Phys. Rev. A* **31**, 1695 (1985).

[227] G. J. Martyna, M. L. Klein and M. Tuckerman, *J. Chem. Phys.* **97**, 2635 (1992).

[228] M. Julien-Pouzol, S. Jaulmes, M. Guittard and F. Alapini, *Acta Cryst. B* **35**, 2848 (1979).

[229] P. Giannozzi, S. Baroni, N. Bonini, M. Calandra, R. Car, C. Cavazzoni, D. Ceresoli, G. L. Chiarotti, M. Cococcioni, I. Dabo, A. Dal Corso, S. de Gironcoli, S. Fabris, G. Fratesi, R. Gebauer, U. Gerstmann, C. Gougoussis, A. Kokalj, M. Lazzeri, L. Martin-Samos, N. Marzari, F. Mauri, R. Mazzarello, S. Paolini, A. Pasquarello, L. Paulatto, C. Sbraccia, S. Scandolo, G. Sclauzero, A. P. Seitsonen, A. Smogunov, P. Umari and R. M. Wentzcovitch, *J. Phys.: Condens. Matter* **21**, 395502 (2009).

[230] J. Kalikka, J. Akola and R. O Jones, *J. Phys: Condens. Matter* **25**, 115801 (2013).

[231] R. Bader, *Atoms in Molecules: A Quantum Theory*, Oxford University Press, New York (1990).

[232] J. Behler, *RuNNer - A Neural Network Code for High-Dimensional Potential-Energy Surfaces*; Lehrstuhl für Theoretische Chemie, Ruhr-Universität Bochum, Bochum, Germany.

[233] W. Smith and T. R. Forester, *J. Mol. Graph.* **14**, 136 (1996).

[234] G. Bussi, D. Donadio and M. Parrinello, *J. Chem. Phys.* **126**, 01410 (2007).

[235] L. Giacomazzi, P. Umari and A. Pasquarello, *Phys. Rev. B.* **74**, 155208 (2006).

[236] G. C. Sosso, D. Donadio, S. Caravati, J. Behler and M. Bernasconi, *Phys. Rev. B* **86**, 104301 (2012).

[237] E. Engel and S. H. Vosko, *Phys. Rev. B* **47**, 13164 (1993).

[238] P. J. Steinhardt, D. R. Nelson and M. Ronchetti, *Phys. Rev. B* **28**, 784 (1983).

[239] J. S. van Duijneveldt and D. Frenkel, *J. Chem. Phys.* **96**, 4655 (1992).

[240] A. Barducci, M. Bonomi and M. Parrinello, *Wires Comp. Mat. Sci.* **1**, 826 (2011).